UNIVERSITÉ PARIS

THÈSE DE DOCTORAT
DE L'UNIVERSITÉ PSL

Préparée à MINES Paris

A global level-set based full-field numerical framework to simulate diffusive solid-state phase transformation in polycrystalline metallic materials
Développement d'un cadre numérique en champ complet basé sur l'approche level-set pour simuler la transformation de phase diffusive à l'état solide dans les matériaux métalliques en polycristaux

Soutenue par
Nitish CHANDRAPPA
Le 08 February, 2024

École doctorale n°364
Sciences Fondamentales et Appliquées (ED SFA)

Spécialité
Mécanique Numérique et Matériaux

Composition du jury :

Carl E. KRILL III Prof., Ulm University, Germany	*Président*
Julien BRUCHON Prof., MINES Saint-Etienne, IMT, France	*Rapporteur*
Lukasz MADEJ Prof., AGH University, Poland	*Rapporteur*
Nicolas CHARBONNIER Dr., ArcelorMittal, France	*Examinateur*
Madeleine BIGNON Dr., MINES Paris, France	*Examinateur*
Marc BERNACKI Prof., MINES Paris, France	*Directeur de thèse*

MINES PARIS | PSL

Acknowledgements

I would like to extend my deepest gratitude to my parents, and the rest of my family for their unwavering love, encouragement, and sacrifices throughout my academic journey. Their endless support and motivation have been the cornerstone of my success, and I am forever grateful for their belief in me.

I owe a debt of gratitude to my supervisor, Prof. Marc Bernacki, for his mentorship, insightful guidance, and unwavering moral support throughout the entirety of my research journey. His constant encouragement, and wisdom have been instrumental in keeping me motivated and grounded on the right track during this thesis.

I am immensely thankful to Mines Paris university and the CEMEF laboratory for providing the necessary resources and academic environment conducive to learning and research. I would also like to thank ARMINES and all the associated industrial partners for funding this research.

Special thanks to the MSR team for their collaboration, support, and valuable insights during the course of this study. Their contributions have enriched the quality of my research.

To all the friends I made along this journey, especially Marion ROTH, who shared the same workspace with me, thank you for your camaraderie, encouragement, and shared experiences. Your friendship has made this academic endeavor all the more rewarding and enjoyable with a plethora of memories to cherish.

Lastly, I extend my sincere appreciation to all the individuals who have supported me in various capacities, whether through their participation in this study or their words of encouragement along the way. Your contributions have been invaluable, and I am deeply grateful for your support.

Contents

List of Symbols

$\boldsymbol{n}$	Outward unit normal on the interface
T	Temperature
T_{A3}	Equilibrium solvus temperature
p	Pressure
G	Gibbs free energy of the system
G_m	Molar Gibbs free energy of the system
ΔG	Difference in Gibbs free energies
G^α	Gibbs free energy of phase α
G^γ	Gibbs free energy of phase γ
G_{eq}	Minimum Gibbs free energy of the system
D_p	Driving pressure
μ	Chemical potential of a solute
μ_A^α	Chemical potential of a solute A in phase α
μ_A^γ	Chemical potential of a solute A in phase γ
n_j	Number of moles of solute j
f^α	Fraction of phase α
f^γ	Fraction of phase γ
x_0	Nominal alloy composition
x_{eq}^γ	Equilibrium composition of phase γ
x_{eq}^α	Equilibrium composition of phase α
σ	Interface energy
$\sigma_{\gamma/\alpha}$	Interface energy of the γ/α phase boundary
ΔG^*	Nucleation barrier or activation energy for nucleation
ΔG_d	Gibbs free energy released due to annihilation of defects
r^*	Critical nucleus size
$\dot{I}$	Nucleation rate per unit volume
$\boldsymbol{x}$	Spatial coordinate vector
t	time
Z	Non-equilibrium Zeldovich factor
β_n	Frequency factor
N_s	Nucleation site density
k_B	Boltzmann constant
τ	Incubation time
Δg_V^α	Driving pressure for the nucleation of phase α

x_n^α	α phase nucleus composition
V_m^α	Molar volume of phase α
$\boldsymbol{v}$	Interface velocity field
M	Scalar interface mobility
P	Driving pressure
P_C	Chemical driving pressure
P_κ	Capillarity induced driving pressure
P_S	Driving pressure due to the stored energy
$\Delta G_{\gamma\rightarrow\alpha}$	Driving pressure for phase transformation from γ to α phase
$\Delta\theta$	Disorientation angle
R	Universal gas constant
Q_m	Activation energy for grain boundary migration
M_0	Pre-exponential mobility factor
κ	Trace of the curvature tensor
D_α^i	Diffusivity of solute i in α phase
D_γ^i	Diffusivity of solute i in γ phase
$\boldsymbol{J}$	Solute flux
Γ	Interface
x_Γ^γ	Interfacial concentration in γ phase
x_Γ^α	Interfacial concentration in α phase
x_i^γ	Concentration of solute i in γ phase
x_i^α	Concentration of solute i in α phase
$x_i^\gamma\big\|_{eq}$	Equilibrium concentration of solute i in γ phase
$x_i^\alpha\big\|_{eq}$	Equilibrium concentration of solute i in α phase
$u_i^{p_h}$	u-fraction of solute i in phase p_h
P_{SD}	Solute drag driving pressure
ΔG_{SD}	Magnitude of the solute drag pressure
D_Γ^X	Diffusivity of solute X within the interfacial region
E	Interaction energy profile
v_n	Norm of the interface velocity
N_V	Number of solute atoms per unit volume
E_0	Binding energy of the solute to the interface
α_C	Cahn's solute drag pressure parameter
β_C	Cahn's solute drag pressure parameter
φ	Level-set function
φ_i	ith global level-set function
φ_α	Level-set function characterizing the regions belonging to α phase
φ_{max}	Maximum of all the global level-set functions
Ω	Global domain
$\boldsymbol{n_e}$	Extended unit normal
$\boldsymbol{v_e}$	Extended velocity field
l_e	Extension length
Δt	Resolution time step

N_{LS}	Number of level-set functions
N_G	Number of grains
ϕ	Diffuse phase interface function
η	Diffuse interface thickness
x_i	Total concentration of solute i
k_p^i	Partitioning ratio for solute i
$k_{p_{eq}}^i$	Equilibrium partitioning ratio for solute i
D^*	Mixed diffusivity
ψ	Test function
$\mathcal{E}$	Stored energy
$\chi_{\gamma\gamma}$	Characteristic function of the grain interfaces belonging to γ phase
$\chi_{\gamma\alpha}$	Characteristic function of the phase interfaces between γ and the α phase
$\chi_{\alpha\alpha}$	Characteristic function of the grain interfaces belonging to α phase
$\mathscr{M}_{SD}$	Solute drag pressure coefficient
$\boldsymbol{v}_{[\![\mathcal{E}]\!]}$	Interface kinetics due to the stored energy
$\boldsymbol{v}_{\boldsymbol{\Delta G_{\gamma\alpha}}}$	Interface kinetics due to the phase transformation
χ_{G_i}	Characteristic function of grain i
β_e	Parameter controlling the degree of smoothness of velocity field
G_i	ith grain
M_{ij}	Interface mobility between grains i and j
δ_{cf}	Distance threshold for computing interface characteristic function
$\mathscr{F}_s$	Sense function
χ_α	Characteristic function of α phase
χ_γ	Characteristic function of γ phase
$M_{\gamma\alpha}$	Phase interface mobility
ϵ	Half of reinitialization thickness
Υ	Proportionality factor
T^R	Reference temperature
ΔT	Local undercooling
T^{eq}	Equilibrium temperature
H	Enthalpy
S	Entropy
$m_{A-i}^{\alpha/(\alpha+\gamma)}$	Slope of the solvus boundary line of the α phase in $A-i$ binary phase diagram
$m_{A-i}^{\gamma/(\alpha+\gamma)}$	Slope of the solvus boundary line of the γ phase in $A-i$ binary phase diagram
$x_i^\alpha\big\|_R$	Concentration of solute i in α phase at the reference temperature

$x_i^{\gamma}\big\|_R$	Concentration of solute i in γ phase at the reference temperature
$x_i^{\alpha}\big\|_R^{PE}$	Concentration of solute i in α phase at the reference temperature under para-equilibrium conditions
$x_i^{\gamma}\big\|_R^{PE}$	Concentration of solute i in γ phase at the reference temperature under para-equilibrium conditions
$\Delta S^{\gamma\alpha}$	Entropy difference between phases γ and α at the temperature T
$\Delta S_{A3}^{\gamma\alpha}$	Entropy difference between phases γ and α at the $A3$ temperature
$\Delta S_R^{\gamma\alpha}$	Entropy difference between phases γ and α at the reference temperature
f_R^{α}	Equilibrium fraction of phase α at the reference temperature
f_R^{γ}	Equilibrium fraction of phase γ at the reference temperature
$\boldsymbol{n}_b$	Outward unit normal to the domain boundary
T_{N_s}	Nucleation start temperature
δT_N	Nucleation temperature range
ΔT_N	Nucleation undercooling
δl_N	Nucleation shield distance
ρ_N	Nucleation density
n_N	Number of nuclei
$\dot{n}_N$	Nucleation rate
$\dot{T}$	Cooling rate
χ_{sn}	Nucleation site characteristic function

List of Abbreviations

FCC	Face Centered Cubic
BCC	Body Centered Cubic
ReX	Recrystallization
GG	Grain Growth
SSPT	Solid-State Phase Transformation
DSSPT	Diffusive Solid-State Phase Transformation
CNT	Classical Nucleation Theory
GBM	Grain Boundary Migration
GB	Grain Boundary
PB	Phase Boundary
HAGB	High Angle Grain Boundary
LE-P	Local equilibrium - Partitioning
LE-NP	Local equilibrium - Negligible Partitioning
OE	Ortho-Equilibrium
PE	Para-Equilibrium
LS	Level-Set
GLS	Global Level-Set
FE	Finite Element
EF	Éléments Finis
JMAK	Johnson-Mehl-Avrami-Kolmogorov
MFM	Mean Field Models
FFM	Full-Field Models
DRX	Dynamic Recrystallization
PDRX	Post-Dynamic Recrystallization
PF	Phase-Field
MPF	Multi Phase-Field
PFM	Phase-Field Method
CA	Cellular Automata
MC	Monte Carlo potts
RVE	Representative Volume Element
VTM	Voronoi Tessellation Method
LVTM	Laguerre-Voronoi Tessellation Method
VIIM	Voronoi Implicit Interface Method
CDR	Convective-Diffusive-Reactive

CD	Convective-Diffusive
IMEX	IMplicit-EXplicit
SDK	Software Development Kit
SPP	Second Phase Particle
LSW	Lifshitz - Slyozof - Wagner
OR	Ostwald Ripening
LS-NM	Level-set Numerical Model
PF-NM	Phase Field Numerical Model
SAM	Semi-Analytical Model
CFL	Courant–Friedrichs–Lewy

Introduction

Change is an inherent, perpetual force woven into the very fabric of our universe. Much like how we maneuver life's transitions with adaptability and resilience, materials similarly adjust their structures and properties in response to external stimuli. Thus, engineering of materials with desirable properties suitable for a particular condition is not sufficient. It is also important to incorporate how subtle changes in temperature, pressure or material composition drive the transformation of the underlying microstructure. These microstructural transformations hold the potential to significantly impact the functional characteristics of a broad spectrum of industrial components across various applications. Hence, being cognizant of how to control these changes and their effects in reshaping the fundamental fabric of materials is essential to modern engineering of materials. A significant aspect of this comprehension is linked to understanding and predicting the underlying microstructural evolution. Numerical modeling serves as the guiding light, illuminating the path toward deeper insights into complex processes governing the microstructural evolution.

Acknowledging prevailing environmental concerns and economic pressures, especially amidst intense international competition among metallurgical industries, the digitization of material engineering processes emerges as an integral element in shaping the materials of the future. Numerical predictions assist in optimizing the process chain for fabricating metallurgical products tailored for specific applications. Thus there is an increased demand for predicting models due to its direct economic and societal impact on the industries. Consequently, materials of the future are envisioned to take form digitally before materializing in reality.

Around 20 years ago, the predictive capacities of numerical models available to metallurgical industries were somewhat unreliable due to limitations in the modeling scale and hence a restricted description of the involved physics. However, recent advancements in computational resources and the evolution of efficient modeling approaches have sparked a significant demand for mesoscopic numerical models. These models possess the ability to offer more realistic depictions of evolutionary aspects while maintaining a balance between computational expense and accuracy. Mesoscopic models are also pivotal in enriching the material description at the macroscopic scale. This field is the foundation of the DIGIMU consortium led by MINES Paris, Transvalor, the CEA, major industrial companies such as Aperam, ArcelorMittal, Ascometal, Aubert & Duval, Constellium, Framatome, Safran, Timet, and supported by the ANR through the DIGIMU and RealIMotion ANR industrial chairs (grants ANR-16-CHIN-0001 and ANR-22-CHIN-0003, respectively). My Ph.D. work came to life within this consortium.

The microstructural evolution in metallic alloys in the context of hot metal forming typically involves a complex interplay of multiple phenomena occurring simultaneously. The industrial metallurgical products are often subjected to complex thermomechanical treatments or processing conditions such as high plastic deformation at elevated temperatures. Under these conditions, solid-state phase transformations within alloyed materials becomes inevitable, alongside other concurrent phenomena. Currently, most state-of-the-art numerical predictions primarily focus on single-phase microstructural evolution or exclusively model phase transformation, often neglecting the consideration of other coexisting phenomena. While delving into individual phenomena provides valuable insights, focusing solely on singular aspects might inadvertently lead to oversights and limitations in comprehending the holistic behavior of these materials. Such a narrow focus could lead to overlooking crucial interactions that may influence the alloy's mechanical strength, thermal stability, or its susceptibility. Moreover, materials engineering often demands a comprehensive understanding of how these diverse phenomena coalesce to define the macroscopic properties of alloys. Neglecting the concomitant nature of these transformation aspects could limit our ability to predict and optimize material performance under diverse operating conditions. Thus, one of the objectives of this work is to develop a numerical model with a generalized kinetic framework capable of simultaneously and seamlessly accounting for different aspects of microstructural evolution, including diffusive solid-state phase transformation (DSSPT), recrystallization and grain growth.

Each numerical method has its unique scope of application, with some better suited to specific scenarios than others. For modeling recrystallization and grain growth under high plastic deformation, the level-set method stands out as a robust choice and has been effectively utilized. However, regarding diffusive phase transformation at the solid-state, the potential of level-set methods remains largely unexplored. Therefore, the primary goal of this work is to develop a numerical formulation based on the level-set method for modeling DSSPT.

Therefore, within this Ph.D. work, a global level-set based numerical formulation with a generalized kinetic framework, capable of accounting diverse microstructural phenomena will be presented. The primary emphasis with the proposed numerical model will be on diffusive solid-state phase transformation in biphasic polycrystalline context. The application of the level-set method for modeling DSSPT using this proposed framework will be explored through illustrative cases, principally examining austenite decomposition in steels.

Chapter 1 will introduce the concept of microstructural stability and delve into the physical theory of diffusive solid-state phase transformation in metallic alloys.

Chapter 2 will offer insights into the numerical modeling of microstructural evolution. This chapter will comprehensively outline the proposed numerical framework, detailing both the formulation and techniques used.

Chapter 3 will cover the initial analyses of the proposed numerical model, employing benchmarking cases within simple domains to study austenite decomposition in steels. This chapter aims to verify the model's capability to replicate the expected physical aspects of this decomposition. It will also include a sensitivity analysis of critical numerical parameters.

Chapter 4 will showcase the potential of the numerical model in simulating austenite decomposition within complex biphasic polycrystalline microstructures. Additionally, it will illustrate the versatility of the model in simulating other diffusive solid-state phenomena.

Chapter 5 will shed light on the potential outcomes and takeaways of this work, and lay the groundwork for future prospective endeavors.

Chapter 1

General aspects of phase transformation theory in metallic materials

Abstract

In the context of industrial applications, the metallic materials in use are generally subjected to various thermomechanical loads and fluctuations depending on their processing and working conditions. In response, the underlying microstructure of these materials could undergo different kinds of transformation in a quest to recover the stability linked to its composition and the considered thermomechanical conditions. Among the different types of transformation mechanisms, allotropic phase transformation is frequently observed in alloyed materials. Considering that different phases could exhibit different material properties. It may be desirable to stimulate particular phases into the microstructure for their favorable effects on the material. On the other hand, it could be necessary to avoid transforming into some phases that could impart undesirable macroscopic properties into the material. It is thus of great interest to understand phase transformation of a material under different conditions.

As a precursor, this chapter introduces the notion of microstructural stability and transformation for metallic materials at the solid-state. The emphasis is then primarily shifted to diffusive solid-state phase transformation where the important aspects of phase transformation theory are discussed for binary alloys, ternary alloys and beyond.

Résumé

Les matériaux métalliques utilisés dans les applications industrielles sont généralement exposés à diverses charges et fluctuations thermomécaniques en fonction de leurs conditions de traitement et d'utilisation. En conséquence, la microstructure de ces matériaux peut subir différents types de transformation afin de retrouver l'état de stabilité inhérent à sa composition et les conditions thermomécaniques considérées. Entre les différents types de mécanismes de transformation, la transformation de phase allotropique est fréquemment observée dans les alliages métalliques. En considérant que différentes phases peuvent posséder des propriétés différentes, il peut être souhaitable de favoriser l'introduction de certaines phases dans la microstructure pour leur effet bénéfique sur le matériau. D'autre part, il peut être nécessaire d'éviter la transformation vers certaines phases qui pourraient apporter des propriétés macroscopiques

indésirables au matériau. Il est donc essentiel de bien comprendre la transformation de phase d'un matériau sous différentes conditions.

Ce chapitre présente tout d'abord la notion de stabilité et de transformation des microstructures pour les matériaux métalliques à l'état solide. Nous allons ensuite nous concentrer sur la transformation de phase diffusive à l'état solide, où les aspects importants concernant la théorie de la transformation de phase sont discutés pour les alliages binaires, les alliages ternaires et au-delà.

1.1 Introduction: stability and transformation of a microstructure in the solid-state

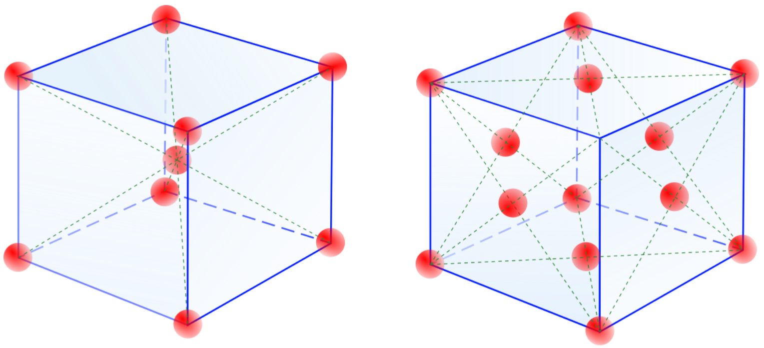
(a) Body Centered Cubic (BCC) (b) Face Centered Cubic (FCC)

Figure 1.1: Examples of simple crystal lattices

A material is said to be crystalline if it has a patterned or structured and periodic arrangement of atoms or molecules within a solid. This well defined, repetitive atomic structure within a particular unit cell constitutes a crystal lattice. Fig.1.1 shows some examples of simple crystal lattices. A perfect monocrystalline material is quite rare (though it is highly desirable for some critical applications). Most metallic materials are polycrystalline with certain inherent defects, comprising of several crystals of varying crystallographic orientation packed together to form a 3D network of internal boundaries. An arrangement of repetitive crystal lattices with the same crystallographic orientation makes up a grain. When two grains belonging to the same phase with the same crystal structural basis but oriented differently come in contact, the disordered or disoriented region between these two grains form the grain boundary. However, if two adjacent grains are made up of different phases with different crystal structural bases, and/ or potentially different chemical compositions, then the boundary formed between them is qualified as a phase boundary (interphase boundary). The topological distribution and arrangement of these grains, phases, their interfacial boundaries, and other potential defects comprises the microstructure of the material. Fig.1.2 illustrates a simple representative 2-D microstructure composed of several grains showing the grain/ phase boundaries. Γ_{12} represents the grain boundary, while Γ_{34} is an example of a phase boundary between grains of different phases (say α and γ). In 3-D, if we ignore the translation vector characterizing the inter-displacement between two crystals (which is relevant at the mesoscopic scale), 5 parameters are essential to mathematically define a grain/ phase boundary

[1]: three Euler angles to define the crystallographic disorientation between the two grains, two parameters to define the inclination angle of the grain boundary plane through a unit normal (***n***). The underlying microstructure of the material with its topological arrangement of grains and their size distribution, composition of phases, and the presence of defects directly dictate the properties of the material depending on the processing conditions relevant to the application.

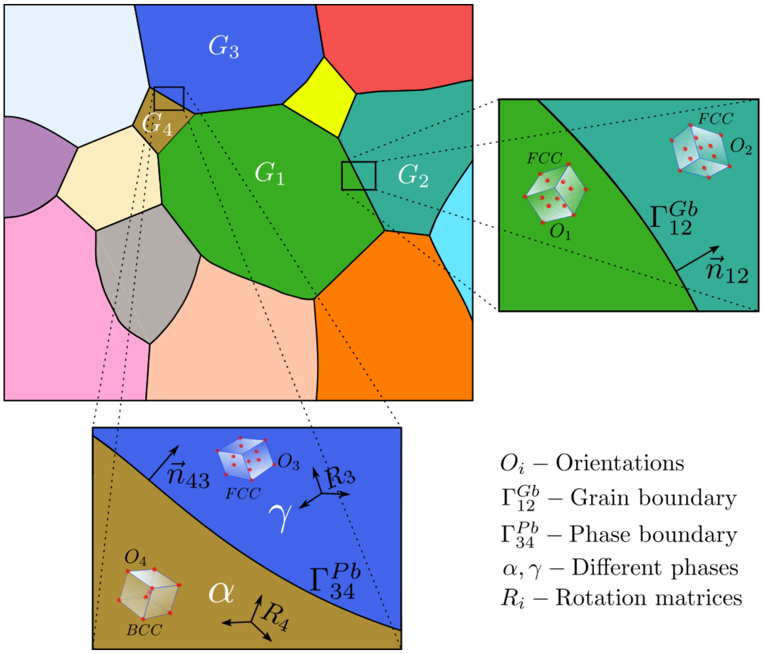

Figure 1.2: Representative 2-D microstructure showing grain and phase boundaries

A microstructure of a system under the influence of certain thermomechanical fluctuations could render itself into a transitory configuration with unstable atomic arrangements. Such systems by nature are thermodynamically driven towards more stable configurations by undergoing necessary atomic rearrangements. In a thermodynamic sense, stability corresponds to minimum free energy configurations of the system at the given conditions. The process of undergoing these atomic rearrangements to lower the free energy of the system constitutes a transformation in general. During the course of a transformation, in the quest for stability, it is possible that a system reaches some intermediate states or configurations corresponding to the local minima of the free energy instead of directly going to the most stable equilibrium state. Such states are classically referred as metastable states having relatively higher free energy than the intended more stable state. The need to negotiate through some potential metastable configurations with higher energy to attain the more stable state act as barriers to a transformation. Thus, for some transformations to take place completely, a certain activation energy (owing to thermal and/or mechanical influences) is required to liberate the system out of metastability. Mathematically, for a closed system at a fixed temperature (T) and pressure (p) with no gradients ($dT = 0, dp = 0$), the stable equilibrium condition is [2]:

$$dG = 0, \tag{1.1}$$

where G is the Gibbs free energy of the system.

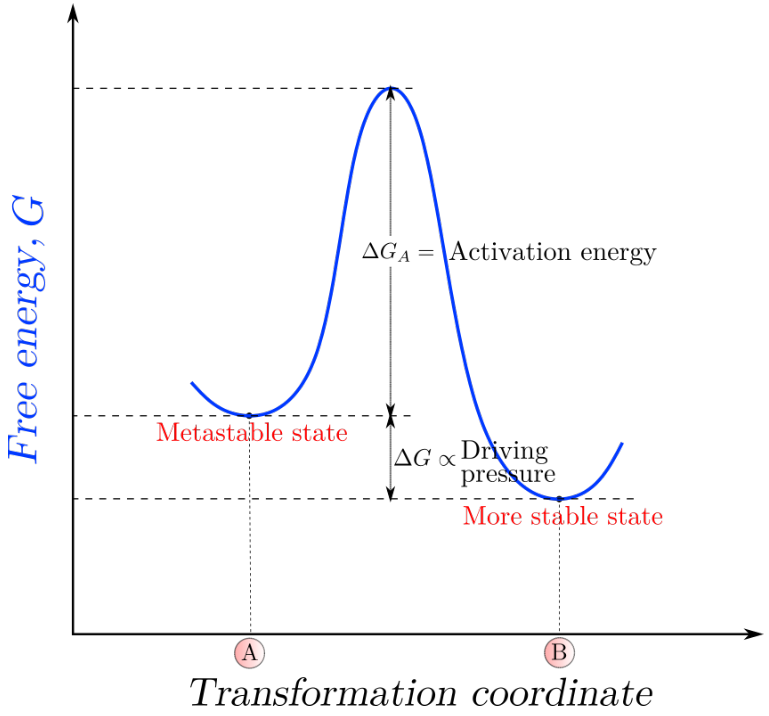

Figure 1.3: Evolution of Gibbs free energy (G) at different system configurations during a transformation [3]

Fig.1.3 illustrates the variation of the free energy of the system at a fixed temperature and pressure, against any variable (ξ) governing the progress of the transformation. The microstructural configurations at both A and B respect the equilibrium condition in Eq.(1.1). However, the A configuration with a higher free energy represents one of the local minima and reflects metastability relative to B. For the system to naturally reach the more stable state at B, it would need to pass through configurations with much higher free energy which is thermodynamically unfavorable. The system would continue to occupy A for a prolonged period unless an activation energy, ΔG_A, is provided to overcome the transformation barrier and undergo the necessary microstructural changes to reach the state B. Other than A and B, all the other configurations having $dG \neq 0$ represent instability and instantly undergo transformation towards the nearest and the favorable free energy minima. In reality, it is almost impossible to reach the true or the most stable state possible for a system at a certain set of conditions as it could require an infinite duration of time to realize, or could be bound by strong transformation barriers. So, within the characteristic time scales of interest, a microstructure at equilibrium would likely occupy one of the metastable states (relative to the global minimum) with as lower free energy as possible or permissible.

The difference in free energies between the initial state and the final transformed state (ΔG) provides a thermodynamic potential that constitutes a driving pressure (D_p) depending on the degree of any internal process relevant to the transformation. It is this driving pressure that powers the transformation and controls the associated kinetics. D_p is defined as [4]:

$$D_p = -\left(\frac{\partial G}{\partial \xi}\right)_{T,p}, \tag{1.2}$$

where ξ is a variable representing the degree of the internal process relevant to the transformation. The system continues to remain unstable and transform as long as the driving pressure is positive or $\left(\frac{\partial G}{\partial \xi}\right)_{T,p} < 0$.

Within a microstructure, all the characteristics such as the point defects, dislocations, surface defects (in the form of grain and interphase boundaries), volume defects, and the bulk of the system itself contribute to the free energy of the system. The notion of a microstructure tending towards a "minimum free energy configuration" implies that the excess free energy accumulated due to these defects is equilibrated through a minimization. The kind of transformation transpiring as a result is generally qualified based on the principal mechanism (depending on the source of the excess free energy) motoring the excess free energy liberation. Consequently, the resultant microstructural changes could include changes in the material phase(s) (with or without modifying the composition), compositional changes, modification of grain characteristics including the grain size distribution, texture, crystallographic orientation, etc., depending on the underlying mechanisms. The sources of instabilities responsible for excess free energy build-up (and the resultant driving pressures for minimization) could be broadly classified to be chemical, strain, or interfacial free energies [3]:

- ***Chemical free energy*** could be characterized by an increase in free energy due to unstable solute concentrations, instabilities of some phases over others at certain temperatures or pressures, differences in chemical potentials of the system component(s) between two or more coexisting phases, inhomogeneities in chemical potentials of the solute (or compositional fluctuations) within a stable system phase. The excess free energy built up as a result is then equilibrated by homogenizing the chemical potentials for all the system components through thermally activated mechanisms like diffusion, and/ or by undergoing phase transformations or decompositions. Solid-state phase transformations [5] such as homogenization of cored solid solutions [6, 7], spinodal decomposition [8, 9], matrix phase transformations (e.g., austenite formation [10] and decomposition [11]), precipitation of secondary phases from supersaturated solid solutions [12], precipitate dissolution [13], etc., are all driven by chemical free energy as the principal component.

- ***Strain free energy*** could be principally associated with an increase in free energy of a crystalline system due to the defects or plastic strains accumulated during plastic deformation. A portion of the work done in a deformation process is stored in the microstructure in the form of dislocations and interfaces, often referred to as stored energy. The presence of these defects render the system thermodynamically unstable. As a result, under thermally favorable conditions, transformation mechanisms such as Recovery, or Recrystallization (ReX) [14] are activated to decrease the stored energy through minimization of the dislocation densities. The contributions arising from elastic misfit strains [15, 16], potentially present between different co-existing phases also fall under this category.

- ***Interfacial free energy*** accounts for the additional free energy stemming from the atoms and their broken atomic bonds at the interfaces. In the context of a polycrystalline microstructure, broadly two types of interfaces could exist that potentially contribute to an increase in free energy: (i) a **grain boundary**, (ii) a **phase boundary**. Under the relevant thermal activation, the excess free energy due to the presence of interfaces creates a driving pressure for the minimization of the interfacial area and hence the associated interface energy to lower the overall system free energy. This makes way for transformations such as the classical Grain Growth (GG) [17, 18], spheroidization [19, 20] (involving also surface diffusion mechanism), precipitate coarsening also well known as Ostwald ripening [21] (though Ostwald ripening is in fact more a phenomenon resulting from a competition between both the chemical and the interfacial contributions).

While the above classification and most of the corresponding transformation mechanisms could be globally characterized by different kinds of driving pressures involved, it is not possible for a complete distinction between them. They could have mutual effects and contributions affecting each other as the mechanisms involved in a microstructural evolution are often concomitant. For example, phase transformations involving changes in the crystal lattice structure could introduce misfit elastic strains at the interphase boundaries to accommodate the potential changes in volume which could result in a strain energy contribution. Another example could be the alteration of the chemical composition between two phases in the presence of curved interfaces resulting in small chemical potential gradients.

Although the above classification takes into account the principal sources of microstructural instabilities, it is non-exhaustive. Instabilities could also be brought about under the influence of irradiation, heterogeneous temperature distribution, electrical, magnetic, and gravitational fields, resulting in some interesting microstructural changes [22–24].

In the following, the discussions will be limited to solid-state phase transformations within the scope of this chapter. The interested readers are directed to cited references for detailed discussions on other kinds of transformation mechanisms.

1.2 Solid-State Phase Transformation (SSPT)

A material undergoing allotropic transmutations from one solid phase to another, under favorable thermomechanical conditions constitute solid-state phase transformations. An allotropic phase could be characterized by a distinct crystal structure and/ or its chemical composition (in the case of alloys). Only certain pure metals exhibit allotropy, albeit under potentially strict or specific thermodynamic conditions. The addition of suitable alloying elements to pure metals at the right proportions can enhance allotropic transformations as they tend to stabilize particular phases over the others. Considering that certain allotropic phases could be desirable for their positive impact on material properties [25], alloying is widely practiced. Alloying elements tend to give the necessary degree of freedom to alter the properties as per the requirements by influencing the evolution processes and their dynamics. So, in the case of metallic alloys, depending on the temperature, pressure, and potentially chemical composition, a particular phase may be more stable with a lower Gibbs free energy than the unstable parent phase. As the system tends to prefer a more stable phase, crystallographic changes occur through lattice rearrangement of the parent phase into the lattice of the product phase. In addition, in the case of diffusive phase transformations, differences in solubility of solutes between different phases cause redistribution of solutes, creating compositional fluctuations.

As depicted in Fig.1.4, phase transformations could be broadly classified into two categories based on the mechanisms involved [26]: (i) Phase transformations involving nucleation and growth

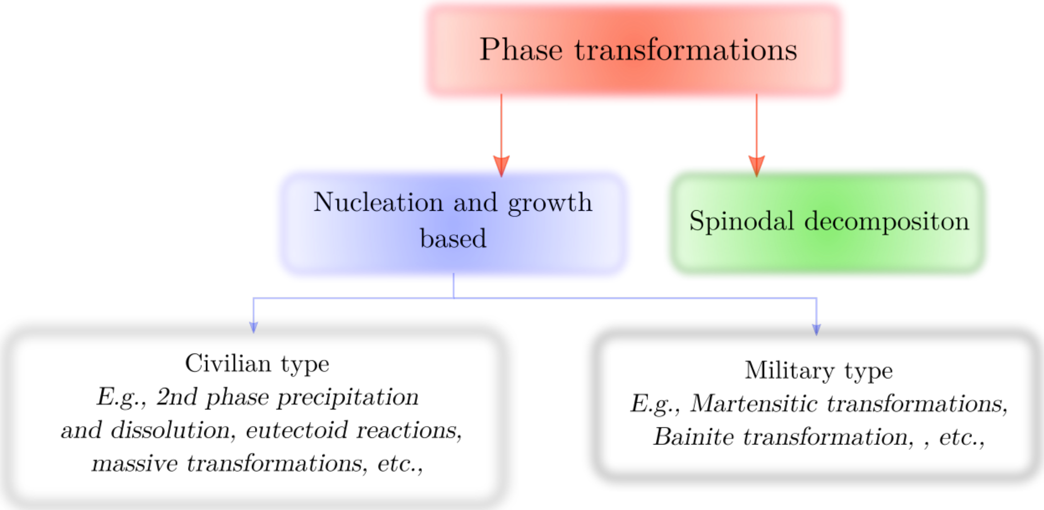

Figure 1.4: Broad classification of phase transformation at the solid-state

mechanisms, and (ii) Spinodal decomposition which involves spontaneous evolution through phase separation, potentially without a nucleation step [27]. Nucleation and growth based phase transformation are generally further classified as: (i) Civilian type transformations, and (ii) Military type transformations. Civilian transformations are characterized by uncoordinated or chaotic atomic movements across non-glissile interfaces. On the other hand, military transformations involve cooperative or coordinated, spontaneous atomic movements across glissile interfaces. Civilian transformations are generally diffusive, resulting in redistribution of solutes through short and long range diffusion of solutes, e.g., precipitation of second phase, precipitate dissolution, eutectoid reactions. However, certain reactions such as massive transformations, austenite formation in pure iron, etc., show the characteristics of civilian type atomic transfer without the change in composition and are generally referred as diffusionless civilian transformations. Military transformations are generally diffusionless involving only changes in the crystal lattice structure, e.g., martensitic transformations. However, in the case of bainitic transformations, diffusion is potentially involved despite showing a military type transformation. The diffusionless military transformation are sometimes also referred to as displacive transformations [28].

In the scope of this work, only diffusive civilian type solid-state phase transformations will be of interest and shall be discussed in detail.

1.2.1 Diffusive solid-state phase transformation (DSSPT)

As described earlier, diffusive transformation is associated with a gradual reorganization of the lattice through short and long-range diffusion of the solute atoms. In metallic alloys, for DSSPT, various phase changes are governed by the variation of Gibbs free energy of each phase with solute composition along with the temperature and the pressure of the system. A priori, to better express the equilibrium conditions of phase transformation in alloys, it is important to define the notion of a chemical potential (μ) of a solute, say i. Chemical potential of a solute i in a system is associated with the change in free energy of the system for a change in the number of solute atoms in the system. Given T, p, and the number of moles of solute j (n_j) are held constant, μ_i is the partial Gibbs free energy [2]:

$$\mu_i = \left(\frac{\partial G}{\partial n_i}\right)_{T,P,n_{j,j\neq i}} \tag{1.3}$$

Consider a simple binary alloy system, A-B, with phases α and γ. For this binary system, if $n = n_A + n_B$ is the total moles of solutes in the system, with $x_A = n_A/n$ and $x_B = n_B/n$ being the molar fractions of the components A and B respectively, then $x_A + x_B = 1$. The molar Gibbs free energy of the system could be expressed as, $G_m = G/n$. The definition of the chemical potential in (1.3) could be rewritten in terms of molar Gibbs free energy as:

$$\left.\begin{aligned} \mu_A^k &= \left(\frac{\partial\left(nG_m\right)}{\partial n_A}\right)_{T,P,n_B} \\ \mu_B^k &= \left(\frac{\partial\left(nG_m\right)}{\partial n_B}\right)_{T,P,n_A} \end{aligned}\right. \quad ,\forall k \in \{\alpha,\gamma\}. \tag{1.4}$$

Making use of the following relations [29]: $x_j = n_j/\sum n_i$; $\partial x_j/\partial n_j = \left(n - n_j\right)/n^2 = \left(1 - x_j\right)/n$; $x_l = n_l/\sum n_i$; $\partial x_l/\partial n_j = -n_l/n^2 = -x_l/n$, we can obtain alternative definitions for the chemical potentials of each phase in terms of the molar fractions of the components for the assumed binary system:

$$\left.\begin{aligned} \mu_A^k &= G_m^k - x_B\frac{\partial G_m^k}{\partial x_B} \\ \mu_B^k &= G_m^k + (1 - x_B)\frac{\partial G_m^k}{\partial x_B} \end{aligned}\right. \quad ,\forall k \in \{\alpha,\gamma\}. \tag{1.5}$$

In the following, the subscript "m" for G used to represent the molar quantity shall be dropped for simplicity, and G shall be implicitly qualified as molar Gibbs free energy unless stated otherwise.

From Eqs.(1.5), the total molar Gibbs free energy of each phase for the considered binary system could be written as:

$$\begin{aligned} G^\alpha &= \mu_A^\alpha x_A^\alpha + \mu_B^\alpha x_B^\alpha, \\ G^\gamma &= \mu_A^\gamma x_A^\gamma + \mu_B^\gamma x_B^\gamma. \end{aligned} \tag{1.6}$$

In general, the total molar Gibbs free energy of a system could be expressed as:

$$G = \sum \mu_i x_i, \tag{1.7}$$

with x_i being the mole fraction of a component i, such that $\sum x_i = 1$.

On the other hand, the total Gibbs free energy of a potential mixture of two phases could be written as:

$$G = f^\alpha G^\alpha + f^\gamma G^\gamma, \tag{1.8}$$

where f^α and f^γ are the phase fractions such that $f^\alpha + f^\gamma = 1$. Phase fractions are a measure of the amount of each phase coexisting in the mixture. As discussed in the previous section, DSSPT aims to minimize this G as much as possible.

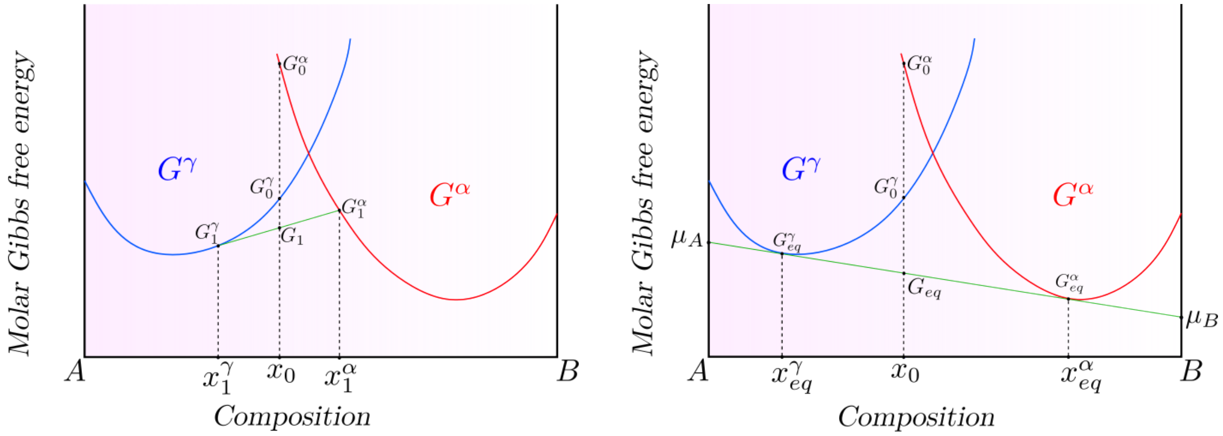

(a) at certain compositions out of equilibrium

(b) at equilibrium

Figure 1.5: Variation of Gibbs free energy with composition for a mixture of phases α and γ at T and p

Fig.1.5 illustrates a typical variation of the molar Gibbs free energy with the composition (mole fraction), for each phase at a certain temperature, T, and pressure, p. For simplicity, let $x_B = x$, then $x_A = 1 - x$. If we consider a nominal alloy composition of x_0, if the system was to configure into a homogeneous phase, then between the phases α and γ, the free energy would be lowest for the γ phase ($G_0^\gamma < G_0^\alpha$). However, as shown in the Fig.1.5a, the system can lower its overall free energy to G_1 ($< G_0^\gamma$) if the system configures into a heterogeneous mixture of the phases α and γ at the compositions x_1^α and x_1^γ respectively. From Eq.(1.8), $G_1 = f^\alpha G_1^\alpha + f^\gamma G_1^\gamma$, where the phase fractions could be computed using the classical lever rule. If the solutes A and B redistribute between the two phases until the compositions x_{eq}^γ and x_{eq}^α, the overall free energy of the system could be further reduced to G_{eq} as shown in the Fig.1.5b. For this nominal alloy composition of x_0, at the given T and p, G_{eq} marks the minimum Gibbs free energy configuration possible and the system is said to be in equilibrium between the two phases with the corresponding equilibrium compositions for each of the phases. The equilibrium compositions, x_{eq}^γ and x_{eq}^α, correspond to the intersection points associated with the common tangent line to the two curves, G^γ and G^α. If we compute the slope of the common tangent line, we obtain:

$$m = \frac{G_{eq}^\gamma - G_{eq}^\alpha}{x_{eq}^\gamma - x_{eq}^\alpha}. \tag{1.9}$$

We can also express the slope as:

$$m = \left.\frac{\partial G^\gamma}{\partial x}\right|_{x_{eq}^\gamma} = \left.\frac{\partial G^\alpha}{\partial x}\right|_{x_{eq}^\alpha}. \tag{1.10}$$

Using Eqs.(1.9) and (1.10), and writing back $x = x_B$, we can deduce:

$$G_{eq}^\gamma - \left.\left(x_B \frac{\partial G^\gamma}{\partial x}\right)\right|_{x_{B,eq}^\gamma} = G_{eq}^\alpha - \left.\left(x_B \frac{\partial G^\alpha}{\partial x}\right)\right|_{x_{B,eq}^\alpha}. \tag{1.11}$$

From the definitions of the chemical potential in Eqs.(1.5), at the equilibrium compositions, $(x^{\gamma}_{B,eq}, x^{\alpha}_{B,eq})$, we get:

$$\mu^{\gamma}_{A} = \mu^{\alpha}_{A}, \tag{1.12}$$

and similarly:

$$\mu^{\gamma}_{B} = \mu^{\alpha}_{B}. \tag{1.13}$$

We thus recover the diffusion equilibrium conditions with the equality of the chemical potentials. So, for complete phase equilibrium in a heterogeneous mixture, the thermodynamic conditions imply that the chemical potentials in both the phases must be equal for all the components in the system.

Going back to the Fig.1.5b, the same equilibrium state could be reached for all those nominal alloy compositions between the two equilibrium compositions, with differences only in their relative phase fractions. For any alloy composition outside these limits, the minimum free energy lies either on the G^{γ} or the G^{α} curve and the system configures into a corresponding homogeneous single phase.

For a multiphase system containing N components with m stable phases, the phase equilibrium conditions can be generalized as:

$$\mu_i^{\alpha_1} = \mu_i^{\alpha_2} = \ldots = \mu_i^{\alpha_m} \qquad \forall i \in \{A, B, \ldots, N\} \tag{1.14}$$

Phase diagrams and tie-lines: In the previous example, phase equilibrium was illustrated at a specific temperature and pressure. While the pressure is usually fixed, the phase equilibria can be calculated as seen previously, at different temperatures. The loci of the equilibrium compositions obtained for the relevant stable phases, at various temperatures, constitute a global picture illustrating the stability and coexistence of various possible phases (while respecting the Gibbs phase rule). This global picture for an alloy constitutes a phase diagram that defines the potential phase regions and phase transition boundaries at different ranges of temperatures and compositions.

Fig.1.6 illustrates a simple representative binary phase diagram showing the domains of homogeneous single phase regions and the stable domain for the coexistence of the phases γ and α. The green lines within the two phase region represent the tie-lines (also known as conodes). In the context of a binary phase diagram, for any alloy in the two phase region, tie-lines are the isothermal lines that reflect the equilibrium compositions of the two phases as they intersect the respective solvus lines (the red and the blue dashed lines in Fig.1.6) at the temperature of interest. Corresponding to any given alloy composition x_0, T_{A3} represents the equilibrium solvus temperature or the transition temperature below which the phase γ is no longer stable to remain as a homogeneous phase, and so α phase starts forming.

1.2.1.1 Phase transformation mechanisms

DSSPT belongs to the category of Nucleation and growth based transformation mechanisms, where the phase transformation is initiated through the **nucleation** of the stable product phase and followed by the **growth** of these new phase nuclei into grains until the relevant phase equilibrium:

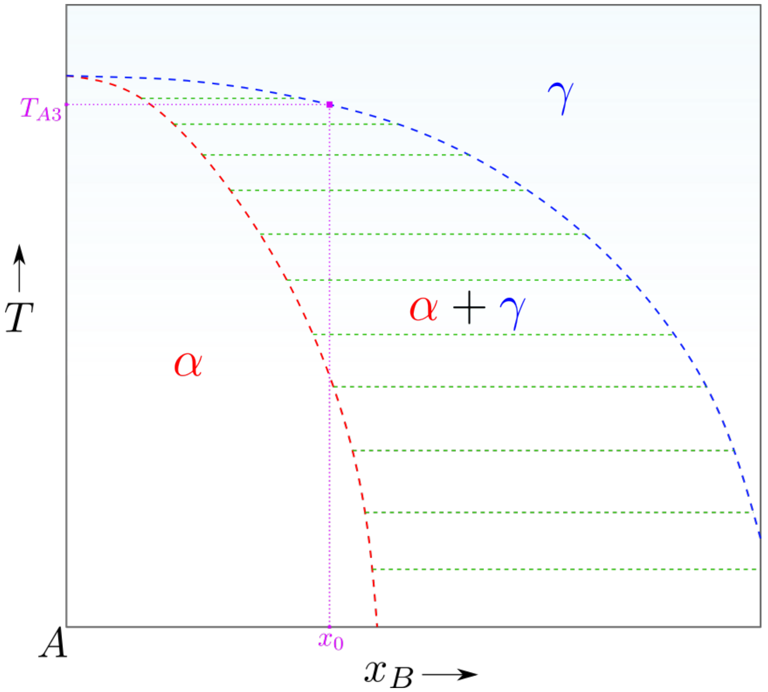

Figure 1.6: Phase diagram of a simple binary alloy showing different phase regions with the green dashed lines representing the tie-lines in the two phase region

1.2.1.1.1 Nucleation in phase transformation

Despite a thorough theoretical description of the nucleation event that could be found in the literature, the exact understanding of the origin of a nucleus and the quantification of certain nucleation process parameters remains complex, especially at the mesoscopic scale (length scales ranging between a few $10nm$ and the macroscopic scale). In spite of some of its shortcomings, the classical theory of nucleation (CNT) [30–33] has been widely accepted as a valid foundation to describe a nucleation event. The classical nucleation theory hypothesizes that under favorable conditions, small clusters of atoms configure spontaneously into the lattice structure of the new product phase known as a phase nucleus. This nucleus can either grow or shrink depending on the evolution of the free-energy with the characteristic size of the nucleus. The classical theory of nucleation is based on the assumption that the nucleus - parent phase interface is sharp and that the thermodynamic properties of the nucleus are homogeneous.

According to the classical nucleation theory, the change in free energy (ΔG) in a microstructural system in the event of nucleation of a new phase α in the parent phase γ can be generalized as follows:

$$\Delta G = -V_\alpha \left(\Delta g_V^\alpha - \Delta g_V^{mf}\right) + A_{\gamma/\alpha}\sigma_{\gamma/\alpha} - \Delta G_d, \tag{1.15}$$

where V_α is the volume of the nucleus, Δg_V^α is the Gibbs free energy difference between the unstable parent phase and the new product stable phase that is liberated per unit volume of the new phase α, as it appears. Δg_V^α is also termed as the driving pressure available for the nucleation of the phase α. Δg_V^{mf} is the Gibbs free energy per unit volume necessary to account for any elastic misfits between the two phases. The second term represents the energy necessary to create the interphase boundary between the parent phase γ and the nucleus α. Thus, $A_{\gamma/\alpha}$ is the area of the phase boundary i.e., the surface area of the nucleus, and $\sigma_{\gamma/\alpha}$ is the γ/α phase interface energy. The last term in ΔG_d represents the Gibbs free energy released due to the annihilation of the defects (e.g., the existing γ/γ interfaces) to accommodate the nucleus.

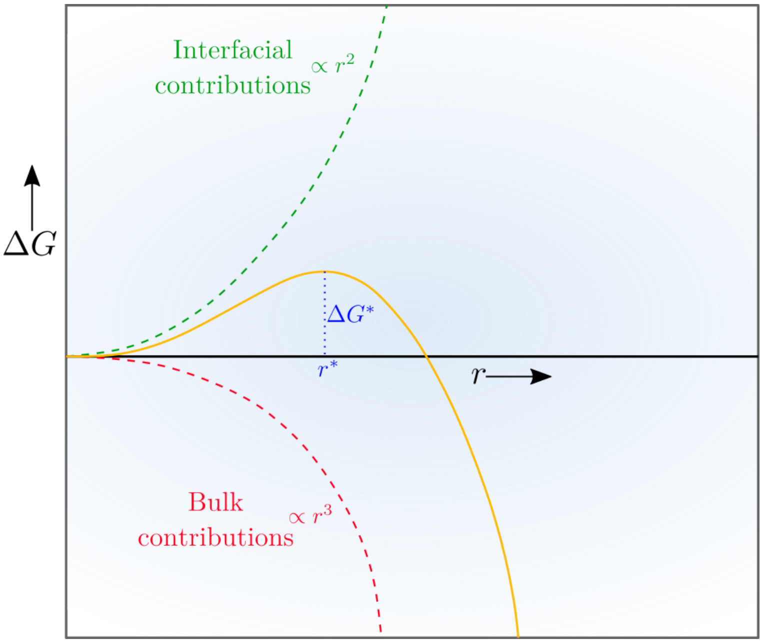

Figure 1.7: Variation of the change in free energy due to a nucleation event with the characteristic size of the nucleus

If we observe the above Eq.(1.15) (assuming $\Delta g_V^{mf} = \Delta G_d = 0$ for simplicity) as illustrated in the Fig.1.7, ΔG remains positive for smaller nucleus sizes, as the positive surface area term dominates over the negative volume term. A maximum in ΔG is attained as the nucleus size increases to a point where the negative volume term starts dominating more over the positive area term. This point of maximum in ΔG with the characteristic nucleus size represents the activation or the critical energy (ΔG^*) essential for nucleation, and the corresponding nucleus size is often referred to as the critical size of nucleation (r^*). These concepts stem from the fact that the positive terms in Eq.1.15 act as barriers to nucleation, and the nucleus will only come into existence and continue to grow if it attains the critical size by overcoming the nucleation barrier. Any subcritical nucleus will shrink and eventually dissolve as ΔG would increase with size in the subcritical zone which is not thermodynamically favorable. This is synonymous to the concept of metastability and the activation energy illustrated earlier in the Fig.1.3, where a microstructure with grains of potentially destabilized parent phase could remain metastable unless a sufficient activation energy is provided to create stable nuclei of the new phase which can eventually grow and transform the microstructure into the stable product phase. As illustrated in the Fig.1.8, the influence of the Δg_V^{mf} term is to increase the activation barrier or increase the critical nucleus size necessary for growth, thus making it more demanding to create stable phase nuclei. The other way to look at it is to say that the positive misfit term reduces the effective driving pressure available for nucleation of the new phase. On the other hand, ΔG_d term plays the role of lowering the energy barrier, making it easy for the nucleation of stable nuclei as we shall see later in this discussion.

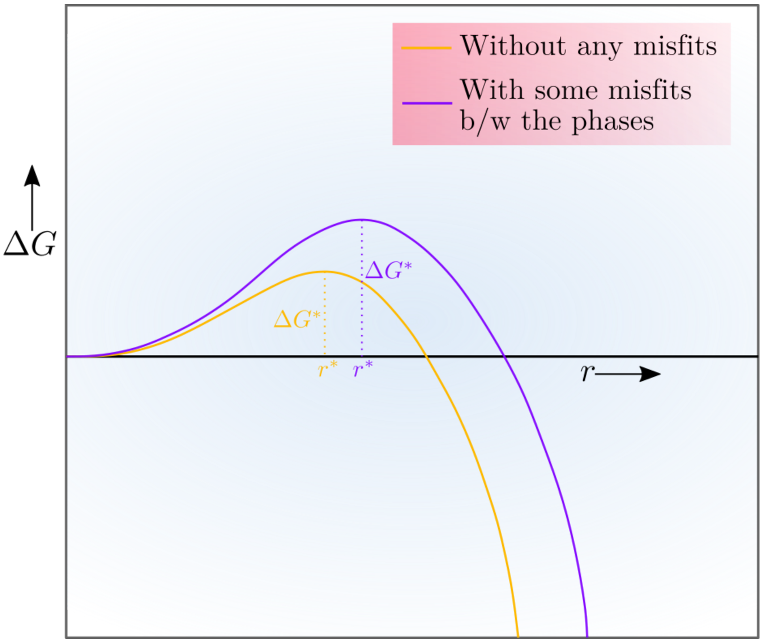

Figure 1.8: Influence of presence of any misfits between the two phases on the nucleation barrier

On the basis of the spatial preferences for a nucleus to form, nucleation could be classified to be homogeneous or heterogeneous:

Homogeneous nucleation: For homogeneous nucleation, there are no particular preferential sites for nuclei irrespective of the presence of defects or any kind of inhomogeneities in the microstructure. The probability of nucleating is thus the same everywhere. The change in Gibbs free energy in the system due to a nucleus is thus:

$$\Delta G = -V_\alpha \left(\Delta g_V^\alpha - \Delta g_V^{mf}\right) + A_{\gamma/\alpha}\sigma_{\gamma/\alpha}. \tag{1.16}$$

From the above equation, since it is desirable to have a smaller nucleation barrier (ΔG^*), the shape of the nucleus should be such that the surface area to its volume ratio must be as low as possible. Thus, for homogeneous nucleation, the ideal nucleus shape would be a sphere. Assuming a spherical nucleus of size r, the activation energy and the corresponding critical nucleus size could be found as follows:

$$\frac{\partial\left(\Delta G\right)}{\partial r} = 0. \tag{1.17}$$

$$-\left(\Delta g_V^\alpha - \Delta g_V^{mf}\right)\frac{\partial\left(\frac{4\pi r^3}{3}\right)}{\partial r} + \sigma_{\gamma/\alpha}\frac{\partial\left(4\pi r^2\right)}{\partial r} = 0.$$

Eventually, we obtain:

$$r^* = \frac{2\sigma_{\gamma/\alpha}}{\left(\Delta g_V^\alpha - \Delta g_V^{mf}\right)}, \tag{1.18}$$

$$\Delta G^* = \Delta G|_{r=r^*} = \frac{16\pi\sigma^3_{\gamma/\alpha}}{3\left(\Delta g^\alpha_V - \Delta g^{mf}_V\right)^2}. \tag{1.19}$$

It would be interesting to contrast the aforementioned activation energy with that attributed to heterogeneous nucleation.

Heterogeneous nucleation: Since a metallic material is generally polycrystalline, the microstructure is far from being perfect and defect free. From Eq.(1.15), it is clear that nucleating over the defects is more favorable as ΔG^* is lowered owing to the annihilation of the defects which is thermodynamically favorable. The free energy released during this annihilation to replace them with the nucleus is taken into account through the term ΔG_d, which is negative in Eq.(1.15). Thus, the presence of defects such as the grain boundaries (junctions between 2 adjacent grains), grain edges (linear junctions between three grains), grain corners (quadruple grain junctions), dislocations, impurities, and other potential inhomogeneities act as the preferential sites for nucleation compared to nucleating in the bulk of the parent phase. A classic example is nucleation over the γ/γ grain boundaries such that, $\Delta G_d = \Delta A_{\gamma/\gamma}\sigma_{\gamma/\gamma}$, where $\Delta A_{\gamma/\gamma}$ accounts for the interfacial area destroyed to accommodate the new phase, and $\sigma_{\gamma/\gamma}$ is the associated grain boundary energy.

The Gibbs free energy change as a nucleus appears in this case could be written as:

$$\Delta G = -V_\alpha\left(\Delta g^\alpha_V - \Delta g^{mf}_V\right) + A_{\gamma/\alpha}\sigma_{\gamma/\alpha} - \Delta A_{\gamma/\gamma}\sigma_{\gamma/\gamma}. \tag{1.20}$$

Unlike in the case of homogeneous nucleation, a heterogeneous nucleus doesn't necessarily have an ideal shape. So, we shall generalize the shape and the characteristic size (r) using some shape factors ($K^V, K^A, \ldots$) to express the activation energy and the critical nucleus size:

$$V_\alpha = K^V_\alpha r^3; \qquad A_{\gamma/\alpha} = K^A_{\gamma/\alpha} r^2; \qquad \Delta A_{\gamma/\gamma} = K^A_{\gamma/\gamma} r^2. \tag{1.21}$$

For heterogeneous nucleation, the activation energy and the critical nucleus size is thus obtained to be:

$$r^* = \frac{2\left(K^A_{\gamma/\alpha}\sigma_{\gamma/\alpha} - K^A_{\gamma/\gamma}\sigma_{\gamma/\gamma}\right)}{3K^V_\alpha\left(\Delta g^\alpha_V - \Delta g^{mf}_V\right)}, \tag{1.22}$$

$$\Delta G^* = \frac{4\left(K^A_{\gamma/\alpha}\sigma_{\gamma/\alpha} - K^A_{\gamma/\gamma}\sigma_{\gamma/\gamma}\right)^3}{27\left[K^V_\alpha\left(\Delta g^\alpha_V - \Delta g^{mf}_V\right)\right]^2} = \frac{\Psi}{\left(\Delta g^\alpha_V - \Delta g^{mf}_V\right)^2}, \tag{1.23}$$

where $\Psi = \frac{4\left(K^A_{\gamma/\alpha}\sigma_{\gamma/\alpha} - K^A_{\gamma/\gamma}\sigma_{\gamma/\gamma}\right)^3}{27\left(K^V_\alpha\right)^2}$ is a factor accounting for the creation and the destruction of the interfaces and this parameter comprises all the information about the shape factors of the nucleus and the interfacial energies.

If we assume the nucleus shape to be spherical, perfectly bisected in half by the grain boundaries as depicted in Fig.1.9, with $\Delta A_{\gamma/\gamma} = \pi r^2$, it could be shown that $\Psi = \frac{\pi\left(4\sigma_{\gamma/\alpha} - \sigma_{\gamma/\gamma}\right)^3}{12}$. For the sake

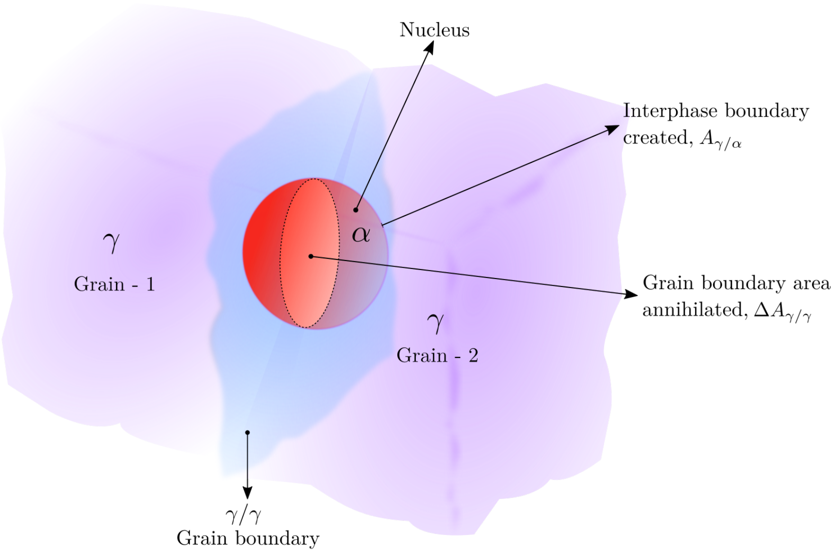

Figure 1.9: A cut out illustration of a spherical nucleus appearing at the grain boundary of the parent phase

of comparison, if we further assume $\sigma_{\gamma/\alpha} = k\sigma_{\gamma/\gamma}$, where k is some constant, we can show that $\Psi_{Het} = \frac{\pi(4k-1)^3\sigma^3_{\gamma/\gamma}}{12}$, when compared to $\Psi_{Hom} = \frac{16\pi k^3\sigma^3_{\gamma/\gamma}}{3}$ as we see in Eq.(1.19). For $\frac{\Psi_{Het}}{\Psi_{Hom}} < 1$, we can deduce that $k < 5/4$. Therefore, if the interface energy of the phase boundary remains below 1.25 times the interface energy of the grain boundary, it implies that the activation energy required for stable nuclei formation in heterogeneous nucleation is lower and more favorable compared to that in homogeneous nucleation, assuming the same nucleus geometry. In the scenario where the phase boundary energy exceeds 1.25 times the grain boundary energy, homogeneous nucleation dominates. However, in reality, the general observation leans towards heterogeneous nucleation as the preferred form. This suggests that the phase boundary energy is often lower or falls within the range of the grain boundary energy.

Fig.1.10 illustrates the nucleation energy barriers for the case where $k < 5/4$.

On the basis of the temporal mode of nucleation, one could classify nucleation to be: i) **Site saturated**, or ii) **Continuous**. Site saturated nucleation refers to the case where all the potential nucleation sites are exhausted at the same instant as the intended fraction of the new phase nuclei appear, and the nucleation regime of the transformation ceases to exist. In the case of a continuous nucleation, the nucleation regime takes place over a duration of a time as the nuclei appear continuously at the potential nucleation sites. So the nucleation site saturation is gradual in this case. With the help of the activation energy previously discussed, the classical nucleation theory provides an expression for the continuous nucleation rate ($\dot{I}$) as a function of time (t):

$$\dot{I} = Z\beta_n N_s \exp\left(-\frac{\Delta G^*}{k_B T}\right)\exp\left(-\frac{\tau}{t}\right), \qquad \left[\mathrm{m}^{-3}\cdot\mathrm{s}^{-1}\right], \tag{1.24}$$

where Z is the non-equilibrium Zeldovich factor that is a measure of the portion of the critically sized nuclei that become stable, as a critical nucleus may not necessarily become a stable nu-

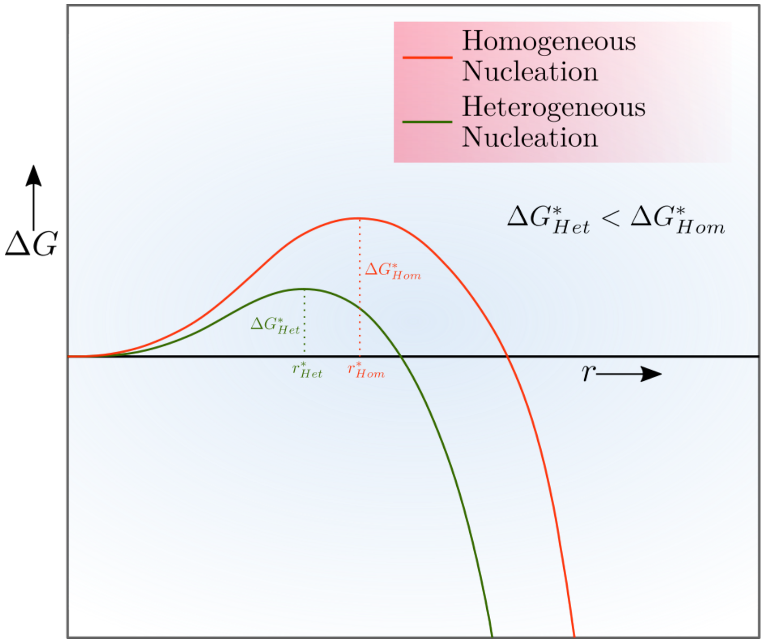

Figure 1.10: Comparison of homogeneous and heterogeneous nucleation

cleus and grow, but may instead shrink back to subcritical size and dissolve. β_n is a frequency factor that corresponds to the rate of attachment of atoms to the nuclei, N_s is the nucleation site density corresponding to the type of site where the nucleus forms. k_B is the Boltzmann constant (1.381×10^{-23} J·K^{-1}). T is the current absolute temperature during the transformation. τ is the incubation time that corresponds to a time period before which essentially no nucleation takes place. In other words, τ characterizes a time lag or a transient regime that exists before steady state nucleation ($\dot{I} \rightarrow const.$) could be observed as demonstrated in the Fig.1.11. There have been several works [34–37] that describe or quantify some of the parameters of the Eq.(1.24). However, the specifics of it will not be discussed in this manuscript, and the interested readers could refer the cited references.

Driving pressure for nucleation: By considering again the Fig.1.6, if we suppose an alloy with a composition of x_0 composed of a homogeneous phase in γ, and a cooling to a certain temperature T, below its relevant equilibrium solvus temperature (T_{A3}), we could observe the $\gamma \rightarrow \alpha$ transformation as γ would be no longer stable as a single homogeneous phase. The driving pressure available for the nucleation (Δg_V^{α}) of this new phase α could be deduced if we revisit the representative curves illustrating the molar Gibbs free energy variation for the phases α and γ at the temperature, T, as shown in the Fig.1.12.

We observe that for the composition x_0, the molar Gibbs free energy of the system reduces from G_0^{γ} to G_{eq} due to the precipitation of the new phase. The net difference in these two free energies, $\Delta G_{\gamma\alpha} = G_{eq} - G_0^{\gamma}$ provides a thermodynamic potential proportional to the total driving pressure available for the transformation. However, this does not correspond to the driving pressure that motors the nucleation process of the α phase. Let us suppose the nucleus composition to be x_n^{α}. If we consider a localized cluster of atoms in the phase γ but with a composition of x_n^{α} while still

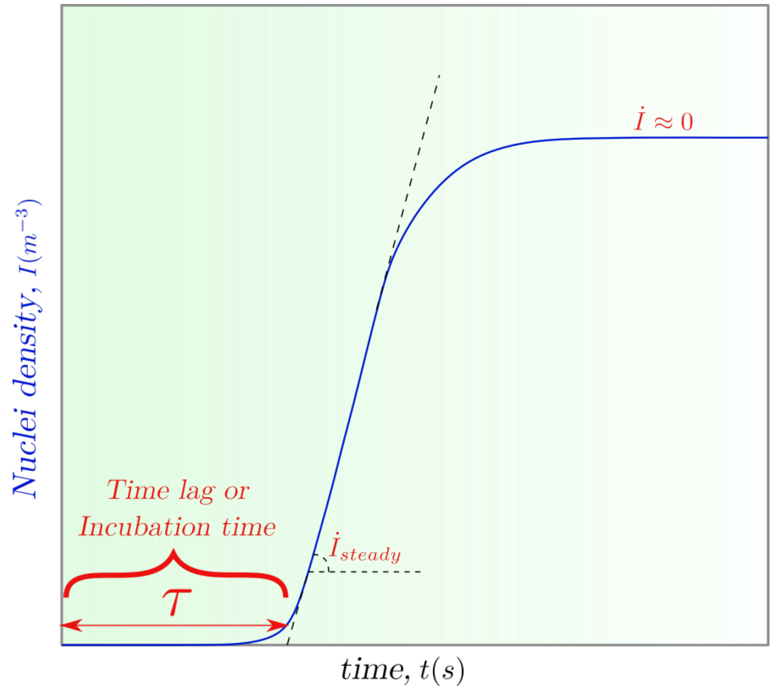

Figure 1.11: A representative evolution of the nucleation rate showing the transient regime with an incubation time

comprising the crystal structure of the parent γ phase, from Eq.(1.6) the molar Gibbs free energy of this localized region could be written as:

$$G_1^n = \mu_A^\gamma \left(1 - x_n^\alpha\right) + \mu_B^\gamma x_n^\alpha. \tag{1.25}$$

This corresponds to the point M in the Fig.1.12. Now, if this cluster of atoms at the composition, x_n^α, get rearranged into the crystal structure of the α phase, the molar Gibbs free energy of this localized region could now be written as:

$$G_2^n = \mu_A^\alpha \left(1 - x_n^\alpha\right) + \mu_B^\alpha x_n^\alpha. \tag{1.26}$$

This state now corresponds to the point N in the Fig.1.12.

The decrease in free energy between the above two states (M, N), associated to the nucleation event, provides the thermodynamic potential proportional to the driving pressure for nucleation:

$$\Delta G^n = G_2^n - G_1^n. \tag{1.27}$$

This difference corresponds to the length MN in the Fig.1.12. If V_m^α is the molar volume of the phase α, then the driving pressure available for nucleation could be written as:

$$\Delta g_V^\alpha = \frac{|\Delta G^n|}{V_m^\alpha}. \tag{1.28}$$

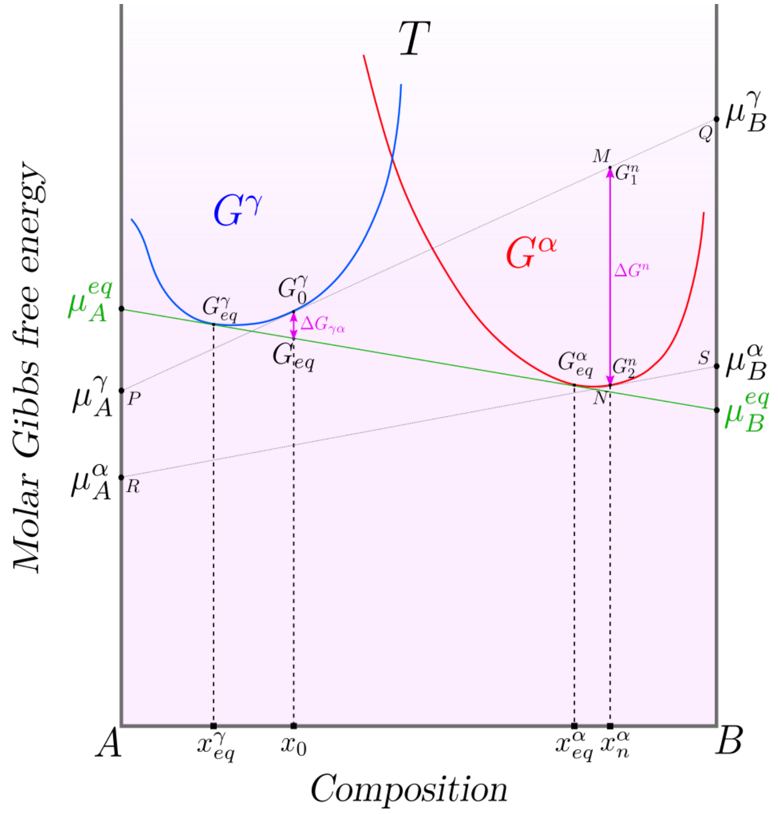

Figure 1.12: Illustration of the driving pressure for nucleation

Making use of the Eqs.(1.5), the Eqs.(1.25) and (1.26) could be further simplified to express in terms of the molar Gibbs free energy and the compositions. Eventually, Δg_V^α could also be expressed as:

$$\Delta g_V^\alpha = \frac{1}{V_m^\alpha} \left| G^\alpha|_{x_n^\alpha} - G^\gamma|_{x_0} + \left(x_0 - x_n^\alpha\right) \left.\frac{\partial G^\gamma}{\partial x}\right|_{x_0} \right| . \tag{1.29}$$

In the above example, we considered the nucleus composition or the composition at the interface of the nucleus to be x_n^α, and it could be established that the driving pressure available for the formation of α nucleus depends on the choice of this composition. The driving pressure demonstrated in the Fig.1.12 does not correspond to the maximum driving pressure available for nucleation. To obtain the maximum or the most favorable driving pressure, the tangential line RS must be constructed to be parallel to the line PQ. This would then correspond to a nucleus composition, $x_{n_{max}}^\alpha$, that yields the most favorable driving pressure for nucleation (ΔG_{max}^n) as illustrated in the Fig.1.13.

Mathematically, for ΔG_{max}^n, find $x = x_{n_{max}}^\alpha$ such that:

$$\left.\frac{\partial G^\alpha}{\partial x}\right|_{x=x_{n_{max}}^\alpha} = \left.\frac{\partial G^\gamma}{\partial x}\right|_{x_0} . \tag{1.30}$$

All of the vertical lines inside the G^α curve as illustrated in the Fig.1.13 represent the driving pressures possible at various nucleus interface compositions ($x_{n_i}^\alpha$). Thermodynamically, it should

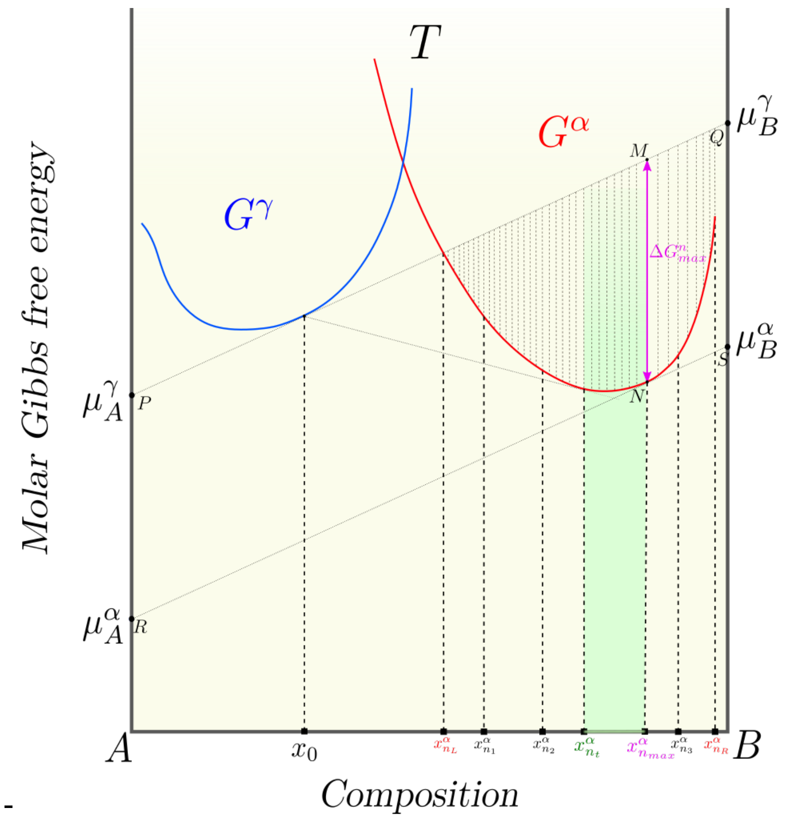

Figure 1.13: Illustration of different possible driving pressures for nucleation and their corresponding nuclei compositions

be possible to form the critical α nuclei with any composition between the limits: $x^\alpha_{n_L}$ and $x^\alpha_{n_R}$. However, the vertical line MN in the Fig.1.13 yields the largest driving pressure. Assuming that the interfacial energy ($\sigma_{\gamma/\alpha}$) and the molar volume (V^α_m) are not dependent on the nucleus composition, the composition corresponding to the largest driving pressure would ideally be the most favorable composition for a critical nucleus ($x^\alpha_{n_{cr}}$). However, as Hillert emphasizes in [38], the critical nucleus composition may not necessarily correspond to the most favorable one. Hillert further demonstrates that the actual limiting cases for the composition of a critical nucleus would lie somewhere between $x^\alpha_{n_t}$ and $x^\alpha_{n_{max}}$, highlighted by the green zone in the Fig.1.13. Interested readers are encouraged to refer [38] to understand more on the specifics of the derivation of these limiting cases.

Remarks on the nuclei shapes, the preferential sites, and the nucleation criteria for DSSPT: In the case of heterogeneous nucleation, since there is no ideal critical nucleus shape independent of the interfacial energies, the understanding of nucleus geometry is not straightforward. It is apparent from Eqs.(1.22) and (1.23) that the activation energy barrier (and hence the nucleation rate) is highly sensitive to this geometry, and to the interfacial energies. Depending on the type of nucleation site, several models have been proposed and analyzed in the literature. Broadly, the most common models in the state-of-the-art are the spherical caps model, and the pillbox model. These two approaches have been extended to different kinds of nucleation sites and certain hybrid models have also been studied.

The spherical caps model, initially proposed by Gibbs [39] has been analyzed in detail by Clemm et al. [40] for grain corners, grain edges, grain faces, and compared with that of homogeneous nucleation. Fig.1.14 illustrates the spherical cap based nucleus geometries at different sites. Fig.1.14 (a) shows two abutting spherical caps at a grain boundary with a 2D perspective along the plane of the boundary, (b) shows the case of a grain edge where 3 spherical caps bound the nucleus, and (c) shows the case of a grain corner (four-order multiple junction) where the nucleus takes the form of a spherical tetrahedron. Spherical models with their curved interfaces have been generally used to represent a disordered type of interface (incoherent boundaries) with high interfacial energy.

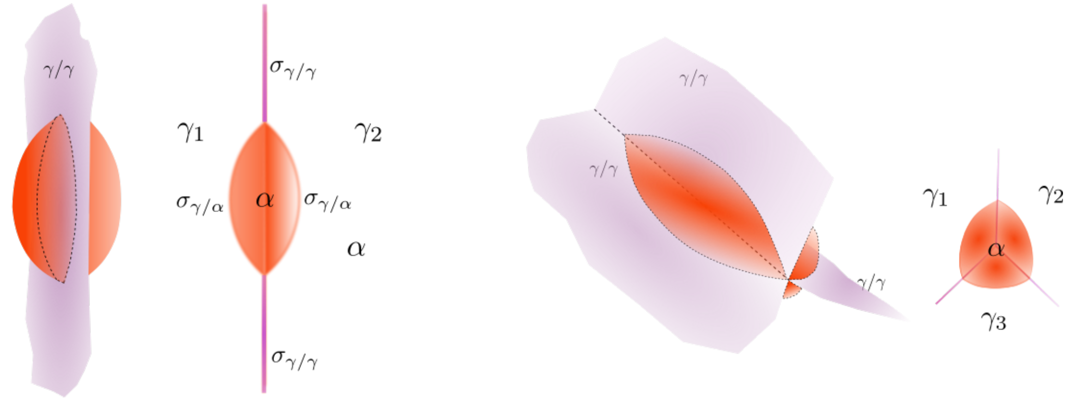

(a) Two abutting spherical caps at a grain face

(b) Three spherical caps at a grain edge

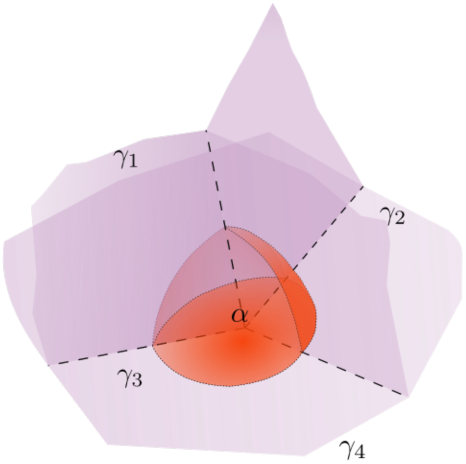

(c) Four spherical caps forming a spherical tetrahedron at a grain corner

Figure 1.14: Spherical caps based nuclei models at different kinds of nucleation sites

On the other hand, faceted pillbox nucleus models have been proposed to depict coherent or semi-coherent interfaces with low interfacial energy. Nucleation at the grain faces has been analyzed for austenite decomposition in Fe-C alloys by Lange et al. [41] using various pillbox based model variants, and spherical caps model with facets. Based on their observation, it was concluded that, for grain faces, only coherent pillbox models and their variants were successful in making certain reasonable predictions when compared with the experimentally observed nucleation rates. Fig.1.15 gives a summary of some of the pillbox nucleus models used in [41] at a grain face. Enomoto et al. [42] extended the idea of coherent and faceted nucleus models at the grain edges by considering an equilateral trigonal prism as illustrated in Fig.1.16. Johnson et al. [35] imply that when the lattices of the parent and the product phase show reasonable coherency, the critical nucleus is likely to be faceted or pillbox based. They claimed that the most probable shape of the critical nucleus is the shape yielding the minimum interfacial energy for a given nucleus volume. Chan et al. [43] consider different nucleus shape forms and give a generalized list of expressions for nucleus shape dependent parameters in the nucleation rate equation. Interested readers may refer it for detailed expressions.

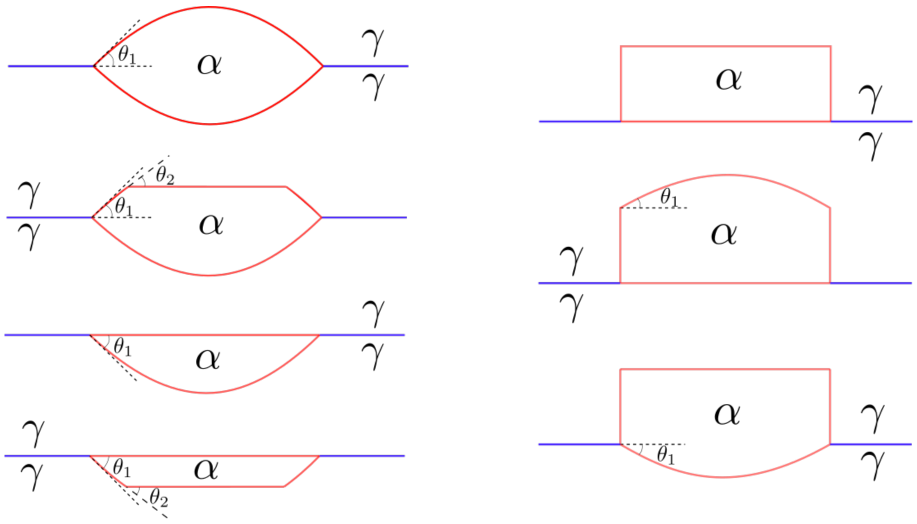

(a) Spherical caps models with facets

(b) Pillbox models and their variants

Figure 1.15: Faceted spherical caps and pill box nuclei models proposed by Lange et al. [41] for nucleation at the grain face

In the case of phase transformation, nucleation is generally accepted to be a stochastic event without any specific or consistent criterion governing the spatial choice of appearance of a nucleus. However, as iterated earlier, certain set of sites could be preferred over the others. Referring to the nucleation rate Eq.(1.24), on the basis of the nucleation site density or the number of nucleation sites available, one could show that this number is highest for nucleation at the grain interiors, followed by grain faces, grain edges and then the grain corners. However, on the basis of the activation energy required for nucleation, it has been demonstrated that the most favored nucleation sites are the grain corners, followed by the grain edges, then the grain faces, with the grain interiors (homogeneous nucleation) being the least energetically favorable sites. Huang et al. [44] have shown that nucleation is mostly dominated at the grain corners along with any other sites (under the influence of other inherent defects) that are energetically similar to that of a grain corner. This is followed by grain edges, and eventually the grain faces. It has also been indicated in [44] that

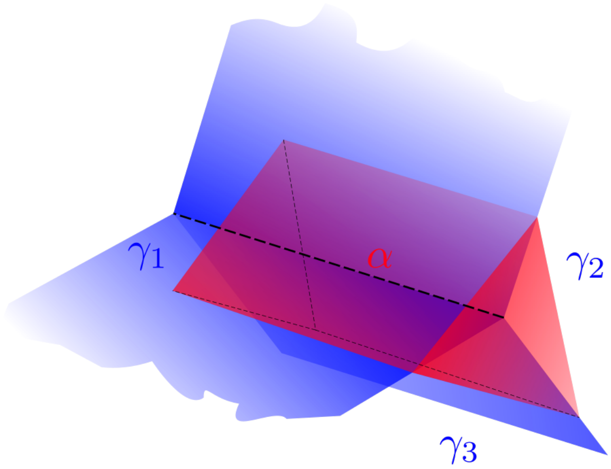

Figure 1.16: An equilateral trigonal prism nucleus model illustrated by Enomoto et al. [42] for nucleation at the grain edge

only about 5 – 7% of the grain corners act as active nucleation sites. In the case of a continuous cooling transformation, the cooling rate also plays a role. At lower cooling rates, with lower nuclei density, most of the nuclei are likely to form at the grain corners. However, at higher cooling rates, as the nuclei density increases, the probability of nucleating at the grain edges and the faces become increasingly significant as the sites at the grain corners start saturating. Offerman et al. [45] have indicated the presence of a particular temperature range for nucleation with this range being larger for higher cooling rates.

Despite a rich literature on the phenomenon of nucleation, a complete and unified description remains a complex issue and an open subject of research due to the experimental complexity to promote 3D in-situ observations of nucleus appearance. This is attributed to the smaller length scales and the shorter time scales involved during a nucleation event. The above analyses and observations reflect the various hypotheses and dimensions one could take into account to model the phenomenon and quantify some of the assumed parameters. Hence, in the current state of the art, nucleation behavior is usually modeled with a reasonably simplistic approach with strong hypotheses, especially at the mesoscopic scale.

1.2.1.1.2 Growth kinetics

Following the establishment of a stable nucleus, the transformation proceeds through growth of the nucleus into a grain of the product phase. The migration of the phase interface with a certain velocity ($\boldsymbol{v}$), primarily under the influence of a local chemical driving pressure ($P_C = \Delta G_{\gamma\rightarrow\alpha}$) at the interface characterizes the growth stage of the phase transformation. Any migrating interface is associated with an intrinsic drag against the motion. An intrinsic parameter is associated with an interface that characterizes the ability of the interface to be mobile against this resistance and is referred to as the interface mobility (M). An interface with high mobility is easier to migrate while the one with low mobility offers high intrinsic drag or resistance against any migration. $1/M$ is sometimes regarded as the intrinsic drag coefficient.

So, an interface is generally associated with inherent properties such as M and σ. The interface mobility is generally heterogeneous and anisotropic [1, 46]. It is expected to depend on the material, processing conditions, disorientation angle ($\Delta\theta$) and also on the local interface features:

$$M = f(\Delta\theta, \boldsymbol{n}, T, c_i(\boldsymbol{x})),$$

where $c_i(\boldsymbol{x})$ represents the solute concentration of a solute i at a spatial point $\boldsymbol{x}$, and $\boldsymbol{n}$ is the outward unit normal vector to the considered interface. Some literature, such as works by Hurley et al. [47] and Yamanaka et al. [48], tentatively propose a disorientation angle dependence of M. However, experimental results typically provide the reduced mobility (= $M\sigma$) rather than the intrinsic mobility (M). Consequently, determining if M explicitly depends on $\Delta\theta$ remains challenging. Similar ambiguity exists regarding the dependence on the local normal vector ($\boldsymbol{n}$), an area of ongoing research. In the context of metal forming, at the polycrystal scale, the temperature dependence of mobility is generally defined through an Arrhenius law [49]:

$$M(T) = M_0 exp(-\frac{Q_m}{RT}), \tag{1.31}$$

where, Q_m is the activation energy for grain boundary migration (GBM) which implies that a certain kind of thermal activation is essential for the interface to be mobile, R is the universal gas constant, and M_0 is a pre-exponential factor. M_0 is sometimes taken as a function of temperature too. On the other hand, Read-Schokley relationship has been classically used to describe the dependence of σ on disorientation [50, 51] for grain boundaries between grains of same phase:

$$\sigma(\Delta\theta) = \begin{cases} \sigma^m \frac{\Delta\theta}{\Delta\theta_m}\left(1 - ln\frac{\Delta\theta}{\Delta\theta_m}\right), & \text{if } \Delta\theta \leq \Delta\theta_m \\ \\ \sigma^m, & \text{if } \Delta\theta > \Delta\theta_m \end{cases}, \tag{1.32}$$

where σ^m is the interfacial energy for high angle grain boundary (HAGB, $\Delta\theta \geq \Delta\theta_m$). $\Delta\theta_m$ is generally taken around 10 to 15°. The dependence of σ on the inclination of the Grain Boundary (GB) ($\boldsymbol{n}$) is not taken into account in this formalism. The above formalism has been consistently used for boundaries between grains of same phase, however in the case of phase boundaries, the notion of disorientation is generally more complex since different crystal lattice structures are involved, potentially causing intricate disorderliness at the phase boundaries. Phase boundaries are hence generally highly incoherent except between phases with simple and similar class of crystal structures (e.g., FCC and BCC crystal lattices). However different disorientation relationship was used in the literature for phase boundary energy in [48, 52] in contrast to the classical Read and Shockley relationship:

$$\sigma_{\gamma/\alpha}(\Delta\theta) = \begin{cases} \frac{\sigma^m}{2} + \frac{\sigma^m}{2}\frac{\Delta\theta}{\Delta\theta_m}\left(1 - ln\frac{\Delta\theta}{\Delta\theta_m}\right), & \text{if } \Delta\theta \leq \Delta\theta_m \\ \\ \sigma^m, & \text{if } \Delta\theta > \Delta\theta_m \end{cases}, \tag{1.33}$$

where the definition of $\Delta\theta$ must be carefully checked.

While in [53], a rather constant value was used for phase boundary energy and Eqs.(1.32) for that of grain boundaries. So, a consistent formalism quantifying the dependence of σ on disorientation angle for phase interfaces still remains an open subject of research.

In the context of microstructural evolution at the mesoscopic scale, the velocity field of interface migration, $\boldsymbol{v}$, is assumed to be a product of the interface mobility (M) and the different local driving pressures (P) describing the involved phenomena at the interface [32]:

$$\boldsymbol{v} = MP\boldsymbol{n}. \tag{1.34}$$

In the presence of curved phase interfaces, along with the chemical free energy contribution, the capillarity effects (Gibbs-Thomson effect) coming from the excess interfacial free energy also play a role. Though the order of magnitude of the chemical free energy contribution is significantly larger, Gibbs-Thomson effect can potentially modify the phase equilibrium position and concentrations. Hence it is important to take into account in the kinetics of transformation. This contribution is described as $P_\kappa = -\kappa\sigma_{\gamma/\alpha}$, where κ is the trace of the curvature tensor of the interface such that $\kappa \longrightarrow 0$ for minimal surfaces (sum of principal curvatures = 0), and $\sigma_{\gamma/\alpha}$ is the interfacial energy. So, the transformation kinetics would be governed by,

$$\boldsymbol{v} = M\left(\Delta G_{\gamma\to\alpha} - \kappa\sigma_{\gamma\alpha}\right)\boldsymbol{n}. \tag{1.35}$$

Fig.1.17 demonstrates the orientation of a velocity vector at a local point A on the phase interface, responsible for its migration during the phase transformation.

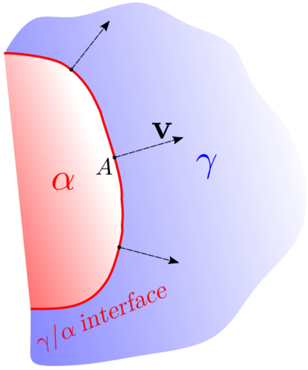

Figure 1.17: Illustration of interface migration or growth kinetics for phase transformation

The solute diffusion in each phase is governed by the Fick's laws of diffusion. Fick's first law yields the following relations for fluxes in each phase ($\boldsymbol{J}_\alpha, \boldsymbol{J}_\gamma$):

$$\boldsymbol{J}_\alpha = -D_\alpha^B \boldsymbol{\nabla} x^\alpha; \quad \boldsymbol{J}_\gamma = -D_\gamma^B \boldsymbol{\nabla} x^\gamma, \tag{1.36}$$

where D_α^B and D_γ^B represent the diffusivity of the solute atoms (say B) in α and γ phases respectively. From Fick's second law, $\partial x/\partial t = -\boldsymbol{\nabla}\cdot\boldsymbol{J} = \boldsymbol{\nabla}\cdot(D\boldsymbol{\nabla}x)$, the diffusion equations for solute partitioning in each phase could be obtained as:

$$\frac{\partial x^{\alpha}}{\partial t} = \boldsymbol{\nabla} \cdot \left(D^{B}_{\alpha} \boldsymbol{\nabla} x^{\alpha}\right); \quad \frac{\partial x^{\gamma}}{\partial t} = \boldsymbol{\nabla} \cdot \left(D^{B}_{\gamma} \boldsymbol{\nabla} x^{\gamma}\right). \tag{1.37}$$

The above equations are well bounded by providing suitable initial and boundary conditions. In addition, Eq.(1.34) and Eqs.(1.37) are constrained by the interfacial jump condition for mass balance:

$$\boldsymbol{v} \cdot \boldsymbol{n} \left(x^{\gamma}_{\Gamma} - x^{\alpha}_{\Gamma}\right) = [\![\boldsymbol{J}]\!]\big|_{\Gamma} \cdot \boldsymbol{n} = D^{B}_{\alpha} \left(\boldsymbol{\nabla} x^{\alpha} \cdot \boldsymbol{n}\right)|_{\Gamma} - D^{B}_{\gamma} \left(\boldsymbol{\nabla} x^{\gamma} \cdot \boldsymbol{n}\right)|_{\Gamma}, \tag{1.38}$$

where Γ represents the interphase position and x^{α}_{Γ}, x^{γ}_{Γ} represent the interfacial concentrations of each phase. As equilibrium is approached, equality of chemical potentials as seen in Eqs.(1.12) and (1.13) are satisfied.

Character of transformation kinetics: It has been described in [54–57] that the excess chemical free energy or the driving pressure available for diffusive phase transformation is dissipated in two parts. A part of the excess free energy is dissipated by diffusion of the solutes while the rest contributes to the migration of the phase interface as the crystal lattice transforms into that of the product phase. So, the growth stage of a phase transformation could be characterized by two basic mechanisms that govern the growth kinetics: (i) the diffusion of solutes across the phase interfaces and in the bulk of the grains which bring about a change in chemical composition, and (ii) the interface migration which causes the gradual lattice rearrangement or structural changes into the crystal structure of the product phase. This description yields three different possible modes of transformation kinetics:

- **Interface controlled mode**: In this case, the diffusion in the parent phase is assumed to be infinitely fast such that the solute concentration is homogeneous in the parent phase. So, all of the excess free energy is dissipated by the mechanism of lattice transformation, and is said to be the rate controlling process for the growth stage. The velocity of interface migration is bound solely by the lattice transformation process.

- **Diffusion controlled mode**: The rate controlling process is said to be diffusion controlled if the lattice transformation is infinitely fast (the interface is infinitely mobile) compared to that of the solute diffusion. In such a case, the solute concentrations at the phase interface would be equal to that of the equilibrium concentrations and hence this mode is often referred as the local equilibrium mode. The velocity of interface migration is bound solely by the solute diffusion process.

- **Mixed mode**: This mode of transformation kinetics is an intermediate mode to the above two extreme cases and is the most realistic mode describing the transformation kinetics. In this case, neither the lattice transformation nor the solute diffusion is assumed to be infinitely fast. So, the solute concentrations at the interface are neither at local equilibrium nor equal to that of the bulk concentration. The velocity of interface migration is bound by both the lattice transformation as well as the solute diffusion process.

Fig.1.18 shows a representation of possible concentration profiles around a planar phase interface for different kinetic modes of transformation. During the transformation, the solubility differences between the two phases cause enrichment of solutes on one side of the interphase boundary which is reflected by the concentration peaks near the interface. If we suppose phase γ to have a higher

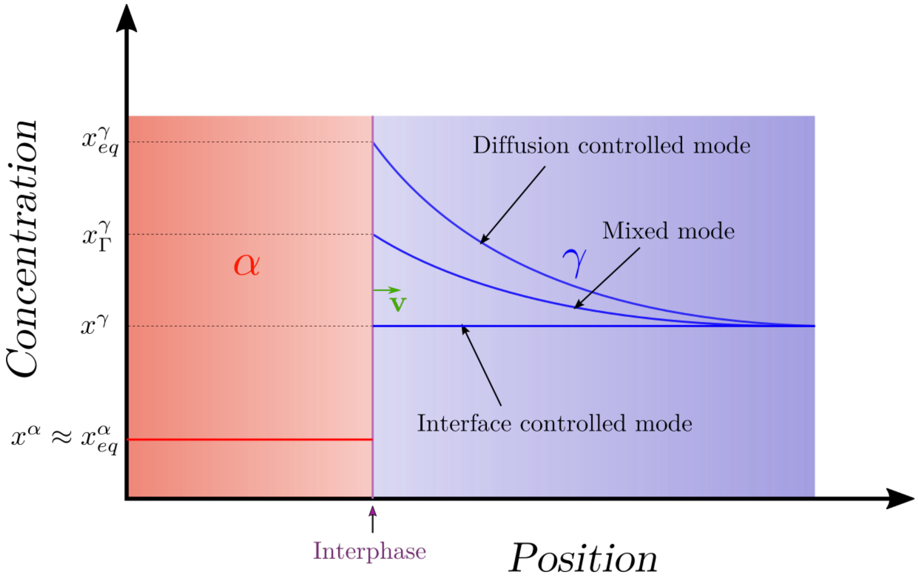

Figure 1.18: Illustration of possible solute concentration profiles around a planar interphase boundary for different transformation kinetic modes

solubility than the phase α, then there would be a flux of solutes across the interface towards the phase γ from the phase α. In this figure, the solute diffusivity in the phase α is assumed to be relatively high and hence a homogeneous profile is attained with a concentration close to the equilibrium concentration for this phase. For interface controlled mode, the flux of solute atoms quickly diffuse into the bulk of the γ phase as a result of the infinitely fast diffusion and the concentration profile attains the average bulk concentration value and is homogeneous. For the other extreme case, the γ concentration at the interface attains the equilibrium concentration right away as the lattice transformation is infinitely fast and a concentration gradient is created between the interface concentration and the bulk concentration. The reaction is then controlled by the diffusivity of the solute in the γ phase. For mixed-mode character of phase transformation, as the lattice transformation is not fast enough, and as the solute diffusion in the γ phase starts depleting the solute atoms near the interface in the γ phase, the interface concentration is decreased and does not attain the equilibrium concentration right away. The local equilibrium is attained gradually.

So, the mixed mode kinetics better describe the transformation character and is closer to reality. As observed in [58], under isothermal conditions, during the initial stages of a phase transformation, interface controlled kinetics are known to dominate, which is also a reflection of maximum interface velocity. As the concentration profile develops due to the enrichment of solutes, mixed mode character is observed. Towards the final stages, as the interface concentrations approach the equilibrium concentrations, and as the interface velocity decreases, a shift towards diffusion controlled kinetics is observed. Thus it can be concluded that the interface migration and the solute diffusion in the parent phase are coupled processes that together control the kinetics of the phase transformation. The transformation kinetics can be cast either in terms of the interfacial processes and the relevant free energy dissipated, or in terms of the long-range diffusion and the corresponding free energy dissipated. In principle, the same interface migration velocity must be obtained from both the approaches.

1.2.1.2 DSSPT in Ternary alloys and beyond

So far, we discussed DSSPT in the context of a binary alloy, however, most metallic materials of industrial interest are alloys having several components. The potential effects of alloying elements on phase transformation kinetics depend whether they are of the interstitial type (e.g., C, O, N, S, etc.) or substitutional type (e.g., Ni, Co, Mn, Si, Nb, V, etc.). Some of these alloying elements tend to stabilize particular phases over the others which could be of interest if certain phases introduce some desirable properties in the material. Also, some alloying elements tend to induce drag effects on the grain growth kinetics which could be used as a way to limit the mean grain size if necessary. In the case of a ternary system, the phase diagram at a fixed pressure would be a 3D plot [59] (generally plotted in the form of an equilateral triangular prism) composed by a vertical temperature axis and horizontal compositional axes of any two alloy components as shown in the Fig.1.19. The tie-lines as seen in the case of 2D phase diagrams of binary systems would translate to 2D horizontal planes in the case of ternary systems. Ternary systems are generally simplified by considering a section of a phase diagram either at a fixed temperature (isothermal plots) or at a fixed composition of one of the elements (isopleth plots). A more general alloy system would be associated with inconceivable hyperdimensional phase diagrams and tie-lines would be composed by hyperplanes.

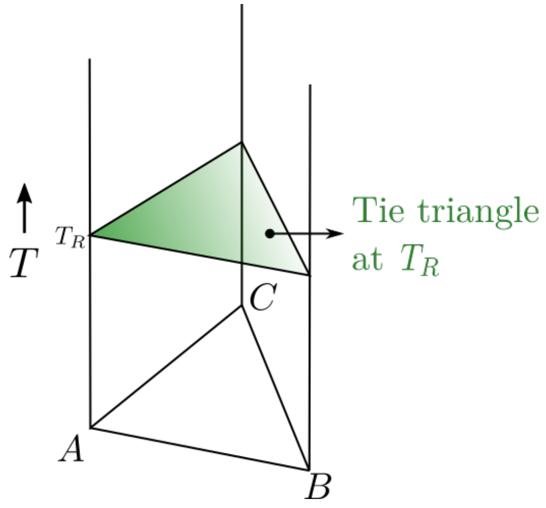

Figure 1.19: Illustration of a representative equilateral triangular prism used for 3D ternary phase diagrams

Let us suppose an alloy system, A-B-C-...-N with N components including the principal element, A, undergoing a $\gamma \rightarrow \alpha$ diffusive phase transformation. As discussed earlier through Eq.(1.14), the fundamental thermodynamic condition for equilibrium would be the equality of chemical potentials in both the phases for all the components in the alloy:

$$\mu_i^{\gamma} = \mu_i^{\alpha} \qquad \forall i \in \{A, B, ..., N\} \tag{1.39}$$

Referencing the diffusion Eqs.(1.37), in the case of a general alloy system, the solute diffusion would be governed by $N-1$ diffusion equations in each phase for the $N-1$ alloying elements:

$$\frac{\partial x_i^\alpha}{\partial t} = \boldsymbol{\nabla} \cdot \left(D_\alpha^i \boldsymbol{\nabla} x_i^\alpha\right); \quad \frac{\partial x_i^\gamma}{\partial t} = \boldsymbol{\nabla} \cdot \left(D_\gamma^i \boldsymbol{\nabla} x_i^\gamma\right) \qquad \forall i \in \{B, ..., N\}, \tag{1.40}$$

where $\forall\ p_h \in \{\gamma, \alpha\}$, $D_{p_h}^i$ represents diffusivity of solute element i in the phase p_h, $x_i^{p_h}$ is the concentration fraction of solute i in the phase p_h such that $\sum_{i\in\{A,B,...,N\}} x_i^{p_h} = 1$.

Likewise, there would be $N-1$ interfacial conditions for solute mass balance:

$$\boldsymbol{v} \cdot \boldsymbol{n} \left(x_i^\gamma\big|_\Gamma - x_i^\alpha\big|_\Gamma\right) = D_\alpha^i \left(\boldsymbol{\nabla} x_i^\alpha \cdot \boldsymbol{n}\right)\big|_\Gamma - D_\gamma^i \left(\boldsymbol{\nabla} x_i^\gamma \cdot \boldsymbol{n}\right)\big|_\Gamma \qquad \forall i \in \{B, ..., N\}. \tag{1.41}$$

The above $N-1$ equations need to be simultaneously satisfied for the interface velocity, $\boldsymbol{v}$.

Notions of different types of phase equilibria in ternary systems In most cases, the diffusivities of certain solute elements (generally substitutional elements) could be extremely low comparatively to the faster diffusing elements (usually interstitial). In such a scenario, all of the Eqs. in (1.41) may not be satisfied simultaneously at a certain interface migration velocity for the true tie-line passing through the nominal alloy compositions, $\left(x_A^0, x_B^0, ..., x_N^0\right)$. Within the characteristic time scale of interest in industrial applications, the diffusion effects of such slow diffusing elements could be considered to be negligible. It could take an extremely long time (unrelated to the order of magnitude of the physical times discussed in this Ph.D. thesis) before all the elements in the alloy system completely diffuse to attain the true phase equilibrium with equilibrium concentrations corresponding to the true tie-line. To overcome this situation, the concept of modified or constrained phase equilibria has been introduced in the literature.

To better understand, let us consider a simple ternary alloy system of the form A-B-X with the nominal compositions of, $\left(x_B^0, x_X^0\right)$, where B is a fast diffusing interstitial element, while X is a substitutional element (that potentially has several lower orders of diffusivity). For simplicity, let us suppose that the diffusion in the α phase is rapid relative to that in the parent γ phase for both the solute elements, such that, $\left(\boldsymbol{\nabla} x_B^\alpha \cdot \boldsymbol{n}\right)\big|_\Gamma \approx 0$; $\left(\boldsymbol{\nabla} x_X^\alpha \cdot \boldsymbol{n}\right)\big|_\Gamma \approx 0$. So, the concentration profiles in the α phase are assumed to be homogeneous. We can now define the following types of phase equilibria:

- **Full local equilibrium or Ortho-equilibrium**: This is a case of phase equilibria with the classical thermodynamic conditions where the equality of chemical potentials are satisfied for all the 3 components in the alloy:

  $$\begin{aligned} \mu_A^\alpha &= \mu_A^\gamma \\ \mu_B^\alpha &= \mu_B^\gamma, \\ \mu_X^\alpha &= \mu_X^\gamma \end{aligned} \tag{1.42}$$

  and the mass balances at the phase interface are satisfied simultaneously for both the solute elements:

  $$\begin{aligned} \boldsymbol{v} \cdot \boldsymbol{n} \left(x_B^\gamma\big|_\Gamma - x_B^\alpha\big|_\Gamma\right) &= -D_\gamma^B \left(\boldsymbol{\nabla} x_B^\gamma \cdot \boldsymbol{n}\right)\big|_\Gamma \\ \boldsymbol{v} \cdot \boldsymbol{n} \left(x_X^\gamma\big|_\Gamma - x_X^\alpha\big|_\Gamma\right) &= -D_\gamma^X \left(\boldsymbol{\nabla} x_X^\gamma \cdot \boldsymbol{n}\right)\big|_\Gamma \end{aligned}. \tag{1.43}$$

The true tie-line is sought after by satisfying these conditions. This type of phase equilibria is feasible only if the order of diffusivities of both the solute elements (D_γ^B and D_γ^X) in the γ phase do not differ by a large margin.

- **Constrained local equilibrium**: When $D_\gamma^X/D_\gamma^B \ll 1 (\approx 10^{-6})$, it is not possible to satisfy the mass balances simultaneously for the true tie-lines. In such a case, other suitable tie-lines are sought after under certain imposed constraints, such that the mass balance equations could be satisfied simultaneously while still maintaining local equilibria for all the alloy components, which justifies the terminology "constrained local equilibrium". Depending on the nature of constraints imposed, one could further classify into the following two types [60]:
  - **Local equilibrium - Partitioning (LE-P) condition**: Consider a representative isothermal section of the A-B-X alloy phase diagram as shown in the Fig.1.20. The nominal alloy composition is highlighted by the red point. For this scenario, instead of the true tie-line passing through the red point, LE-P condition consists of assuming another tie-line (ab) such that, $x_B^\gamma\big|_{eq} \rightarrow x_B^0$. This way, ∇x_B^γ is rendered negligible, which would slow down the flux of B solute atoms to a rate consistent with that of X solute diffusion, such that the mass balance Eqs.in (1.43) could be respected simultaneously. In addition, significant concentration differences between $x_X^\gamma\big|_\Gamma$ at the interface and x_X^0 in the bulk could be achieved which potentially results in considerable partitioning and long range diffusion of X into the γ phase, which explains the terminology, "local equilibrium with partitioning". The kinetics of transformation under this condition are considerably slow

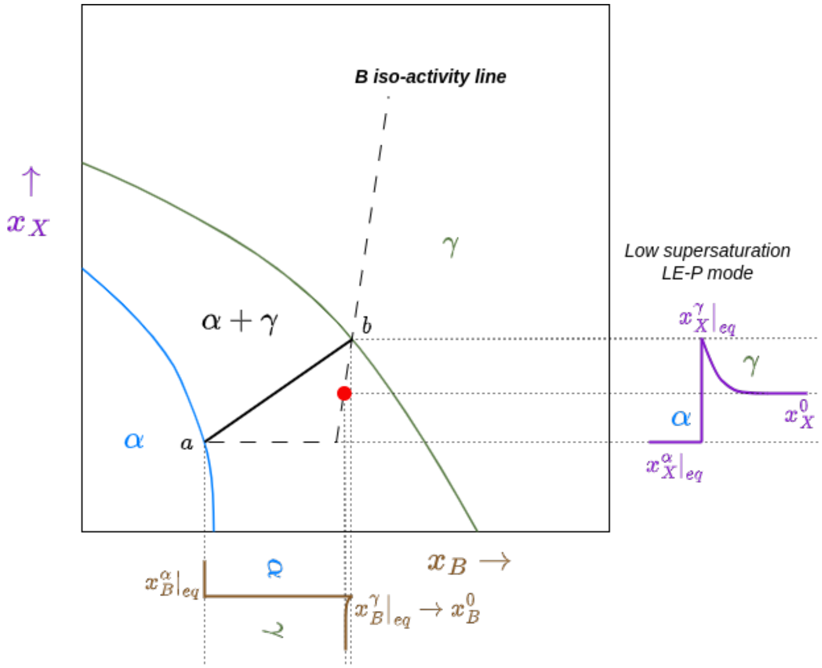

Figure 1.20: Representative isothermal section of a phase diagram illustrating the Local Equilibrium - Partitioning (LE-P) constraint. The red point corresponds to the nominal alloy composition

as they are effectively controlled by the bulk diffusion of the slow diffusing X element in the parent phase.

- **Local equilibrium - Negligible Partitioning (LE-NP) condition**: Consider another representative isothermal section of the A-B-X alloy phase diagram as depicted in the Fig.1.21. Once again, the nominal alloy composition is highlighted by the red point. Under LE-NP constraints, a tie-line (cd) is assumed such that, $x_X^{\alpha}\big|_{eq} \approx x_X^0$, and consequently, $\boldsymbol{\nabla} x_X^{\gamma}$ is significantly increased. Due to the drastic increase in $\boldsymbol{\nabla} x_X^{\gamma}$, it would now be possible to keep up with the diffusion rate of B solute atoms and thus satisfy the mass balance conditions. The name local equilibrium with negligible partitioning stems from the fact that the partitioning of the X atoms into the parent phase is negligible as the X solute concentration in the product phase is approximately close to that of the nominal composition of X. The transformation kinetics in this case are much faster than that of LE-P as the bulk diffusion of the faster diffusing B element in the parent phase is the chief rate controlling process. However, the build up of spike in X solute concentration in front of the phase interface in the parent γ phase could have an effect of slowing down the transformation kinetics.

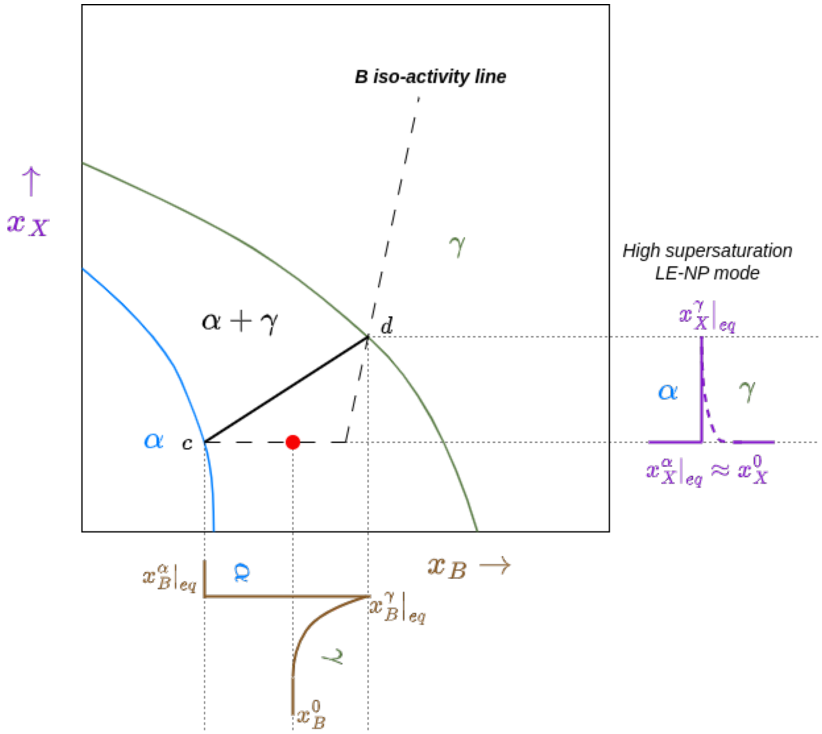

Figure 1.21: Representative isothermal section of a phase diagram illustrating the Local Equilibrium - Negligible Partitioning (LE-NP) constraint. The red point corresponds to the nominal alloy composition

It should be remarked that a transformation for a given alloy at a given temperature can either of the type LE-P or LE-NP and not both.

- **Para-equilibrium (PE)**: This is a special case of phase equilibria where a particular tie-line

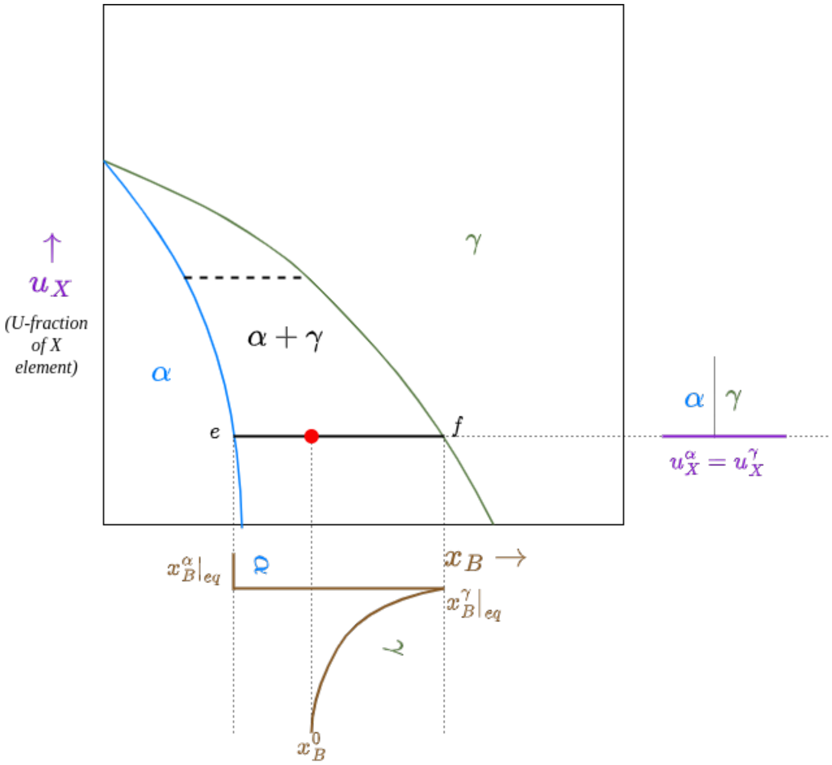

Figure 1.22: Representative isothermal section of a phase diagram illustrating the notion of Para-equilibrium (PE). The red point corresponds to the nominal alloy composition. The abscissa is represented by U-fractions of element X

is sought after such the slow diffusing X element is assumed to be completely immobile and only the fast diffusing B element is assumed to redistribute between the two phases, and hence local equilibrium is satisfied only for the B element [61]. This hypothesis is generally suitable when the diffusion of X element is not possible within the timespan of interest of the experiment or the heat treatment adopted. To understand the concept of para-equilibrium, it is important to first define the notion of u-fractions of an element. The u-fraction of an element i in a phase p_h ($u_i^{p_h}$) is defined as the ratio of the molar fraction of the element i ($x_i^{p_h}$) to the sum of molar fractions of all the elements in the alloy (except the interstitial element B) in the concerned phase p_h:

$$u_i^{p_h} = \frac{x_i^{p_h}}{\sum\limits_{\substack{j \in \{A,X\} \\ j \neq B}} x_j^{p_h}} = \frac{x_i^{p_h}}{1 - x_B^{p_h}}. \tag{1.44}$$

It should be reminded to the reader that, $x_A^{p_h} + x_B^{p_h} + x_X^{p_h} = 1$.

The alloy system under PE conditions could be seen as a pseudo-binary system of the form $M_C - B$ [62] where M_C is composed of all the other elements (including the major element) other than the fast diffusing interstitial element B. The equality of chemical potentials for this pseudo-binary system could then be imposed as:

$$\begin{gathered}\mu_B^\alpha = \mu_B^\gamma \\ \mu_{M_C}^\alpha = \mu_{M_C}^\gamma\end{gathered}, \tag{1.45}$$

where $\mu_{M_C}^\alpha$, $\mu_{M_C}^\gamma$ are defined as,

$$\mu_{M_C}^\alpha = \sum_{\substack{i\in\{A,X\}\\ i\neq B}} u_i^\alpha \mu_i^\alpha \quad and \quad \mu_{M_C}^\gamma = \sum_{\substack{i\in\{A,X\}\\ i\neq B}} u_i^\gamma \mu_i^\gamma. \tag{1.46}$$

The essence of PE condition is in the fact that the u-fractions of A and X elements are equal in both the phases:

$$u_A^\alpha = u_A^\gamma = u_A, \quad and \quad u_X^\alpha = u_X^\gamma = u_X. \tag{1.47}$$

By inducting Eqs.(1.47) and Eqs.(1.46) into the Eqs.(1.45), the thermodynamic conditions under PE could be summarized as:

$$\begin{gathered}\mu_B^\alpha = \mu_B^\gamma \\ u_A\left(\mu_A^\gamma - \mu_A^\alpha\right) + u_X\left(\mu_X^\gamma - \mu_X^\alpha\right) = 0\end{gathered}. \tag{1.48}$$

One could further show that:

$$\frac{x_A^\gamma}{x_A^\alpha} = \frac{x_X^\gamma}{x_X^\alpha} \tag{1.49}$$

Fig.1.22 illustrates an isothermal section of the phase diagram under PE conditions with u-fractions of the slow diffusing substitutional element X plotted along the abscissa. In this case, the tie lines remain virtually parallel to the x_B composition axis. Though the u-fractions of X and A remain equal in both the phases, the usual concentration fractions of these elements would differ slightly in the two phases. Kinetics of a transformation under PE are generally much faster than that of LE-NP hypothesis since the reaction is principally controlled solely by partitioning of B element until the equality of their chemical potentials, where PE constrained equilibrium concentrations are attained.

Solute drag effects of the substitutional elements: Due to their low influence and involvement in solute diffusion, the contribution of the slow diffusing substitutional elements could sound insignificant towards the transformation kinetics. However, it has been experimentally observed [63, 64] that the addition of these substitutional elements could induce additional dissipation effects as they interact with the migrating interface due to the solute segregation within the interface. Potentially a solute concentration spike is developed in the vicinity of the interface. As the interface is driven, these solute atoms can either be dragged along with or pushed ahead of this migrating interface. In the process, a certain free energy is dissipated which could be attributed as a resistance or a drag pressure against the interface motion. These effects have been classically qualified as "solute drag effects", that have the global effect of slowing down the rate of interface migration as a part of the driving pressure available for phase transformation is consumed to overcome the resistance.

Fig.1.23 illustrates a classification proposed by Hutchinson et al. [63] of some of the common substitutional elements (X) in the context of Fe-C-X alloys based on their interaction with Carbon (C), and their interaction with phase interface (linked to solute drag effects). This classification serves as a foundation to qualify the importance of accounting for the solute drags effects depending on the substitutional element in play. It has been observed that the kinetics in the case of Fe-C-Ni alloys (for example) showed small solute drag effects which could be linked to their considerably low interface interaction. However in the case of Fe-C-Mo alloys, the solute drag effects are more important because of the strong interaction of Mo solutes with the interface. While in the case of Mn element, though it is not expected to show substantial solute drag effects, it is still non-negligible. In general, the X-interface interaction has been associated with the binding energy of the X solute atoms to the interface such that, a stronger binding energy implies a stronger interface interaction and hence stronger solute drag effects. It must be highlighted that the classification in the Fig.1.23 could be subject to changes according to the heat treatment conditions adopted.

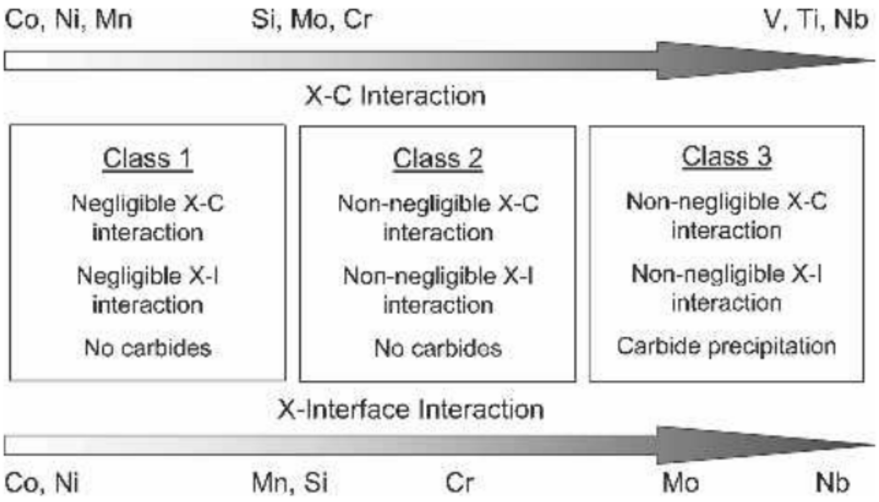

Figure 1.23: From [63]: Classification of some of the common substitutional elements (X) based on their effects on phase transformation kinetics in steels

If a drag pressure (P_{SD}) is correlated to the solute drag effects, Eq.(1.35) could be modified with this additional contribution as:

$$\boldsymbol{v} = M \left(\Delta G_{\gamma\to\alpha} - \kappa\sigma_{\gamma\alpha} + P_{SD}\right) \boldsymbol{n}. \tag{1.50}$$

The magnitude of the solute drag pressure ($\Delta G_{SD} = |P_{SD}|$) is generally assumed to be a function of the interface migration velocity itself, $\Delta G_{SD} = f(\boldsymbol{v})$, which has the effect of making Eq.(1.50) non-linear. The dependence on the velocity is such that, in the vicinity of zero velocity, or at sufficiently high interfacial velocities, the drag pressure should theoretically vanish. The latter is due to the fact that at high velocities, there is not enough scope or time for the solute atoms to interact with the rapidly migrating interface, thus reducing the potential to impart any retardation effects of significance.

Cahn [65] was one of the first to provide the foundations of solute drag theory, albeit for grain boundary migration in a single phase alloy. Purdy and Brechet [66] later extended Cahn's theory for interphase boundaries. Hillert et al. [67, 68] on the other hand provided a different perspective of solute drag effects in the form of a dissipation of Gibbs energy in their works. In the scope of this chapter, the foundations of the solute drag theory as described by Cahn and its extension by Purdy and Brechet will be detailed.

The 1D segregation profile of an element X within the interface region at the quasi-steady state is governed by,

$$D_\Gamma^X \frac{\partial^2 x_X}{\partial z^2} + \frac{\partial x_X}{\partial z}\left[\frac{\partial D_\Gamma^X}{\partial z} + \frac{D_\Gamma^X}{k_B T}\frac{\partial E}{\partial z} + v_n\right] + \frac{x_X}{k_B T}\left[\frac{\partial D_\Gamma^X}{\partial z}\frac{\partial E}{\partial z} + D_\Gamma^X \frac{\partial^2 E}{\partial z^2}\right] = 0, \tag{1.51}$$

where D_Γ^X is the diffusivity of X element within the interfacial region of segregation, $E(z)$ is the interaction energy profile of X, x_X is the concentration of solute X, x_X^0 is the bulk composition of the solute, and v_n is the norm of the interface velocity, $\boldsymbol{v}$.

By taking into account the contribution of all the segregating atoms on the interfacial region, Cahn described the magnitude of the net solute drag driving pressure as:

$$\Delta G_{SD} = -N_V \int_{-\infty}^{\infty} \left(x_X - x_X^0\right) \frac{\partial E}{\partial z}\, dz, \tag{1.52}$$

where N_V is the number of solute atoms per unit volume.

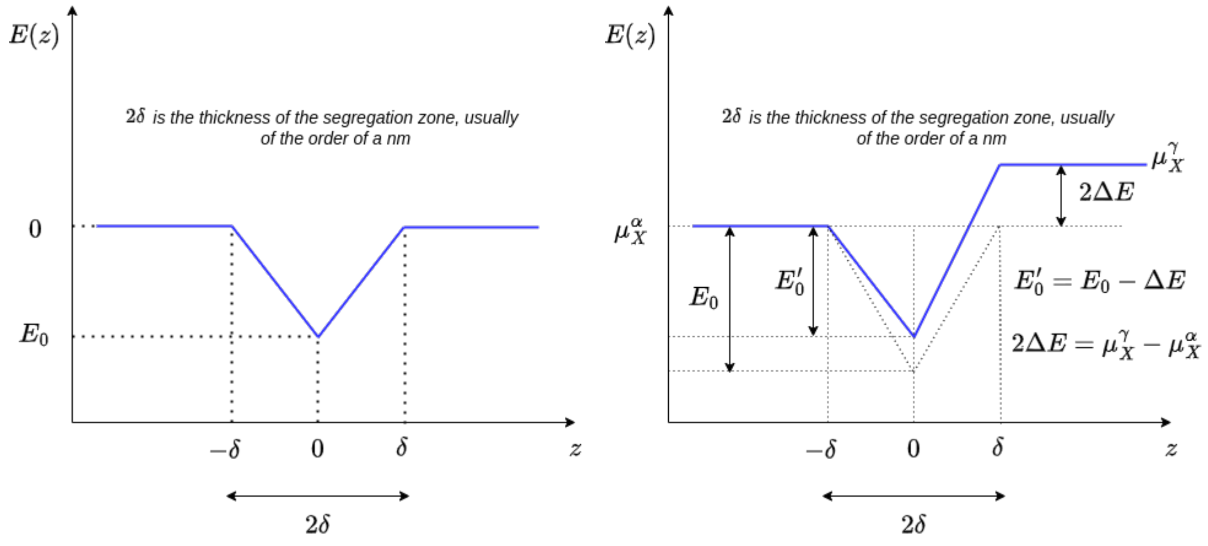

(a) Cahn's assumption [65]

(b) Purdy and Brechet's assumption [66]

Figure 1.24: Interaction energy profiles, $E(z)$, assumed across an interface of width 2δ

Fig.1.24a illustrates the interaction energy or potential profile of X with the interface as assumed by Cahn [65] across an interface of finite width 2δ, while Fig.1.24b represents the one assumed by Purdy and Brechet [66]. Here, $2\Delta E$ is assumed to be a measure of the chemical potential difference of X between the two phases, and E_0 is the binding energy of X to the interface. In the case of Cahn's profile, the chemical potential difference of the solute X amounts to zero since it is supposed for a single phase alloy, thus yielding a symmetrical wedge shaped well for the interaction potential. In contrast, Purdy and Brechet aimed to extend the method for phase interfaces and hence assumed an asymmetrical wedge shaped well with a difference in the X chemical potential across the interfaces.

If we suppose the diffusivity, D_Γ^X, to be constant with space, then Eq.(1.51) could be simplified to the following form:

$$D_\Gamma^X \frac{\partial x_X}{\partial z} + \frac{D_\Gamma^X x_X}{k_B T} \frac{\partial E}{\partial z} + v_n \left(x_X - x_X^0 \right) = 0. \tag{1.53}$$

If the above equation is resolved for the profile assumed in Fig.1.24b, we obtain the following analytical expressions for the solute segregation profile:

$$\frac{x_X(z)}{x_X^0} = \begin{cases} 1 & \text{if } z < -\delta \\ \dfrac{1+a \exp\left(-\frac{v_n (1+a)(z+\delta)}{D_\Gamma^X}\right)}{1+a} & \text{if } -\delta < z < 0 \\ \dfrac{1+a+\left[a(1+b)\exp\left(-\frac{v_n(1+a)\delta}{D_\Gamma^X}\right)+b-a\right]\exp\left(-\frac{v_n(1+b)z}{D_\Gamma^X}\right)}{(1+a)(1+b)} & \text{if } 0 > z > \delta \\ 1+\exp\left(-\frac{v_n z}{D_\Gamma^X}\right)\left[\dfrac{a\exp\left(-\frac{v_n(a+b+1)\delta}{D_\Gamma^X}\right)}{1+a} + \dfrac{(b-a)\exp\left(-\frac{v_n\delta b}{D_\Gamma^X}\right)}{(1+a)(1+b)} - \dfrac{b\exp\left(\frac{v_n\delta}{D_\Gamma^X}\right)}{1+b}\right] & \text{if } z > \delta \end{cases}, \tag{1.54}$$

where $a = \frac{D_\Gamma^X(\Delta E - E_0)}{k_B T v_n \delta}$, and $b = \frac{D_\Gamma^X(\Delta E + E_0)}{k_B T v_n \delta}$. If we impose $\Delta E = 0$ into the Eqs.(1.54), we can recover the expressions of segregation profiles for the Cahn's case. Figs.1.25 illustrate the segregation profiles across and around the interface at different ranges of interface velocity for the two cases. For stationary interfaces ($v_n \rightarrow 0$), we observe that the Cahn's case gives a symmetric segregation profile across the interface due to the symmetric interaction energy profile, while Purdy and Brechet's case yields asymmetric profile due to the inherent asymmetric interaction potential well. From the definition of solute drag pressure in Eq.(1.52), it is evident that ΔG_{SD} is non-zero only when there exists an asymmetric segregation profile and/ or an asymmetric interaction energy profile. Thus Cahn's theory correctly predicts zero drag pressure for stationary interfaces, while Purdy and Brechet's assumptions do not vanish the drag pressure under this condition. The asymmetry in Cahn's segregation profile and hence the solute drag only develop as the interface starts migrating ($v_n > 0$). At significantly high velocities, the profiles flatten out towards the bulk concentration for both the cases and hence as $v_n \rightarrow \infty$, $\Delta G_{SD} \rightarrow 0$.

The solute drag pressure could be evaluated by imposing the composition profile expressions such as Eq.(1.54) (computed for a chosen $E(z)$ and $D_\Gamma^X(z)$) into the Eq.(1.52) and integrating it.

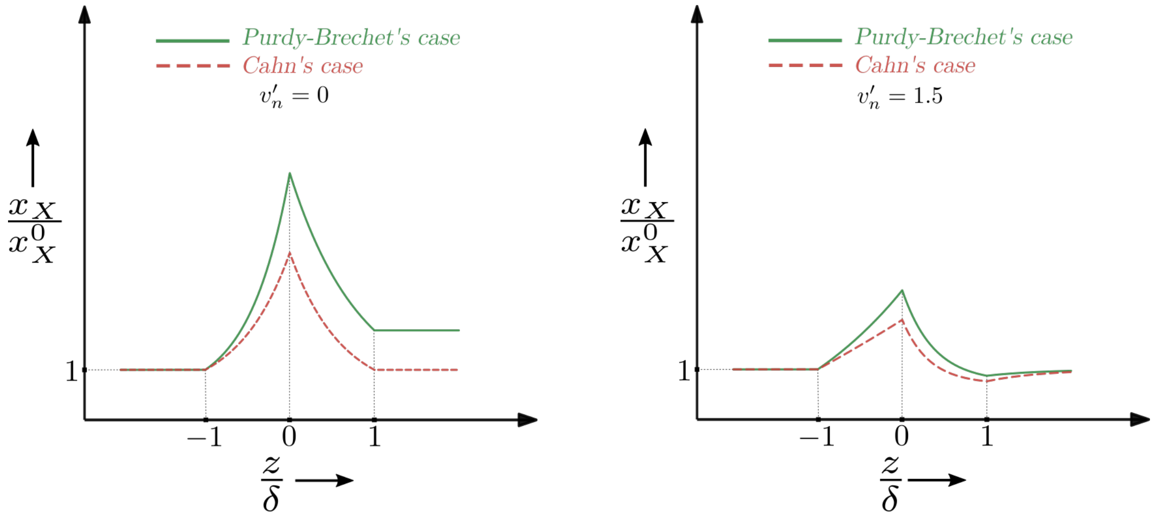

(a) Stationary interface, $v'_n = 0$

(b) $v'_n = 1.5$

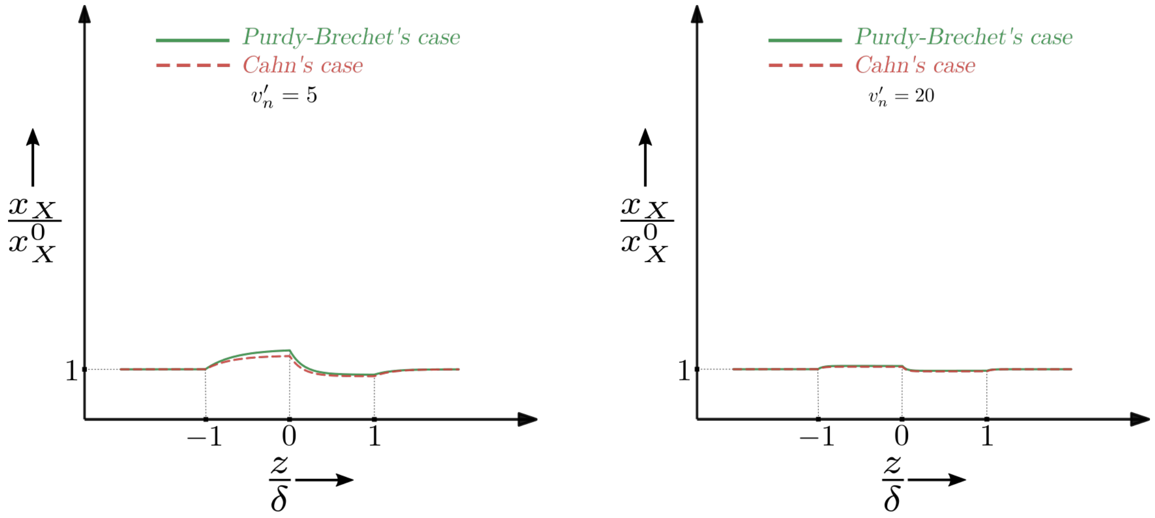

(c) $v'_n = 5$

(d) Significantly high velocity, $v'_n = 20$

Figure 1.25: Illustration of the segregation profiles at different non-dimensional velocities, $v'_n = v_n\delta/D_\Gamma^X$, for the two cases

Considering the complexity of the integrated expression of ΔG_{SD} for arbitrary $E(z)$, and $D_{\Gamma}^{X}(z)$, Cahn formulated an approximate and a simple expression for the solute drag pressure that could potentially fit for various velocity regimes:

$$\Delta G_{SD} = \frac{\alpha_C x_X^0 v_n}{1 + \beta_C^2 v_n^2}, \tag{1.55}$$

where α_C and β_C are parameters defined as functions of temperature, interfacial solute diffusivity, interface width and the binding energy. Cahn proposed the following definitions for these parameters:

$$\alpha_C = 4N_V k_B T \int_{-\infty}^{+\infty} \frac{\sinh^2\left(\frac{E(z)}{2k_B T}\right)}{D_{\Gamma}^{X}(z)}\, dz \tag{1.56}$$

$$\frac{\alpha_C}{\beta_C^2} = \frac{N_V}{k_B T} \int_{-\infty}^{+\infty} \left(\frac{\partial E}{\partial z}\right)^2 D_{\Gamma}^{X}(z)\, dz \tag{1.57}$$

For the interaction energy profile considered in the Fig.1.24a, and a constant interfacial solute diffusivity hypothesis, the following expressions can be deduced for these parameters:

$$\alpha_C = \frac{4N_V k_B^2 T^2 \delta}{D_{\Gamma}^{X} E_0} \left[\sinh\left(\frac{E_0}{k_B T}\right) - \frac{E_0}{k_B T}\right] \tag{1.58}$$

$$\beta_C^2 = \frac{\alpha_C k_B T \delta}{2N_V D_{\Gamma}^{X} E_0^2} \tag{1.59}$$

For the case of Purdy and Brechet, interested readers could refer the appendix-A for the complex integrated expression of the solute drag pressure for the considered interaction energy profile (Fig.1.24b) and constant interfacial solute diffusivity assumption. Fig.1.26 gives an illustration of the variation of the solute drag pressure with the interface migration velocity and compares it for the two cases for a certain set of parameters. We observe that the solute drag pressure reaches a maximum value for a certain velocity before decreasing again for high velocity limits. We also observe that as the binding energy of the solute to the interface is increased, the magnitude of the solute drag effects are also increased. The difference between the two models is more evident as the potential difference term becomes more important indicating the influence of a phase interface in contrast to a grain interface. As previously touched upon, for the Cahn's case, the driving pressure rightfully vanishes for stationary and high interface velocity limits. On the other hand, though Purdy-Brechet's hypotheses has a physical sense and significance for phase interfaces, it fails to capture the expected zero driving pressure for stationary interface limit. Fazeli et al. [69] proposed a correction to force the driving pressure predicted by Purdy-Brechet model to vanish for stationary interfaces. They suggested the following modifications for the concentration and the derivative of

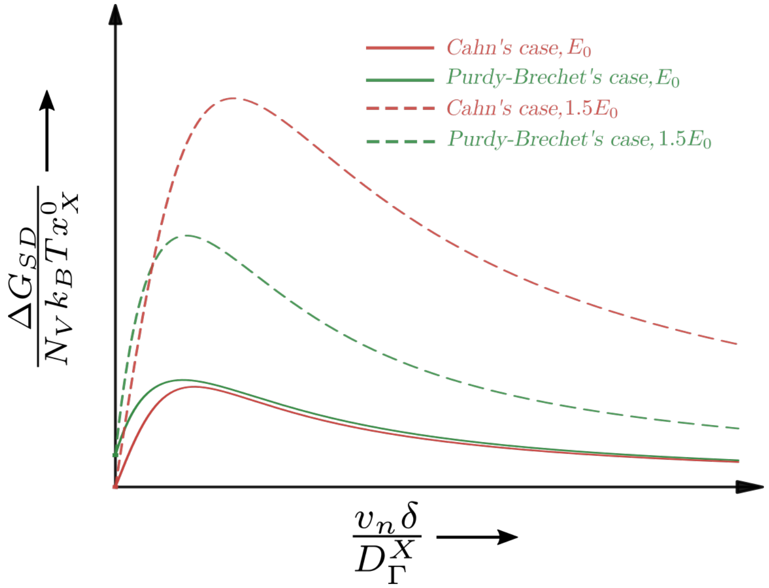

(a) Influence of the binding energy, E_0

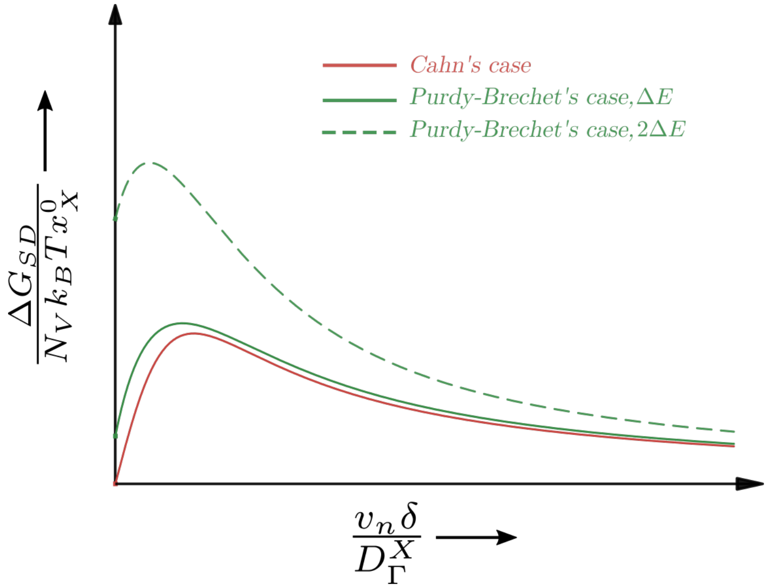

(b) Influence of the chemical potential difference, ΔE

Figure 1.26: Variation of the solute drag pressure (non-dimensional) with the interface velocity (non-dimensional) for a certain set of parameters for the two models

the interaction energy, before imposing them into the Eq.(1.52) to compute the drag pressure:

$$x_X|_{new} = x_X \exp\left(\frac{\Delta E z}{k_B T \delta}\right), \tag{1.60}$$

$$\left.\frac{\partial E}{\partial z}\right|_{new} = \frac{\partial E}{\partial z} - \frac{\Delta E}{\delta}. \tag{1.61}$$

The above modifications enforce symmetry for $x_X|_{new}$ at $v_n = 0$ within the interfacial region, and also ensure that the modified derivative is an odd function which helps vanish the integral in Eq.(1.52) for a stationary interface. However, such a correction remains to be a mere mathematical manipulation and fails to give any physical sense.

1.3 Summary

A microstructure of a material is composed by a topological distribution and arrangement of grain(s), phase(s), the grain/ phase boundary network, and other potential defects. An unstable microstructural configuration is thermodynamically driven towards a stable configuration through a minimization of the excess Gibbs free energy built-up in the system. This process constitutes a microstructural transformation, where the type of transformation is qualified based on the source of instabilities and the underlying mechanism driving the minimization of the free energy. The sources of excess free energy build-up could be broadly classified as chemical free energy, strain free energy, and interfacial free energy. Phase transformation is principally driven by excess chemical free energy as the principal source of stimulus. Allotropic phase transformation is characterized by evolution from an unstable parent phase to a more stable product phase by undergoing crystallographic changes, and/ or potential compositional changes. Diffusive solid-state phase transformation (DSSPT) in particular is associated with gradual rearrangement of the crystal lattice into that of the product phase through short and long range diffusion of the solutes at the solid-state. From a thermodynamic point of view, complete phase equilibrium is achieved through equality of chemical potentials in all the phases in play for all the components of the alloy. DSSPT broadly involves two basic mechanisms: nucleation of the stable product phase, and the growth of these product phase nuclei into grains until the phase equilibria for the heterogeneous phase mixture is achieved.

Phase nucleation involves formation of local cluster of atoms with the crystal structure of the product phase in place of the existing unstable parent phase. A nucleation event is synonymous to the concept of metastability, where the system with the unstable parent phase structure remains metastable unless a certain activation energy is provided to overcome the nucleation barrier to create stable nuclei of the product phase. The presence of any inherent defects in the parent microstructure act as preferential sites of nucleation (heterogeneous nucleation) as it is favorable to destroy the defects and lower the free energy of the system. As a result, the nucleation barrier is lowered making it easier to nucleate stable nuclei. Due to the limitations of physically observing a nucleus and understanding its formation, a complete unified description of the nucleation event is still lacking despite a rich literature. The existing models have plenty of leeway to make several hypotheses and assume several complex parameters to describe the phenomena. Thus, especially at the mesoscopic scale, nucleation event is generally described with reasonably simplistic approaches based on strong hypotheses. During the growth stage, the stable nuclei formed from the nucleation stage continue to grow into grains of the product phase, governed by the interface migration kinetics. In the process, a part of the driving pressure available for phase transformation is dissipated by interfacial processes involving lattice rearrangement and the rest by long-range solute diffusion. For a realistic description of transformation kinetics, the character of transformation is of the mixed-mode type, where a finite interface mobility controls the interfacial processes, and a finite diffusivity controls the solute diffusion in the bulk, such that the local equilibrium at the interface is rather gradually achieved.

In the case of ternary alloys and beyond consisting of one or more slowly diffusing substitutional elements, complete local phase equilibrium (ortho-equilibrium) may not be feasible within the characteristic time scales of industrial interest. This stems from the fact that the rates of diffusion of the rapidly diffusing interstitial elements may not be consistent with the rates of diffusion of the substitutional elements, thus making it difficult to satisfy the mass balances of all the solutes simultaneously. This is generally overcome by making constrained phase equilibria hypotheses to describe the transformation kinetics, where instead of the true tie-line (conode) passing through the nominal alloy composition, different tie-lines are sought after subject to certain constraints. The potential interaction of substitutional solutes with the migrating interface could render sluggish transformation kinetics. The solute segregation within the interface foster a drag resistance towards the interface migration resulting in the consumption of a part of the driving pressure available for phase transformation. These effects have been classically characterized as the solute drag effects. The magnitude of these drag effects have been directly associated with the binding energy of the solute to the interface.

References

[1] G. Gottstein and L.S. Shvindlerman. *Grain boundary migration in metals: thermodynamics, kinetics, applications*. CRC press, 2009.

[2] D.A. Porter, K.E. Easterling, and M.Y. Sherif. *Phase transformations in metals and alloys*. CRC press, 2021.

[3] J.W. Martin, R.D. Doherty, and B. Cantor. *Stability of microstructure in metallic systems*. Cambridge University Press, 1997.

[4] K.G.F. Janssens et al. *Computational materials engineering: an introduction to microstructure evolution*. Academic Press, 2010.

[5] C.M. Wayman. “Solid-state phase transformations”. In: *Annual Review of Materials Science* 1.1 (1971), pp. 185–218.

[6] G.S. Cole. “Inhomogeneities and their control via solidification”. In: *Metallurgical Transactions* 2 (1971), pp. 357–370.

[7] A. Roosz, Z. Gacsi, and E.G. Fuchs. “Solute redistribution during solidification and homogenization of binary solid solution”. In: *Acta Metallurgica* 32.10 (1984), pp. 1745–1754.

[8] J.W. Cahn. “On spinodal decomposition”. In: *Acta Metallurgica* 9.9 (1961), pp. 795–801. ISSN: 0001-6160. DOI: `https://doi.org/10.1016/0001-6160(61)90182-1`.

[9] J.W. Cahn. “Phase separation by spinodal decomposition in isotropic systems”. In: *The Journal of chemical physics* 42.1 (1965), pp. 93–99.

[10] N.C. Law and D.V. Edmonds. “The formation of austenite in a low-alloy steel”. In: *Metallurgical and Materials Transactions A* 11 (1980), pp. 33–46.

[11] G. Krauss and S.W. Thompson. “Ferritic microstructures in continuously cooled low-and ultralow-carbon steels”. In: *ISIJ international* 35.8 (1995), pp. 937–945.

[12] R. Wagner, R. Kampmann, and P.W. Voorhees. “Homogeneous second-phase precipitation”. In: *Phase transformations in materials* (2001), pp. 309–407.

[13] H.B. Aaron and G.R. Kotler. “Second phase dissolution”. In: *Metallurgical transactions* 2 (1971), pp. 393–408.

[14] A. Rollett, G.S. Rohrer, and J. Humphreys. *Recrystallization and Related Annealing Phenomena*. Elsevier Science, 2017. ISBN: 9780080982694. URL: `https://books.google.fr/books?id=GhZETAEzYOIC`.

[15] P. Fratzl, O. Penrose, and J. L. Lebowitz. "Modeling of phase separation in alloys with coherent elastic misfit". In: *Journal of Statistical Physics* 95 (1999), pp. 1429–1503.

[16] H.-J. Jou, P.H. Leo, and J.S. Lowengrub. "Microstructural evolution in inhomogeneous elastic media". In: *Journal of Computational Physics* 131.1 (1997), pp. 109–148.

[17] G.T. Higgins. "Grain-boundary migration and grain growth". In: *Metal Science* 8.1 (1974), pp. 143–150.

[18] B. Ralph. "Grain growth". In: *Materials Science and Technology* 6.11 (1990), pp. 1136–1144.

[19] K.M. Vedula and R.W. Heckel. "Spheroidization of binary Fe-C alloys over a range of temperatures". In: *Metallurgical Transactions* 1 (1970), pp. 9–18.

[20] Y.L. Tian and R.W. Kraft. "Mechanisms of pearlite spheroidization". In: *Metallurgical transactions A* 18 (1987), pp. 1403–1414.

[21] P.W. Voorhees. "The theory of Ostwald ripening". English (US). In: *Journal of Statistical Physics* 38.1-2 (Jan. 1985). Copyright: Copyright 2007 Elsevier B.V., All rights reserved., pp. 231–252. ISSN: 0022-4715. DOI: `10.1007/BF01017860`.

[22] Y.D. Zhang et al. "Microstructural features induced by a high magnetic field in a hypereutectoid steel during austenitic decomposition". In: *Scripta Materialia* 54.11 (2006), pp. 1897–1900. ISSN: 1359-6462. DOI: `https://doi.org/10.1016/j.scriptamat.2006.02.009`.

[23] H. Wollenberger. "Phase transformations under irradiation". In: *Journal of nuclear materials* 216 (1994), pp. 63–77.

[24] J.D. Guo, X.L. Wang, and W.B. Dai. "Microstructure evolution in metals induced by high density electric current pulses". In: *Materials science and technology* 31.13 (2015), pp. 1545–1554.

[25] R.W. Cahn and P. Haasen. *Physical metallurgy*. Vol. 1. Elsevier, 1996.

[26] J.W. Gibbs. "On the equilibrium of heterogeneous substances". In: *Transactions of Connecticut Academy of Arts and Sciences* (1876), pp. 108–248.

[27] E.P. Favvas and A.C. Mitropoulos. "What is spinodal decomposition". In: *J. Eng. Sci. Technol. Rev* 1.1 (2008), pp. 25–27.

[28] R.D. James. "Displacive phase transformations in solids". In: *Journal of the Mechanics and Physics of Solids* 34.4 (1986), pp. 359–394.

[29] M. Hillert. *Phase equilibria, phase diagrams and phase transformations: their thermodynamic basis*. Cambridge university press, 2007.

[30] A. Weber. "Keimbildung in übersättigten Gebilden". In: *Zeitschrift für physikalische Chemie* 119.1 (1926), pp. 277–301.

[31] R. Becker and W. Döring. "Kinetische behandlung der keimbildung in übersättigten dämpfen". In: *Annalen der physik* 416.8 (1935), pp. 719–752.

[32] J.W. Christian. *The theory of transformations in metals and alloys*. Newnes, 2002.

[33] V.I. Kalikmanov. "Classical nucleation theory". In: *Nucleation theory*. Springer, 2012, pp. 17–41.

[34] K.C. Russell. "Grain boundary nucleation kinetics". In: *Acta Metallurgica* 17.8 (1969), pp. 1123–1131.

[35] W.C. Johnson et al. "Influence of crystallography on aspects of solid-solid nucleation theory". In: *Metallurgical Transactions A* 6 (1975), pp. 911–919.

[36] E. Clouet. "Modeling of nucleation processes". In: *arXiv preprint arXiv:1001.4131* (2010).

[37] H.A. Landheer. "Nucleation of ferrite in austenite: The role of crystallography". PhD thesis. Delf University of Technology, 2010.

[38] M. Hillert and M. Rettenmayr. “Deviation from local equilibrium at migrating phase interfaces”. In: *Acta materialia* 51.10 (2003), pp. 2803–2809.

[39] J.W. Gibbs. *The Collected Works of J. Willard Gibbs: Thermodynamics*. The Collected Works of J. Willard Gibbs. Yale University Press, 1948. URL: `https://books.google.fr/books?id=UzwPAQAAMAAJ`.

[40] P.J. Clemm and J.C. Fisher. “The influence of grain boundaries on the nucleation of secondary phases”. In: *Acta Metallurgica* 3.1 (1955), pp. 70–73.

[41] W.F. Lange, M. Enomoto, and H.I. Aaronson. “The kinetics of ferrite nucleation at austenite grain boundaries in Fe-C alloys”. In: *Metallurgical Transactions A* 19 (1988), pp. 427–440.

[42] M. Enomoto, W.F. Lange, and H.I. Aaronson. “The kinetics of ferrite nucleation at austenite grain edges in Fe-C and Fe-CX alloys”. In: *Metallurgical Transactions A* 17 (1986), pp. 1399–1407.

[43] K.S. Chan et al. “Generalization of the nucleus shape-dependent parameters in the nucleation rate equation”. In: *Metallurgical Transactions A* 9 (1978), pp. 1016–1017.

[44] W. Huang and M. Hillert. “The role of grain corners in nucleation”. In: *Metallurgical Transactions, A* 27.2 (1996).

[45] S.E. Offerman et al. “Grain nucleation and growth during phase transformations”. In: *Science* 298.5595 (2002), pp. 1003–1005.

[46] G.S. Rohrer. “Grain boundary energy anisotropy: a review”. In: *Journal of materials science* 46 (2011), pp. 5881–5895.

[47] P.J. Hurley and F.J. Humphreys. “Modelling the recrystallization of single-phase aluminium”. In: *Acta materialia* 51.13 (2003), pp. 3779–3793.

[48] A. Yamanaka, T. Takaki, and Y. Tomita. “Multi-phase-field modeling of diffusive solid phase transition in carbon steel during continuous cooling transformation”. In: *Journal of Crystal Growth* 310.7-9 (2008), pp. 1337–1342.

[49] S.R. Logan. “The origin and status of the Arrhenius equation”. In: *Journal of Chemical Education* 59.4 (1982), p. 279.

[50] W.T. Read and W. Shockley. “Dislocation models of crystal grain boundaries”. In: *Physical review* 78.3 (1950), p. 275.

[51] W.T. Read. *Dislocations in crystals*. McGraw-Hill, 1953.

[52] M. Tong, D. Li, and Y. Li. “Modeling the austenite–ferrite diffusive transformation during continuous cooling on a mesoscale using Monte Carlo method”. In: *Acta materialia* 52.5 (2004), pp. 1155–1162.

[53] N. Xiao et al. “Coupled simulation of the influence of austenite deformation on the subsequent isothermal austenite–ferrite transformation”. In: *Acta materialia* 54.5 (2006), pp. 1265–1278.

[54] M. Hillert. “Diffusion and interface control of reactions in alloys”. In: *Metallurgical Transactions A* 6 (1975), pp. 5–19.

[55] Z.-K. Liu. “Theoretic calculation of ferrite growth in supersaturated austenite in Fe C alloy”. In: *Acta materialia* 44.9 (1996), pp. 3855–3867.

[56] J. Svoboda et al. “Kinetics of interfaces during diffusional transformations”. In: *Acta Materialia* 49.7 (2001), pp. 1249–1259.

[57] X. Liu, H. Li, and M. Zhan. “A review on the modeling and simulations of solid-state diffusional phase transformations in metals and alloys”. In: *Manufacturing Review* 5 (2018), p. 10.

[58] J. Sietsma and S. van der Zwaag. “A concise model for mixed-mode phase transformations in the solid state”. In: *Acta Materialia* 52.14 (2004), pp. 4143–4152.

[59] D.R.F. West. *Ternary phase diagrams in materials science*. Routledge, 2017.

[60] H.K.D.H. Bhadeshia. “Diffusional formation of ferrite in iron and its alloys”. In: *Progress in Materials Science* 29.4 (1985), pp. 321–386.

[61] M. Hillert and J. Ågren. “On the definitions of paraequilibrium and orthoequilibrium”. In: *Scripta Materialia* 50.5 (2004), pp. 697–699.

[62] G. Inden. “Diffusion and Phase Transformations in Multi-Component Systems”. In: Defect and Diffusion Forum 263 (Mar. 2007), pp. 11–20. DOI: `10.4028/www.scientific.net/DDF.263.11`.

[63] C.R. Hutchinson, H.S. Zurob, and Y. Brechet. “The growth of ferrite in Fe-CX alloys: The role of thermodynamics, diffusion, and interfacial conditions”. In: *Metallurgical and Materials Transactions A* 37 (2006), pp. 1711–1720.

[64] G. Purdy et al. “ALEMI: A ten-year history of discussions of alloying-element interactions with migrating interfaces”. In: *Metallurgical and Materials Transactions A* 42 (2011), pp. 3703–3718.

[65] J.W. Cahn. “The impurity-drag effect in grain boundary motion”. In: *Acta metallurgica* 10.9 (1962), pp. 789–798.

[66] G.R. Purdy and Y.J.M. Brechet. “A solute drag treatment of the effects of alloying elements on the rate of the proeutectoid ferrite transformation in steels”. In: *Acta metallurgica et materialia* 43.10 (1995), pp. 3763–3774.

[67] M. Hillert and B. Sundman. “A solute-drag treatment of the transition from diffusion-controlled to diffusionless solidification”. In: *Acta Metallurgica* 25.1 (1977), pp. 11–18.

[68] M. Hillert. “Solute drag in grain boundary migration and phase transformations”. In: *Acta materialia* 52.18 (2004), pp. 5289–5293.

[69] F. Fazeli and M. Militzer. “Application of solute drag theory to model ferrite formation in multiphase steels”. In: *Metallurgical and Materials Transactions A* 36 (2005), pp. 1395–1405.

Chapter 2

Numerical modeling of microstructural evolution: diffusive solid-state phase transformation

---

Abstract

Numerical modeling and predicting the evolution aspects of a material's microstructure have gained growing significance, especially for vital industrial sectors. They serve as valuable tools for metallurgists, enabling them to precisely manage process parameters and manipulate material properties. Numerical simulation also plays a crucial role in emulating and observing complex microstructural evolution traits that are typically challenging to capture experimentally.

In this chapter, as a precursor, several numerical approaches used in the context of microstructural evolution for various phenomena are enumerated. Special emphasis is placed on full-field numerical methods capable of precisely modeling microstructural transformations at the mesoscopic scale. The focus is then predominantly shifted towards full-field modeling of diffusive solid-state phase transformation in metallic materials. A numerical formulation based on the level-set (LS) method is elaborated in a finite element context. This numerical framework is formulated primarily to simulate diffusive phase transformation kinetics in a biphasic polycrystalline but also has the potential to consider other types of transformations concurrently, thanks to a generalized interface kinetics description.

Résumé

La modélisation numérique et la prédiction de l'évolution des microstructures des matériaux lors de leur mise en forme prennent de plus en plus d'importance, en particulier dans les secteurs industriels critiques. Elles constituent des outils indispensables pour les métallurgistes, leur permettant de gérer avec plus de précision les paramètres des procédés et de manipuler les propriétés des matériaux. La simulation numérique joue également un rôle crucial dans l'émulation et l'observation des caractéristiques complexes de l'évolution des microstructures, qui sont généralement difficiles à saisir expérimentalement.

Dans ce chapitre, plusieurs approches numériques utilisées dans le contexte de migration d'interfaces pour différents phénomènes sont introduites. L'accent est mis sur les méthodes numériques en champ complet capables de modéliser avec précision les transformations microstructurales à l'échelle mésoscopique. Ensuite, la modélisation en champ complet de la transformation de phase diffusive à l'état solide dans les matériaux métalliques est au centre de la discussion. Une formulation numérique basée sur la méthode de level-set (LS) est détaillée dans un contexte éléments finis (EF). Ce modèle numérique est formulé principalement pour simuler la cinétique de la transformation de phase diffusive dans un polycristal biphasé, mais il a également le potentiel de modéliser d'autres types de transformations, grâce à une description généralisée de la cinétique de l'interface.

2.1 Introduction: state of the art of numerical models for microstructural evolution

As highlighted in the previous chapter, in-use materials can undergo several types of microstructural transformations depending on their processing conditions. These transformations can eventually influence various material properties, which, in turn, may affect its in-service life. Therefore, it is paramount to control the process parameters responsible for microstructural transformations and to predict and monitor the evolution of the material's properties, especially for critical industrial applications. Numerical modeling of microstructural evolution has thus gained momentum to help with the comprehensive understanding of the underlying phenomena and assist in manipulating the processes involved and determining the in-service material performance.

To simulate microstructural evolution, depending on the level of description desired and the scale of modeling, one can use the analytical and empirical models, mean-field models, full-field models, or the molecular dynamics based models (atomistic models). The analytical and the empirical models [1–6] are generally based on significantly strong assumptions through simplification of the physics involved. Empirical models predict homogenized behavior based on the phenomenological laws such as the Johnson-Mehl-Avrami-Kolmogorov (JMAK) equations [7–9]. Despite their simplicity in implementation and minimal demand for computational resources, their predictions are generally limited to the statistics of the involved phenomena in the range of data used for their parameterization. So, to improve the scope of application of numerical models and to extend the ability to capture the involved physics, mean field models (MFM) [10–18] based on physical laws have been developed. MFM is based on an averaged and implicit description of the microstructure, where grains or precipitates are treated as spherical entities, and it encompasses statistical transformations associated with various attributes such as grain size, precipitate size, phase fraction, dislocation density, etc. MFM are known for their computational efficiency, however, their predictive capabilities are still limited and they fall short in reproducing certain microstructural features as they do not involve precise modeling of the topological changes during the evolution. Advances in computational resources have paved the way for more intricate models (such as atomistic and full-field mesoscopic models) based on a complete and an explicit representation of the microstructure. These models enable to closely follow the topological evolution of the microstructure during a transformation and have the potential to capture complex evolution aspects and hence their predictive capabilities are much wider. Molecular dynamics [19–21] approaches consider the basic building blocks of material, atoms, as the smallest entity. Such models provide a profound description of the involved mechanisms at the atomistic scale, but also require large computational resources. Thus, these models are often considered to analyze or quantify certain characteristics over a localized region of the microstructure limited to a few interfaces. By simplifying the interface description and approximating the interface properties and kinetics, while still maintaining the explicit description of the microstructure topology at the polycrystalline scale, the so-called full-field models (FFM) [22] have emerged. These models typically consider a few thousand to a few tens of thousands of grains in 2D or 3D. FFM provide a tool to study the unsteady state features and their dynamics at the mesoscopic scale, while also providing a basis for calibrating many mean field models. FFM has proven to be highly capable of simulating a wide spectrum of microstructural transformations, including the precise modeling of phenomena such as recrystallization (ReX) [23–25] under both dynamic (DRX) and post-dynamic (PDRX) conditions, Grain growth (GG) [23], diffusive solid-state phase transformation (DSSPT) [26, 27], spheroidization [28], sintering [29], etc.

In the context of full-field modeling of microstructural evolution, depending on the methodology adopted to follow the topological evolution, broadly two types of numerical techniques are classically employed: the front tracking/ vertex, and the front capturing methods. Front tracking/ vertex methods [30–32] track the interface explicitly, making use of a discrete set of marker nodes localized on the interface. These nodes are then used to approximate the interface, thanks to interpolation. As the interface evolves, the marker nodes are advected in a Lagrangian sense. Front tracking methods face difficulties in handling topological changes in the interface. On the other hand, front capturing methods do not make use of any explicit elements to localize the interface. Instead, interfaces are implicitly represented and reconstructed using suitable field variables. This technique provides capabilities to handle topological changes in a natural way. It also gives the freedom to use non-conforming meshes. However, the numerical cost of front-capturing methods is generally more important, especially in a finite element (FE) context using unstructured grid. Front capturing methods mainly comprise the following numerical methods: Phase-Field (PF) or Multi Phase-Field (MPF) [27, 33–35], and Level-Set (LS) models [36–42].

In the context of DSSPT, phase-field methods (PFM) are popular and extensively used. The thermodynamic consistency and the ability to model arbitrary complex morphological changes without any presumption on their shape or mutual distribution make PFM a powerful and an attractive tool. The early works of Wheeler et al. [43], Steinbach et al. [44, 45] on solidification using PFM provided some of the mathematical foundations of phase-field modeling for multi-component, multi-phase systems involving solute diffusion. Yeon et al. [46] presented one of the first phase-field simulations of DSSPT, where austenite-ferrite transitions in the Fe-Mn-C system were modeled under para-equilibrium [47] assumptions. Pariser et al. [48] studied the phase transformation behavior in ULC (Ultra Low Carbon) and IF (Interstitial free) grade steels using the well-known MICRESS software [49] based on the multi-component, multi phase-field method. Huang et al. [50] performed 2D PF simulations for $\gamma \longrightarrow \alpha$ transformation in low carbon steels by considering an arbitrary number of grains at a large spatial scale. The P.h.D. works of Mecozzi along with Militzer et al. [51, 52] were dedicated to the first 3D simulations of DSSPT for $\gamma \longrightarrow \alpha$ transformation in a Fe-Mn-C system. In addition to austenite decomposition in steels, there have been works dedicated to other alloyed materials also. 1D PF simulations for phase transformation in aluminum alloys have been studied in [53]. Malik et al. [54] have used 2D PFM to simulate the formation and growth of $\sigma-$phase precipitates in a super duplex stainless steel alloy. In addition to PFM, some works based on Monte Carlo potts (MC) [55] and Cellular Automata (CA) methods [56, 57] could also be found for DSSPT. In most of these reported works, the grain growth aspects were either completely neglected or only the grain growth of the product phase was accounted for while ignoring that of the parent phase. According to the author's knowledge, DSSPT modeling using LS method has not been explored to its full potential in the state of the art. The developments of Bzowski et al. [58] is one of the only few works based on level-set method for DSSPT. A multiple level-set approach is used in [58] with the classical technique of one level-set function per grain. To model solute diffusion, the diffusion equation has been resolved only in the parent phase while that in the product phase has been considered to be negligible.

In the context of industrial processes where high plastic deformation can be achieved, none of the existing approaches provide easily an appropriate framework to perform simulations of DRX concomitant with phase transformation in multi-phase materials. On the other hand, level-set (LS) method has been successfully used to simulate DRX [59] and GG phenomena [60–62] for single-phase materials. So, in the current state of the art, most of the numerical predictions are dedicated to single-phase microstructural evolution, or only based on phase transformation without taking into account other phenomena such as ReX or GG. Such numerical approaches can then be insufficient when complex and realistic thermomechanical treatments with large temperature ranges are investigated. Thus, there is a need for a generalized numerical framework capable of making predictions of DSSPT, DRX, and GG in a multi-phase polycrystalline context [63]. So, the perspective of this work is to explore the potential of the LS method for the modeling of DSSPT. We thus propose a finite element based generalized global level-set formalism capable of simulating diffusive phase transformation and, potentially, ReX in the context of large plastic deformation for two phase polycrystalline materials by considering the driving pressures acting on grain and phase interfaces.

2.2 Fundamental concepts of Level-set (LS) method

Level-set method [38, 39, 64] is a front-capturing numerical method that is used to define domains and implicitly describe interfaces through a continuous field variable, φ. Level-set description is popularly used to model and simulate the motion of dynamic interfaces resulting from relevant physical phenomena. The interface position at any instant is implicitly tracked with the help of iso-contours of the level-set function, $\varphi(\boldsymbol{x}, t)$.

Considering the interface of interest, Γ, of a closed sub-domain G in a global domain Ω as illustrated in Fig.2.1, level-sets are classically initialized as a signed Euclidean distance function to Γ such that the zero iso-values of this function localize the interface Γ:

$$\begin{cases} \varphi(\boldsymbol{x}, t) = \pm d(\boldsymbol{x}, \Gamma(t)), & \boldsymbol{x} \in \Omega \\ \Gamma(t) = \partial G = \{\boldsymbol{x} \in \Omega \mid \varphi(\boldsymbol{x}, t) = 0\} \end{cases} \quad \forall\, t, \tag{2.1}$$

where d is the Euclidean distance normal to the interface. Thus, $\varphi(\boldsymbol{x}, t)$ has opposite signs inside and outside of the sub-domain G with a change of signs across the interface. In other words, if we

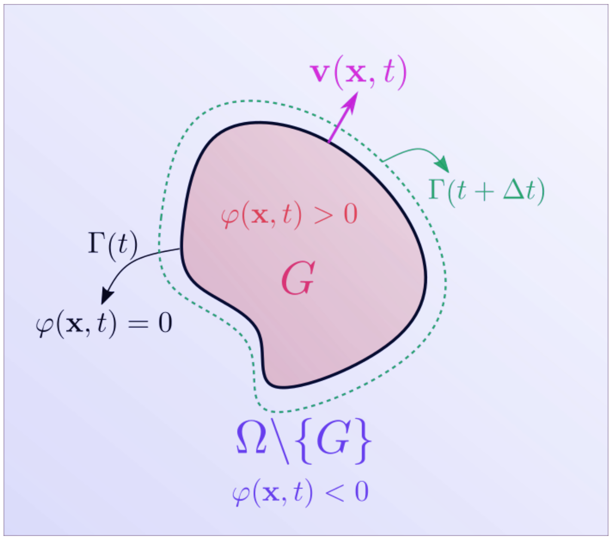

Figure 2.1: Level-set method used to describe a sub-domain G in a global domain Ω

adopt the convention of having positive values inside the sub-domain, then we have:

$$\begin{cases} \varphi(\boldsymbol{x},t) > 0 & \forall \boldsymbol{x} \in G\backslash\{\partial G\} \\ \varphi(\boldsymbol{x},t) < 0 & \forall \boldsymbol{x} \in \Omega\backslash\{G\} \\ \varphi(\boldsymbol{x},t) = 0 & \forall \boldsymbol{x} \in \partial G = \Gamma(t) \end{cases} \tag{2.2}$$

Fig.2.2 illustrates a typical computation of a signed Euclidean distance LS function in an unstructured finite element (FE) mesh to an interface, highlighted in black (reflecting the iso-zero contour of the LS function).

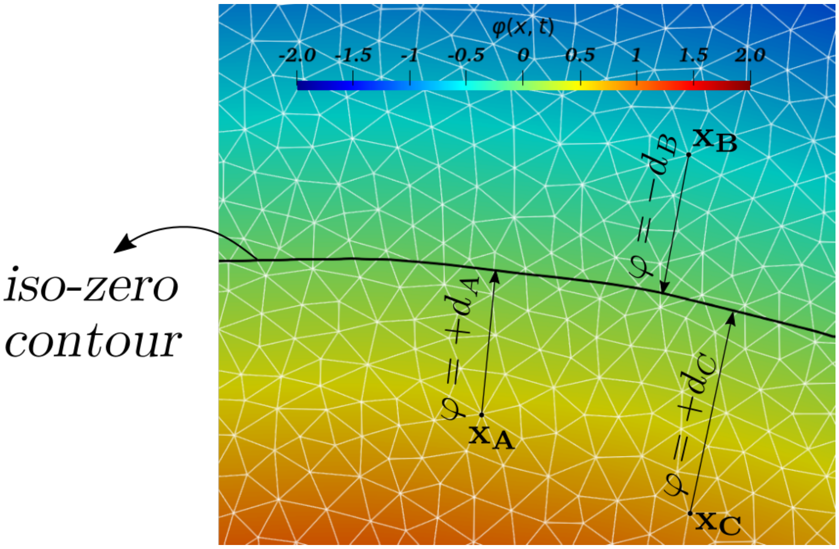

Figure 2.2: Representation of a signed distance function to an interface in a FE mesh

A classical signed Euclidean distance LS function has certain inherent metric properties such as:

$$\begin{gathered} \|\boldsymbol{\nabla}\varphi\| = 1 \\ \boldsymbol{n} = -\frac{\boldsymbol{\nabla}\varphi}{\|\boldsymbol{\nabla}\varphi\|} = -\boldsymbol{\nabla}\varphi \implies \kappa = \boldsymbol{\nabla}\cdot\boldsymbol{n} = -\Delta\varphi \quad \forall \boldsymbol{x} \in \Gamma, \end{gathered} \tag{2.3}$$

where $\boldsymbol{n}$ is the outward unit normal to the closed sub-domain G at the interface, and κ is the trace of the curvature tensor. It should be remarked that the negative sign in the definition of $\boldsymbol{n}$ arises if the LS function is defined to be positive inside the sub-domain G as proposed previously.

Considering $\boldsymbol{v}$ to describe the kinetics of the Γ interface, at any time, $\Gamma(t)$ can be obtained by solving the following convective LS transport equation [38]:

$$\begin{cases} \frac{\partial\varphi}{\partial t} + \boldsymbol{v}\cdot\boldsymbol{\nabla}\varphi = 0 \\ \varphi(\boldsymbol{x}, t=0) = \varphi^0(\boldsymbol{x}) \end{cases} \quad \text{in} \quad \Omega. \tag{2.4}$$

The kinetics prescribed through the velocity, $\boldsymbol{v}$, is generally computed depending on the physical phenomena involved behind the migration of the interface. Thus, LS method is generally coupled with some external physics.

Reinitialization of level-sets: Depending on the formulation and the numerical resolution procedure adopted, it is of great interest to ensure that φ stays a signed distance function (i.e., $\|\boldsymbol{\nabla}\varphi\| = 1$). Even though the initial LS function, $\varphi^0(x)$, could be initialized as a signed distance function, this property may not be conserved during the resolution of the LS transport Eq.(2.4). $\varphi(\boldsymbol{x}, \boldsymbol{t})$ may localize the zero iso-contours properly, however its gradient could take any value causing φ to become irregular which could potentially generate numerical instabilities. A periodic redistancing or a reinitialization [65] procedure is essential to restore the metric properties of φ, post the resolution of Eq.(2.4). This ensures φ regularity, thus preserving numerical stability and good conditioning of the LS transport equation. In certain problems involving the contribution of the interface curvature in the kinetics, a signed distance function allows for avoiding an expensive exact computation of the curvature term by implicitly accounting for the curvature through its metric properties (Eqs.(2.3)). In addition, by keeping φ a signed distance function, certain numerical models involving remeshing algorithms can be properly based on the notion of Euclidean distance to the interface. It is thus paramount to conserve the metric properties for several reasons depending on the numerical application. Figs.2.3 represent the iso-contours of a typical LS function around an interface. The figure on the top illustrates the irregularity of the LS function having lost its character of a signed distance function. The figure on the bottom shows the same LS function after a reinitialization procedure which helps restore the signed distance property and hence the regularity in its iso-contours.

One of the fundamental approaches is the Fast Marching Method proposed by Sethian [67] which involves an efficient numerical scheme to solve the Eikonal equation of the form, $\|\boldsymbol{\nabla}\varphi\| = 1$. However this classical approach is generally limited to structured grids. It is complex to implement for unstructured meshes in a finite element framework, especially at higher dimensions. An effective strategy of conserving the metric properties of a level-set function is to extend the prescribed velocity field. In most problems of physics, the velocity field, $\boldsymbol{v}$, prescribed into the LS transport Eq.(2.4) generally has sense only at the concerned interface. However, the front capturing nature of LS

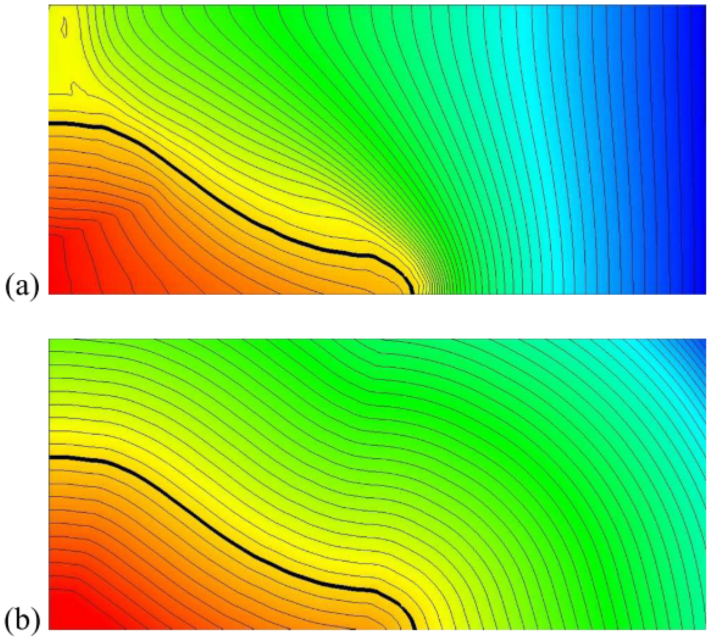

Figure 2.3: From [66]: (a) Iso contours of an irregular level-set function, potentially post the resolution of the level-set transport equation, (b) The same representation after reinitialization. The interface is characterized in bold, corresponding to the iso-zero contour

transport equation in (2.4) imposes that the velocity field be defined almost near the iso-zero value, and not just on the interface itself (for the iso-zero level-set). So, $\boldsymbol{v}$ must be defined at least over a narrow band around the propagating interface, $\Gamma(t)$. The process of extending the velocity field around the propagating interface is referred as velocity extension or velocity smoothing [68]. The extended velocity should match with the actual velocity prescribed on the interface. One of the classical ways to extend the velocity is to solve the following equation:

$$\text{At any instant } t, \begin{cases} \boldsymbol{\nabla}\left(\boldsymbol{v_e} \cdot \boldsymbol{n_e}\right) \cdot \boldsymbol{\nabla}\varphi = 0 & \text{in} \quad \Omega \backslash \{\Gamma(t)\} \\ \boldsymbol{v_e}(\boldsymbol{x}, t) = \boldsymbol{v}(\boldsymbol{x}, t) & \text{on} \quad \Gamma(t) \end{cases}, \tag{2.5}$$

where $\boldsymbol{v_e}$ is the extended velocity and $\boldsymbol{n_e}$ is the extended normal (on neighboring level-sets). It is to be ensured that φ is a signed distance function a priori. The solution to the above equation would yield a velocity field with constant velocities along the extended normal with velocity gradients being orthogonal to the extended normal. The constant velocities along the extended normal aid in migrating the neighboring level-sets by the same amount as the interface, ensuring preservation of the metric properties of the LS function without requiring reinitialization at each time step. In this case, periodic reinitialization would only be necessary to safeguard the metric properties from potential errors during the evolution.

Another classical approach to reinitialize φ is to resolve the following Hamilton-Jacobi equation [38, 69]:

$$\begin{cases} \frac{\partial \varphi^*}{\partial \tau_f} + \text{sign}(\varphi^*)\left[\|\boldsymbol{\nabla}\varphi^*\| - 1\right] = 0 \\ \varphi^*(\boldsymbol{x}, \tau_f = 0) = \varphi(\boldsymbol{x}, t) \end{cases} \quad \text{in} \quad \Omega, \tag{2.6}$$

where τ_f is a fictitious time step. At a certain instant t, the LS transport equation resolution is frozen and the above equation is resolved over a short duration of the fictitious time. The solution φ^* thus obtained is traded with φ to obtain a signed distance function over a certain thickness around the interface and without changing the iso-zero values corresponding to the current interface position, $\Gamma(t)$. The resolution of the LS equation is then resumed after reinitialization. A modified formulation (coined as automatic reinitialization) accounting for both the LS transport Eq.(2.4) and the Hamilton-Jacobi reinitialization Eq.(2.6) into a single resolution step through one convective equation was also developed. One of these formulations is depicted in [40]. However, as we shall see in the following, in the context of a polycrystalline microstructure involving multiple sub-domains, the presence of multiple junctions would demand an additional numerical treatment to avoid any kinematic incompatibilities. Such treatments would again require a post reinitialization step, hence the automatic reinitialization formulation is not adopted in this context. So it would be better off to use the classical LS transport equation for resolution, followed by the necessary numerical treatments at the multiple junctions, and then a reinitialization procedure. More on this shall be discussed in the following. So, among other various techniques in the state of the art, a recent reinitialization strategy [70] that involves a fast, direct calculation of φ based on an optimized brute force algorithm is adopted in the context of this work.

2.2.1 Application of LS description in a polycrystalline microstructure

Previously, we reviewed the fundamental ideas behind the LS description of a single sub-domain G consisting of an inside and an outside region. However, if we consider a polycrystal consisting of several grains, with each of these grains representing a closed sub-domain, a single signed distance LS function, φ, is not enough to represent all the grains in the whole microstructure since there is no longer a notion of inside and outside regions. The classical approach is to consider one level-set function per grain as seen in some of the first developments of LS based numerical modeling of microstructural evolution [40, 60, 66]. So, a microstructure with N_G grains would need N_G LS functions, with a necessity to resolve each of these LS functions (N_G transport equations to resolve). Fig.2.4 shows an illustration of a simple microstructure with each grain represented by its own LS function, φ_i. The color map in Fig.2.4 characterizes each grain having its own LS function.

Digital generation of a polycrystalline microstructure: Given certain statistical data such as mean grain size or a grain size distribution, to construct a digital microstructure in the form of representative volume elements (RVE), the earliest LS based developments were based on the method of Voronoi tessellation (VTM) [71] to generate the grains. Given a set of N randomly placed seeds (sites) in a domain (microstructure), VTM aims to partition the domain into a set of N convex polyhedrons. It does so by introducing planes perpendicularly bisecting the segments connecting two nearest neighboring points such that the interception of several perpendicular bisecting planes out of the nearest neighboring lines form edges, vertices, faces and volumes to create a collection of polyhedrons. In other words, each seed is associated with a polyhedron that occupies some space in the domain such that the distance to this seed from any point inside this polyhedron is less than or equal to the distance to any other seed in the domain. Fig.2.5 illustrates a simple representative microstructure constructed from a certain set of seeds using the VTM. Each polyhedron represents a grain, and the connectivities between two or more polyhedrons make up the geometrical or topological entities of the microstructure such as grain boundaries, edges and corners. A statistical

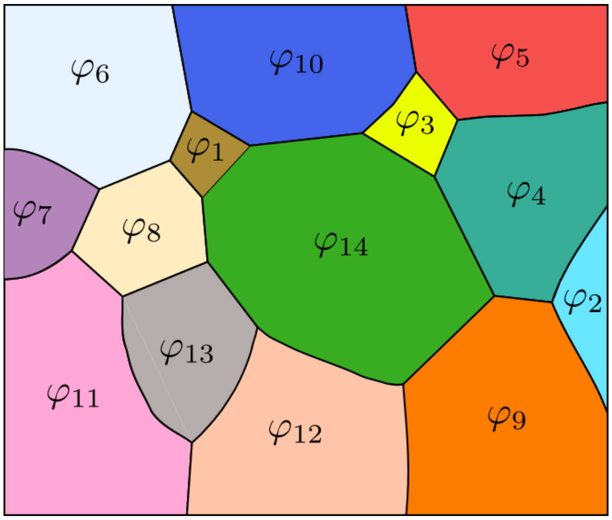

Figure 2.4: A representative microstructure with 14 grains with their colors indicating the characteristic functions corresponding to their parent level-set functions (14 φ_i)

distribution is used to describe the ensemble of polyhedrons (grains) formed as a result. Despite being an effective method in creating grains with reasonable geometric correlation, VTM fails to respect a given statistical grain size distribution as indicated in [72]. Another method of generation is based on the Laguerre-Voronoi tessellation method (LVTM) which follows the same principles as the VTM, except that the inter-distance between two seeds may not be bisected equally. This allows a particular grain to be preferentially larger or smaller. This is established with the help of a radius or a weight assigned to each seed in a quest to respect the statistical grain size distribution [73]. In a FE context, the VTM and LVTM can be analytically expressed and used to compute (initialize) the level-sets (φ_i) describing the polyhedrons or the grains. If we suppose N_G grains, with S_i denoting the Voronoi sites, with the sign convention that, $\varphi_i > 0$ inside G_i and $\varphi_i < 0$ outside. For the VTM, for any node n_p at $\boldsymbol{x}$ we can express in the following way [66]:

$$\begin{cases} \alpha_{ij} = \frac{1}{2} \| \vec{S_i S_j} \| - \frac{\vec{S_i S_j} \cdot \vec{S_i n_p}}{\| \vec{S_i S_j} \|} & 1 \leq i, j \leq N_G, j \neq i \\ \varphi_i(\boldsymbol{x}, 0) = \min\limits_{\substack{j \in \{1, \ldots, N_G\} \\ j \neq i}} \alpha_{ij}(\boldsymbol{x}) & 1 \leq i \leq N_G \end{cases}, \tag{2.7}$$

where $\alpha_{ij}(\boldsymbol{x})$ measures the signed distance of node $n_p(\boldsymbol{x})$ to the perpendicular bisector of the line segment connecting the sites S_i and S_j.

Similarly, in the case of LVTM, we have the following [74]:

$$\begin{cases} \alpha_{ij} = \frac{1}{2} \left(\| \vec{S_i S_j} \| + \frac{r_i^2 - r_j^2}{\| \vec{S_i S_j} \|} \right) - \frac{\vec{S_i S_j} \cdot \vec{S_i n_p}}{\| \vec{S_i S_j} \|} & 1 \leq i, j \leq N_G, j \neq i \\ \varphi_i(\boldsymbol{x}, 0) = \min\limits_{\substack{j \in \{1, \ldots, N_G\} \\ j \neq i}} \alpha_{ij}(\boldsymbol{x}) & 1 \leq i \leq N_G \end{cases}, \tag{2.8}$$

where r_k represents the weight assigned to the Voronoi site S_k. These weights are usually specified in the form of radii associated with a site and the radii are chosen in accordance with a grain size distribution law.

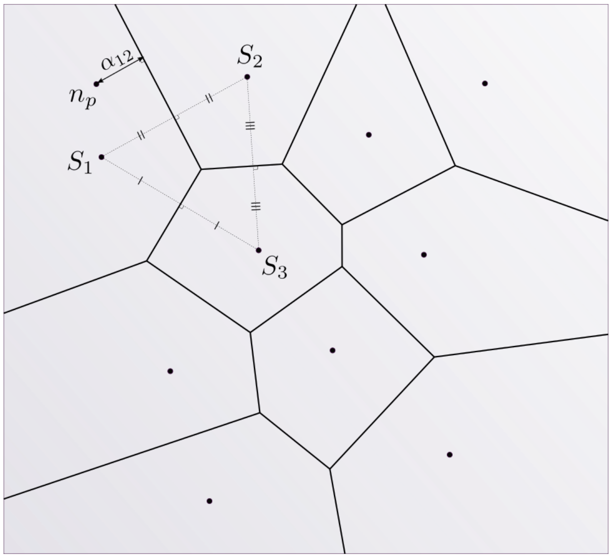

Figure 2.5: An illustration of the Voronoi tessellation method to digitally construct a microstructure

While the methods explained in Eqs.(2.7) and Eqs.(2.8) are easy to implement, they are numerically taxing in a FE context. A more efficient and precise generation of equiaxial polycrystals and powder RVEs in a FE context has been proposed in [74] by considering the dual of the Voronoi tessellation which corresponds to the Delaunay triangulation. Analogously, for the LVTM, weighted Delaunay triangulation is considered. In Eqs.(2.7) and (2.8), the computation of φ_i of the grain G_i involves comparison with all the other grains in the domain. However, the property of Delaunay triangulation limits this comparison only to a graph of the Voronoi site S_i, composing of a small set of its neighbors in the Delaunay triangulation. So, the LS function of the grain G_i is now computed as:

$$\varphi_i(\boldsymbol{x},0) = \min_{j \in \text{Graph}(S_i)} \alpha_{ij}(\boldsymbol{x}) \quad 1 \leq i \leq N_G \tag{2.9}$$

Interested readers could refer the cited article for more details on the method. In the case where a digital microstructure needs to be generated from an experimental image of a micrograph (EBSD maps), it can be established by calculating the distance functions to the grey levels of each grain interface as illustrated in Fig.2.6 [75], thus easily immersing the micrograph.

Grain coloration/ recoloration: When we consider a large scale simulation potentially consisting of thousands of grains, the classical approach of characterizing each grain with its own LS function (as seen in [40, 41, 58]) is totally inefficient considering each LS function needs to be resolved independently. Moreover, storage memory considerations can also present complexities. Saye et al. [76] proposed a new approach, that they called as the Voronoi implicit interface method (VIIM). This method is based on an interaction between the Voronoi diagrams and an implicit interface method like the LS method, and hence the name. This approach makes use of a single unsigned distance LS function in the whole domain. An unsigned distance function holds the same sign

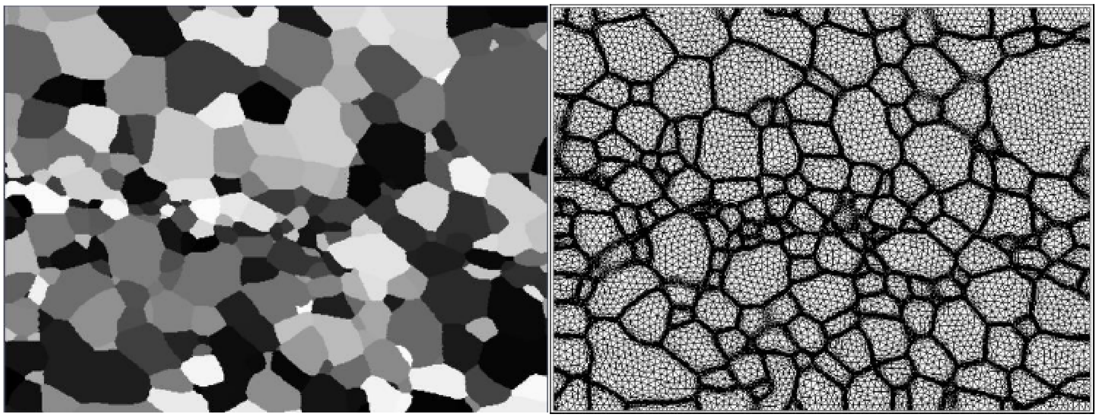

Figure 2.6: From [75]: Immersion of an experimental 2D micrograph (left) obtained by EBSD (each grain being plotted with a different gray level) into a finite element mesh (right)

(generally positive) inside all of the sub-domains, while approaching towards 0 at the interfaces. So, while it is able to localize the overall interface network, it cannot uniquely characterize one grain from the other. This method relies on resolving the unsigned distance LS transport equation for a short duration of time (Δt), and then the interface network of interest is reconstructed as the Voronoi interface of the nearby ϵ_{LS} level-sets. The Voronoi interface reconstruction is based on the same principles as the VTM as seen previously, except that it is now applied for a set of hypersurfaces (lines in 2D, surfaces in 3D). The reconstructed Voronoi interface network is then used to compute a new unsigned LS distance function at that instant by resolving an Eikonal equation, and then a new loop step begins. Fig.2.7 shows an illustration of the Voronoi interface reconstruction around a triple junction (junction formed by 3 sub-domains in 2D, analogous to quadruple junctions in 3D). While the VIIM is attractive for its high computational efficiency, especially for cases involving large number of grains, their applications are generally restricted to cases involving isotropic evolution. They may not converge to accurate solutions for the interface position in the case of anisotropic evolution as pointed out in [77]. In addition, the notion of normal and curvature computed out of an unsigned distance function is perplexing and may lack accuracy. So VIIM currently fails to give a consistent unified framework for modeling different kinds of kinetics.

Another popular approach developed by Scholtes et al. [42, 78] relies on drastically reducing the total number of LS functions required to represent the total grains in the domain. So a microstructure with N_G grains would need only N_{LS} level-set functions such that $N_{LS} << N_G$. The essence of this method lies in the scheme of grain coloration, inspired by the principles of four color theorem [79]. For a 2D domain with multiple connected sub-domains (grains), the four color theorem states that no more than 4 colors are needed to color each of these sub-domains such that no two adjacent grains have the same color. Similar principles are applied in the case of a microstructure, where several non-neighboring grains can be grouped and represented by a set of global level-set (GLS) functions. In other words, a set of grains fairly distant from each other are represented by a single signed distance LS function (known as the GLS function). This is synonymous to using one color to represent a set of regions. Theoretically, for a 2D case with N_G grains, only 4 GLS functions are

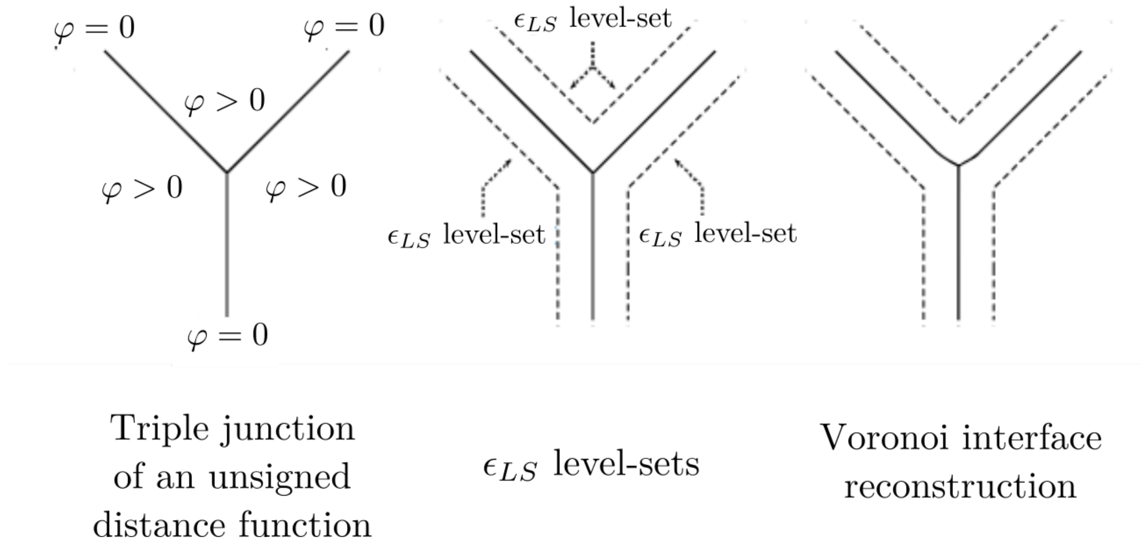

Triple junction of an unsigned distance function

ϵ_{LS} level-sets

Voronoi interface reconstruction

Figure 2.7: Adopted from [76]: Illustration of the Voronoi implicit interface method used to reconstruct a triple point from an unsigned distance function and the Voronoi interface

sufficient to represent all of the grains. Fig.2.8 shows an illustration of the same 2D microstructure as seen in 2.4 but represented by only 4 GLS functions, where each color corresponds to one family of GLS function (φ_i).

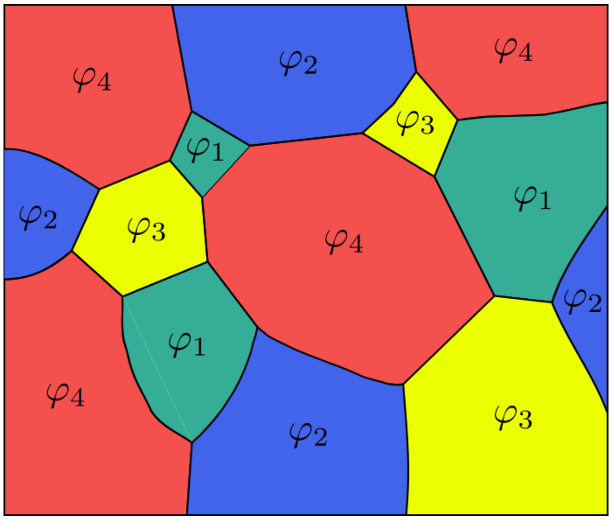

Figure 2.8: Illustration of the grain coloration scheme to represent a microstructure with 14 grains using only 4 global level-set functions

However, depending on the imposed kinetics, as the microstructure topology evolves, by only using 4 GLS functions, we run the risk of numerical coalescence of grains belonging to the same family of GLS function. This stems from the fact that, two or more regions represented by the same LS function naturally coalesce/ combine when they come in contact. Fig.2.9 demonstrates the phenomenon of numerical coalescence where two grains of the same color (same GLS function) combine as they come in contact.

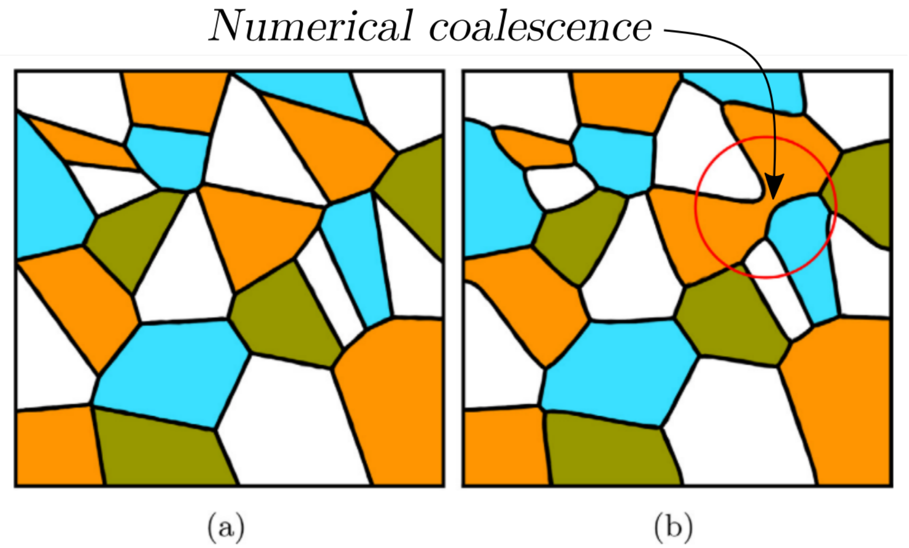

Figure 2.9: From [42]: (a) A microstructure of 25 grains represented by 4 global level-set functions colored in white, green, orange and blue, (b) Numerical coalescence of two child grains (grains belonging to the same family) highlighted inside the red circle

In order to minimize the risk of this undesirable effect of numerical coalescence, the grains are colored (or associated with a GLS function) by respecting a constraint of separation between them. This constraint is chosen in the form of minimum number of grains separating any two grains belonging to the same family of GLS function, φ_i. So, in practice, a few more than 4 GLS functions are used to represent the grains in 2D depending on the degree of intergranular separation. Fig.2.10 illustrates the same microstructure as in Fig.2.9 but now with a different grain coloration using 10 GLS functions with a degree of separation of 2 grains at a minimum, which adds a level of security against coalescence.

In addition, with time, as the grains evolve, a periodic grain recoloration procedure is employed which automatically checks for grains of the same GLS function under the risk of numerical coalescence (i.e., no longer respecting a certain minimum intergranular distance threshold). If there are any risks of numerical coalescence, the grain recoloration scheme then ensures to swap the color (GLS family) of those grains under risk to some other GLS family such that the minimum intergranular distance is respected. In the event where there are no eligible GLS functions to be swapped into from the existing set, a new GLS family is dynamically created for those grains under risk. The degree of intergranular separation is a fine balance between the reduction in computational time and the risks of numerical coalescence. Since there are no generalizations of the four color theorem in 3D cases, there is no theoretical minimum number that could represent the grains in a 3D microstructure. The number of GLS functions needed usually ranges around $4-10$ in 2D cases, while around $19-30$ in 3D cases, depending on the intergranular separation desired. The grain recoloration/ swapping algorithm developed by Scholtes et al. [78] also ensures that, during a swap of a grain, the **dependence** of any other grain specific fields connected to their respective

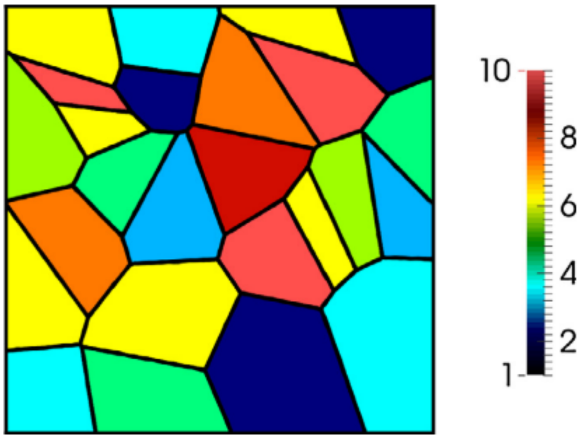

Figure 2.10: From [42]: A microstructure represented using 10 global level-set functions (instead of the classical 4) separated by at least 2 grains. The colors indicate the family of GLS function to which they belong

GLS function (to be swapped) is also safely transferred to the new GLS family of the swapped grain.

So, in the current work, the above grain coloration/ recoloration scheme that dynamically manages the representation and distribution of the grains in a microstructure has been adopted.

2.3 Level-set based numerical formulation of DSSPT

Full-field modeling of diffusive solid-state phase transformation at the mesoscopic scale is basically composed of two governing equations: (i) a diffusion equation that governs the partitioning of solute atoms across different phases and their diffusion in the bulk, and (ii) a migration/ transport equation that governs the resulting evolution of the interface network. Additionally, the formulation is well bounded with necessary initial, boundary, and interface jump conditions imposed.

As mentioned earlier, our interest is to use a global LS formalism to simulate the considered phenomena, where the grains of a multi-phase polycrystalline microstructure are represented by a set of level-set functions, and the LS transport equation is used to conveniently migrate the multi-phase grain boundary network influenced by the solute diffusion phenomenon. In the context of DSSPT, along with the GLS functions used to distinguish different grains in the polycrystal, secondary LS functions are needed to distinguish the different phases in the polycrystal. So, for a biphasic polycrystal composed of phases α and γ, φ_i act as the primary basis LS functions representing different grains, while φ_α acts as a secondary basis LS function to distinguish the domains belong to α and γ phases.

2.3.1 Solute redistribution modeling

For the resolution of the diffusion equation, the sharp interface approach (theoretically at least) considered in a classical LS framework would require resolving separate diffusion equations in domains of each phase (for each solute) while respecting the necessary jump conditions at the phase interface as seen previously in Eqs.(1.40) and (1.41) in Chapter 1 under 1.2.1.1.2:

$$\begin{aligned} \frac{\partial x_i^\alpha}{\partial t} &= \boldsymbol{\nabla}\cdot\left(D_\alpha^i \boldsymbol{\nabla} x_i^\alpha\right) \quad \text{in} \quad \Omega_{\varphi_\alpha(\boldsymbol{x},t)} \mid \varphi_\alpha(\boldsymbol{x},t) > 0 \\ \frac{\partial x_i^\gamma}{\partial t} &= \boldsymbol{\nabla}\cdot\left(D_\gamma^i \boldsymbol{\nabla} x_i^\gamma\right) \quad \text{in} \quad \Omega_{\varphi_\gamma(\boldsymbol{x},t)} \mid \varphi_\gamma(\boldsymbol{x},t) > 0 \qquad , \qquad \forall i \in \{B, ..., N\}, \\ \boldsymbol{v}\cdot\boldsymbol{n}\left(x_i^\gamma\big|_\Gamma - x_i^\alpha\big|_\Gamma\right) &= D_\alpha^i \left(\boldsymbol{\nabla} x_i^\alpha \cdot \boldsymbol{n}\right)\big|_\Gamma - D_\gamma^i \left(\boldsymbol{\nabla} x_i^\gamma \cdot \boldsymbol{n}\right)\big|_\Gamma \quad \text{on} \quad \Gamma \end{aligned} \tag{2.10}$$

where $\Omega_{\varphi_\alpha(\boldsymbol{x},t)}$ represents the domain of the α-phase grains in the microstructure described by the $\varphi_\alpha(\boldsymbol{x},t)$ LS function, while $\Omega_{\varphi_\gamma(\boldsymbol{x},t)}$ represents that of the γ-phase grains described by the $\varphi_\gamma(\boldsymbol{x},t)$ LS function. Γ represents the positions of the phase interface with 0-iso-values of the LS functions $\left(\varphi_\alpha(\boldsymbol{x},t) = \varphi_\gamma(\boldsymbol{x},t) = 0, \ \forall \boldsymbol{x} \in \Gamma\right)$. It should be remarked that, $\varphi_\alpha(\boldsymbol{x},t) = -\varphi_\gamma(\boldsymbol{x},t), \ \forall \boldsymbol{x} \in \Omega$, with Ω representing the overall microstructural domain.

The above sharp interface approach enforces explicit consideration of interface jump conditions under the presence of any inherent material discontinuities across the phase interfaces. Consequently, this demands explicit localization of the interface at each instant to numerically treat the necessary jump conditions. Thus, to avoid this cumbersome step, we propose to consider a diffuse interface hypothesis across the phase interfaces during the resolution of the diffusion equation. In other words, while we represent and migrate the multi-phase grain interface network using a sharp interface based LS description, the resolution of the diffusion equation is based on a diffuse interface assumption for the phase interfaces. The diffuse interface description is realized using a hyperbolic tangent smoothing function which ensures that any material discontinuities across the interfaces are naturally smoothed and rendered continuous. This enables us to resolve a single global diffusion equation in the whole computational domain without the need for any explicit treatment of the interface jump conditions.

The transition to a diffuse interface description is established, thanks to a hyperbolic tangent relation [51, 80] of the following form between a phase-field like smooth function (ϕ) and a signed distance LS function (φ_α) of the α phase:

$$\phi = \frac{1}{2} tanh\left(\frac{3\varphi_\alpha}{\eta}\right) + \frac{1}{2}, \tag{2.11}$$

where η is a diffuse interface thickness parameter. This function is synonymous to a hyperbolic tangent level-set description. In the following, we shall refer this smoothing function (ϕ) yielding the diffuse interface as the phase-field function. Fig.2.11 illustrates the trend of this function in a 1D context. Let us consider a simple ternary alloy system, M_e-C-X, with an interstitial element (C), and a substitutional element (X). After having established a diffuse interface description, $\forall i \in \{C, X\}$, a total concentration field variable (x_i) can be expressed as a continuous field between the concentrations in the two phases:

$$x_i = \phi x_i^\alpha + (1-\phi) x_i^\gamma. \tag{2.12}$$

Likewise, we then assume continuity of the solute fluxes of each phase ($\boldsymbol{J}_\gamma^i, \boldsymbol{J}_\alpha^i$) weighted by the phase-field variable across the phase interface:

$$\boldsymbol{J^i} = \phi \boldsymbol{J}_\alpha^i + (1-\phi)\boldsymbol{J}_\gamma^i. \tag{2.13}$$

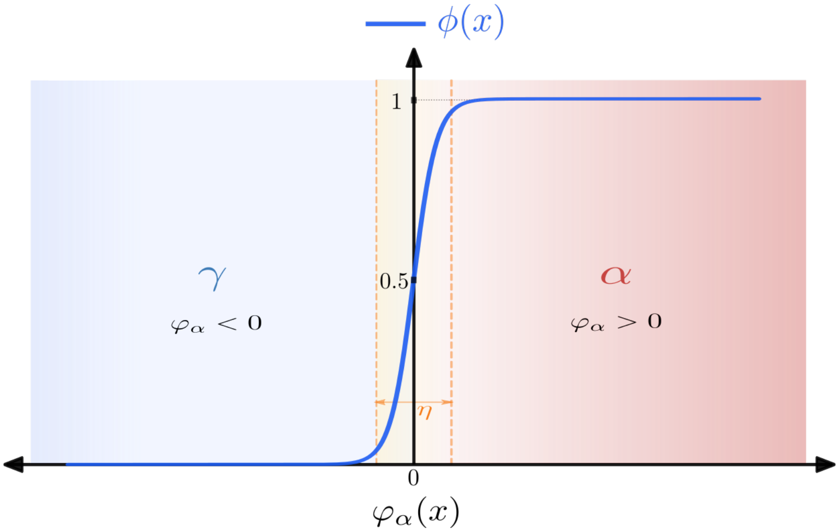

Figure 2.11: Hyperbolic tangent relation yielding the diffuse phase interface between phases α and γ

Fig.2.12 illustrates a profile of the smoothed total concentration field across a phase interface, thanks to the diffuse interface description. The diffuse phase interface is assumed to be composed of a mixture of the two phases. A constant concentration ratio is imposed between the two phases at the interface at all instants, such that the redistribution of the solute atoms between the parent and the product phase respects a partitioning ratio (k_p^i) equal to the equilibrium partitioning ratio

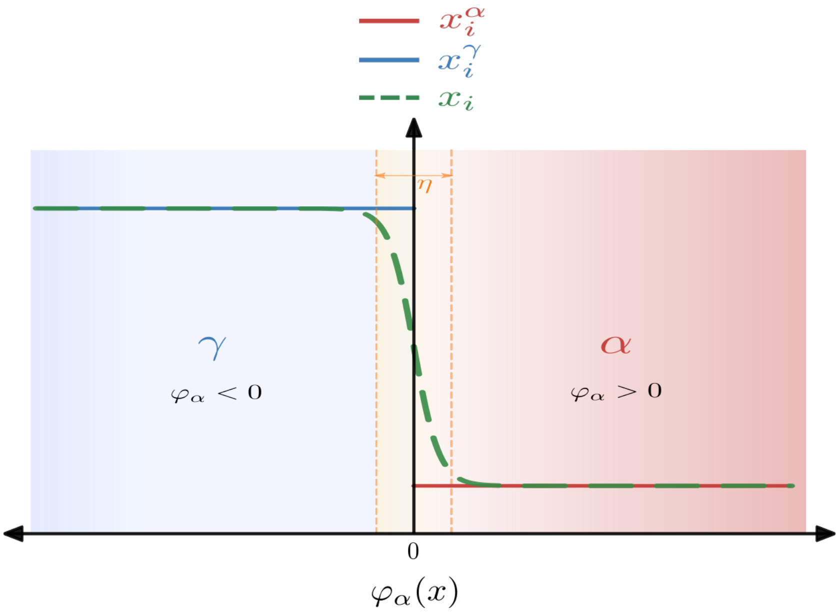

Figure 2.12: Demonstration of a continuous total concentration field established across the diffuse phase interface

($k^i_{p_{eq}}$), corresponding to the conditions at that instant t:

$$k^i_p\,(t) = \frac{x_i^\alpha}{x_i^\gamma} \approx k^i_{p_{eq}}\,(t) = \frac{x_i^\alpha\big|_{eq}}{x_i^\gamma\big|_{eq}}, \tag{2.14}$$

where $x_i^\alpha\big|_{eq}$ and $x_i^\gamma\big|_{eq}$ are the equilibrium concentrations of α and γ phases respectively at temperature T and instant t.

By imposing the above hypothesis into the Eq.(2.12), the individual phase concentrations could be expressed as:

$$\begin{aligned} x_i^\alpha &= \frac{k^i_p x_i}{1+\phi(k^i_p-1)} \\ x_i^\gamma &= \frac{x_i}{1+\phi(k^i_p-1)} \end{aligned}. \tag{2.15}$$

Following Fick's laws of diffusion, the diffusion equation for carbon partitioning can be expressed as:

$$\frac{\partial x_i}{\partial t} = -\boldsymbol{\nabla}\cdot\boldsymbol{J}^i = -\boldsymbol{\nabla}\cdot\left[\phi\boldsymbol{J}^i_\alpha + (1-\phi)\boldsymbol{J}^i_\gamma\right],$$

with,

$$\boldsymbol{J}^i_\alpha = -D^i_\alpha\boldsymbol{\nabla}x_i^\alpha; \quad \boldsymbol{J}^i_\gamma = -D^i_\gamma\boldsymbol{\nabla}x_i^\gamma.$$

We then obtain,

$$\frac{\partial x_i}{\partial t} = \boldsymbol{\nabla}\cdot\left[\phi D^i_\alpha\boldsymbol{\nabla}x_i^\alpha + (1-\phi)D^i_\gamma\boldsymbol{\nabla}x_i^\gamma\right], \tag{2.16}$$

where D^i_α and D^i_γ represent the diffusivity of the ith solute element in α and γ phases respectively.

Invoking Eqs.(2.15) into Eq.(2.16), a modified solute diffusion equation similar to that of the phase-field model [45, 51] is obtained:

$$\frac{\partial x_i}{\partial t} = \boldsymbol{\nabla}\cdot\left\{D^*(\phi)\left[\boldsymbol{\nabla}x_i - \frac{x_i(k^i_p-1)}{1+\phi(k^i_p-1)}\boldsymbol{\nabla}\phi\right]\right\}, \tag{2.17}$$

where $D^*(\phi)$ is called "mixed diffusivity" and is defined as,

$$D^*(\phi) = \frac{D^i_\gamma + \phi(k^i_p D^i_\alpha - D^i_\gamma)}{1+\phi(k^i_p-1)}. \tag{2.18}$$

With further simplifications, the above Eq.(2.17) can be transformed into a Convective-Diffusive-Reactive (CDR) form as follows:

$$\frac{\partial x_i}{\partial t} = \boldsymbol{\nabla}\cdot\left[D^*(\phi)\boldsymbol{\nabla}x_i - x_i\boldsymbol{\mathcal{A}}(\phi)\right] \tag{2.19}$$

$$\frac{\partial x_i}{\partial t} + (\boldsymbol{\mathcal{A}} - \boldsymbol{\nabla}D^*)\cdot\boldsymbol{\nabla}x_i - D^*\Delta x_i + \mathcal{R}x_i = 0, \tag{2.20}$$

where,

$$\mathcal{A}(\phi) = \frac{D^*(\phi)(k_p^i - 1)}{1 + \phi(k_p^i - 1)}\boldsymbol{\nabla}\phi, \quad \text{and} \quad \mathcal{R} = \boldsymbol{\nabla}\cdot\mathcal{A}. \tag{2.21}$$

It should be highlighted that this equation physically still represents pure diffusion. The convective and the reactive parts purely have a numerical sense. The strong formulation in Eq.(2.20) comprises of a gradient of the mixed diffusivity term ($\boldsymbol{\nabla}D^*$) that generally involves abrupt or strong evolution across a phase interface. If we consider the weak formulation of the Eq.(2.20), it could be shown that this gradient vanishes.

Let $\psi \in H^1(\Omega)$ be a test function, the FE weak formulation of Eq.(2.20) can be written as follows:

$$\int_\Omega \frac{\partial x_i}{\partial t}\psi \, d\Omega + \int_\Omega (\mathcal{A} - \boldsymbol{\nabla}D^*)\cdot\boldsymbol{\nabla}x_i\psi \, d\Omega - \int_\Omega D^*\Delta x_i\psi \, d\Omega + \int_\Omega \mathcal{R}x_i\psi \, d\Omega = 0. \tag{2.22}$$

Applying the divergence theorem to the third term upon expansion in the above equation, we have:

$$\int_\Omega D^*\Delta x_i\psi \, d\Omega = \int_{\partial\Omega} \psi D^*\boldsymbol{\nabla}x_i \cdot \boldsymbol{n}_b \, dS - \int_\Omega \boldsymbol{\nabla}(D^*\psi)\cdot\boldsymbol{\nabla}x_i \, d\Omega,$$

where $\boldsymbol{n}_b$ in this context is the outward unit normal to the domain boundary. Substituting the above term in Eq.(2.22), and after simplification, we get:

$$\int_\Omega \frac{\partial x_i}{\partial t}\psi \, d\Omega + \int_\Omega \mathcal{A}\cdot\boldsymbol{\nabla}x_i\psi \, d\Omega + \int_\Omega D^*\boldsymbol{\nabla}\psi\cdot\boldsymbol{\nabla}x_i \, d\Omega + \int_\Omega \mathcal{R}x_i\psi \, d\Omega - \int_{\partial\Omega} \psi D^*\boldsymbol{\nabla}x_i\cdot\boldsymbol{n}_b \, dS = 0. \tag{2.23}$$

We thus observe that the weak formulation is void of the $\boldsymbol{\nabla}D^*$ term which is of great interest in terms of numerical stability, considering the challenges posed by the presence of such terms to the numerical resolution procedure. The last boundary integral term in Eq.(2.23) is subject to the imposed boundary conditions.

Boundary conditions: Given the model focuses on pure solute diffusion within the computational domain without any influx or outflux of solute atoms, solute mass should remain conserved throughout. From a physical perspective, at first thought, one might consider employing pure Neumann-type boundary conditions on the concentration variable. However, from a mathematical perspective in Eq.2.19, employing only Neumann-type boundary conditions on x_i conserves solely the diffusive flux ($-D^*\boldsymbol{\nabla}x_i$), while the advective flux ($x_i\mathcal{A}$) remains non-conserved. If we consider the Reynolds's transport theorem on x_i for a fixed domain boundary, for mass conservation:

$$\frac{d}{dt}\int_\Omega x_i d\Omega = \int_\Omega \frac{\partial x_i}{\partial t} d\Omega = 0. \tag{2.24}$$

Plugging Eq.(2.19), and applying the divergence theorem, we obtain:

$$\frac{d}{dt}\int_\Omega x_i d\Omega = \int_\Omega \frac{\partial x_i}{\partial t} d\Omega = \int_{\partial\Omega} [D^*(\phi)\boldsymbol{\nabla}x_i - x_i\mathcal{A}(\phi)]\cdot\boldsymbol{n}_b dS = 0. \tag{2.25}$$

Thus, the above equation holds true for:

$$[-D^*(\phi)\boldsymbol{\nabla} x_i + x_i \boldsymbol{\mathcal{A}}(\phi)] \cdot \boldsymbol{n}_b|_{\partial\Omega} = 0. \tag{2.26}$$

The aforementioned Robin-type condition constitutes the correct and complete boundary condition for Eq.2.19.

Equation (2.21) implies that $\boldsymbol{\mathcal{A}} \rightarrow 0$ far from a phase interface where $\boldsymbol{\nabla}\phi \rightarrow 0$. In this scenario, Eq.(2.26) simplifies to a pure Neumann-type boundary condition, i.e., $-D^*\boldsymbol{\nabla} x_i \cdot \boldsymbol{n}_b|_{\partial\Omega} = 0$. Therefore, a pure Neumann-type boundary condition is a particular case, applicable only when the local boundary region does not interact with any phase interface. In cases where phase interfaces approach certain sections of the boundary region, locally imposing Robin-type conditions becomes necessary.

Thus, for the resolution of the solute redistribution, there's a continuous local switch between the two boundary condition types based on the interaction of the phase interfaces with the domain boundaries during the phase transformation. The following chapter will offer a more specific and concrete example on this.

Applying the generic Robin-type boundary condition to the weak form in Eq.(2.23), we eventually obtain:

$$\int_\Omega \frac{\partial x_i}{\partial t}\psi \, d\Omega + \int_\Omega \boldsymbol{\mathcal{A}} \cdot \boldsymbol{\nabla} x_i \psi \, d\Omega + \int_\Omega D^* \boldsymbol{\nabla}\psi \cdot \boldsymbol{\nabla} x_i \, d\Omega + \int_\Omega \mathcal{R} x_i \psi \, d\Omega - \int_{\partial\Omega} x_i \psi \boldsymbol{\mathcal{A}} \cdot \boldsymbol{n}_b \, dS = 0. \tag{2.27}$$

Analytical expressions for $\boldsymbol{\mathcal{A}}(\phi)$ and $\mathcal{R}(\phi)$: Numerically computing $\boldsymbol{\mathcal{A}}$ and $\mathcal{R}$ for Eq.(2.27) within the context of P1 finite elements requires multiple transformations (extrapolations) from a P0 field to a P1 field due to the presence of derivatives. This process might be error-prone, especially given the abrupt evolution of these fields across and around the diffuse phase interface. In an attempt to avoid the multiple extrapolations, analytical expressions can be deduced to compute these fields.

So, given φ_α, preserving its metric property ($\|\varphi_\alpha\|$=1), having computed ϕ from Eq.(2.11), and having numerically computed $\boldsymbol{\nabla}\varphi_\alpha$ and $\Delta\varphi_\alpha$, the remaining dependent fields could be computed analytically using the following expressions:

$$\boldsymbol{\mathcal{A}}(\phi) = \frac{D^*(\phi)(k_p^i - 1)}{1 + \phi(k_p^i - 1)}\boldsymbol{\nabla}\phi = \frac{3D^*(\phi)(k_p^i - 1)}{2\eta\left[1 + \phi(k_p^i - 1)\right]} sech^2\left(\frac{3\varphi_\alpha}{\eta}\right)\boldsymbol{\nabla}\varphi_\alpha, \tag{2.28}$$

and

$$\begin{aligned} \mathcal{R}(\phi) = \frac{\left(k_p^i - 1\right)}{\left[1 + \phi(k_p^i - 1)\right]^3}\Bigg\{ & D^*\Delta\phi\left[1 + \phi(k_p^i - 1)\right]^2 + \\ & \|\boldsymbol{\nabla}\phi\|^2\left[k_p^i\left(D_\alpha^i - D_\gamma^i\right) - \left(k_p^i - 1\right)\left(D_\gamma^i + \phi\left(k_p^i D_\alpha^i - D_\gamma^i\right)\right)\right]\Bigg\}, \end{aligned} \tag{2.29}$$

with $D^*(\phi)$ computed using Eq.(2.18), and the rest are computed using the following expressions:

$$
\begin{gathered}
\boldsymbol{\nabla}\phi = \frac{3}{2\eta} sech^2\left(\frac{3\varphi_\alpha}{\eta}\right)\boldsymbol{\nabla}\varphi_\alpha \\
\|\boldsymbol{\nabla}\phi\| = \frac{3}{2\eta} sech^2\left(\frac{3\varphi_\alpha}{\eta}\right) \\
\Delta\phi = \frac{3}{2\eta} sech^2\left(\frac{3\varphi_\alpha}{\eta}\right)\Delta\varphi_\alpha - \frac{9}{\eta^2} sech^2\left(\frac{3\varphi_\alpha}{\eta}\right) tanh\left(\frac{3\varphi_\alpha}{\eta}\right)
\end{gathered}
. \tag{2.30}
$$

Therefore, this approach involves extrapolation on a field that evolves gradually (φ_α), eliminating the need for further extrapolations and allowing the use of analytical expressions. This usage of analytical expressions is also computationally less intensive compared to the repeated use of numerical methods to compute the gradient and divergence operators.

2.3.2 Interface migration modeling

As described in 2.2, the external physics (e.g., diffusion of solutes) is coupled with the level-set method. Post the resolution of the solute diffusion equation, the resulting solute distribution affects the interface migration kinetics, along with other inherent effects depending on the various considered phenomena. To govern the resultant motion of the multi-phase grain interface network, we revert back to the classical LS description for the interfaces from our previous hypothetical diffuse interface description. Thus, for a polycrystalline microstructure with N_G grains whose interface network is represented by a set of N_{LS} GLS functions, the following convective equations (as seen in Eq.(2.4)) need to be resolved for modeling the evolution:

$$
\begin{cases}
\frac{\partial\varphi_i}{\partial t} + \boldsymbol{v}\cdot\boldsymbol{\nabla}\varphi_i = 0 \\
\varphi_i(\boldsymbol{x}, t=0) = \varphi_i^0(\boldsymbol{x})
\end{cases}
\quad \forall i \in \{1, 2, ..., N_{LS}\}. \tag{2.31}
$$

So each GLS function is resolved independently with its own convective equation by prescribing suitable kinetics through the velocity field, $\boldsymbol{v}$. The velocity field in this application is based as a function of various driving pressures affecting the microstructural evolution.

Typically, in the context of hot metal forming, the principal driving pressures leading to phase and grain evolution are: (i) $P_C = \Delta G_{\gamma\to\alpha}$, which is the driving pressure for phase transformation of γ phase into α phase, and is the principal component responsible for diffusive phase transformation, generally taken as a function of the temperature and the solute distribution due to diffusion, (ii) $P_S = [\![\mathcal{E}]\!]$, which is the jump in stored energy ($\mathcal{E}$) due to plastic deformation, responsible for recrystallization phenomenon, (iii) $P_\kappa = -\kappa\sigma$, where κ is the trace of the curvature tensor of the interface and σ is the interfacial energy, and this driving pressure corresponds to the capillarity effects due to the presence of grain and phase interfaces (well known as the Gibbs-Thomson effect), (iv) $P_{SD} = -\Delta G_{SD}\frac{(\boldsymbol{v}\cdot\boldsymbol{n})}{\|\boldsymbol{v}\|}$, which corresponds to an additional dissipation in the presence of any substitutional solute element with non-negligible solute drag effects in the material. So, in the context of hot metal forming, the net driving pressure acting on the relevant interface could be assembled as the sum of various contributions:

$$
P = \Delta G_{\gamma\to\alpha} + [\![\mathcal{E}]\!] - \kappa\sigma + P_{SD}. \tag{2.32}
$$

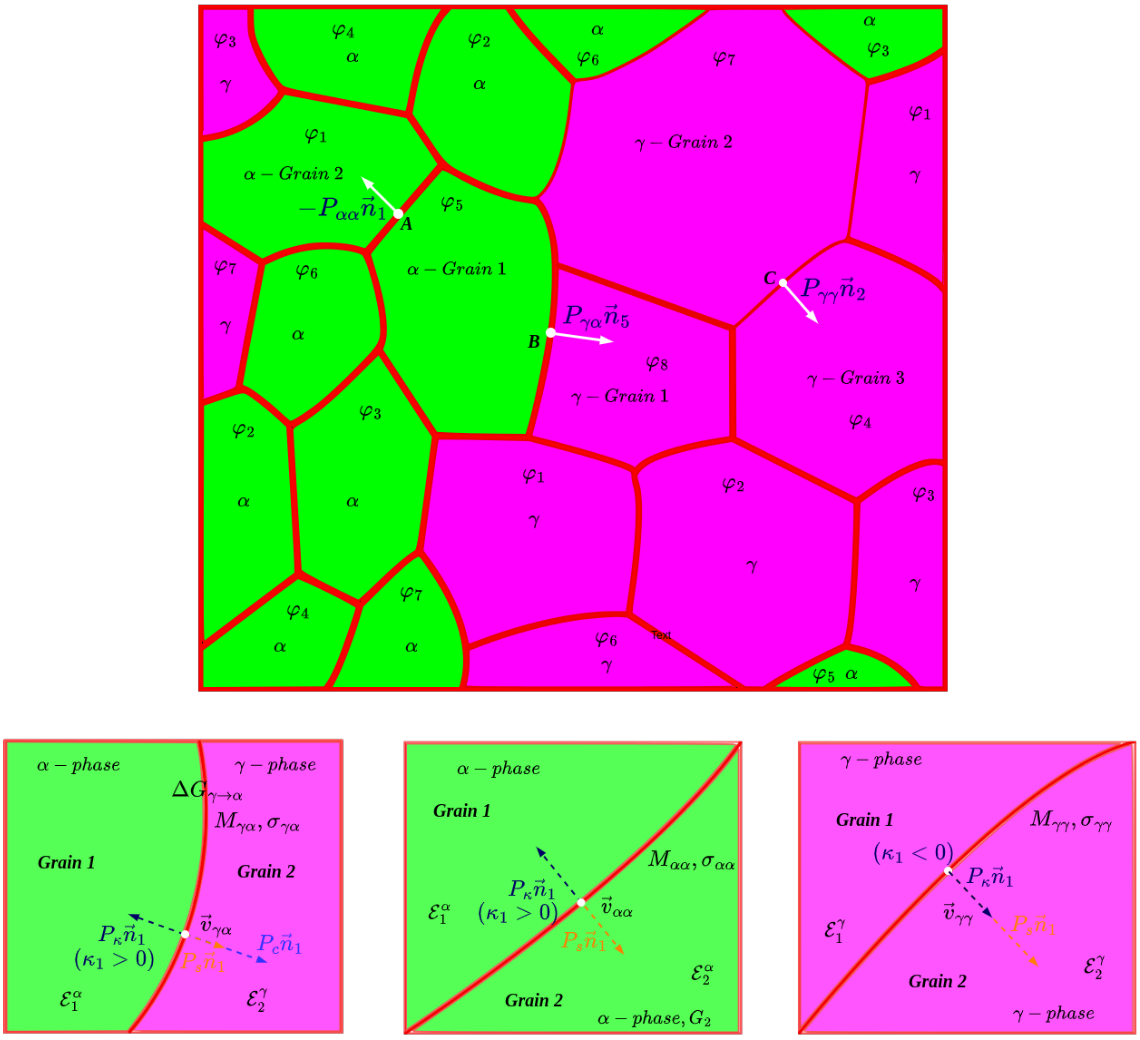

α/γ *phase boundary* α/α *grain boundary* γ/γ *grain boundary*

Figure 2.13: A two-phase polycrystal with grains of phases α and γ illustrating the net pressure at different types of interfaces

In the context of a biphasic polycrystalline microstructure with phases γ and α, three types of interfaces could then be encountered: γ/α phase interface, α/α grain interface, and the γ/γ grain interface. Depending on the type of interface in consideration, certain driving pressures may be absent or may have different sense or definition. For instance, the $\Delta G_{\gamma\to\alpha}$ pressure holds significance only across the phase interfaces. Also, the sense and magnitude of interface mobility, and interface energy could be different depending on the type of interface. Figs.2.13 demonstrate simple illustrations of different possible driving pressures relevant across different types of interfaces in a typical two phase polycrystal. We can observe that the P_C driving pressure acts only across the α/γ phase interface and is oriented towards the γ phase grain for a $\gamma \longrightarrow \alpha$ transformation. If we consider the capillarity driving pressure, $P_\kappa = -\kappa\sigma$, the driving pressure is oriented towards the center of local curvature of the interface. So, from the perspective of a grain (say grain 1) in 2D, $\kappa_1(\boldsymbol{x}, t) > 0$ if the local characteristic of the interface is convex, $\kappa_1(\boldsymbol{x}, t) < 0$

if the interface is locally concave, and $\kappa_1(\boldsymbol{x}, t) = 0$ if the interface is locally minimal (e.g., planar interfaces). It should be remarked that, in 3D, at any point ($\boldsymbol{x}$), a surface is said to be minimal if the principal curvatures are equal and opposite at that point. The driving pressure due to the stored energy, P_S, is oriented towards the grain with locally higher stored energy relative to its neighboring grain. In this illustration, the solute drag driving pressure (P_{SD}) has not been explicitly shown, but it should be understood that the influence of this driving pressure is passively present (passive effect), acting against the direction of net motion of the interface due to the net active driving pressures.

Thus, Eq.(2.32) needs to be tailored to accommodate various driving pressure contributions relevant to specific interfaces. So, the net driving pressure acting on the interface could be rewritten in the following form through interface characteristic functions:

$$P = \chi_{\gamma\alpha}\Delta G_{\gamma\to\alpha} + \sum_{l\in\mathcal{S}} \chi_l \left([\![\mathcal{E}]\!]_l - \kappa\sigma_l + [P_{SD}]_l \right). \tag{2.33}$$

where $\mathcal{S} = \{\gamma\gamma, \gamma\alpha, \alpha\alpha\}$ with $\chi_{\gamma\gamma}, \chi_{\gamma\alpha}$, and $\chi_{\alpha\alpha}$ being the interface characteristic functions of the grain boundaries between two γ grains ($\Gamma_{\gamma\gamma}$), phase boundaries between γ and α grains ($\Gamma_{\gamma\alpha}$), and grain boundaries between two α grains ($\Gamma_{\alpha\alpha}$), respectively. These characteristic functions are defined in the following way:

$$\chi_{\gamma\gamma}(\boldsymbol{x}) = \begin{cases} 1 & \text{if } \boldsymbol{x} \in \Gamma_{\gamma\gamma} \\ 0 & \text{otherwise} \end{cases}, \tag{2.34}$$

$$\chi_{\gamma\alpha}(\boldsymbol{x}) = \begin{cases} 1 & \text{if } \boldsymbol{x} \in \Gamma_{\gamma\alpha} \\ 0 & \text{otherwise} \end{cases}, \tag{2.35}$$

$$\chi_{\alpha\alpha}(\boldsymbol{x}) = \begin{cases} 1 & \text{if } \boldsymbol{x} \in \Gamma_{\alpha\alpha} \\ 0 & \text{otherwise} \end{cases}, \tag{2.36}$$

such that $\chi_{\gamma\gamma} + \chi_{\gamma\alpha} + \chi_{\alpha\alpha} = 1,\ \forall\, \boldsymbol{x} \in \Gamma$, where Γ is the ensemble of grain/phase interface network ($\Gamma = \Gamma_{\gamma\gamma} \cup \Gamma_{\gamma\alpha} \cup \Gamma_{\alpha\alpha}$) in the microstructure.

The interface mobility could also be reformulated as:

$$M = \sum_{l\in\mathcal{S}} \chi_l M_l. \tag{2.37}$$

Hence, taking into account interface specific properties and driving pressures from the phase interfaces as well as the grain interfaces of both the parent and the product phase, we can formulate a generalized kinetic framework based on the Eq.(1.34):

$$\boldsymbol{v} = MP\boldsymbol{n} = \left(\sum_{q\in\mathcal{S}} \chi_q M_q \right) \left[\chi_{\gamma\alpha}\Delta G_{\gamma\to\alpha} + \sum_{l\in\mathcal{S}} \chi_l \left([\![\mathcal{E}]\!]_l - \kappa\sigma_l + [P_{SD}]_l \right) \right] \boldsymbol{n}. \tag{2.38}$$

Considering the following properties of interface characteristic functions,

$$\chi_l \chi_q = \begin{cases} \chi_l & \text{if } l = q \\ 0 & \text{if } l \neq q \end{cases} \qquad \forall l, q \in \{\gamma\gamma, \gamma\alpha, \alpha\alpha\}, \tag{2.39}$$

we can obtain:

$$\boldsymbol{v} = \left[\chi_{\gamma\alpha} M_{\gamma\alpha} \Delta G_{\gamma\to\alpha} + \sum_{l\in\mathcal{S}} \chi_l M_l \left([\![\mathcal{E}]\!]_l - \kappa\sigma_l + [P_{SD}]_l \right) \right] \boldsymbol{n}. \tag{2.40}$$

If we prescribe the above interface migration velocity field into the LS transport Eqs.(2.31), then for the ith GLS function, we obtain the following equation:

$$\begin{aligned} \frac{\partial\varphi_i}{\partial t} + \left[\chi_{\gamma\alpha} M_{\gamma\alpha} \Delta G_{\gamma\to\alpha} + \sum_{l\in\mathcal{S}} \chi_l M_l [\![\mathcal{E}]\!]_l \right] \boldsymbol{n}_i \cdot \boldsymbol{\nabla}\varphi_i + \left[\sum_{l\in\mathcal{S}} \chi_l M_l \, [P_{SD}]_l \right] \boldsymbol{n}_i \cdot \boldsymbol{\nabla}\varphi_i \\ - \left[\sum_{l\in\mathcal{S}} \chi_l M_l \sigma_l \right] \kappa_i \boldsymbol{n}_i \cdot \boldsymbol{\nabla}\varphi_i = 0, \qquad \forall i \in \{1, 2, ..., N_{LS}\} \end{aligned} . \tag{2.41}$$

By verifying the metric property of a signed distance function, $\|\boldsymbol{\nabla}\varphi_i\| = 1$ all along the simulation, and imposing the geometric properties (Eqs.(2.3)) of the ith GLS function, we can write:

$$\frac{\partial\varphi_i}{\partial t} + \left[\boldsymbol{v}_{\boldsymbol{\Delta G}_{\gamma\alpha}} + \boldsymbol{v}_{[\![\mathcal{E}]\!]} \right]_i \cdot \boldsymbol{\nabla}\varphi_i - \sum_{l\in\mathcal{S}} \chi_l M_l \, [P_{SD}]_l = \left[\sum_{l\in\mathcal{S}} \chi_l M_l \sigma_l \right] \Delta\varphi_i, \qquad \forall i \in \{1, 2, ..., N_{LS}\}, \tag{2.42}$$

where,

$$\boldsymbol{n}_i = -\frac{\boldsymbol{\nabla}\varphi_i}{\|\boldsymbol{\nabla}\varphi_i\|} = -\boldsymbol{\nabla}\varphi_i \implies \kappa_i = \boldsymbol{\nabla} \cdot \boldsymbol{n}_i = -\Delta\varphi_i, \tag{2.43}$$

with,

$$\begin{aligned} \boldsymbol{v}_{\boldsymbol{\Delta G}_{\gamma\alpha}} &= \chi_{\gamma\alpha} M_{\gamma\alpha} \Delta G_{\gamma\to\alpha} \boldsymbol{n}, \\ \boldsymbol{v}_{[\![\mathcal{E}]\!]} &= \left[\sum_{l\in\mathcal{S}} \chi_l M_l [\![\mathcal{E}]\!]_l \right] \boldsymbol{n}. \end{aligned} \tag{2.44}$$

For modeling the solute drag driving pressure (P_{SD}), as discussed in Chapter-1 in 1.2.1.2, Cahn's solute drag model [81] provides a simplified description in Eq.(1.55) for the magnitude of the drag pressure (ΔG_{SD}), especially considering the non-linearity of a solute drag pressure on the velocity field. Even though Cahn's model lacks physical sense across interphase boundaries and is more apt for grain boundaries, the simplicity in its description is attractive for numerical implementation, especially in a FE framework. So, considering the complexity of the integral expressions obtained for Purdy-Brechet model [82] (and even for its modified version), along with other issues discussed in 1.2.1.2, we shall consider Cahn's simplified description in this work to model solute drag pressure. Thus, in this context, the magnitude of the solute drag pressure can be expressed as:

$$\Delta G_{SD}(\boldsymbol{v}) = \frac{\alpha_C x_X^0 \|\boldsymbol{v}\|}{1 + \beta_C^2 \|\boldsymbol{v}\|^2}. \tag{2.45}$$

Its driving pressure can then be written as:

$$P_{SD}(\boldsymbol{v}, \boldsymbol{n}) = -\Delta G_{SD} \frac{(\boldsymbol{v} \cdot \boldsymbol{n})}{\|\boldsymbol{v}\|} = -\frac{\alpha_C x_X^0 (\boldsymbol{v} \cdot \boldsymbol{n})}{1 + \beta_C^2 \|\boldsymbol{v}\|^2}. \tag{2.46}$$

With the application of Cahn's solute drag model even for phase interfaces, for the parameters, $(\alpha_C, \beta_C)|_{l=\gamma\alpha}$, instead of using the analytical definitions provided by Cahn in Eq.(1.56) and Eq.(1.57), the idea is to consider them as a set of temperature dependent model parameters to be fitted in accordance with relevant experimental results. This avoids the complexity of precisely quantifying some of the physical parameters required by their analytical definitions, especially across phase interfaces. In addition, as exhibited by the Figs.1.26 in section 1.2.1.2, Cahn's simplified drag pressure is capable of capturing the general trends expected for solute drag effects whether it is for grain interfaces or phase interfaces. So, by selectively controlling the two parameters (α_C, β_C), we could attempt to converge to expected magnitudes for the drag pressure across phase interfaces.

As discussed before, the solute drag pressure renders the velocity field non-linear. if we consider a fully implicit time discretization scheme for the resolution of Eq.(2.42), we will obtain a non-linear formulation. Considering Euler implicit time discretization, Eq.(2.42) could be discretized as:

$$\frac{\partial \varphi_i}{\partial t} \approx \frac{\varphi_i^{k+1} - \varphi_i^k}{\Delta t} = \mathcal{F}(\varphi_i^{k+1}), \qquad \forall i \in \{1, 2, ..., N_{LS}\}, \tag{2.47}$$

where

$$\mathcal{F}(\varphi_i^{k+1}) = \left[\sum_{l \in \mathcal{S}} \chi_l M_l \sigma_l\right] \Delta\varphi_i^{k+1} + \sum_{l \in \mathcal{S}} \chi_l M_l \left[P_{SD}(\boldsymbol{v}^{k+1})\right]_l - \left[\boldsymbol{v}_{\boldsymbol{\Delta G}_{\gamma\alpha}} + \boldsymbol{v}_{[\![\mathcal{E}]\!]}\right]_i \cdot \boldsymbol{\nabla}\varphi_i^{k+1}, \tag{2.48}$$

is a time dependent operator, with k being the index of time stepping.

If we consider P_{SD}^{k+1} in the second term in Eq.(2.48), we have from Eq.(2.46),

$$P_{SD}(\boldsymbol{v}^{k+1}) = -\frac{\alpha_C x_X^0 (\boldsymbol{v} \cdot \boldsymbol{n})^{k+1}}{1 + \beta_C^2 \left\|\boldsymbol{v}^{k+1}\right\|^2}. \tag{2.49}$$

Since the interface migration velocity is normal to the interface, at any position $\boldsymbol{x}$, for the **signed distance** ith GLS function, such that $\varphi_i^{k+1}(\boldsymbol{x}) \geq 0$, it is possible to express:

$$(\boldsymbol{v} \cdot \boldsymbol{n})^{k+1} = \frac{\varphi_i^{k+1} - \varphi_i^k}{\Delta t} \approx \frac{\partial \varphi_i}{\partial t}, \tag{2.50}$$

and,

$$\left\|\boldsymbol{v}^{k+1}\right\| = \frac{\left|\varphi_i^{k+1} - \varphi_i^k\right|}{\Delta t}. \tag{2.51}$$

So, P_{SD}^{k+1} would then become:

$$P_{SD}^{k+1} = -\frac{\alpha_C x_X^0 \left(\frac{\varphi_i^{k+1} - \varphi_i^k}{\Delta t}\right)}{1 + \beta_C^2 \left(\frac{\varphi_i^{k+1} - \varphi_i^k}{\Delta t}\right)^2}. \tag{2.52}$$

Clearly the term in the denominator due to $\left\|\boldsymbol{v}^{k+1}\right\|$ manifests the operator $\mathcal{F}$ in Eq.(2.48) and hence the time discretized formulation in Eq.(2.47) non-linear. To avoid this non-linearity and simplify the resolution procedure, as seen in the works of [83], the following explicit scheme based assumption is made:

$$\left\|\boldsymbol{v}^{k+1}(\boldsymbol{x})\right\|^2 \approx \left\|\boldsymbol{v}^{k}(\boldsymbol{x})\right\|^2 = \left(\frac{\varphi_i^k(\boldsymbol{x}) - \varphi_i^{k-1}(\boldsymbol{x})}{\Delta t}\right)^2 = \left\|\boldsymbol{v}^{old}(\boldsymbol{x})\right\|^2 \qquad \text{for } i \mid \varphi_i^k(\boldsymbol{x}) \geq 0, \tag{2.53}$$

where $\boldsymbol{v}^k$ or $\boldsymbol{v}^{old}$ is the net migration velocity field prescribed to compute the GLS solution φ_i^k at the current state. Even though this formulation deviates slightly from the fully implicit time scheme, for the small ranges of time steps expected to be considered in the FE resolution, the errors accumulated are expected to be of the small order while considerably simplifying the resolution procedure, thanks to the linearization. Taking this into account, Eq.(2.52) could be rewritten as:

$$P_{SD}^{k+1} \approx -\left(\frac{\alpha_C x_X^0}{1+\beta_C^2\left\|\boldsymbol{v}^{old}\right\|^2}\right)\left(\frac{\varphi_i^{k+1} - \varphi_i^k}{\Delta t}\right). \tag{2.54}$$

This would then linearize the operator $\mathcal{F}$ in Eq.(2.48) and hence the time discretized formulation in Eq.(2.47). Although not exactly, but such a strategy of splitting the operator $\mathcal{F}$ into implicit and explicit parts weakly mimics the ideologies of IMplicit-EXplicit (IMEX) time integration methods [84, 85]. Substituting Eq.(2.54) into the time discretized formulation and going back to the continuum description in Eq.(2.42), we obtain:

$$\frac{\partial \varphi_i}{\partial t} + \left[\boldsymbol{v}_{\boldsymbol{\Delta G}_{\gamma\alpha}} + \boldsymbol{v}_{[\![\varepsilon]\!]}\right]_i \cdot \boldsymbol{\nabla}\varphi_i + \sum_{l\in\mathcal{S}} \chi_l M_l \left(\frac{\alpha_C x_X^0}{1+\beta_C^2\left\|\boldsymbol{v}^{old}\right\|^2}\right)_l \frac{\partial \varphi_i}{\partial t} = \left[\sum_{l\in\mathcal{S}} \chi_l M_l \sigma_l\right] \Delta\varphi_i. \tag{2.55}$$

By imposing,

$$\mathscr{M}_{SD} = 1 + \sum_{l\in\mathcal{S}} \chi_l M_l \left(\frac{\alpha_C x_X^0}{1+\beta_C^2\left\|\boldsymbol{v}^{old}\right\|^2}\right)_l , \tag{2.56}$$

we obtain:

$$\mathscr{M}_{SD}\frac{\partial \varphi_i}{\partial t} + \left[\boldsymbol{v}_{\boldsymbol{\Delta G}_{\gamma\alpha}} + \boldsymbol{v}_{[\![\varepsilon]\!]}\right]_i \cdot \boldsymbol{\nabla}\varphi_i = \left[\sum_{l\in\mathcal{S}} \chi_l M_l \sigma_l\right] \Delta\varphi_i. \tag{2.57}$$

Eventually, we can express the above equation into the following linearized convective-diffusive (CD) formulation:

$$\frac{\partial \varphi_i}{\partial t} + \frac{1}{\mathscr{M}_{SD}}\left[\boldsymbol{v}_{\boldsymbol{\Delta G}_{\gamma\alpha}} + \boldsymbol{v}_{[\![\varepsilon]\!]}\right]_i \cdot \boldsymbol{\nabla}\varphi_i = \frac{1}{\mathscr{M}_{SD}}\left[\sum_{l\in\mathcal{S}} \chi_l M_l \sigma_l\right] \Delta\varphi_i, \qquad \forall i \in \{1, 2, ..., N_{LS}\}, \tag{2.58}$$

with $\mathcal{S} = \{\gamma\gamma, \gamma\alpha, \alpha\alpha\}$. In the following, we shall refer $\mathscr{M}_{SD}$ as the solute drag pressure coefficient. When the solute drag effects are absent or negligible, $\mathscr{M}_{SD} \rightarrow 1$, while when they are non-negligible, $\mathscr{M}_{SD} > 1$, which has the effect of lowering the interface mobility (or increasing the drag resistance) for migration.

2.3.2.1 Better description for $\boldsymbol{v}_{\Delta G_{\gamma\alpha}}$ and $\boldsymbol{v}_{[\![\mathcal{E}]\!]}$: Polycrystal context

Since $\boldsymbol{v}_{\Delta G_{\gamma\alpha}}$, and generally $\boldsymbol{v}_{[\![\mathcal{E}]\!]}$ has only significance on the interfaces, the velocity field described in Eqs.(2.44) should be extended at least to nearby nodes in the vicinity of the interface to avoid discontinuous velocity fields. In addition, in the case of a polycrystal, they could also cause kinematic incompatibilities at the multiple junctions. So, Bernacki et al. [66] suggested that it is more efficient to work with a common velocity field for all the N_{LS} global level-set functions and the velocity field needs to be as regular as possible around the multiple junctions. In the context of a multi level-set method, Bernacki et al. [66] proposed an expression for smoothing the $\boldsymbol{v}_{[\![\mathcal{E}]\!]}$ component in their work dedicated to the simulation of recrystallization in single-phase polycrystals:

$$\boldsymbol{v}_{[\![\mathcal{E}]\!]}(\boldsymbol{x},t) = \sum_{i=1}^{N_{LS}} \sum_{\substack{j=1 \\ j\neq i}}^{N_{LS}} \chi_{G_i}(\boldsymbol{x},t) M_{ij} \exp\left(-\beta_e|\varphi_j|\right) [\![\mathcal{E}]\!]_{ij}(\boldsymbol{x},t)(-\boldsymbol{n}_j), \tag{2.59}$$

where χ_{G_i} is the characteristic function of the grain G_i, M_{ij} is the interface mobility between the neighboring grains i and j, the exponential term plays the role of the decreasing function, $f = \exp\left(-\beta_e|\varphi_j|\right)$ that varies from 1 to 0 on either side of the interface and has the function of smoothing the velocity field across the interface, β_e is a positive parameter that controls the degree of smoothness and is inversely proportional to the length of smoothing (l_e), $[\![\mathcal{E}]\!]_{ij}(\boldsymbol{x},t) = \mathcal{E}_j(\boldsymbol{x},t) - \mathcal{E}_i(\boldsymbol{x},t)$ is the jump in stored energy of two neighboring grains i and j where $\mathcal{E}_j(\boldsymbol{x},t)$ and $\mathcal{E}_i(\boldsymbol{x},t)$ can be the average stored energies of the grains j and i respectively depending only on time [66], or can be based rather on local approximations [86], and $\boldsymbol{n}_j$ is the outward unit normal to the neighboring grain j. The above proposition would only make sense if the stored energies associated to a grain are extended outwards into the neighboring grain normally from the interface for a certain distance (chosen in line with the degree of smoothing desired). Scholtes et al. [78] improved the direct reinitialization strategy developed by Shakoor et al. [70] such that, along with the reinitialization procedure, simultaneously certain fields could also be extended normally from the interface. This also allowed for an efficient simultaneous computation of gradients of the level-set functions. In [87], this strategy was used successfully to normally extend the stored energies to a few nodes away from the interface to facilitate the computation of their jump and thus yield smooth velocity fields using Eq.(2.59). Figs.2.14 illustrate the idea of extension of a stored energy field initially defined as an average energy (constant) in the grain and extended normally from the interface on either sides. The stored energy can also be defined as an average on the interface but the idea remains the same. Recently [88], this strategy was also extended to avoid any average in the bulk of the grain. It should be highlighted that if the mobility is heterogeneous and/or anisotropic along the interface, it should also be extended along with the stored energy field.

Adapting Eq.(2.59) to a biphasic polycrystalline, in general, we can write:

$$\boldsymbol{v}_{[\![\mathcal{E}]\!]}(\boldsymbol{x},t) = \sum_{i=1}^{N_{LS}} \sum_{\substack{j=1 \\ j\neq i}}^{N_{LS}} \chi_{G_i}(\boldsymbol{x},t) f\left(\varphi_j, \beta_e\right) \left[\sum_{l\in\{\gamma\gamma,\gamma\alpha,\alpha\alpha\}} \chi_l M_l [\![\mathcal{E}]\!]_l \right]_{ij} (-\boldsymbol{n}_j). \tag{2.60}$$

Now, for $\boldsymbol{v}_{\Delta G_{\gamma\alpha}}$ component, we could take inspiration from the above equations and propose an

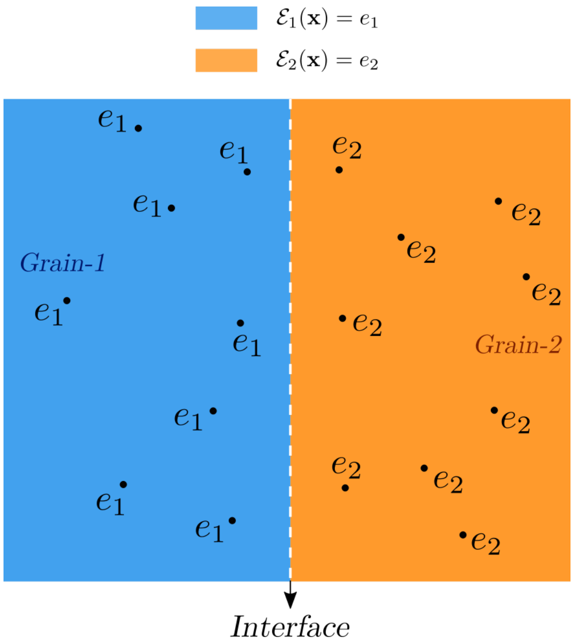

(a) Stored energy fields before extension

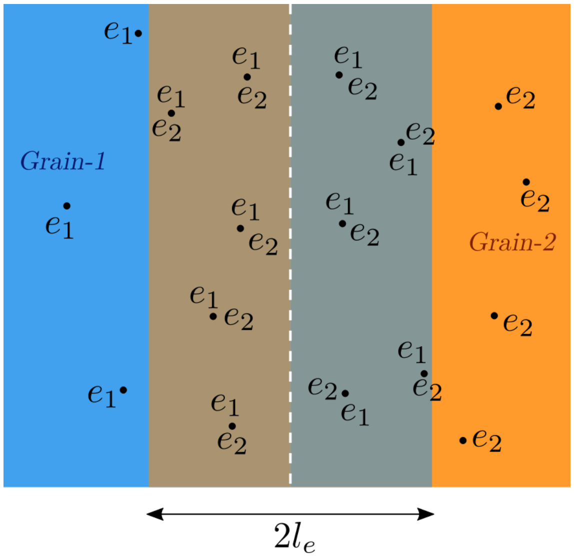

(b) Stored energy fields after extension

Figure 2.14: illustration of outward normal extension of stored energies ($\mathcal{E}$) into the neighboring nodes for a case

analogous formulation, albeit with a couple of additional functions:

$$\boldsymbol{v}_{\Delta \boldsymbol{G}_{\gamma\alpha}}(\boldsymbol{x},t) = \sum_{i=1}^{N_{LS}} \sum_{\substack{j=1 \\ j\neq i}}^{N_{LS}} \chi_{G_i} M_{ij} f\left(\varphi_j, \beta_e\right) \chi_{\gamma\alpha} \Delta G_{\gamma\to\alpha} \mathscr{F}_s(-\boldsymbol{n}_j), \tag{2.61}$$

where $\chi_{\gamma\alpha}$, as seen earlier, helps to filter this component of velocity field only on the phase interfaces. In Eq.(2.59), the jump in stored energies $[\![\mathcal{E}]\!]_{ij}$ ensures that the velocity vectors are oriented in a consistent direction on the nodes close to both the sides of the interface, thanks to a flip in sign ($[\![\mathcal{E}]\!]_{ij} = -[\![\mathcal{E}]\!]_{ji}$) as shown in Fig.2.15a. However in Eq.(2.61), since $\Delta G_{\gamma\to\alpha}$ already gives a measure of the Gibbs free energy difference on the phase interface (common to the neighboring grains) there is no natural flip in sign. Hence $\mathscr{F}_s$ is used as a sense function that ensures that the velocity vectors of this component on the nodes close to either side of the phase interface are oriented consistently as observed in Fig.2.15b. $\mathscr{F}_s$ in the context of a transformation, $\gamma \longrightarrow \alpha$, is defined as follows:

$$\mathscr{F}_s(\boldsymbol{x},t) = \chi_\alpha(\boldsymbol{x},t) - \chi_\gamma(\boldsymbol{x},t) = 2\chi_\alpha(\boldsymbol{x},t) - 1, \tag{2.62}$$

where $\chi_\alpha(\boldsymbol{x},t)$ and $\chi_\gamma(\boldsymbol{x},t)$ are the characteristic functions of α and γ phase respectively, such that $\chi_\alpha(\boldsymbol{x},t) + \chi_\gamma(\boldsymbol{x},t) = 1$.

As we shall see in section 2.3.4, $\Delta G_{\gamma\to\alpha}$ description gives a continuous heterogeneous field taking values away from the interface as well. So it is possible to directly apply Eq.(2.61) without any extension procedure, and a smooth but non-symmetric velocity field (in the plane orthogonal to the interface) could be obtained as exhibited by Fig.2.16. The curve in blue in Fig.2.16 is the heterogeneous velocity field obtained without multiplying with the smoothing function ($f\left(\varphi_j,\beta_e\right)$). It is possible to get away with this description, especially since the velocity field values only at the iso-zeros on the phase interfaces are important. However, a non-symmetric velocity field may potentially cause bunching and stretching of the neighboring level-sets rendering φ_i very steep or flat. Since $\Delta G_{\gamma\to\alpha}$ has significance only on the phase interfaces, for a nice level-set representation, it is recommended to perform a normal outwards extension of $\Delta G_{\gamma\to\alpha}$ by taking its values only on the phase interfaces. Fig.2.17 gives a representation of the velocity field computed using the extended $\Delta G_{\gamma\to\alpha}$ based off its value at the interface, as observed in a plane orthogonal to the interface at a certain point. This extension is carried out, thanks to the strategy developed by Scholtes et al. [78].

In Eq.(2.61), the use of all the N_{LS} level-set functions is not necessary unlike in the case of stored energy component, since $\Delta G_{\gamma\to\alpha}$ is valid only on the phase interfaces and not on the entire grain/phase interface network. So, an alternative and simple approach could be proposed that takes into account only the secondary level-set function representing all the α phase grains, φ_α:

$$\boldsymbol{v}_{\boldsymbol{\Delta G}_{\gamma\alpha}}(\boldsymbol{x},t) = M_{\gamma\alpha}\chi_{\gamma\alpha} f\left(\varphi_\alpha,\beta_e\right)\Delta G_{\gamma\to\alpha}(\boldsymbol{x},t)(-\boldsymbol{\nabla}\varphi_\alpha), \tag{2.63}$$

where $f\left(\varphi_\alpha,\beta_e\right)$ is a smoothing function. We can observe that the consistent orientation of the velocity field is naturally handled by the vector $-\boldsymbol{\nabla}\varphi_\alpha = \boldsymbol{n}_\alpha$ which is an outward unit normal of α grains. It should be emphasized again that $\Delta G_{\gamma\to\alpha}$ could be extended, along with $M_{\gamma\alpha}$ (in case it is not a constant). In the presence of solute drag effects, since the solute drag pressure coefficient ($\mathscr{M}_{SD}$) effectively lowers the mobility, it can be embedded directly into the above velocity description by considering the phase interface mobility as, $M'_{\gamma\alpha} = M_{\gamma\alpha}/\mathscr{M}_{SD}$. The inherent heterogeneity of $\mathscr{M}_{SD}$ also leads to heterogeneous effective interface mobility in this scenario.

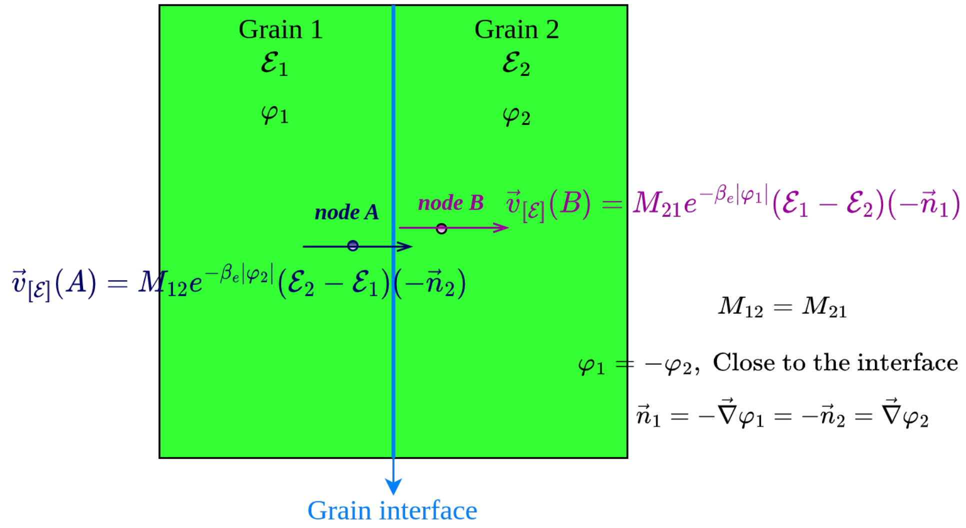

(a) $\boldsymbol{v}_{[\![\mathcal{E}]\!]}$ component

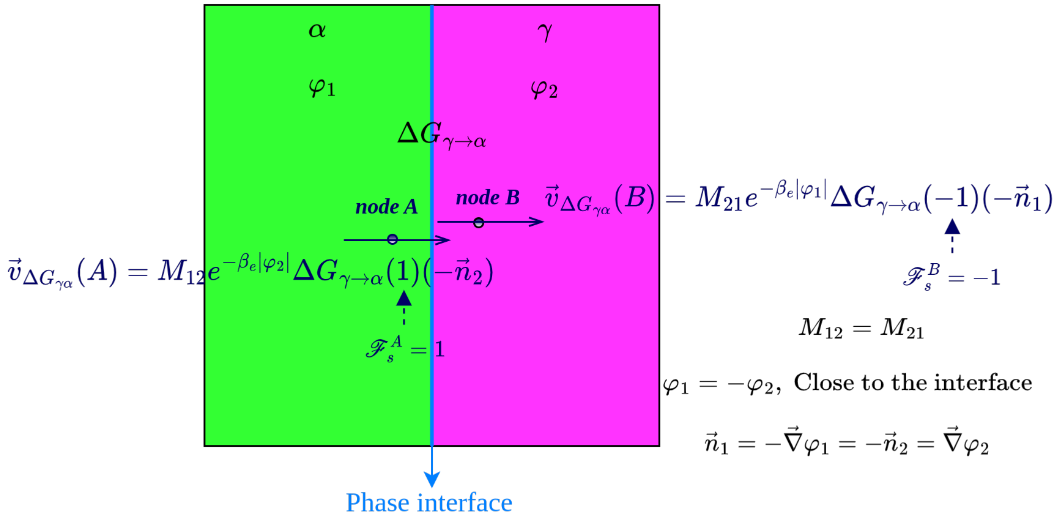

(b) $\boldsymbol{v}_{\Delta G_{\gamma\alpha}}$ component

Figure 2.15: Consistent orientation of velocity vectors on nodes A and B, close to either side of the migrating interface

2.3.3 Additional numerical considerations in the context of polycrystals

The computation of certain fields complementing the previous formulation by acting as key ingredients are described here. In addition, particular numerical treatments aimed to support certain aspects of the simulation shall be discussed in brief.

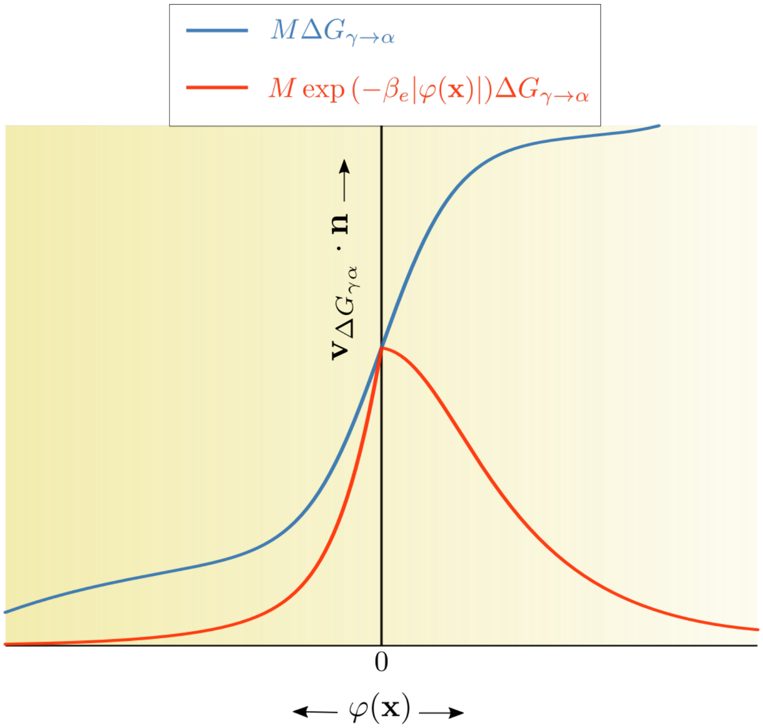

Figure 2.16: Illustration of an example of velocity smoothing without extending the heterogeneous $\Delta G_{\gamma\to\alpha}$ field, yielding smooth but non-symmetric velocity profile (in red) in a plane orthogonal to the interface at a certain point

.

Computation of $\varphi_\alpha(\boldsymbol{x},t)$ and the diffuse phase interface function, $\phi(\boldsymbol{x},t)$: The characteristic function of the α phase, χ_α, is defined such that:

$$\chi_\alpha(\boldsymbol{x},t) = \begin{cases} 1 & \forall\, \boldsymbol{x} \in \Omega_\alpha(t) \\ 0 & \text{otherwise} \end{cases}, \tag{2.64}$$

where $\Omega_\alpha(t)$ denotes the part of the domain occupied by all those grains of the type α phase, such that $\Omega_\alpha(t) \cup \Omega_\gamma(t) = \Omega$. This characteristic function (also referred as Phase-ID field) is initialized depending on the grain/phase distribution of the initial microstructure input to the model. For, $t > 0$, it is updated at each time step after the resolution of Eq.(2.58) using a tracking model developed by Scholtes et al. [78] in order to follow the updated configuration of the grain/phase morphology.

Once the Phase-ID field (χ_α) is computed, φ_α (which is a signed distance LS function that represents all the zones of the α phase in the overall domain) is obtained through the reinitialization of the $\mathscr{F}_s(\boldsymbol{x},t)\varphi_{max}(\boldsymbol{x},t) = [2\chi_\alpha(\boldsymbol{x},t)-1]\,\varphi_{max}(\boldsymbol{x},t)$ function through an imposed 2ϵ thickness around its 0 iso-value. So the α-phase domain LS function is computed as:

$$\varphi_\alpha(\boldsymbol{x},t) = \text{Reinitialization}\Big([2\chi_\alpha(\boldsymbol{x},t)-1]\,\varphi_{max}(\boldsymbol{x},t)\Big), \tag{2.65}$$

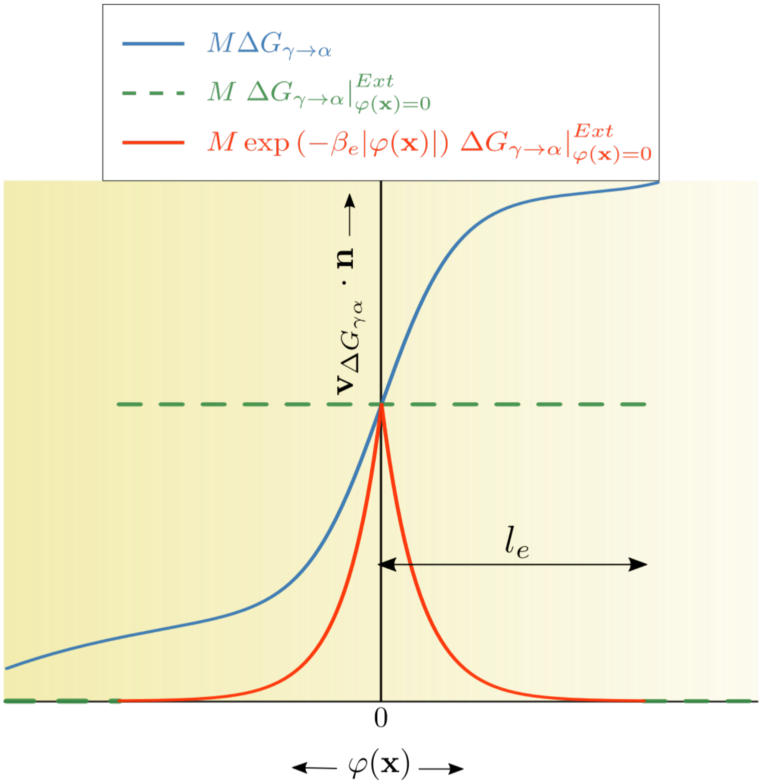

Figure 2.17: Illustration of an example of velocity smoothing through an extension of the $\Delta G_{\gamma\to\alpha}$ value at the interface, yielding smooth and symmetric velocity profile (in red) in a plane orthogonal to the interface at a certain point

.

with,

$$\varphi_{max}(\boldsymbol{x},t) = \max_{i\in\{1,\ldots,N_{LS}\}} \varphi_i(\boldsymbol{x},t). \tag{2.66}$$

The idea behind this expression is in two folds. Firstly from Eq.(2.62), $\mathscr{F}_s(\boldsymbol{x},t)$ takes 1 inside $\Omega_\alpha(t)$, and -1 inside $\Omega_\gamma(t)$. Secondly, the maximum LS function in Eq.(2.66) is an unsigned distance function that is positive inside every grain, while approaching 0 at the interface (as explained in the case of VIIM). So, when these two functions are multiplied, the resulting function takes positive values inside the grains belonging to $\Omega_\alpha(t)$, and negative values inside that of $\Omega_\gamma(t)$, which is the essence of a signed distance function describing $\Omega_\alpha(t)$ sub-domain. Considering that this LS function is crucial in the computation of the diffuse phase interface (ϕ) using the Eq.(2.11), the reinitialization step ensures that this LS function precisely localizes the 0 iso-values corresponding to the phase interfaces. It also ensures that the LS function is regular, at least around a distance, $2\epsilon > \eta$, from the interface, so that $\phi(\boldsymbol{x},t)$ is properly defined. A similar result can be obtained by a direct reinitialization of the discontinuous $\mathscr{F}_s(\boldsymbol{x},t)$ function since there is an inherent change of sign across the phase interfaces, but the interest to multiply it by the $\varphi_{max}(\boldsymbol{x},t)$ function is to increase the 0 iso-contour precision before the reinitialization.

So, once φ_α is computed, the hyper tangent relation in Eq.(2.11) is then applied to compute the phase-field function that gives the diffuse interface description across the updated phase interfaces for the next computation loop to resolve the solute redistribution equation Eq.(2.20). Figs.2.18 illustrate the representation of various functions involved at each step in the computation of ϕ.

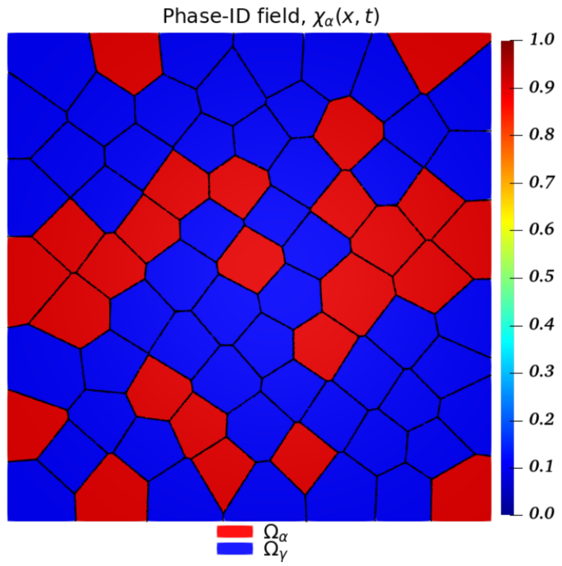

(a) α-phase characteristic field with the interfaces highlighted in black for visualization

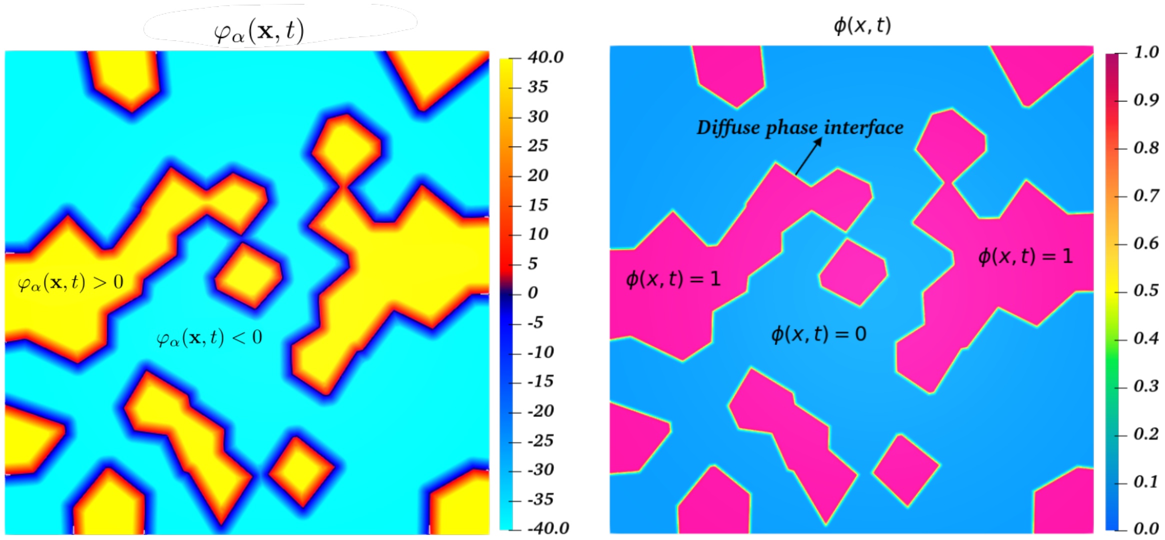

(b) α-phase signed distance level-set function

(c) Phase-field function

Figure 2.18: Illustrations for computing phase-field function in a two-phase polycrystal

Computation of the interface characteristic functions: Having computed the, φ_α and the φ_{max} functions, they are used to compute at each instant the various interface characteristic functions defined in Eqs.(2.34), (2.35), and (2.36). They are computed in the following way:

$$
\begin{aligned}
\chi_{\gamma\alpha}(\boldsymbol{x},t) &= \begin{cases} 1 & \text{if} \quad |\varphi_\alpha(\boldsymbol{x},t)| < \delta_{cf} \\ 0 & \text{otherwise} \end{cases} \\
\chi_{\alpha\alpha}(\boldsymbol{x},t) &= \begin{cases} \left[1 - \chi_{\gamma\alpha}(\boldsymbol{x},t)\right] \chi_\alpha(\boldsymbol{x},t) & \text{if} \quad \varphi_{max}(\boldsymbol{x},t) < \delta_{cf} \\ 0 & \text{otherwise} \end{cases}, \\
\chi_{\gamma\gamma}(\boldsymbol{x},t) &= \begin{cases} 1 - \chi_{\gamma\alpha}(\boldsymbol{x},t) - \chi_{\alpha\alpha}(\boldsymbol{x},t) & \text{if} \quad \varphi_{max}(\boldsymbol{x},t) < \delta_{cf} \\ 0 & \text{otherwise} \end{cases}
\end{aligned}
\tag{2.67}
$$

where δ_{cf} is a small positive distance threshold chosen based on the mesh resolution at the interface such that δ_{cf} is always smaller than ϵ. Figs.2.19 shows an illustration of these functions. These interface characteristic functions of the updated grain/phase interface network are then used in the following resolution loop primarily to describe the interface specific kinetics.

Computation of the solute drag pressure coefficient, $\mathscr{M}_{SD}$: To compute the solute drag pressure coefficient in Eq.(2.56):

$$
\mathscr{M}_{SD} = 1 + \sum_{l \in \mathcal{S}} \chi_l M_l \left(\frac{\alpha_C x_X^0}{1 + \beta_C^2 \left\|\boldsymbol{v}^{old}\right\|^2} \right)_l \qquad \forall l \in \{\gamma\gamma, \gamma\alpha, \alpha\alpha\},
$$

we need the respective laws/ expressions governing $\{\alpha_C(T), \beta_C(T)\}_l$ and $M_l(\boldsymbol{x},t,T)$ provided, and χ_l and $\|\boldsymbol{v}^{old}\|$ need to be computed. We discussed already the computation of χ_l previously. In order to compute $\|\boldsymbol{v}^{old}\|$, let us consider its discrete definition:

$$
\left\|\boldsymbol{v}^{old}(\boldsymbol{x})\right\| = \frac{\left|\varphi_i^k(\boldsymbol{x}) - \varphi_i^{k-1}(\boldsymbol{x})\right|}{\Delta t} \qquad \text{for } i \mid \varphi_i^k(\boldsymbol{x}) \geq 0, \tag{2.68}
$$

where φ_i^k and φ_i^{k-1} are the GLS solutions available at the current and the previous states of time respectively. In practice, the above definition is reformulated as:

$$
\left\|\boldsymbol{v}^{old}(\boldsymbol{x})\right\| = \max_{i \in \{1,\ldots,N_{LS}\}} \left(\mathcal{I}_i^k(\boldsymbol{x}) \frac{\left|\varphi_i^k(\boldsymbol{x}) - \varphi_i^{k-1}(\boldsymbol{x})\right|}{\Delta t} \right), \tag{2.69}
$$

where $\mathcal{I}_i^k(\boldsymbol{x})$ is used as an indicator function associated to the ith GLS function such that $\varphi_i^k(\boldsymbol{x}) \geq 0$, i.e.,

$$
\mathcal{I}_i^k(\boldsymbol{x}) = \begin{cases} 1 & \text{if} \quad \varphi_i^k(\boldsymbol{x}) \geq 0 \\ 0 & \text{otherwise} \end{cases}. \tag{2.70}
$$

At the initial state of time ($k = 0$), $\|v^{old}\| = 0$, as $\varphi_i^0 = \varphi_i^{-1}$ The solute drag pressure coefficient needs to be computed before the next resolution step of Eq.(2.58).

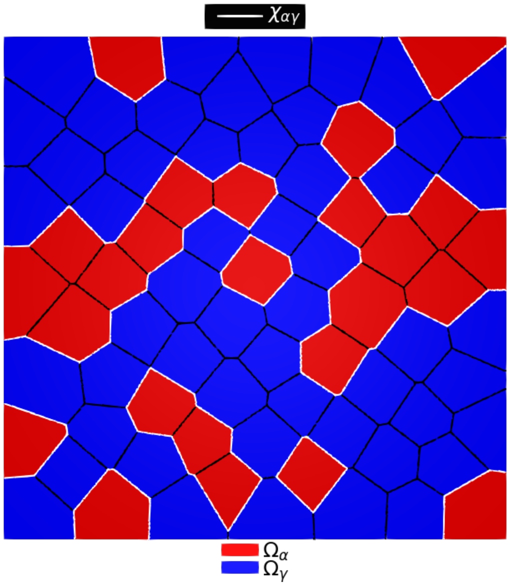

(a) α/γ phase interfaces

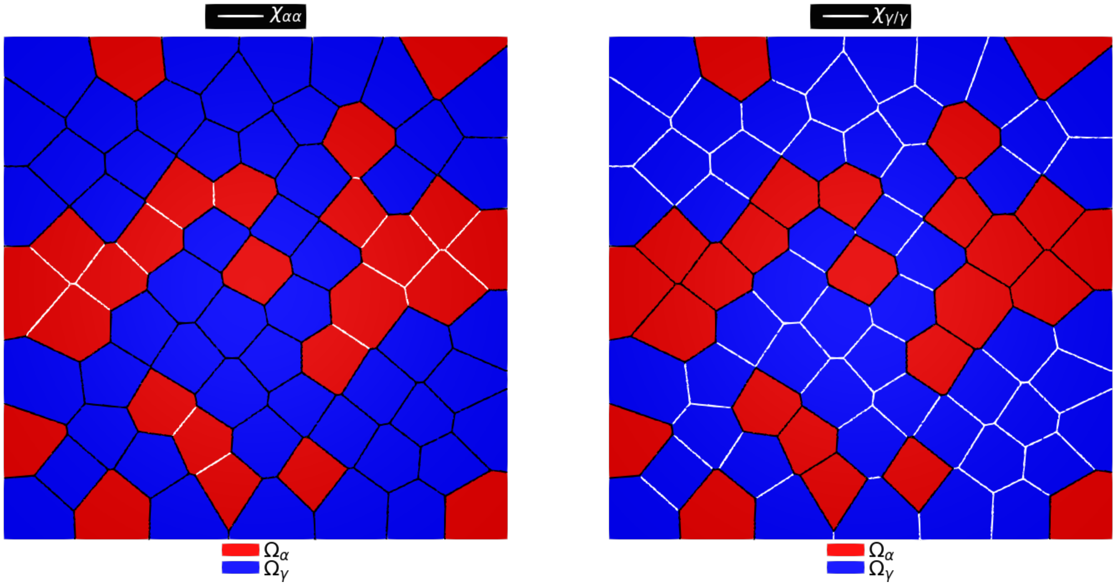

(b) α/α grain interfaces (c) γ/γ grain interfaces

Figure 2.19: Illustrations of various interface characteristic functions in a two-phase polycrystal. Respective interfaces are highlighted in white

Multiple junctions numerical treatment: Following the LS transport resolution, due to the presence of multiple junctions, in order to remove any kinematic incompatibilities at the multiple junctions such as vacuum or overlapping regions as depicted in Figs.2.20, a particular numerical treatment according to [37] is performed to modify the LS functions:

$$\hat{\varphi}_i = \frac{1}{2}\left(\varphi_i - \max_{j\neq i} \varphi_j\right) \quad \forall i \in \{1, ..., N_{LS}\}. \tag{2.71}$$

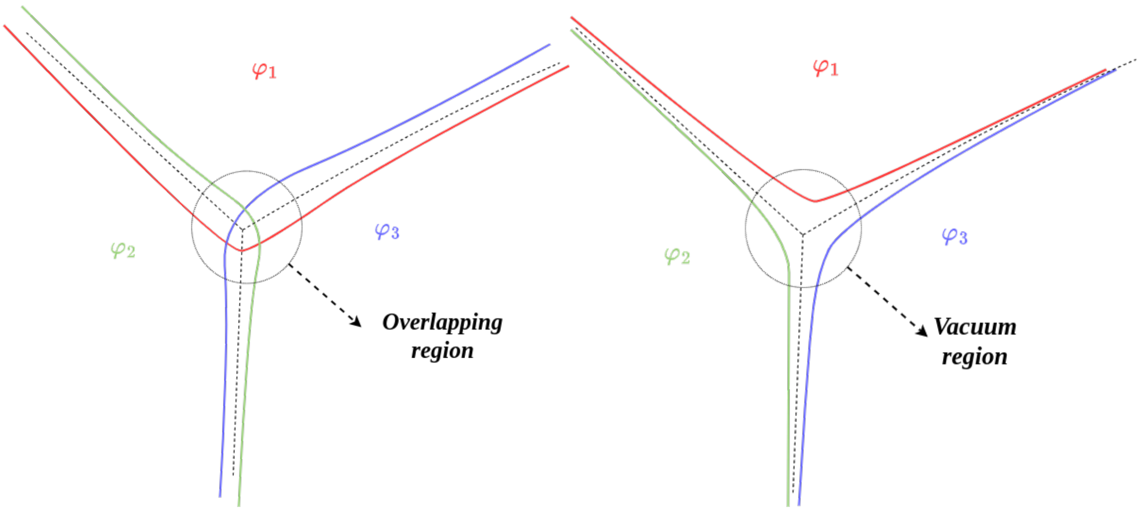

(a) Overlapping region at the triple junction

(b) Vacuum region created at the triple junction

Figure 2.20: Kinematic incompatibilities encountered at the multiple junctions (triple junction in this case)

Following this multiple junctions treatment, $\varphi_i(\boldsymbol{x}, t)$ are then reinitialized in the 2ϵ-narrow band around their 0 iso-values at each time step. The term ϵ is taken to be equal to at least 2 times the η value to ensure that φ_i, φ_{max}, and hence φ_α are all regular and well defined far enough from the corresponding interfaces such that ϕ is properly computed for the considered diffuse interface thickness (η parameter) value.

Smoothing of heterogeneous fields: In Eq.(2.58), the term $\frac{1}{\mathscr{M}_{SD}}\left[\sum_{l\in\mathcal{S}}\chi_l M_l \sigma_l\right] = (M\sigma)_{Het}$ represents a field characterized by heterogeneity and discontinuity. To address this, a smoothing technique, involving the resolution of the Laplace's equation with specific boundary conditions, is applied to both the heterogeneous effective mobility and interface energy fields throughout the computational domain to yield a smooth and a unified field. The effective mobility here refers to the interface mobility lowered by the solute drag pressure coefficient ($\frac{M(\boldsymbol{x},t)}{\mathscr{M}_{SD}(\boldsymbol{x},t)}$).

So, for a smooth effective interface mobility field, $M_{Sm}(\boldsymbol{x}, t)$, we solve:

$$\begin{cases} k_s \Delta M_{Sm} = 0 & \text{in } \Omega \\ M_{Sm} = M_{\gamma\alpha}/\mathscr{M}_{SD} & \text{on } \Gamma_{\gamma\alpha} \\ M_{Sm} = M_{\gamma\gamma}/\mathscr{M}_{SD} & \text{on } \Gamma_{\gamma\gamma} \\ M_{Sm} = M_{\alpha\alpha}/\mathscr{M}_{SD} & \text{on } \Gamma_{\alpha\alpha} \\ [\boldsymbol{\nabla} M_{Sm} \cdot \boldsymbol{n}_b]|_{\partial G} = 0 & \end{cases}, \tag{2.72}$$

where $\boldsymbol{n}_b$ is the normal to the domain boundary, while $\Gamma_{\gamma\alpha}$, $\Gamma_{\gamma\gamma}$, and $\Gamma_{\alpha\alpha}$ represent the ensemble of interfaces on which the necessary Dirichlet boundary conditions are imposed. These conditions reflect the specified interface mobility values corresponding to each interface type. The degree of smoothing is controlled by the numerical diffusion coefficient (k_s) prescribed in the weak formulation of the above equation.

Similarly, for a smooth interface energy field, $\sigma_{Sm}(\boldsymbol{x}, t)$, we solve:

$$\begin{cases} k_s \Delta \sigma_{Sm} = 0 & \text{in } \Omega \\ \sigma_{Sm} = \sigma_{\gamma\alpha} & \text{on } \Gamma_{\gamma\alpha} \\ \sigma_{Sm} = \sigma_{\gamma\gamma} & \text{on } \Gamma_{\gamma\gamma} \\ \sigma_{Sm} = \sigma_{\alpha\alpha} & \text{on } \Gamma_{\alpha\alpha} \\ [\boldsymbol{\nabla}\sigma_{Sm} \cdot \boldsymbol{n}_b]|_{\partial G} = 0 & \end{cases} . \tag{2.73}$$

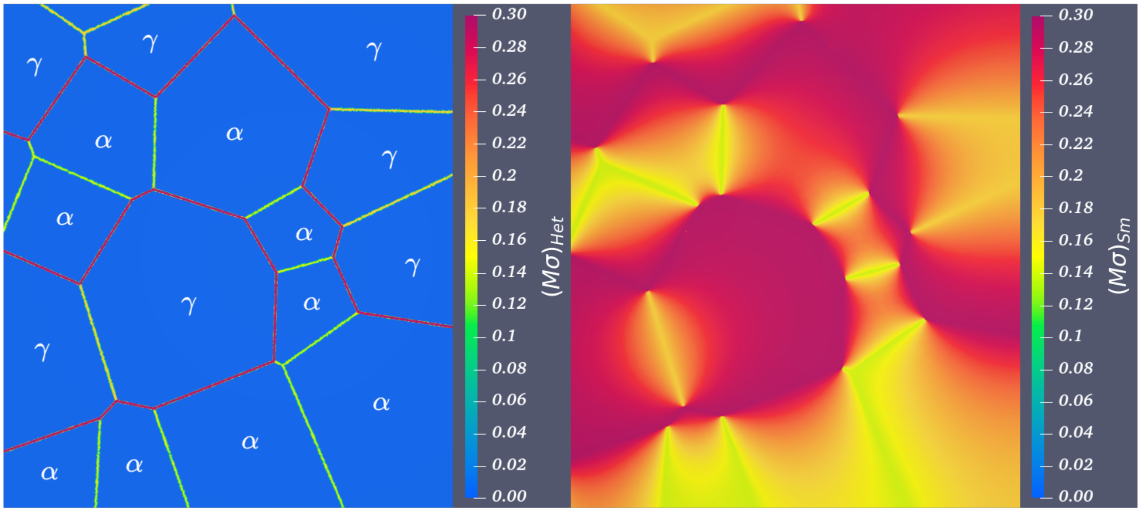

Figure 2.21: Illustration of smoothing of the heterogeneous interface mobility and interface energy fields: Heterogeneous $M\sigma$ product (left), Smoothed $M\sigma$ product (right)

The term $\left[\sum_{l\in\mathcal{S}} \chi_l M_l \sigma_l\right] / \mathscr{M}_{SD}$ is then replaced by the product of the above two smoothed fields, so that the Eq.2.58 becomes:

$$\frac{\partial \varphi_i}{\partial t} + \frac{1}{\mathscr{M}_{SD}} \left[\boldsymbol{v}_{\boldsymbol{\Delta G}_{\gamma\alpha}} + \boldsymbol{v}_{[\![\varepsilon]\!]} \right]_i \cdot \boldsymbol{\nabla}\varphi_i = M_{Sm}\sigma_{Sm}\Delta\varphi_i, \qquad \forall i \in \{1, 2, ..., N_{LS}\}. \tag{2.74}$$

Fig.2.21 provides an illustration comparing the heterogeneous product, $(M\sigma)_{Het}$, on the left, with the smoothed product, $M_{Sm}\sigma_{Sm}$, on the right, employing the described technique. This visualization demonstrates the role of the Laplace's equation in diffusing the discontinuous fields. The smoothing process is executed before the resolution for interface migration at every time step.

Adaptive remeshing for biphasic polycrystals - Metric intersection: In order to capture the strong evolution close to the interfaces with acceptable precision, the front-capturing methods such as level-set demands meshes with finer resolution close to the interface. So, in this numerical framework, a local adaptive isotropic/ anisotropic meshing strategy is adopted with remeshing

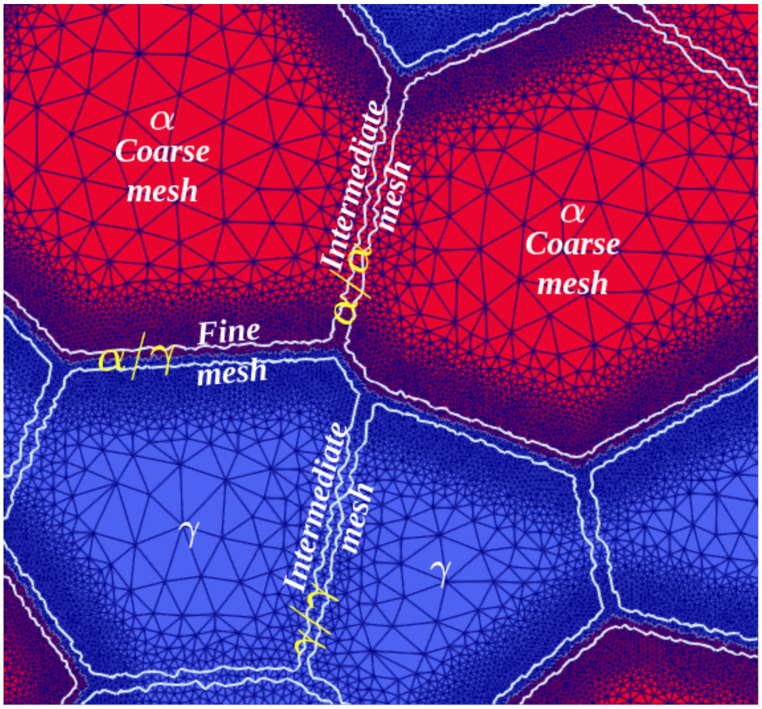

Figure 2.22: Illustration of the dual metric based meshing strategy adopted for two phase polycrystals

capabilities. The local adaptive mesh is generated using a metric based mesher [66, 74] adapted to polycrystals. Such a mesh generation strategy is a geometrical approach based on the normal and/or mean curvature of the grain interface network. In the case of a biphasic polycrystalline microstructure, the precision needed at the phase interfaces is much more important as it involves stronger evolution due to the phase transformation driving pressure when compared to evolution of grain interfaces with relatively weaker driving pressures. Instead of using a single metric tensor to adapt the mesh for the whole grain/phase interface network, two different mesh metric tensors are considered: one metric for the phases interfaces to yield a finer mesh across γ/α, and another metric for the grain interfaces to yield a relatively coarser mesh across the α/α and γ/γ interfaces compared to the phase interfaces, while globally maintaining a very coarse mesh in the bulk. The local adaptive mesh is generated through an intersection of these two different mesh metric tensors based on the works in [89] and using the metric based mesher/ remesher [66]. As the interfaces evolve, a periodic remeshing operation is performed to re-adapt the mesh in line with the current interface network configuration and follow it. Fig.2.22 illustrates a snapshot of a FE mesh in a two phase polycrystal with a coarse mesh in the bulk, a very fine mesh at the phase interfaces, and an adaptive mesh with an intermediate size is generated at the grain interfaces. Such a strategy is important for saving computational time.

2.3.4 Description of the driving pressure, $\Delta G_{\gamma\rightarrow\alpha}$: ThermoCalc coupling

One of the last few key ingredients missing to completely prescribe the above kinetics is the change in Gibbs free energy between the two phases.

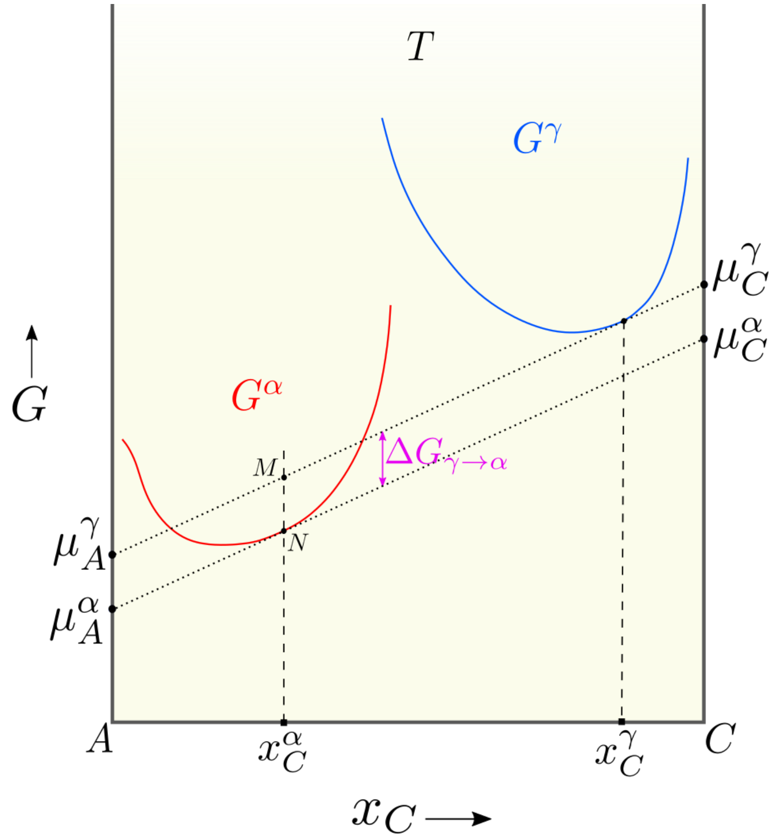

Figure 2.23: Illustration of the driving pressure derived through parallel tangent construction

In most cases, [90–92], the solute concentrations at the phase interfaces are assumed to be at local thermodynamic equilibrium (which is the essence of diffusion controlled kinetics) while globally the system state being far from the equilibrium state. For full-field based models however, to derive the driving pressure at the phase interfaces, small deviations from equilibrium (as explained by Hillert in [93]) can be considered. A popular approach to describe these deviations for solid-state phase transformation or solidification is to consider local quasi-equilibrium hypothesis for locally coexisting phases, as seen in the works of [94–99]. This allows to characterize finite interface kinetics. Fig.2.23 demonstrates the Gibbs free energy variations with composition at a temperature, T, of a solute for the growth of an already formed product phase α in a parent phase γ. The driving pressure is derived through a parallel tangent construction which implies that the diffusional exchange of solutes between the two phases is rapid compared to the phase transformation process. So, in Fig.2.23, the magnitude of the driving pressure ($\Delta G_{\gamma\rightarrow\alpha}$) is thus the difference in free energies between the points M and N. $\Delta G_{\gamma\rightarrow\alpha}$ can be thus expressed as:

$$\Delta G_{\gamma\rightarrow\alpha} = \mu_C^{\gamma} x_C^{\alpha} + \mu_A^{\gamma}\left[1 - x_C^{\alpha}\right] - \left(\mu_C^{\alpha} x_C^{\alpha} + \mu_A^{\alpha}\left[1 - x_C^{\alpha}\right]\right), \tag{2.75}$$

where C is the solute element, and A is the major element in the alloy. The above equation could be reformulated as:

$$\Delta G_{\gamma\rightarrow\alpha} = \mu_A^{\gamma} - \mu_A^{\alpha} - x_C^{\alpha}\left(\left[\mu_A^{\gamma} - \mu_A^{\alpha}\right] - \left[\mu_C^{\gamma} - \mu_C^{\alpha}\right]\right). \tag{2.76}$$

Using the definitions of the chemical potential defined in Chapter 11.2.1 in Eqs.(1.5), Eq.(2.76) could be rewritten as:

$$\Delta G_{\gamma\to\alpha} = G^{\gamma}|_{x_C^{\gamma}} - G^{\alpha}|_{x_C^{\alpha}} - x_C^{\gamma}\left.\frac{\partial G^{\gamma}}{\partial x_C}\right|_{x_C^{\gamma}} + x_C^{\alpha}\left.\frac{\partial G^{\alpha}}{\partial x_C}\right|_{x_C^{\alpha}} - x_C^{\alpha}\left(\left[\mu_A^{\gamma} - \mu_A^{\alpha}\right] - \left[\mu_C^{\gamma} - \mu_C^{\alpha}\right]\right). \tag{2.77}$$

The parallel tangent construction in quasi-equilibrium hypothesis imposes the following constraint at a fixed temperature, T:

$$\left.\frac{\partial G^{\gamma}}{\partial x_C}\right|_{x_C^{\gamma}} = \left.\frac{\partial G^{\alpha}}{\partial x_C}\right|_{x_C^{\alpha}}. \tag{2.78}$$

In addition, it is easy to infer from the Fig.2.23 (as well as mathematically) that, for parallel tangents, $\left[\mu_A^{\gamma} - \mu_A^{\alpha}\right] - \left[\mu_C^{\gamma} - \mu_C^{\alpha}\right] = 0$. We thus obtain:

$$\Delta G_{\gamma\to\alpha} = G^{\gamma}|_{x_C^{\gamma}} - G^{\alpha}|_{x_C^{\alpha}} - \left.\frac{\partial G^{\gamma}}{\partial x_C}\right|_{x_C^{\gamma}}\left(x_C^{\gamma} - x_C^{\alpha}\right). \tag{2.79}$$

In general, for an alloy system with N_C components, the driving pressure could be written as:

$$\Delta G_{\gamma\to\alpha} = G^{\gamma}|_{\boldsymbol{\mathcal{X}}^{\gamma}} - G^{\alpha}|_{\boldsymbol{\mathcal{X}}^{\alpha}} - \sum_{i}^{N_C-1}\left.\frac{\partial G^{\gamma}}{\partial x_i}\right|_{x_i^{\gamma}}\left(x_i^{\gamma} - x_i^{\alpha}\right), \tag{2.80}$$

where $\boldsymbol{\mathcal{X}}^{\alpha}, \boldsymbol{\mathcal{X}}^{\gamma}$ are the vectors of concentrations of all the $N_C - 1$ solute elements in the two phases. So, for a certain fixed pressure (p), $\Delta G_{\gamma\to\alpha}$ is typically dependent on the local composition of the solutes, and the temperature.

In some of the earliest works [94, 97, 100], the description for $\Delta G_{\gamma\to\gamma}$ has been established directly through thermodynamic evaluations of [101, 102] based on Calphad data or ThermoCalc software [103]. For certain sharp interface descriptive models on binary systems, the diffusion in the bulk of the product phase is assumed to be instantaneous and so $\Delta G_{\gamma\to\alpha}$ is simply assumed to be proportional to the deviation in concentration at the interface in the parent phase (x_C^{γ}) from its equilibrium concentration ($x_C^{\gamma}|_{eq}$) [26, 104]:

$$\Delta G_{\gamma\to\alpha} = \Upsilon\left(x_C^{\gamma}|_{eq} - x_C^{\gamma}\right), \tag{2.81}$$

where Υ is a proportionality factor that could be temperature dependent and is derived from thermodynamic databases.

In the current work, $\Delta G_{\gamma\to\alpha}$ is reformulated based on a local linearization of the phase diagram as seen in [45, 51, 105]. Fig.2.24 illustrates the underlying idea where the two solvus lines of the phase diagram (say A-i) are linearized at some reference temperature, T^R, where A is the major element and i is the solute element of the alloy. Let x_i^{α} and x_i^{γ} be the non-equilibrium interface compositions of the solute i at the current temperature T. As represented in the Fig.2.24, let T^{eq} be the equilibrium temperature corresponding to the current interface concentrations such that $\Delta T = T^{eq} - T$ is the undercooling. The undercooling measures the deviation from the local equilibrium temperature. So at the equilibrium temperature, T^{eq}, the driving pressure in Eq.(2.79) could be written as:

$$\Delta G_{\gamma\to\alpha}^{eq} = G_{eq}^{\gamma}\big|_{x_i^{\gamma}} - G_{eq}^{\alpha}\big|_{x_i^{\alpha}} - \left.\frac{\partial G_{eq}^{\gamma}}{\partial x_i}\right|_{x_i^{\gamma}}\left(x_i^{\gamma} - x_i^{\alpha}\right) = 0. \tag{2.82}$$

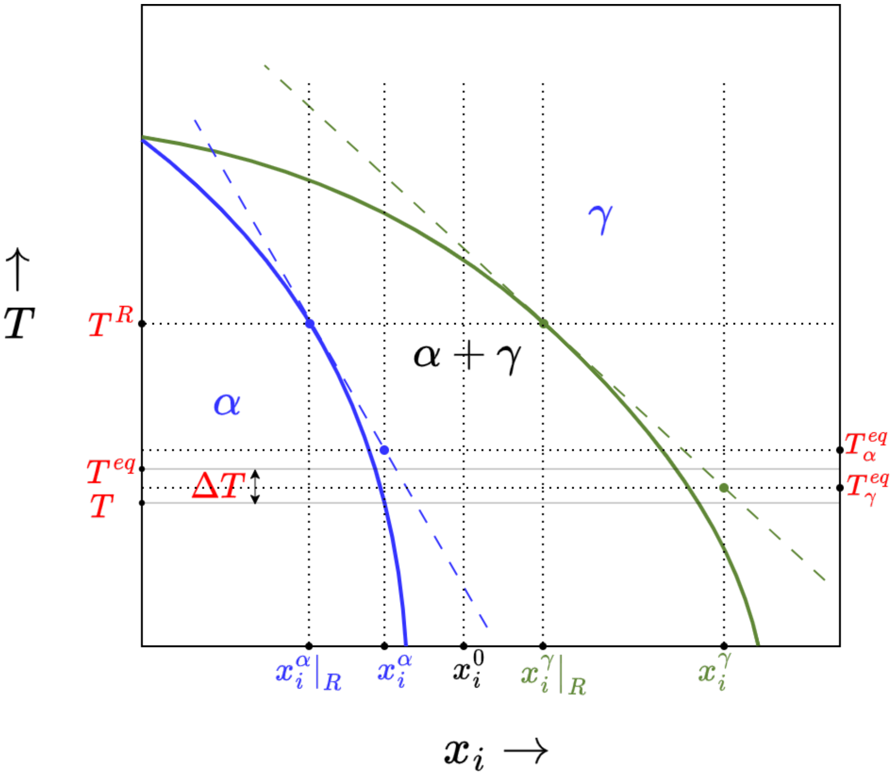

Figure 2.24: Local linearization of the A-i binary phase diagram at T^R

Using the definitions of Gibbs free energy, $G = H - TS$, where H is the enthalpy and S is the entropy, Eq.(2.82) could be written as:

$$\Delta H_{eq}^{\gamma\alpha} - \Delta S_{eq}^{\gamma\alpha} T^{eq} - \left.\frac{\partial G_{eq}^{\gamma}}{\partial x_i}\right|_{x_i^\gamma} \left(x_i^\gamma - x_i^\alpha\right) = 0, \tag{2.83}$$

where $\Delta H_{eq}^{\gamma\alpha} = H_{eq}^{\gamma}\big|_{x_i^\gamma} - H_{eq}^{\alpha}\big|_{x_i^\alpha}$, is the difference in enthalpy between the two phases at T^{eq}, and likewise $\Delta S_{eq}^{\gamma\alpha} = S_{eq}^{\gamma}\big|_{x_i^\gamma} - S_{eq}^{\alpha}\big|_{x_i^\alpha}$ is the difference in entropy. We can thus write,

$$\Delta H_{eq}^{\gamma\alpha} = \Delta S_{eq}^{\gamma\alpha} T^{eq} + \left.\frac{\partial G_{eq}^{\gamma}}{\partial x_i}\right|_{x_i^\gamma} \left(x_i^\gamma - x_i^\alpha\right). \tag{2.84}$$

At the current non-equilibrium state, the driving pressure can be also be written in terms of the enthalpy and entropy differences as:

$$\Delta G_{\gamma\rightarrow\alpha} = \Delta H^{\gamma\alpha} - \Delta S^{\gamma\alpha} T - \left.\frac{\partial G^{\gamma}}{\partial x_i}\right|_{x_i^\gamma} \left(x_i^\gamma - x_i^\alpha\right). \tag{2.85}$$

For small undercoolings, i.e., when the current temperature is close to the equilibrium temperature, the variation of enthalpy and entropy with temperature could be assumed to be negligible [48, 106, 107]. Thus, we can express that:

$$\Delta H^{\gamma\alpha} \approx \Delta H^{\gamma\alpha}_{eq}; \quad \Delta S^{\gamma\alpha} \approx \Delta S^{\gamma\alpha}_{eq}. \tag{2.86}$$

So with the above approximations, using Eq.2.84, the driving pressure in Eq.(2.85) could be rewritten as:

$$\Delta G_{\gamma\to\alpha} = \Delta S^{\gamma\alpha}\Delta T + \left[\left.\frac{\partial G^{\gamma}_{eq}}{\partial x_i}\right|_{x_i^{\gamma}} - \left.\frac{\partial G^{\gamma}}{\partial x_i}\right|_{x_i^{\gamma}} \right] \left(x_i^{\gamma} - x_i^{\alpha}\right). \tag{2.87}$$

The difference in derivatives in the second term represents the variation in the slopes of the tangent line to the G^{γ} curve at a fixed concentration of x_i^{γ} for a variation (undercooling) of ΔT. When ΔT is small, this variation of the slopes in Eq.(2.87) could be neglected and hence the driving pressure could be approximated as:

$$\Delta G_{\gamma\to\alpha} \approx \Delta S^{\gamma\alpha}\Delta T. \tag{2.88}$$

This approximation of the driving pressure has been considered in [45, 48, 51, 52, 104] where they simply assume that the driving pressure is proportional to the small undercooling ΔT. As highlighted previously, the phase diagram is linearized at some reference temperature T^R, and ΔT is extrapolated using this linearization as a function of temperature and local concentrations. So, following Fig.2.24, for each linearized solvus line, we can express,

$$\begin{aligned} T^{eq}_{\alpha} &= T^R + m^{\alpha/(\alpha+\gamma)}_{A-i}\left(x_i^{\alpha} - \left.x_i^{\alpha}\right|_R\right) \\ T^{eq}_{\gamma} &= T^R + m^{\gamma/(\alpha+\gamma)}_{A-i}\left(x_i^{\gamma} - \left.x_i^{\gamma}\right|_R\right), \end{aligned} \tag{2.89}$$

where $m^{\alpha/(\alpha+\gamma)}_{A-i}$ and $m^{\gamma/(\alpha+\gamma)}_{A-i}$ are the slopes of the boundary lines of the α and γ phases respectively, linearized at T^R, and $\left.x_i^{\alpha}\right|_R$ and $\left.x_i^{\gamma}\right|_R$ are the corresponding equilibrium concentrations of solute i at T^R. These are deduced by thermodynamic evaluations using ThermoCalc software [103].

The equilibrium temperature, T^{eq}, can be expressed as the average of T^{eq}_{α} and T^{eq}_{γ}:

$$T^{eq} = \frac{T^{eq}_{\alpha} + T^{eq}_{\gamma}}{2}. \tag{2.90}$$

So, making use of the two Eqs.in (2.89), the undercooling can be expressed as:

$$\Delta T = T^{eq} - T = T^R + 0.5m^{\alpha/(\alpha+\gamma)}_{A-i}\left(x_i^{\alpha} - \left.x_i^{\alpha}\right|_R\right) + 0.5m^{\gamma/(\alpha+\gamma)}_{A-i}\left(x_i^{\gamma} - \left.x_i^{\gamma}\right|_R\right) - T. \tag{2.91}$$

The driving pressure in Eq.(2.88) can thus be formulated as a function of the local concentrations and temperature as follows:

$$\begin{aligned} \Delta G_{\gamma\to\alpha}(T, x_i^{\alpha}, x_i^{\gamma}) = \Delta S^{\gamma\alpha}\Big[&(T^R - T) + 0.5m^{\alpha/(\alpha+\gamma)}_{A-i}\left(x_i^{\alpha} - \left.x_i^{\alpha}\right|_R\right) \\ &+ 0.5m^{\gamma/(\alpha+\gamma)}_{A-i}\left(x_i^{\gamma} - \left.x_i^{\gamma}\right|_R\right)\Big]. \end{aligned} \tag{2.92}$$

With the help of Eqs.(2.12) and (2.14), the above description could be further expressed as a function of the total concentration variable, $x_i(\boldsymbol{x}, t)$, for each configuration of the phase-field function, $\phi(\boldsymbol{x}, t)$:

$$\begin{aligned}\Delta G_{\gamma\to\alpha}(T, x_i) = \Delta S^{\gamma\alpha}\Bigg[T^R - T + 0.5m_{A-i}^{\alpha/(\alpha+\gamma)}\left(\frac{k_p^i x_i}{1+\phi(k_p^i-1)} - x_i^\alpha\big|_R\right)\\ + 0.5m_{A-i}^{\gamma/(\alpha+\gamma)}\left(\frac{x_i}{1+\phi(k_p^i-1)} - x_i^\gamma\big|_R\right)\Bigg]\end{aligned} \tag{2.93}$$

Based on the same linearization, the equilibrium concentrations of solute i of each phase at temperature T can be estimated as follows:

$$x_i^j\Big|_{eq} = x_i^j\Big|_R + \frac{T - T^R}{m_{A-i}^{j/(\alpha+\gamma)}}, \quad \forall j \in \{\alpha, \gamma\}. \tag{2.94}$$

Using Eqs.(2.94), the equilibrium partitioning ratio (k_p^i) can be expressed at each temperature T as:

$$k_p^i(T) = \frac{x_i^\alpha\big|_R + \frac{T-T^R}{m_{A-i}^{\alpha/(\alpha+\gamma)}}}{x_i^\gamma\big|_R + \frac{T-T^R}{m_{A-i}^{\gamma/(\alpha+\gamma)}}}. \tag{2.95}$$

In the description of the driving pressure in Eq.(2.93), the entropy difference ($\Delta S^{\gamma\alpha}$) at the current temperature T could be extrapolated using a linearization based on the thermodynamic data extracted at the T^R temperature and the entropy difference at the T^{A3} temperature ($\Delta S_{A3}^{\gamma\alpha}$) of the $\gamma \longrightarrow \alpha$ phase transformation. As a reminder, the T_{A3} temperature (corresponding to the nominal composition, x_i^0) is the temperature at which the γ phase starts to transform into the α phase. A linear extrapolation of $\Delta S^{\gamma\alpha}$ may be of the form:

$$\Delta S^{\gamma\alpha}(T) = \Delta S_R^{\gamma\alpha} + \frac{\Delta S_{A3}^{\gamma\alpha} - \Delta S_R^{\gamma\alpha}}{T_{A3} - T^R}\left(T - T^R\right), \tag{2.96}$$

where $\Delta S_R^{\gamma\alpha}$ is the entropy difference between the two phases at the reference temperature, T^R. The above extrapolation could be avoided if T^R is chosen to be equal to the current temperature, T.

In the works of Tiaden et al. [45], Mecozzi et al. [51] or Militzer et al. [52], a single reference temperature was used to linearize the solvus lines in the phase diagram. It is evident from the Fig.2.24 that, to better capture the topology of the solvus lines and for better description of the driving pressure, the phase boundary lines need to be piecewise linearized using multiple reference temperatures ($T_{R_1}, T_{R_2}, ..., T_{R_n}$) along the thermal path of the transformation. This is especially important when the solvus lines curve extensively such that the assumption of linear variation of equilibrium concentrations with the temperature becomes weak. This also allows for an interpolated expression for $\Delta S^{\gamma\alpha}$ between any two reference temperatures (T_{R_l}, T_{R_u}) such that $T_{R_l} \leq T \leq T_{R_u}$:

$$\Delta S^{\gamma\alpha}(T) = \Delta S_{R_u}^{\gamma\alpha} + \frac{\Delta S_{R_u}^{\gamma\alpha} - \Delta S_{R_l}^{\gamma\alpha}}{T^{R_u} - T^{R_l}}\left(T - T^{R_u}\right), \tag{2.97}$$

Ternary system: If we consider a ternary system, A-C-X, with nominal compositions of (x_C^0, x_X^0), the driving pressure under ortho-equilibrium (full local equilibrium) conditions can be again derived by locally linearizing the ternary phase diagram at T^R. If $\left(x_i^j\Big|_R, \ \forall j \in \{\alpha,\gamma\} \text{ and } \forall i \in \{C,X\}\right)$ are the equilibrium concentrations extracted at T^R, we first extract the isopleth plots (a section of a ternary phase diagram extracted by fixing the composition of one component) or pseudo-binary plots and then linearize the respective solvus lines as seen previously. As an example, we set $x_X = x_X^\alpha\big|_R$, and extract the pseudo-binary A-C plot to linearize the $\alpha/(\alpha+\gamma)$ solvus line. Similarly, the $\alpha/(\alpha+\gamma)$ solvus line of the A-X isopleth plot is linearized by setting $x_C = x_C^\alpha\big|_R$. Likewise for the $\gamma/(\alpha+\gamma)$ phase boundary lines by setting $x_X = x_X^\gamma\big|_R$ and $x_C = x_C^\gamma\big|_R$. We thus extract the slopes of these linearized diagrams: $m_{A-C}^{\alpha/(\alpha+\gamma)}, m_{A-X}^{\alpha/(\alpha+\gamma)}, m_{A-C}^{\gamma/(\alpha+\gamma)}, m_{A-X}^{\gamma/(\alpha+\gamma)}$. The equilibrium temperature corresponding to the current interface concentrations could then be expressed as:

$$T^{eq} = T^R + 0.5 \sum_{i\in\{C,X\}} \sum_{j\in\{\alpha,\gamma\}} m_{A-i}^{j/(\alpha+\gamma)} \left(x_i^j - x_i^j\Big|_R\right) \tag{2.98}$$

The driving pressure under ortho-equilibrium conditions for a ternary system could thus be expressed in the following way in the form of total concentration variables as in Eq.(2.93):

$$\begin{aligned}\Delta G_{\gamma\to\alpha}(T, x_C, x_X) = \Delta S^{\gamma\alpha}\left(T^R - T\right) + 0.5\Delta S^{\gamma\alpha} \sum_{i\in\{C,X\}} \Bigg[& m_{A-i}^{\alpha/(\alpha+\gamma)}\left(\frac{k_p^i x_i}{1+\phi(k_p^i - 1)} - x_i^\alpha\big|_R\right) \\ & + m_{A-i}^{\gamma/(\alpha+\gamma)}\left(\frac{x_i}{1+\phi(k_p^i - 1)} - x_i^\gamma\big|_R\right)\Bigg].\end{aligned} \tag{2.99}$$

If rather para-equilibrium (PE) conditions (as discussed in 1.2.1.2) are assumed such that the solute element X does not partition between the γ and the α phases, the driving pressure is derived by extracting a para-equilibrium quasi-binary phase diagram ($[A-C]_{PE}$) and locally linearizing it. The solute element X does not explicitly contribute to the driving pressure for the transformation ($\Delta G_{\gamma\to\alpha}$). The thermodynamic data are extracted from ThermoCalc by imposing para-equilibrium constraints. The driving pressure is expressed as:

$$\begin{aligned}\Delta G_{\gamma\to\alpha}^{PE}(T, x_C) = \Delta S_{PE}^{\gamma\alpha}\Bigg[& T^R - T + 0.5 m_{[A-C]_{PE}}^{\alpha/(\alpha+\gamma)}\left(\frac{k_p^C x_C}{1+\phi(k_p^C - 1)} - x_C^\alpha\big|_R^{PE}\right) \\ & + 0.5 m_{[A-C]_{PE}}^{\gamma/(\alpha+\gamma)}\left(\frac{x_C}{1+\phi(k_p^C - 1)} - x_C^\gamma\big|_R^{PE}\right)\Bigg],\end{aligned} \tag{2.100}$$

where $m_{[A-C]_{PE}}^{\alpha/(\alpha+\gamma)}$ and $m_{[A-C]_{PE}}^{\gamma/(\alpha+\gamma)}$ are the slopes of the linearized imaginary solvus lines constructed under PE assumptions, while $x_C^\alpha\big|_R^{PE}$ and $x_C^\gamma\big|_R^{PE}$ are the corresponding constrained equilibrium concentrations at T^R.

2.3.4.1 ThermoCalc coupling

For the early part of this thesis, the coupling with ThermoCalc to extract the thermodynamic data was manual. This limited the number of reference temperatures at which the data could be extracted (generally 1 to 3 reference points). In addition, the ThermoCalc console or its graphical user interface does not allow for seamless calculation of certain thermodynamic data under para-equilibrium conditions. Thus, for the later part of this thesis, the above difficulties motivated to establish or develop a successful liason between the numerical model and the TQ-interface (SDK) of ThermoCalc to enable automatic and fluid computation of relevant thermodynamic data over a large set of reference points under both ortho-equilibrium (OE) as well as para-equilibrium (PE) conditions.

Fig.2.25 gives a general overview of the ThermoCalc coupling framework using the TQ-interface. For a given alloy system and a corresponding thermodynamic database name (supported by ThermoCalc), the desired thermodynamic conditions at which the thermodynamic data are sought after are passed as inputs from the numerical model to the ThermoCalc coupling interface. The first step consists of initializing the computation workspace of ThermoCalc, involving allocation of memory for computations, definition of the given alloy system, loading its thermodynamic database, definition of phases in play (setting the status of relevant phases as "entered" to take part in the computation), and setting up the numerical handles to support the calculation. The next process is to set up the thermodynamic conditions of the system such as the temperature, pressure, nominal solute concentrations, and the number of moles in the system. A primary full local equilibrium calculation is performed based on the minimization of Gibbs free energy. Following this preliminary equilibrium computation, the necessary thermodynamic data are extracted/ calculated depending on the type of equilibrium conditions imposed. The process of thermodynamic data extraction using the TQ-interface in the coupling model has been elaborated in the appendix-B, and interested readers are encouraged to refer it for more details. The coupling model is capable of providing a matrix of desired thermodynamic data for a given range of temperatures over a large set of points. The ThermoCalc data extraction is usually performed as a pre-processing step in the numerical framework. The discrete and rich thermodynamic data-set generated is then exploited in the computational loop with the help of an interpolation model which helps to interpolate the necessary thermodynamic data for any temperature T at each time step. So, it basically implies that the phase diagram is locally linearized at the current temperature, $T^R = T$. This is of great importance as a local piecewise linearization helps to accurately capture any strong topological evolution of the solvus surfaces (or lines) in a phase diagram, especially for non-isothermal or continuous cooling transformation involving a long thermal path ($T_{initial} - T_{final}$). This helps to enrich the driving pressure ($\Delta G_{\gamma \rightarrow \alpha}$) description that is based on strong assumptions and potentially minimize errors.

2.3.5 Nucleation model

As discussed in Chapter-1 (1.2.1.1.1), the literature encompasses various hypotheses and a range of parameters aimed at characterizing nucleation events in phase transformation. These parameters include the nucleation start temperature (T_{N_s}), nucleation temperature range (δT_N), shield distance (δl_N), shield time (δt_N), parameters related to the nucleus shape, along with factors such as composition based on local parent phase features, etc., among numerous others. Additionally, adhering to the CNT introduces supplementary parameters such as incubation time, frequency factor, etc. However, due to experimental constraints in observing nucleation events, quantifying most of these parameters independently presents significant challenges. Precise modeling of a nucleation event at the mesoscopic scale is complex, often more suitable for much lower scales

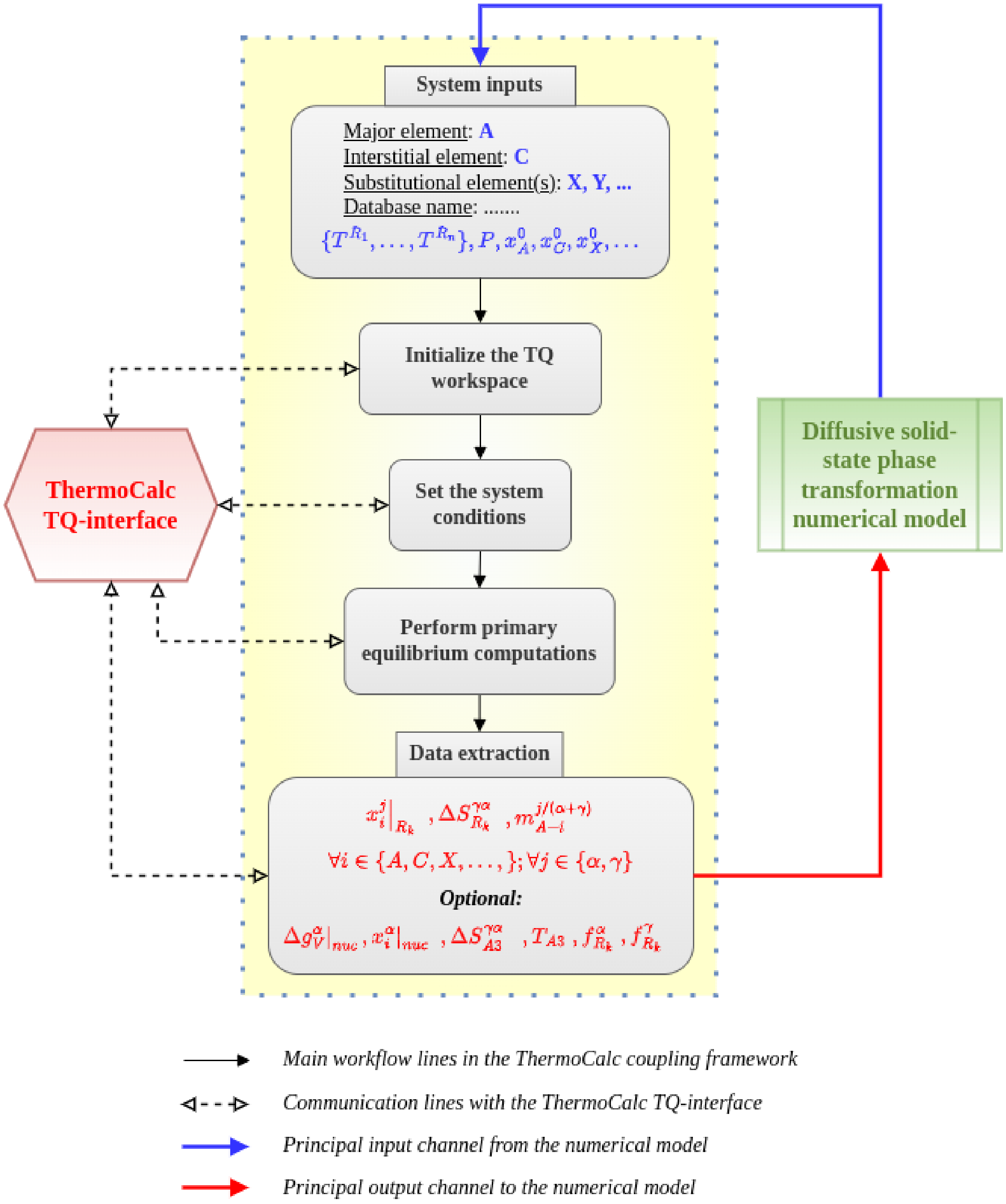

Figure 2.25: General overview of the ThermoCalc coupling with the numerical model

of modeling, such as atomistic simulations. Hence, in this study, a simplified approach will be employed, aiming for potential refinements in subsequent research. The nucleus shape will be assumed to be spherical, and only a select few parameters from the aforementioned list will be taken into account.

In many cases, the critical radii of nuclei are significantly smaller compared to the size of the considered domain. Consequently, due to the substantial computational demands required for accurately capturing these small nuclei, they are rarely precisely prescribed at their critical radii. A minimum radius is set as a requirement based on the underlying mesh resolution. Additionally, to prevent uncharacteristically large nuclei, a maximum size is imposed. So, the numerical radius of a nucleus (r^*_{num}) in this model is based on the following law:

$$r^*_{num} = \min\left(\max\left(r^*_{th}, k_1 h_{min}\right), k_2 h_{min}\right), \tag{2.101}$$

where r^*_{th} is the theoretically estimated critical radius, h_{min} is the minimum size of the underlying mesh resolution, k_1 is a constant governing the minimum number of mesh elements to be included along the radius, and $k_2(> k_1)$ represents another constant limiting the maximum size permissible for a nucleus. The theoretical critical radius technically depends on the site of nucleation, however in this context, it is roughly estimated as follows:

$$r^*_{th} = \frac{(d_i - 1)\sigma_{\gamma\alpha}}{\Delta g^{\alpha}_{V}}, \tag{2.102}$$

where d_i denotes the dimensionality, and $\Delta g^{\alpha}_{V}(T)$ is the driving pressure for nucleation at the current temperature. This driving pressure can be extracted during the pre-processing stage, thanks to the ThermoCalc coupling, and subsequently interpolated at any temperature as previously discussed.

The nucleation start temperature is a challenging variable to quantify as its precise value cannot be predicted through experimental observations. Typically, as the temperature decreases below the T_{A3} transformation temperature, the available driving pressure for the nucleation of the stable phase increases. Considering capillarity aspects, the likelihood of a critical nucleus forming near the T_{A3} temperature is relatively low. Conversely, as the temperature decreases further, with more driving pressure available, the probability increases. Hence, it's reasonable to hypothesize that T_{N_s} is generally offset by some margin from the transformation temperature. This difference between the transformation temperature and the nucleation start temperature is generally referred to as the nucleation undercooling ($\Delta T_N = T_{A3} - T_{N_s}$). In practical terms, T_{N_s} is often chosen based on the temperature at which a certain initial percentage of the product phase fraction is experimentally observed, as noted in works like [108].

The nucleation temperature range is a crucial parameter defining the span within which nucleation is expected to occur. In a study by Offerman et al. [109] investigating nucleation, they highlighted a correlation between the cooling rate and this temperature range. Specifically, they observed that δT_N becomes more noticeable with higher cooling rates while being comparatively smaller at lower cooling rates. Moreover, their findings suggest the existence of a distinct temperature range even at extremely low cooling rates, implying a preference for continuous mode of nucleation over site-saturated scenarios (where $\delta T_N = 0$). δT_N is generally assumed to be a modeling parameter [108] to fit with the relevant experimental results.

The shield distance, as discussed in [108], serves as an inter-nucleation distance parameter shielding the pre-existing nucleus from the formation of additional nuclei in its proximity. One of the physical perspectives behind this parameter is that upon nucleus formation, the surrounding local region becomes less conducive to further nucleation due to subsequent changes in local characteristics, such as solute distribution. Nevertheless, it remains a challenging parameter to consistently quantify due to the lack of substantial physical underpinning, thus primarily serving as a modeling parameter. In the current model, at any instant t, δl_N is taken as, $\delta l_N(t) = k_{sh} r^*_{num}(t)$, where k_{sh} is a shield distance factor. In [108], an additional parameter known as the shield time is utilized which shields the local region around a nucleus, characterized by δl_N, for a certain duration of time before any more nucleation could take place. This parameter is not considered in our model in this work.

The nucleation density (ρ_N), which signifies the number of nuclei per unit volume of the domain, may be estimated using the expected final fraction of the product phase (e.g., f_f^α) and its anticipated average grain size (r_α^f) as outlined in [108]:

$$\rho_N = \frac{3 f_f^\alpha}{4\pi (r_\alpha^f)^3}. \tag{2.103}$$

In 2D, the above relation gets modified to $\rho_N = \frac{f_f^\alpha}{\pi (r_\alpha^f)^2}$. At present, the current model employs a constant nucleation rate for the continuous nucleation scenario. The implementation of CNT has not been included in this work. Considering ρ_N, the approximate number of nuclei can be estimated as $n_N \approx \rho_N V_0$, where V_0 represents the total volume of the domain (or area A_0 in 2D). Utilizing n_N and δT_N, the nucleation rate can be estimated using the cooling rate ($\dot{T}$) as follows:

$$\dot{n_N} = \frac{n_N \dot{T}}{\delta T_N}. \tag{2.104}$$

Hence, $\dot{n_N}$ provides an estimation of the number of nuclei to be introduced per second. It's viable to distribute the number of nuclei to be introduced every second across multiple nucleation checks, enhancing continuity, based on the chosen time step (Δt).

In terms of spatial preference, the most favored sites for nucleating the new phase are the grain corners (triple junctions in 2D, quadruple junctions in 3D), succeeded by grain edges and surfaces. At lower cooling rates, the preference is for grain corners. However, at higher cooling rates, the nucleation density notably rises, increasing the likelihood of saturating the grain corners. This situation consequently opens opportunities for nucleation on grain edges and surfaces [108, 109]. From a modeling perspective, to indicate the sites (and their computational nodes) available for nucleation, a site characteristic function (χ_{sn}) is used:

$$\chi_{sn}(\boldsymbol{x}, t) = \begin{cases} 1 & \text{if } \boldsymbol{x} \in \text{Choice of nucleation site} \\ 0 & \text{otherwise} \end{cases}, \quad \forall t \mid T_{N_s} - \delta T_N < T(t) \leq T_{N_s}. \tag{2.105}$$

If the chosen nucleation site is the grain boundaries, then $\chi_{sn}(\boldsymbol{x}, t) = \chi_{\gamma\gamma}$ qualifies all eligible nodes on the γ-phase grain boundaries. Alternatively, when opting for the nucleation site as the grain corners, the nodes are qualified as follows:

```
Require: $\epsilon_{MJ}, \varphi_i$
  count $\leftarrow 0$
  $i \leftarrow 0$
  for $\boldsymbol{x}$ in $\Omega$ do
    while $i < N_{LS}$ do
      if $|\varphi_i(\boldsymbol{x})| \leq \epsilon_{MJ}$ then
```

```
            count ← count + 1
        end if
    end while
    if count $\geq d_i + 1$ then                                    ▷ $d_i$ is the dimensionality
        $\chi_{sn}(\boldsymbol{x}) \leftarrow 1$
    else
        $\chi_{sn}(\boldsymbol{x}) \leftarrow 0$
    end if
end for
```

Here, ϵ_{MJ} represents a small distance threshold around the multiple junction. In 3D, if a node has at least 4 GLS functions that meet the condition, it qualifies as a multi-junction node available for nucleation. In 2D, the equivalent criterion is fulfilled with 3 GLS functions. A similar criterion can be applied to qualify grain edge nodes in 3D, where the condition is met by 3 GLS functions. Fig.2.26 gives a 2D representation of the small localized region in green around the triple junction satisfying the above condition and hence the nodes within this zone are provisionally qualified as eligible sites. The site characteristic function is however utilized in conjunction with the shield distance, δl_N, to further filter out nodes that are ineligible (i.e., $\varphi_\alpha(\boldsymbol{x}) \geq -\delta l_N$) for nucleation. The shielded zone and the nodes within it are highlighted in red. So, eventually one of the nodes within the green zone is shielded and hence marked as ineligible for nucleation in red.

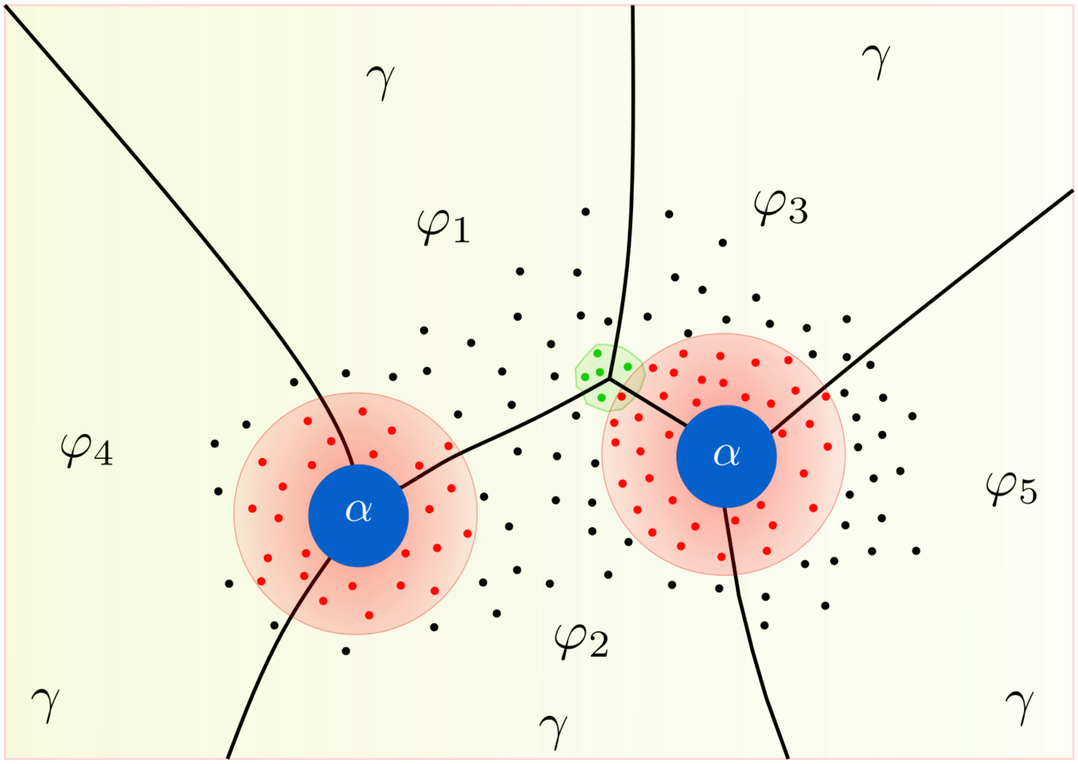

Figure 2.26: Illustration of nucleation site eligibility characterization for grain corners: eligible nodes (green), shielded ineligible nodes (red)

Once a nucleus is created, its introduction triggers the local change of status of the phase through the χ_α function, subsequently altering the local diffusivity field. Following this change, the solute redistribution equation is permitted to naturally modify the local composition. Thus, the local composition isn't manually altered upon nucleus introduction to avoid tampering with the solute mass conservation. At the time of creation, the newly formed nucleus is dynamically integrated into one of the existing GLS functions, φ_i, while respecting the necessary conditions laid out to avoid numerical coalescence outlined in 2.2.1. In the scenario where none of the current GLS functions are eligible to accommodate the nucleus, a new GLS function is created. As χ_α and φ_i undergo updates, the associated dependent fields, including φ_α, ϕ, etc., are correspondingly modified.

All of the concepts outlined above are consolidated and depicted in the Fig.2.27.

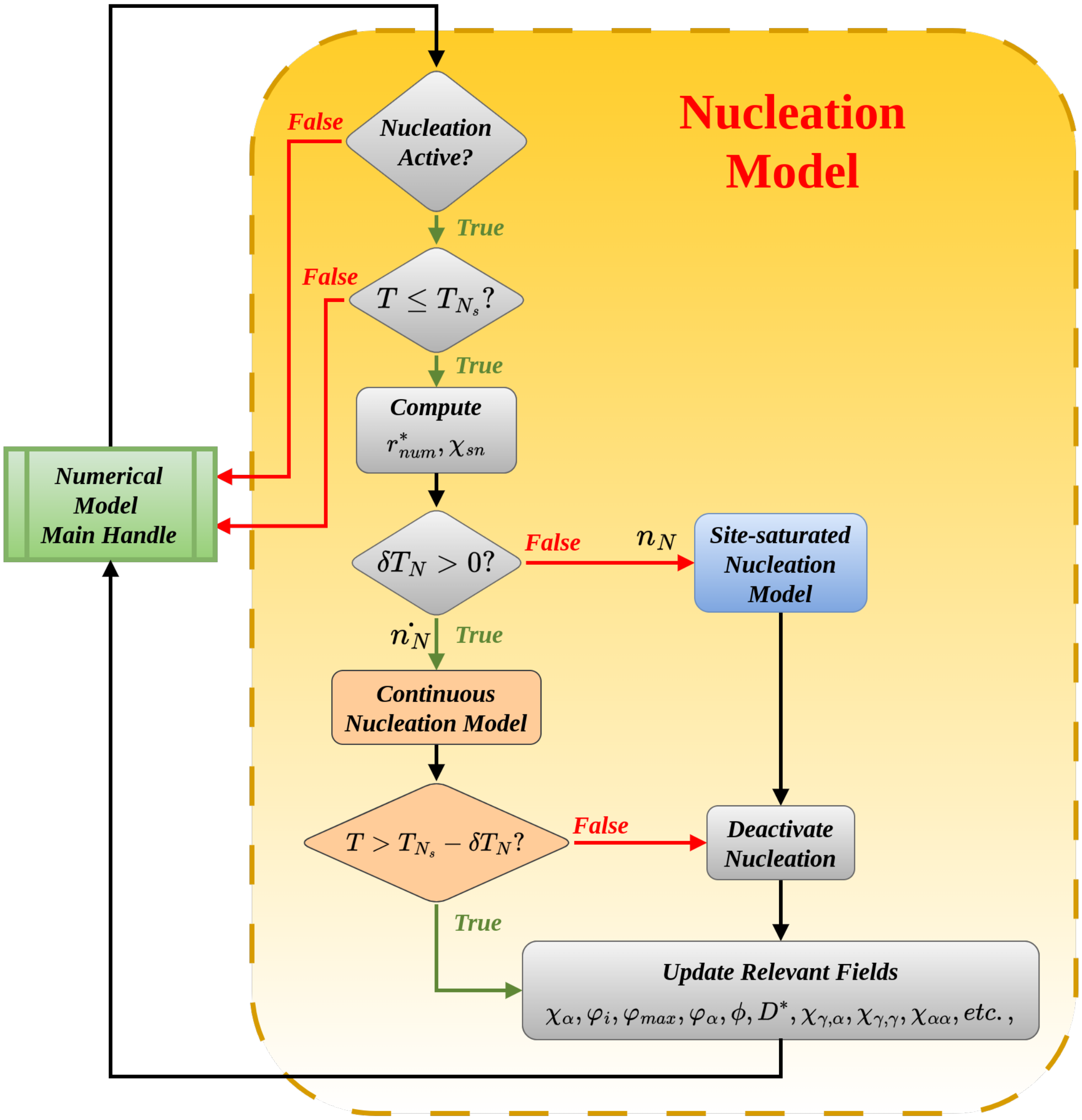

Figure 2.27: General workflow of the nucleation model

2.4 Summary

A finite element (FE) based full-field numerical model is presented, primarily used to simulate diffusive solid-state phase transformation (DSSPT) at the mesoscopic scale in a two phase metallic material. The full-field approach enables tracking the topological evolution of the grain/phase interface network in the microstructure during the transformation process. Among the various full-field approaches available to follow the topological evolution, level-set (LS) method has been adopted in this numerical framework. LS method belongs to the category of front-capturing methods, where the migrating interfaces are implicitly represented with the help of a continuous field variable. In the current work, this continuous field variable (known as the level-set function) is defined as a signed Euclidean distance from the interface of interest, such that the function is positive inside the grain and negative outside the grain while taking 0 at the interface. The LS description is coupled with the physics of diffusive phase transformation, which prescribes the interface kinetics to an LS transport equation that governs the resulting interface network migration. In a polycrystalline context with multiple grains in the microstructure, instead of employing the numerically expensive classical approach of using one LS function per grain, a grain coloration scheme is used. This scheme helps represent a set of grains that are fairly distant from each other under the same LS function. Such an LS function representing a family of grains is referred to as a global level-set (GLS) function. In the event of two or more grains of the same GLS function coming close to each other, to avoid numerical coalescence, provisions for grain recoloration are provided. The grain recoloration model aims to swap the GLS functions of those grains that have the potential for numerical coalescence.

LS based DSSPT modeling involves two critical stages: solute redistribution governed by a diffusion equation, and resulting grain/phase interface network migration governed by an LS transport equation. To be able to resolve a single diffusion equation in the whole computational domain without explicit consideration of the phase interface jump conditions, we adopt a diffuse interface hypothesis by using a tangent hyperbolic LS function. However, for the resolution of the LS transport equation, we revert to a classical LS function description. A generalized description for interface kinetics is presented for a biphasic polycrystalline context, capable of simultaneously taking into account various phenomena along with phase transformation. The contribution of solute drag effects to the interface kinetics due to the presence of any substitutional elements in the alloy is taken into account using the Cahn's simplified description of the solute drag pressure. The non-linearity in the description of kinetics introduced by solute drag effects are linearized through a reasonable approximation. To improve computational efficiency, a particular adaptive meshing and remeshing strategy has been employed. This technique ensures that the mesh refinement is more detailed near the phase interfaces, while it remains somewhat coarser near the grain interfaces involving the same phases. The driving pressure for diffusive phase transformation is assumed to be proportional to a small local undercooling, which is a measure of deviation from the local equilibrium temperature for the phase interface concentrations at the current temperature. The undercooling is formulated by locally linearizing the phase diagram using a thermodynamic database such as the ThermoCalc software. To enrich this driving pressure description, a coupling between ThermoCalc and the numerical model has been established using the TQ-interface (SDK) of ThermoCalc. Such a coupling helps to extract a large thermodynamic data-set that could be used for piecewise linearization of the phase diagram. Nucleation modeling adopts a simplistic approach with spherical-shaped nuclei, acknowledging the challenges in precisely describing the nucleation events at the mesoscopic scale.

The numerical simulations are carried out with unstructured triangular meshes with a P1 interpolation, and using an implicit backward Euler time scheme for the time discretization. Each system linked to Eq.(2.23) and the weak formulation of Eqs.(2.58) is assembled using typical P1 finite elements with a Streamline Upwind Petrov-Galerkin (SUPG) stabilization for the convective terms [110]. The boundary conditions applied to the GLS functions are classical null Neumann BCs, while the solute concentration field is generally imposed with Robin-type conditions. Fig.2.28 presents a general outline of the numerical framework highlighting the key stages and tasks involved. As a part of pre-processing tasks, given the thermodynamic conditions involved during the phase transformation, a thermodynamic data-set is generated using the ThermoCalc coupling interface. The geometry, the initial grain morphology and the corresponding adaptive mesh is generated. The grain coloration scheme described in section 2.2.1 is used to represent the microstructure and initialize the GLS functions. The various characteristic functions and other relevant fields for the initial grain/phase morphology are computed. The nucleation model is invoked to check for nucleation at the initial conditions depending on the type of nucleation and its characteristics chosen. In the event of nucleation, the relevant fields/ functions are updated, the FE mesh is adapted again to any nuclei generated. The total concentration variable of the solute for the initial equilibrium is computed in the domain using Eq.(2.12). The computational loop begins by computing any temperature dependent diffusion and interface parameters. The first critical stage involves the FE resolution of the convective-diffusive-reactive equation in (2.20) for solute redistribution. An interpolation model is used to interpolate the necessary thermodynamic data at the current temperature (using the data-set built during the pre-processing step) to facilitate the computation of the phase transformation kinetics resulting from solute partitioning. Along with the driving pressure due to the diffusive phase transformation, the other forms of driving pressures (depending on the various phenomena considered) responsible for the microstructural evolution are constructed. The interface migration kinetics constructed are then prescribed into the LS transport equation. The convective-diffusive equation in (2.58) is then resolved to obtain the resultant grain/phase interface network migration. This step constitutes another critical stage in this numerical framework. Post this resolution, a numerical treatment is performed on the LS functions using the Eqs.(2.71) to avoid any kinematic incompatibilities as discussed in 2.3.3. It is then followed by a reinitialization (2.2) procedure of the LS functions to restore the property of a signed distance function. The interface characteristic functions, the phase characteristic functions, and other relevant fields are updated for the modified grain morphology. Necessary grain statistics such as the mean grain size, grain size distribution of each phase, phase fractions and other output data relevant for post-processing are computed at that instant. The grain recoloration model is invoked to swap the GLS functions of those grains under the risk of numerical coalescence (2.2.1). The computational loop at any instant ends with a provision for adaptive remeshing if necessary. The following computational loop begins by checking for nucleation again depending on the thermodynamic conditions at that instant and also depending on the chosen nucleation model. If any new nuclei are generated, the relevant fields are updated, and the rest of the process in a computational loop repeats. The computation proceeds until the imposed end time is reached. First illustrations of this global FE resolution scheme are proposed in the next chapter.

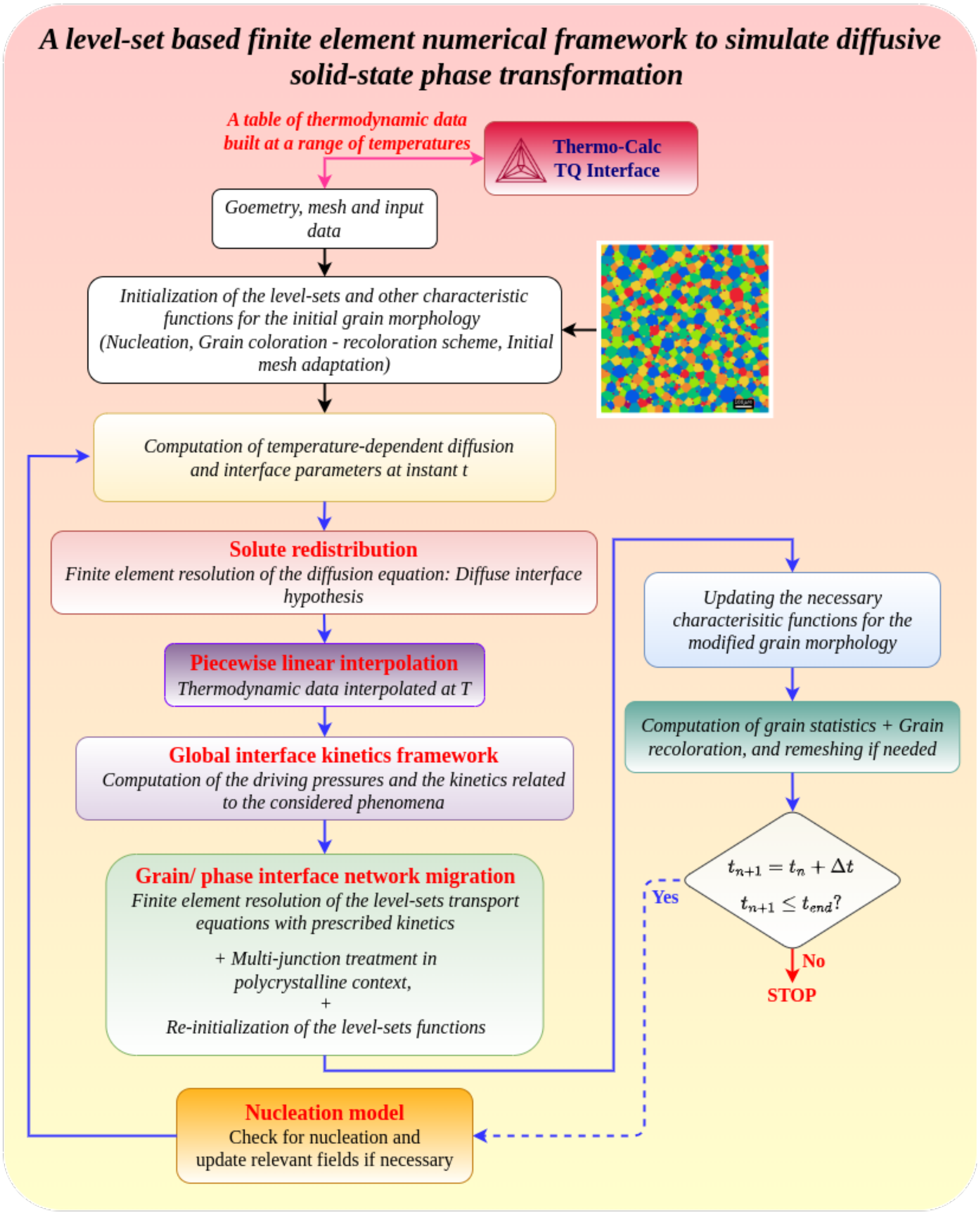

Figure 2.28: General overview of the numerical framework

References

[1] C. Zener. "Theory of growth of spherical precipitates from solid solution". In: *Journal of applied physics* 20.10 (1949), pp. 950–953.

[2] S.F. Medina and C.A. Hernandez. "Modelling of the dynamic recrystallization of austenite in low alloy and microalloyed steels". In: *Acta materialia* 44.1 (1996), pp. 165–171.

[3] J. Sietsma and S. van der Zwaag. “A concise model for mixed-mode phase transformations in the solid state”. In: *Acta Materialia* 52.14 (2004), pp. 4143–4152.

[4] H. Chen and S. van der Zwaag. “Modeling of soft impingement effect during solid-state partitioning phase transformations in binary alloys”. In: *Journal of materials science* 46.5 (2011), pp. 1328–1336.

[5] M.G. Mecozzi, C. Bos, and J. Sietsma. “A mixed-mode model for the ferrite-to-austenite transformation in a ferrite/pearlite microstructure”. In: *Acta Materialia* 88 (2015), pp. 302–313.

[6] H. Li et al. “Non-isothermal phase-transformation kinetics model for evaluating the austenization of 55CrMo steel based on Johnson–Mehl–Avrami equation”. In: *Materials & Design* 92 (2016), pp. 731–741.

[7] M. Avrami. “Kinetics of phase change. I General theory”. In: *The Journal of chemical physics* 7.12 (1939), pp. 1103–1112.

[8] A.N. Kolmogorov. “On the statistical theory of the crystallization of metals”. In: *Bull. Acad. Sci. USSR, Math. Ser* 1.3 (1937), pp. 355–359.

[9] J. William and R. Mehl. “Reaction kinetics in processes of nucleation and growth”. In: *Trans. Metall. Soc. AIME* 135 (1939), pp. 416–442.

[10] J.B. Leblond and J. Devaux. “A new kinetic model for anisothermal metallurgical transformations in steels including effect of austenite grain size”. In: *acta metallurgica* 32.1 (1984), pp. 137–146.

[11] M. Suehiro et al. “Application of mathematical model for predicting microstructural evolution to high carbon steels”. In: *ISIJ international* 32.3 (1992), pp. 433–439.

[12] J. Ronda and G.J. Oliver. “Consistent thermo-mechano-metallurgical model of welded steel with unified approach to derivation of phase evolution laws and transformation-induced plasticity”. In: *Computer Methods in Applied Mechanics and Engineering* 189.2 (2000), pp. 361–418.

[13] F. Montheillet, O. Lurdos, and G. Damamme. “A grain scale approach for modeling steady-state discontinuous dynamic recrystallization”. In: *Acta Materialia* 57.5 (2009), pp. 1602–1612.

[14] D.G. Cram et al. “Modelling discontinuous dynamic recrystallization using a physically based model for nucleation”. In: *Acta Materialia* 57.17 (2009), pp. 5218–5228.

[15] P. Bernard et al. “A two-site mean field model of discontinuous dynamic recrystallization”. In: *Materials Science and Engineering: A* 528.24 (2011), pp. 7357–7367.

[16] I. Milenin, M. Pernach, and M. Pietrzyk. “Application of the control theory for modelling austenite-ferrite phase transformation in steels”. In: *Computer Methods in Materials Science* 15.2 (2015), pp. 327–335.

[17] L. Maire et al. “A new topological approach for the mean field modeling of dynamic recrystallization”. In: *Materials & Design* 146 (2018), pp. 194–207.

[18] A. Seret et al. “A mean field model of agglomeration as an extension to existing precipitation models”. In: *Acta Materialia* 192 (2020), pp. 40–51.

[19] Y.M. Jin and A.G. Khachaturyan. “Atomic density function theory and modeling of microstructure evolution at the atomic scale”. In: *Journal of applied physics* 100.1 (2006), p. 013519.

[20] Y. Mishin, M. Asta, and J. Li. “Atomistic modeling of interfaces and their impact on microstructure and properties”. In: *Acta Materialia* 58.4 (2010), pp. 1117–1151.

[21] M. Biglari. “Simulation of the austenite-ferrite transformation; effect of applied stress”. In: (2013).

[22] K.G.F. Janssens et al. *Computational materials engineering: an introduction to microstructure evolution*. Academic Press, 2010.

[23] A. Rollett, G.S. Rohrer, and J. Humphreys. *Recrystallization and Related Annealing Phenomena*. Elsevier Science, 2017. ISBN: 9780080982694. URL: `https://books.google.fr/books?id=GhZETAEzYOIC`.

[24] M.A. Miodownik. “A review of microstructural computer models used to simulate grain growth and recrystallisation in aluminium alloys”. In: *Journal of Light Metals* 2.3 (2002), pp. 125–135.

[25] H. Hallberg. “Approaches to modeling of recrystallization”. In: *Metals* 1.1 (2011), pp. 16–48.

[26] X. Liu, H. Li, and M. Zhan. “A review on the modeling and simulations of solid-state diffusional phase transformations in metals and alloys”. In: *Manufacturing Review* 5 (2018), p. 10.

[27] M. Militzer. “Phase field modeling of microstructure evolution in steels”. In: *Current Opinion in Solid State and Materials Science* 15.3 (2011), pp. 106–115.

[28] D. Polychronopoulou et al. “Introduction to the level-set full field modeling of laths spheroidization phenomenon in α/β titanium alloys”. In: *International Journal of Material Forming* 12 (2019), pp. 173–183.

[29] J. Bruchon et al. “3D simulation of the matter transport by surface diffusion within a Level-Set context”. In: *European Journal of Computational Mechanics/Revue Européenne de Mécanique Numérique* 19.1-3 (2010), pp. 281–292.

[30] L. Barrales-Mora, G. Gottstein, and L.S. Shvindlerman. “Three-dimensional grain growth: Analytical approaches and computer simulations”. In: *Acta Materialia* 56 (Dec. 2008), pp. 5915–5926. DOI: 10.1016/j.actamat.2008.08.006.

[31] S. Florez et al. “A novel highly efficient Lagrangian model for massively multidomain simulation applied to microstructural evolutions”. In: *Computer Methods in Applied Mechanics and Engineering* 367 (2020), p. 113107.

[32] S. Florez et al. “Statistical behaviour of interfaces subjected to curvature flow and torque effects applied to microstructural evolutions”. In: *Acta Materialia* 222 (2022), p. 117459.

[33] C.E. Krill III and L.-Q. Chen. “Computer simulation of 3-D grain growth using a phase-field model”. In: *Acta Materialia* 50.12 (2002), pp. 3059–3075. ISSN: 1359-6454. DOI: https://doi.org/10.1016/S1359-6454(02)00084-8. URL: https://www.sciencedirect.com/science/article/pii/S1359645402000848.

[34] I. Steinbach. “Phase-field models in materials science”. In: *Modelling and Simulation in Materials Science and Engineering* 17 (July 2009), p. 073001. DOI: 10.1088/0965-0393/17/7/073001.

[35] D. Tourret, H. Liu, and J. LLorca. “Phase-field modeling of microstructure evolution: Recent applications, perspectives and challenges”. In: *Progress in Materials Science* 123 (2022), p. 100810.

[36] S. Osher and J.A. Sethian. “Fronts propagating with curvature-dependent speed: Algorithms based on Hamilton-Jacobi formulations”. In: *Journal of computational physics* 79.1 (1988), pp. 12–49.

[37] B. Merriman, J.K. Bence, and S. Osher. “Motion of multiple junctions: a level set approach”. In: *Journal of Computational Physics* 112 (1994), pp. 334–363.

[38] J.A. Sethian. *Level set methods and fast marching methods: evolving interfaces in computational geometry, fluid mechanics, computer vision, and materials science*. Vol. 3. Cambridge university press, 1999.

[39] S. Osher and R.P. Fedkiw. *Level set methods and dynamic implicit surfaces*. Vol. 1. Springer New York, 2005.

[40] M. Bernacki et al. “Level set framework for the numerical modelling of primary recrystallization in polycrystalline materials”. In: *Scripta Materialia* 58.12 (2008), pp. 1129–1132.

[41] X. Zhang, J.S. Chen, and S. Osher. “A multiple level set method for modeling grain boundary evolution of polycrystalline materials”. In: *Interaction and multiscale mechanics* 1.2 (2008), pp. 178–191.

[42] B. Scholtes et al. “New finite element developments for the full field modeling of microstructural evolutions using the level-set method”. In: *Computational Materials Science* 109 (Nov. 2015), pp. 388–398. DOI: 10.1016/j.commatsci.2015.07.042.

[43] A.A. Wheeler, W.J. Boettinger, and G.B. McFadden. “Phase-field model for isothermal phase transitions in binary alloys”. In: *Phys. Rev. A* 45 (10 May 1992), pp. 7424–7439. DOI: `10.1103/PhysRevA.45.7424`. URL: `https://link.aps.org/doi/10.1103/PhysRevA.45.7424`.

[44] I. Steinbach et al. “A phase field concept for multiphase systems”. In: *Physica D: Nonlinear Phenomena* 94.3 (1996), pp. 135–147. ISSN: 0167-2789. DOI: `https://doi.org/10.1016/0167-2789(95)00298-7`. URL: `https://www.sciencedirect.com/science/article/pii/0167278995002987`.

[45] J. Tiaden et al. “The multiphase-field model with an integrated concept for modelling solute diffusion”. In: *Physica D: Nonlinear Phenomena* 115.1 (1998), pp. 73–86. ISSN: 0167-2789. DOI: `https://doi.org/10.1016/S0167-2789(97)00226-1`. URL: `https://www.sciencedirect.com/science/article/pii/S0167278997002261`.

[46] D.-H. Yeon, P.-R. Cha, and J.-K. Yoon. “A phase field study for ferrite–austenite transitions under paraequilibrium”. In: *Scripta Materialia* 45 (Sept. 2001), pp. 661–668. DOI: `10.1016/S1359-6462(01)01077-6`.

[47] M. Hillert and J. Ågren. “On the definitions of paraequilibrium and orthoequilibrium”. In: *Scripta Materialia* 50.5 (2004), pp. 697–699.

[48] G. Pariser et al. “Simulation of the $\gamma - \alpha$ transformation using the phase-field method”. In: *Steel Research* 72 (Sept. 2001), pp. 354–360. DOI: `10.1002/srin.200100130`.

[49] *Micress, the microstructure evolution simulation software*. `http://www.micress.de/`.

[50] C.J. Huang, D.J. Browne, and S. McFadden. “A phase-field simulation of austenite to ferrite transformation kinetics in low carbon steels”. English. In: *Acta Materialia* 54.1 (2006), pp. 11–21. DOI: `10.1016/j.actamat.2005.08.033`.

[51] M.G. Mecozzi. “Phase field modelling of the austenite to ferrite transformation in steels”. PhD thesis. Delf University of Technology, 2006.

[52] M. Militzer et al. “Three-dimensional phase field modelling of the austenite-to-ferrite transformation”. In: *Acta Materialia* 54 (Sept. 2006), pp. 3961–3972. DOI: `10.1016/j.actamat.2006.04.029`.

[53] I. Kovačević and B. Šarler. “Solid-Solid Phase Transformations in Aluminium Alloys Described by a Multiphase-Field Model”. In: *Solidification and Gravity IV*. Vol. 508. Materials Science Forum. Trans Tech Publications Ltd, Jan. 2006, pp. 579–584. DOI: `10.4028/www.scientific.net/MSF.508.579`.

[54] A. Malik et al. “Phase-Field Modeling of Sigma-Phase Precipitation in 25Cr7Ni4Mo Duplex Stainless Steel”. In: *Metallurgical and Materials Transactions A* (July 2017). DOI: `10.1007/s11661-017-4214-7`.

[55] M. Tong, D. Li, and Y. Li. “A q-state Potts model-based Monte Carlo method used to model the isothermal austenite–ferrite transformation under non-equilibrium interface condition”. In: *Acta Materialia* 53.5 (2005), pp. 1485–1497. ISSN: 1359-6454. DOI: `https://doi.org/10.1016/j.actamat.2004.12.002`. URL: `https://www.sciencedirect.com/science/article/pii/S135964540400727X`.

[56] M. Varma et al. “Cellular automaton simulation of microstructure evolution during austenite decomposition under continuous cooling conditions”. In: *Bulletin of Materials Science* 24 (June 2001), pp. 305–312. DOI: `10.1007/BF02704927`.

[57] Y. Lan, D. Li, and Y. Li. “Modeling austenite decomposition into ferrite at different cooling rate in low-carbon steel with cellular automaton method”. In: *Acta Materialia - ACTA MATER* 52 (Apr. 2004), pp. 1721–1729. DOI: `10.1016/j.actamat.2003.12.045`.

[58] K. Bzowski, L. Rauch, and M. Pietrzyk. “Application of statistical representation of the microstructure to modeling of phase transformations in DP steels by solution of the diffusion equation”. In: *Procedia Manufacturing* 15 (2018), pp. 1847–1855.

[59] L. Maire. “Full field and mean field modeling of dynamic and post-dynamic recrystallization in 3D – Application to 304L steel”. Theses. Université Paris sciences et lettres, Nov. 2018. URL: https://pastel.archives-ouvertes.fr/tel-02418810.

[60] M. Bernacki, R.E. Logé, and T. Coupez. “Level set framework for the finite-element modelling of recrystallization and grain growth in polycrystalline materials”. In: *Scripta Materialia* 64.6 (2011), pp. 525–528.

[61] J. Fausty et al. “A novel level-set finite element formulation for grain growth with heterogeneous grain boundary energies”. In: *Materials & Design* 160 (2018), pp. 578–590. ISSN: 0264-1275. DOI: https://doi.org/10.1016/j.matdes.2018.09.050. URL: https://www.sciencedirect.com/science/article/pii/S0264127518307524.

[62] K. Alvarado et al. “A level set approach to simulate grain growth with an evolving population of second phase particles”. In: *Modelling and Simulation in Materials Science and Engineering* 29.3 (Mar. 2021), p. 035009. DOI: 10.1088/1361-651X/abe0a7. URL: https://hal.archives-ouvertes.fr/hal-03463482.

[63] K.-D. Liss et al. “In situ study of dynamic recrystallization and hot deformation behavior of a multiphase titanium aluminide alloy”. In: *Journal of applied physics* 106.11 (2009), p. 113526.

[64] S. Osher and R.P. Fedkiw. “Level set methods: an overview and some recent results”. In: *Journal of Computational physics* 169.2 (2001), pp. 463–502.

[65] D.L. Chopp. *Computing minimal surfaces via level set curvature flow*. University of California, Berkeley, 1991.

[66] M. Bernacki et al. “Finite element model of primary recrystallization in polycrystalline aggregates using a level set framework”. In: *Modelling and Simulation in Materials Science and Engineering* 17.6 (2009), p. 064006.

[67] J.A. Sethian. “Fast marching methods”. In: *SIAM review* 41.2 (1999), pp. 199–235.

[68] D. Adalsteinsson and J.A. Sethian. “The fast construction of extension velocities in level set methods”. In: *Journal of Computational Physics* 148.1 (1999), pp. 2–22.

[69] G.-S. Jiang and D. Peng. “Weighted ENO schemes for Hamilton–Jacobi equations”. In: *SIAM Journal on Scientific computing* 21.6 (2000), pp. 2126–2143.

[70] M. Shakoor et al. “An efficient and parallel level set reinitialization method–Application to micromechanics and microstructural evolutions”. In: *Applied Mathematical Modelling* 39.23-24 (2015), pp. 7291–7302.

[71] F. Aurenhammer. “Voronoi diagrams—a survey of a fundamental geometric data structure”. In: *ACM Computing Surveys (CSUR)* 23.3 (1991), pp. 345–405.

[72] T. Xu and M. Li. “Topological and statistical properties of a constrained Voronoi tessellation”. In: *Philosophical Magazine* 89.4 (2009), pp. 349–374.

[73] H. Imai, M. Iri, and K. Murota. “Voronoi diagram in the Laguerre geometry and its applications”. In: *SIAM Journal on Computing* 14.1 (1985), pp. 93–105.

[74] K. Hitti et al. “Precise generation of complex statistical Representative Volume Elements (RVEs) in a finite element context”. In: *Computational Materials Science* 61 (2012), pp. 224–238.

[75] M. Bernacki et al. *Numerical Modeling of Recrystallization in a Level Set Finite Element Framework for Application to Industrial Processes*. 2019.

[76] R.I. Saye and J.A. Sethian. “The Voronoi implicit interface method for computing multiphase physics”. In: *Proceedings of the National Academy of Sciences* 108.49 (2011), pp. 19498–19503.

[77] A. Zaitzeff, S. Esedoglu, and K. Garikipati. “On the voronoi implicit interface method”. In: *SIAM Journal on Scientific Computing* 41.4 (2019), A2407–A2429.

[78] B. Scholtes. “Development of an efficient level set framework for the full field modeling recrystallization in 3D”. PhD thesis. Université Paris sciences et lettres, 2016.

[79] G. Gonthier et al. “Formal proof–the four-color theorem”. In: *Notices of the AMS* 55.11 (2008), pp. 1382–1393.

[80] E. Olsson and G. Kreiss. “A conservative level set method for two phase flow”. In: *Journal of Computational Physics* 210.1 (2005), pp. 225–246. ISSN: 0021-9991. DOI: https://doi.org/10.1016/j.jcp.2005.04.007. URL: https://www.sciencedirect.com/science/article/pii/S0021999105002184.

[81] J.W. Cahn. “The impurity-drag effect in grain boundary motion”. In: *Acta metallurgica* 10.9 (1962), pp. 789–798.

[82] G.R. Purdy and Y.J.M. Brechet. “A solute drag treatment of the effects of alloying elements on the rate of the proeutectoid ferrite transformation in steels”. In: *Acta metallurgica et materialia* 43.10 (1995), pp. 3763–3774.

[83] J. Furstoss et al. “On the role of solute drag in reconciling laboratory and natural constraints on olivine grain growth kinetics”. In: *Geophysical Journal International* 224.2 (2021), pp. 1360–1370.

[84] M. Crouzeix. “Une méthode multipas implicite-explicite pour l’approximation des équations d’évolution paraboliques”. In: *Numerische Mathematik* 35.3 (1980), pp. 257–276.

[85] U.M. Ascher, S.J. Ruuth, and R.J. Spiteri. “Implicit-explicit Runge-Kutta methods for time-dependent partial differential equations”. In: *Applied Numerical Mathematics* 25.2-3 (1997), pp. 151–167.

[86] D.N. Ilin et al. “Full field modeling of recrystallization: Effect of intragranular strain gradients on grain boundary shape and kinetics”. In: *Computational Materials Science* 150 (2018), pp. 149–161. ISSN: 0927-0256. DOI: https://doi.org/10.1016/j.commatsci.2018.03.063. URL: https://www.sciencedirect.com/science/article/pii/S0927025618302222.

[87] B. Scholtes et al. “3D level set modeling of static recrystallization considering stored energy fields”. In: *Computational Materials Science* 122 (2016), pp. 57–71.

[88] V. Grand et al. “Modeling CDRX and MDRX during hot forming of zircaloy-4”. In: *Modelling and Simulation in Materials Science and Engineering* 31.8 (2023), p. 085008.

[89] C. Gruau. “Metric generation for anisotropic mesh adaptation, with numerical applications to material forming simulation”. PhD Thesis. École Nationale Supérieure des Mines de Paris, Dec. 2004. URL: https://pastel.archives-ouvertes.fr/pastel-00000989.

[90] J.I. Goldstein and E. Randich. “Variation of interface compositions during diffusion controlled precipitate growth in ternary systems”. In: *Metallurgical Transactions A* 8 (1977), pp. 105–109.

[91] K.J. Lee et al. “Mathematical modelling of transformation in Nb microalloyed steels”. In: *ISIJ international* 32.3 (1992), pp. 326–334.

[92] J. Ågren. “Computer simulations of diffusional reactions in complex steels”. In: *ISIJ International* 32.3 (1992), pp. 291–296.

[93] M. Hillert and M. Rettenmayr. “Deviation from local equilibrium at migrating phase interfaces”. In: *Acta materialia* 51.10 (2003), pp. 2803–2809.

[94] G.P. Krielaart, J. Sietsma, and S. Van Der Zwaag. “Ferrite formation in Fe-C alloys during austenite decomposition under non-equilibrium interface conditions”. In: *Materials Science and Engineering: A* 237.2 (1997), pp. 216–223.

[95] S.G. Kim, W.T. Kim, and T. Suzuki. “Phase-field model for binary alloys”. In: *Physical review e* 60.6 (1999), p. 7186.

[96] J. Eiken, B. Böttger, and I. Steinbach. “Multiphase-field approach for multicomponent alloys with extrapolation scheme for numerical application”. In: *Physical review E* 73.6 (2006), p. 066122.

[97] C.-J. Huang, D.J. Browne, and S. McFadden. “A phase-field simulation of austenite to ferrite transformation kinetics in low carbon steels”. In: *Acta materialia* 54.1 (2006), pp. 11–21.

[98] J. Eiken. *A phase-field model for technical alloy solidification*. Shaker Verlag, 2009.

[99] B. Böttger, J. Eiken, and M. Apel. “Multi-ternary extrapolation scheme for efficient coupling of thermodynamic data to a multi-phase-field model”. In: *Computational Materials Science* 108 (2015), pp. 283–292.

[100] I. Loginova et al. “The phase-field approach and solute drag modeling of the transition to massive $\gamma \rightarrow \alpha$ transformation in binary Fe-C alloys”. In: *Acta Materialia* 51.5 (2003), pp. 1327–1339.

[101] M. Hillert and L.I. Staffansson. “Regular-solution model for stoichiometric phases and ionic melts”. In: *Acta chem. scand.* 24.10 (1970), pp. 3618–3626.

[102] P. Gustafson. “A thermodynamic evaluation of the Fe–C system”. In: *Scand. J. Metall.* 14.5 (1985), pp. 259–267.

[103] *Thermo-Calc Software*. `http://www.thermocalc.se/`.

[104] M.G. Mecozzi et al. “Quantitative comparison of the phase-transformation kinetics in a sharp-interface and a phase-field model”. In: *Computational Materials Science* 50.6 (2011), pp. 1846–1853.

[105] A. Viardin. “Modélisation par champ de phases de la croissance de la ferrite allotriomorphe dans les aciers Fe-C-Mn”. PhD thesis. Institut National Polytechnique de Lorraine, 2010.

[106] M. Hillert. *Phase equilibria, phase diagrams and phase transformations: their thermodynamic basis*. Cambridge university press, 2007.

[107] U. Grafe et al. “Coupling of multicomponent thermodynamic databases to a phase field model: application to solidification and solid state transformations of superalloys”. In: *Scripta Materialia* 42.12 (2000), pp. 1179–1186.

[108] M.G. Mecozzi et al. “The role of nucleation behavior in phase-field simulations of the austenite to ferrite transformation”. In: *Metallurgical and Materials Transactions A* 39 (2008), pp. 1237–1247.

[109] S.E. Offerman et al. “Grain nucleation and growth during phase transformations”. In: *Science* 298.5595 (2002), pp. 1003–1005.

[110] A.N. Brooks and T.J.R. Hughes. “Streamline upwind/Petrov-Galerkin formulations for convection dominated flows with particular emphasis on the incompressible Navier-Stokes equations”. In: *Computer Methods in Applied Mechanics and Engineering* 32.1 (1982), pp. 199–259. ISSN: 0045-7825. DOI: `https://doi.org/10.1016/0045-7825(82)90071-8`.

Chapter 3

Illustration of diffusive solid-state phase transformation: Benchmarking cases

Abstract

Emphasizing the model's preliminary evaluation, this chapter focuses on benchmarking cases to illustrate diffusive solid-state phase transformation. Comparative assessments against established software and analytical models serve to validate the numerical framework's predictive capabilities, particularly concerning austenite decomposition in steels. An assessment of parameter sensitivity explores the model's convergence behavior with critical model parameters. Ultimately, this study aims to evaluate the model's proficiency in replicating predicted physical dynamics, thereby providing insights into its potential for handling realistic industrial microstructures.

Résumé

En mettant l'accent sur l'évaluation préliminaire du modèle, ce chapitre se concentre sur des cas de référence pour illustrer la transformation de phase diffusive à l'état solide. Grâce à des évaluations comparatives avec des logiciels et des modèles analytiques existants, les capacités prédictives de ce modèle numérique sont validées, notamment pour la décomposition de l'austénite dans les aciers. Une analyse de sensibilité des paramètres examine le caractère de convergence du modèle tout en exhibant les eléments critiques à quantifier soigneusement. Cette étude vise enfin à établir la capacité du modèle à reproduire les caractéristiques physiques attendues, offrant ainsi des perspectives sur son potentiel pour traiter des microstructures industrielles réalistes.

3.1 Introduction

The preceding chapter extensively delved into the level-sets based numerical formulation, primarily aimed at simulating diffusive solid-state phase transformation (DSSPT). While the overarching objective of the numerical model remains the simulation of realistic industrial microstructures, it's paramount to begin by evaluating the model's performance using simpler academic cases.

Therefore, in the spirit of assessing the early potential of the numerical framework, this chapter emphasizes illustrating DSSPT through benchmarking cases. As comparative baselines, Thermo-Calc software [1] and state-of-the-art semi-analytical models capable of giving good quantitative predictions will be utilized to compare against the numerical results. Through this comparison, the objective is to evaluate the numerical model's proficiency in replicating expected physical behavior, specifically in simulating prevalent phase transformation processes.

As with any numerical framework, comprehending the influence of selected model parameters is crucial. Therefore, a sensitivity analysis will be conducted to assess the impact of key model parameters—such as mesh resolution, time step, diffuse interface thickness, etc., on numerical predictions. This evaluation seeks to understand their correlation with other model parameters and their consequential impact on the overall simulation outcomes.

The illustrations within this chapter primarily focus on austenite decomposition ($\gamma \rightarrow \alpha$) in steels. Austenite decomposition involves a diffusive solid-state phase transformation from the parent austenite phase (γ) to the more stable ferrite phase (α) below the austenitization temperature. Throughout this phase transformation, the interface mobility is modeled with a temperature-dependent Arrhenius-type law [2] as already depicted in Eq.(1.31). The solute diffusivities in the two phases are also given a temperature dependence using a similar Arrhenius type law:

$$\begin{aligned} D_\alpha^i &= D_\alpha^i\big|_0 \exp\left(-\frac{Q_\gamma^i}{RT}\right) \\ D_\gamma^i &= D_\gamma^i\big|_0 \exp\left(-\frac{Q_\gamma^i}{RT}\right) \end{aligned}, \tag{3.1}$$

where i is the solute, Q_α^i, and Q_γ^i are the activation energies for solute diffusion in the α and the γ phases, respectively. Unless explicitly specified, within the defined scope, this work assumes the interface mobility and interfacial energy to be homogeneous in the computational domain.

3.2 DSSPT in simple domains

3.2.1 Pseudo-1D case

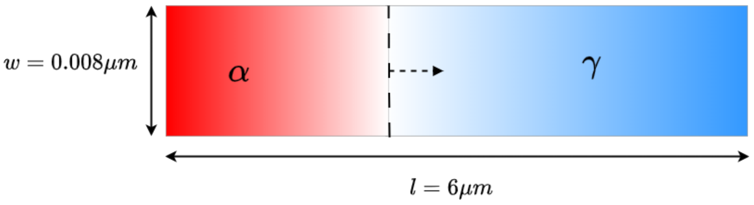

Figure 3.1: Pseudo-1D case ($w << l$) with a planar interface between a ferrite (red) and an austenite (blue) phase

For our initial case, we examine phase transformation in a slender 2D domain (Pseudo-1D since $w << l$) featuring a planar interface between a single austenite grain and a ferrite grain as shown in

Fig.3.1. This initial configuration is adopted as our solvers were developed in 2D and 3D, and not in 1D. A simple metallic alloy Fe - 0.02 wt%C is assumed for austenite decomposition. The initial condition is assumed to be at a temperature, $T^i = 1173\,\mathrm{K}$, under fixed atmospheric pressure, and with corresponding initial concentrations of $x^{\alpha}_{C,i} = 0.0014022$ wt%C and $x^{\gamma}_{C,i} = 0.024575$ wt%C (extracted from ThermoCalc [1]). The α/γ phase interface is initially imposed to be at $\Gamma_i = 1.1838\,\mu\mathrm{m}$ from the left boundary, corresponding to the initial ferrite fraction of 0.197297 at 1173 K. A reference temperature of $T^R = 1140\,\mathrm{K}$ is taken and the necessary thermodynamic data (summarized in table 3.1) are extracted using ThermoCalc. The final state is imposed to be at a temperature, $T^f = 1140\,\mathrm{K}$, and the corresponding equilibrium thermodynamic data is the same as the one summarized in table 3.1. The final steady state interface position is expected to be at, $\Gamma_{eq} = 5.11296\,\mu\mathrm{m}$, computed based on the expected equilibrium ferrite fraction ($f^{\alpha}_{eq} = 0.85216$) by ensuring complete solute mass conservation for the considered domain. Capillarity effects are irrelevant for the planar interface due to null curvature. The thickness of the diffuse phase interface for this case is taken as $\eta = 0.5\,\mu\mathrm{m}$. An adaptive finite element (FE) mesh with triangular elements as depicted in Figs.3.2 is adopted. The mesh size within the supposed diffuse interface, h_{min}, is set to 0.4 nm, while the far-field mesh size, h_{max}, is set to 2 nm. Only a small snippet of the mesh is illustrated in figs3.2 as the domain is elongated and significantly longer than its width. A smooth linear transition in mesh resolution is ensured between h_{min} and h_{max} over a certain chosen distance parameter. The time step, Δt is fixed to 1 ms.

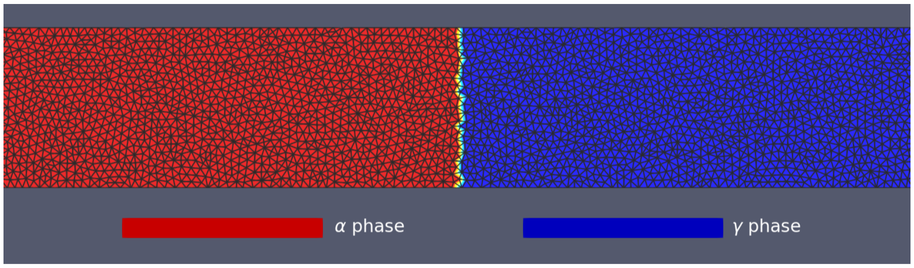

(a) Around the phase interface

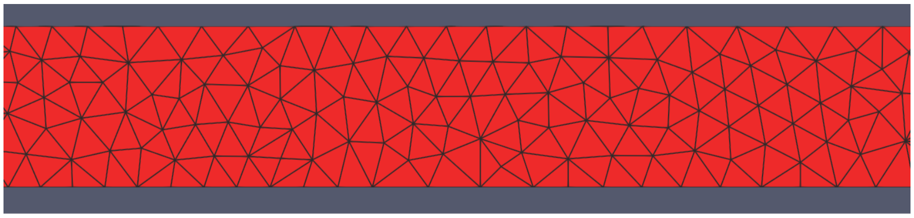

(b) Far-field, in the α-phase

Figure 3.2: Mesh resolution depicting the discretization near the interface compared to the far-field mesh for the pseudo-1D case

The activation energy for grain/ phase boundary migration (Q_m) is taken as 140 $\mathrm{kJ{\cdot}mol^{-1}}$ [3], and the mobility pre-exponential factor (M_0) is taken as $2{\times}10^{17}\,\mu\mathrm{m^4{\cdot}J^{-1}{\cdot}s^{-1}}$ for low cooling rates or as $6{\times}10^{17}\,\mu\mathrm{m^4{\cdot}J^{-1}{\cdot}s^{-1}}$ for high cooling rates [4]. Carbon diffusivities in the two phases are assumed

T^R (K)	$x_C^\alpha\big\|_R$ (wt%)	$x_C^\gamma\big\|_R$ (wt%)	ΔS ($\mathrm{J{\cdot}K^{-1}{\cdot}\mu m^{-3}}$)	$m_{Fe-C}^{\alpha/(\alpha+\gamma)}$ ($\mathrm{K{\cdot}wt\%^{-1}}$)	$m_{Fe-C}^{\gamma/(\alpha+\gamma)}$ ($\mathrm{K{\cdot}wt\%^{-1}}$)	f_{eq}^α
1140	0.0051473	0.10593	3.28138×10^{-13}	−9127.94266	−360.7063	0.8522

Table 3.1: ThermoCalc data extracted at 1140 K for Fe - 0.02 wt%C

as:

$$\begin{aligned} D_\alpha^C &= 2.2 \times 10^8 \exp\left(\frac{-Q_\gamma^C}{RT}\right) \quad \text{in} \quad \mathrm{\mu m^2{\cdot}s^{-1}} \\ D_\gamma^C &= 1.5 \times 10^7 \exp\left(\frac{-Q_\gamma^C}{RT}\right) \quad \text{in} \quad \mathrm{\mu m^2{\cdot}s^{-1}} \end{aligned} , \tag{3.2}$$

where $Q_\alpha^C = 122.5\,\mathrm{kJ{\cdot}mol^{-1}}$, and $Q_\gamma^C = 142.1\,\mathrm{kJ{\cdot}mol^{-1}}$. The carbon diffusivity pre-factors and the activation energies for the two phases have been taken from [4, 5].

Three different scenarios of cooling are considered from $T^i = 1173\,\mathrm{K}$ to $T^f = 1140\,\mathrm{K}$: (i) instantaneous cooling, thus giving isothermal phase transformation, at 1140 K, (ii) rapid cooling at the rate of $10\,\mathrm{K{\cdot}s^{-1}}$ until 1140 K and thereafter the temperature is maintained, and (iii) slow cooling at the rate of $0.5\,\mathrm{K{\cdot}s^{-1}}$ until 1140 K and thereafter the temperature is maintained.

The snapshots of the phase evolution during austenite decomposition at various instants are displayed in Figs.3.3 for the instantaneous cooling scenario. The progression reveals the gradual consumption of the austenite phase (γ) in blue by the ferrite phase (α) depicted in red. As the system is abruptly pushed out of its initial equilibrium due to instantaneous cooling, the transformation kinetics immediately accelerate to their maximum and gradually decelerate as the system converges toward its new equilibrium. Upon reaching the steady state, the transformation halts, and the phase interface stabilizes at a position aligning with the equilibrium conditions. Fig.3.4 illustrates the associated evolution of carbon concentration along the length of the domain at different times for the instantaneous cooling case. The solute distribution illustrated in Fig.3.4 represent the total concentration of carbon ($x_C = \phi x_C^\alpha + (1 - \phi) x_C^\gamma$), not to be confused with the individual phase concentrations. They corresponding to the individual phase concentrations only in the bulk of the phase, away from the assumed diffuse phase interface. As the interface begins to migrate, peaks in the profiles near the interface on the austenite side develop due to carbon build up resulting from the ferrite phase's rejection of carbon into the austenite phase. This indicates the expected solute enrichment in austenite during the transformation as carbon is generally more soluble in austenite than ferrite. In the ferrite phase, due to higher carbon diffusivity, the bulk diffusion is faster and hence the concentration gradients are less pronounced as the concentration quickly attains plain profiles. The concentration on the austenite side continues to increase until reaching a steady state between the two phases, aligning with their corresponding equilibrium concentrations. As the steady state is reached, plain carbon profiles are obtained in both the phases. At steady state, the simulated equilibrium concentrations are found to be: $x_{eq,\ num}^\alpha = 0.0051456\,\mathrm{wt\%C}$ and $x_{eq,\ num}^\gamma = 0.10587\,\mathrm{wt\%}C$. These values clearly align well with the ThermoCalc predictions (see Tab.3.1).

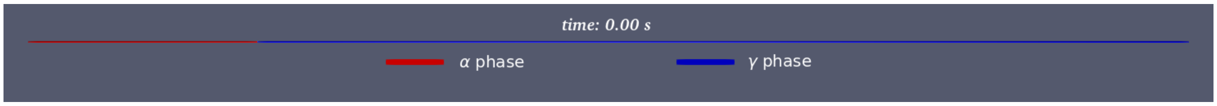

(a) $t = 0$ s, initial state

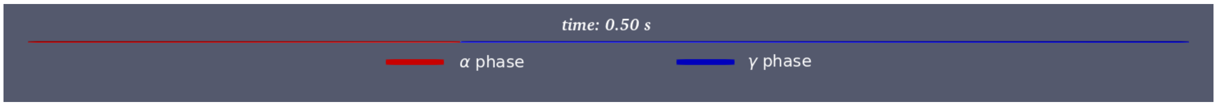

(b) $t = 0.5$ s

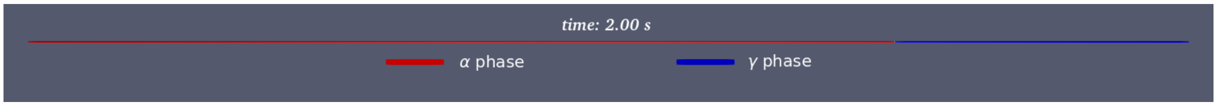

(c) $t = 2$ s

(d) $t = 10$ s, steady state

Figure 3.3: Phase evolution in a pseudo-1D domain during austenite decomposition for the instantaneous cooling case (red: ferrite, blue: austenite)

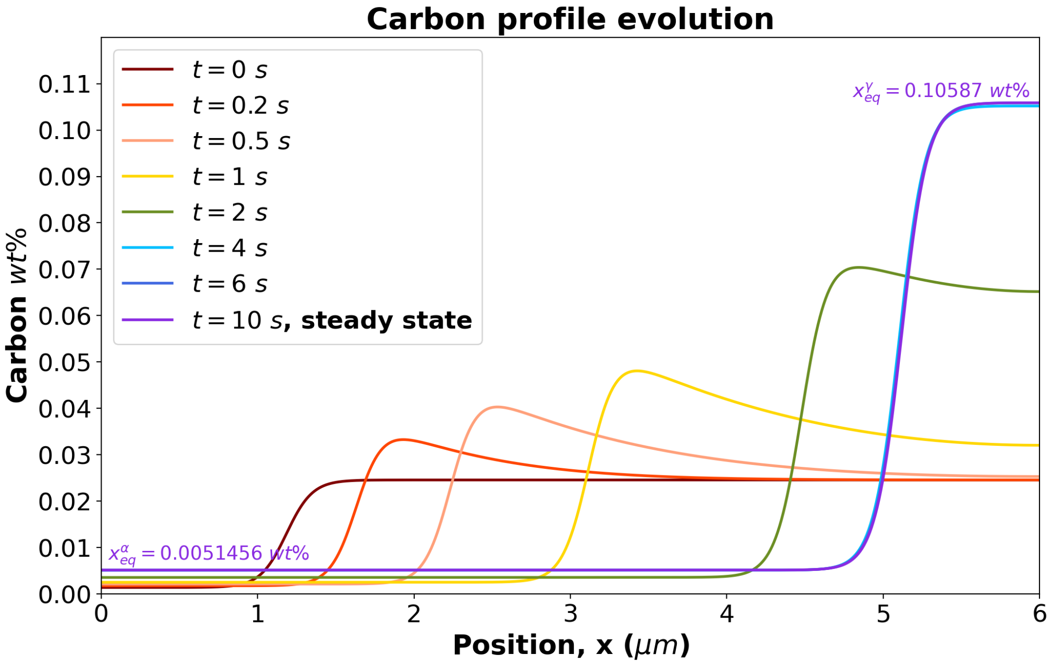

Figure 3.4: Evolution of carbon concentration profiles at different instants till the steady state (instantaneous cooling case)

On the other hand, Fig.3.5 and Fig.3.6 demonstrate the evolution of the carbon profiles for the rapid cooling and slow cooling cases, respectively. In the rapid cooling case, although the peaks in the profiles remain visible, they are not as pronounced as they were in the case of instantaneous cooling. In the scenario of slow cooling, the profiles appear consistently plain over time, gradually approaching the equilibrium value as the concentration levels increase. This stems from the fact that, at any instant, smaller amounts of carbon accumulate in the austenite side due to slower kinetics. The slower pace allows sufficient time for diffusion to evenly redistribute the small influx of carbon into the bulk at any instant.

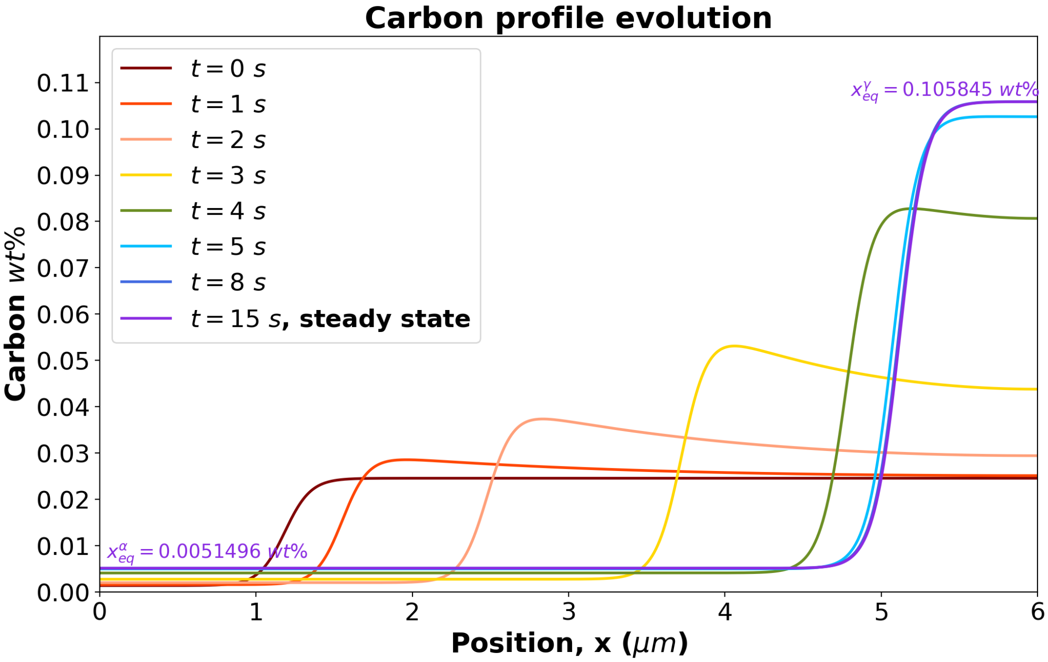

Figure 3.5: Evolution of carbon concentration profiles at different instants till the steady state (rapid cooling case)

Fig.3.7 illustrates the evolution of the phase interface for all three cooling scenarios as they converge toward a steady state position. Clearly, the case with slow cooling is sluggish to start as the system steadily departs from the initial equilibrium state, and is the slowest to reach the new equilibrium state corresponding to the final conditions. Conversely, the case with instantaneous cooling takes off immediately and swiftly reaches the steady state. The zoomed-in section of the curves emphasizes the stark differences in interface kinetics between slow cooling and the other two cases. The instantaneous and rapid cooling scenarios reach their steady state positions within approximately $10 - 15$s, while the slow cooling case requires around 100 s. All three cases yield similar steady states with differences only in their kinetics. The steady state positions predicted for the three cases are: (i) $\Gamma^{num}_{eq} = 5.1167\,\mu\text{m}$ for the instantaneous cooling case, (ii) $\Gamma^{num}_{eq} = 5.1227\,\mu\text{m}$ for the rapid cooling case, and (iii) $\Gamma^{num}_{eq} = 5.0826\,\mu\text{m}$ for the slow cooling case. These numerically predicted positions are in good agreement with the expected interface position of 5.11296 µm. Any small differences in the predicted values from the expected value is a consequence of the error in ensuring

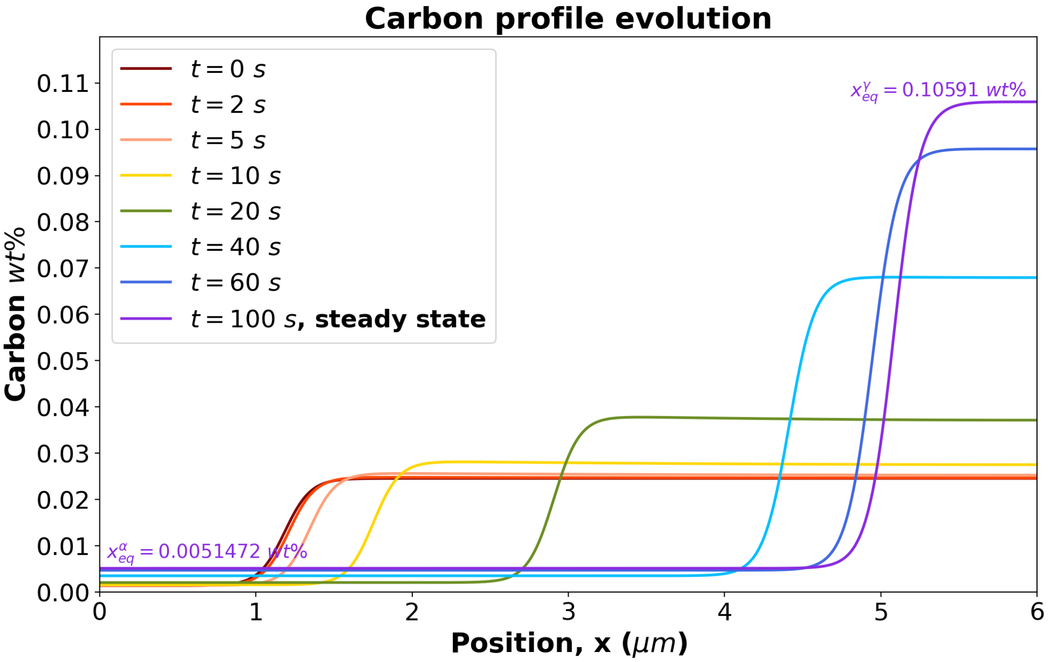

Figure 3.6: Evolution of carbon concentration profiles at different instants till the steady state (slow cooling case)

complete solute mass conservation in the computational domain during the simulation. Fig.3.8 quantifies the quality of mass conservation established during the course of the simulation. The maximum variation is limited to 0.39288%, 1.6284%, and 3.6532% for the instantaneous, rapid, and slow cooling cases, respectively. This variation generally stems from the mesh quality, the choice of the time step, diffuse interface thickness (η) etc. A positive error percent is a reflection of numerical addition of the solute, while a negative percent reflects numerical loss of solute mass.

3.2.2 2D matrix-precipitate case

We now consider a 2D square matrix representing the parent phase, which includes a circular precipitate acting as the product phase. In the previous pseudo-1D illustration, the driving pressure due to the capillarity effects of the phase interface were irrelevant. However, in higher dimensions, the curvature of the interfaces becomes a factor, introducing additional contributions to the transformation kinetics. To highlight the subtle yet important effects of capillarity, we investigate an isothermal phase transformation in a 2D matrix-precipitate test case, comparing scenarios with and without consideration of capillarity aspects. A square domain with a side of 10µm is considered. The same steel alloy, Fe - 0.02 wt%C, is assumed with the same initial conditions at $T^i = 1173\,\mathrm{K}$ for austenite decomposition. However, the final conditions are set to $T^f = 1160\,\mathrm{K}$ to ensure that the final ferrite fraction is sufficiently small, allowing the ferrite precipitate to remain circular at the steady state. The precipitate is initially imposed at a radius of $r^i_\alpha = 2.50604\,\mu\mathrm{m}$ corresponding to the initial ferrite fraction. The domain is discretized with an adaptive mesh, with privileges for remeshing around the precipitate interface. The interface thickness is kept as $\eta = 0.5\,\mu\mathrm{m}$ with

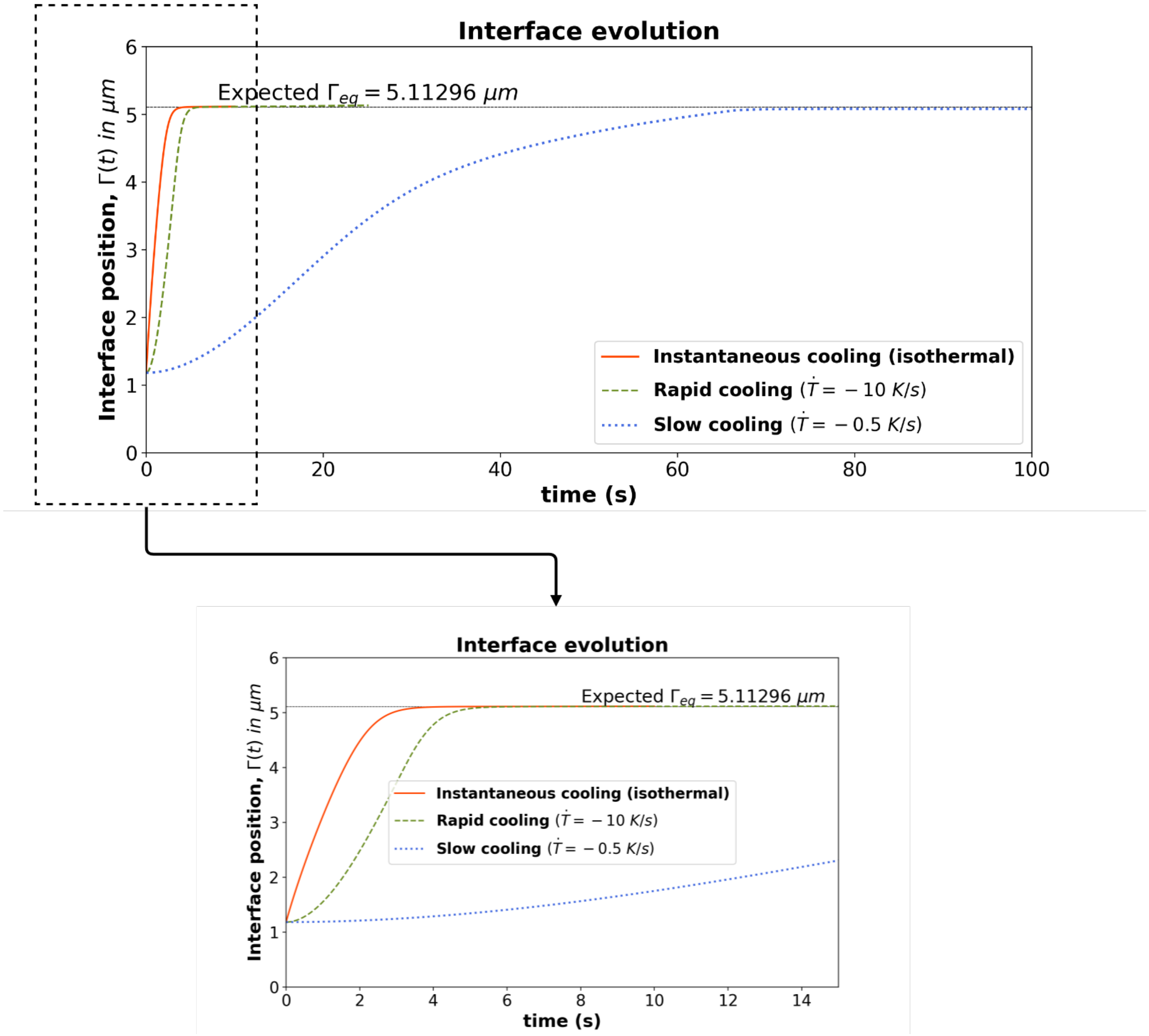

Figure 3.7: Comparison of the kinetics of interface evolution for different scenarios of cooling

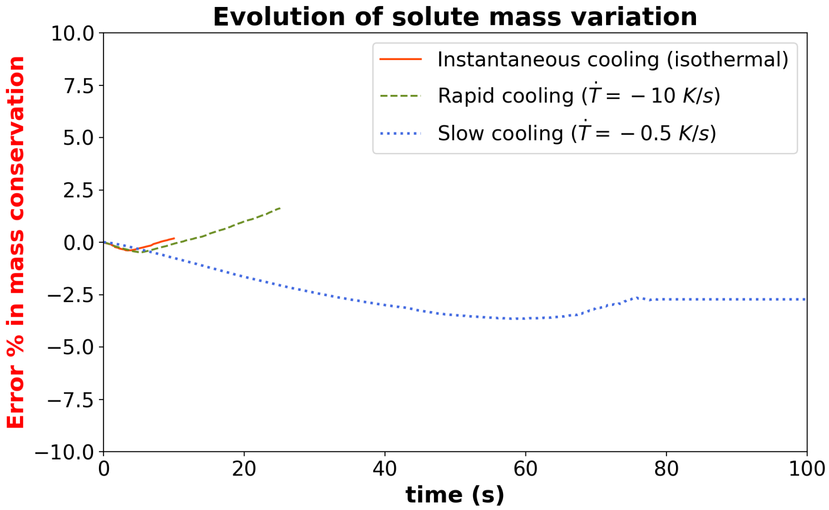

Figure 3.8: Variation of solute mass in the domain during the simulation

$h_{min} = 0.01$ µm and $h_{max} = 0.1$ µm. The time step is fixed at $\Delta t = 0.001$ s.

T^R (K)	$x_C^\alpha\big\|_R$ (wt%)	$x_C^\gamma\big\|_R$ (wt%)	ΔS (J·K^{-1}·µm^{-3})	$m_{Fe-C}^{\alpha/(\alpha+\gamma)}$ (K·wt%$^{-1}$)	$m_{Fe-C}^{\gamma/(\alpha+\gamma)}$ (K·wt%$^{-1}$)	f_{eq}^α
1160	0.002908	0.05429	2.84812×10^{-13}	−8746.564	−416.959	0.667

Table 3.2: ThermoCalc data extracted at 1160 K for Fe - 0.02 wt%C

Tab.3.2 summarizes the ThermoCalc data extracted at the final temperature, which is also the reference temperature considered for the phase diagram linearization. The expected equilibrium ferrite fraction estimated by ThermoCalc corresponds to an equivalent precipitate radius at the steady state position of approximately 4.6075 µm. It's crucial to note that ThermoCalc predictions are computed under the assumption of a planar interface, disregarding the influence of capillarity aspects. The mobility and the diffusivity data remain the same as assumed for the previous illustration. Mobility and interfacial energy are assumed to be homogeneous along the phase interface. The value for the interface energy is adopted from [6, 7], where $\sigma_{\gamma\alpha} = 1.0{\times}10^{-6}$ J·mm^{-2}.

Fig.3.9 depicts snapshots of the simulation at three different instants. The left-side images showcase the evolution of the ferrite precipitate (red) within the austenite matrix (blue), while the right-side images give an account of the corresponding solute redistribution in the domain. The left-side images also emphasize the position of the phase interface contours, highlighted in white. The final set of images at $t = 10$ s represents the system's steady state.

The same test case is re-simulated but without the capillarity effects. In Fig.3.10, the white and black circles represent the iso-zero contours of the phase interface mapped at the steady state for the cases with and without capillarity effects, facilitating a comparison of their respective steady state positions. This comparison distinctly highlights minor differences in the steady state positions between

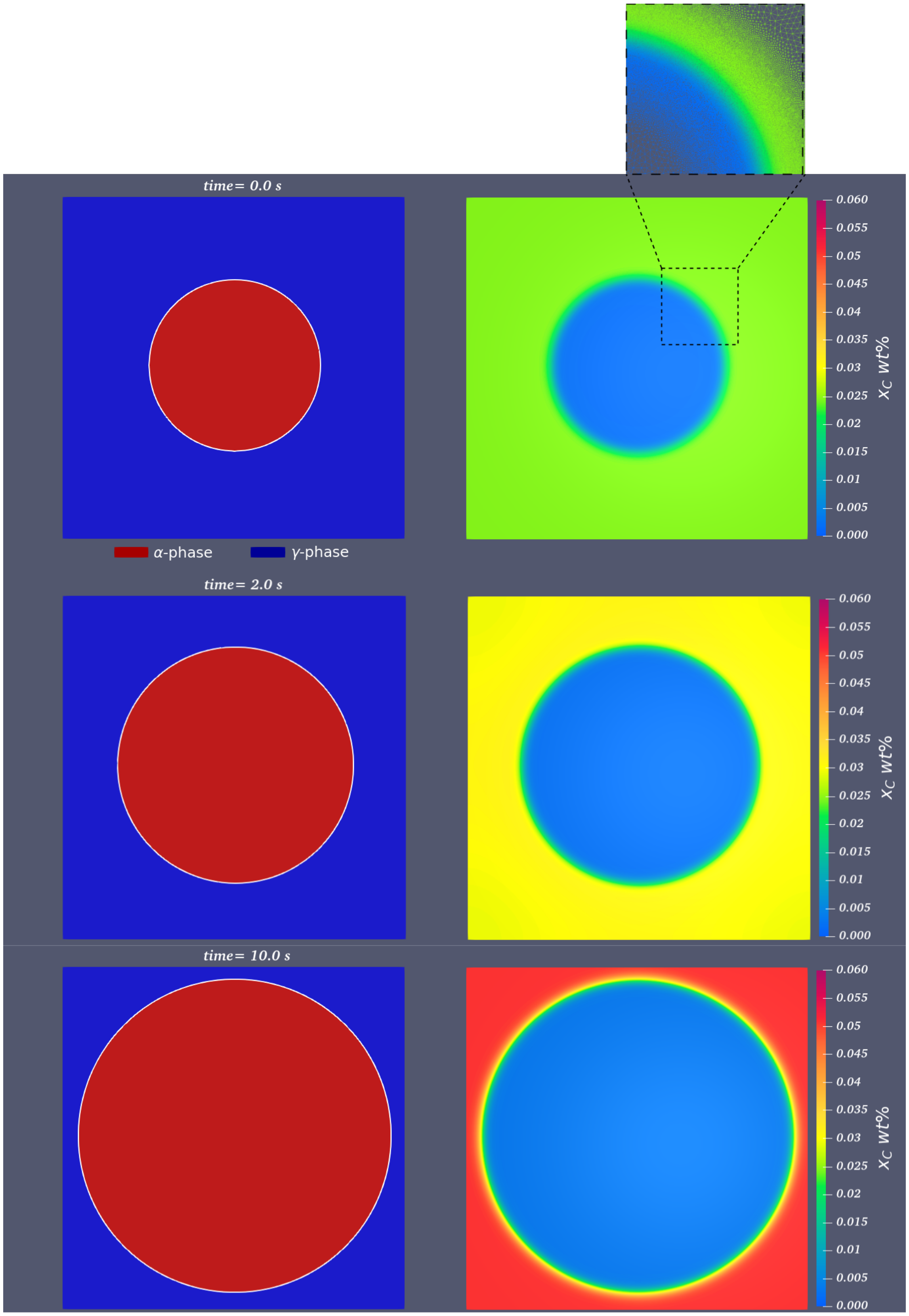

Figure 3.9: Snapshots of the transformation in the matrix-precipitate case by accounting for the capillarity effects: phase evolution on the left, carbon distribution map on the right

the two cases. Accounting for capillarity effects predicts a final precipitate radius of approximately 4.5676 µm, while the other case predicts around 4.6376 µm. We can observe the impact of the capillarity induced driving pressure which in this case slightly lowers the transformation kinetics and reduces the steady state position achieved. The presence of interfaces increases the system's overall Gibbs free energy, consequently introducing an additional driving pressure to minimize the interfacial area of the growing precipitate under the influence of the principal driving pressure due to phase transformation. The magnitude of this capillarity induced pressure is several orders lower compared to the phase transformation driving pressure, leading to its oversight in certain numerical models. While the differences in final positions may seem inconsequential, their notable impact on transformation kinetics is evident in Fig.3.11, which compares the evolution of precipitate radius during the transformation. At the onset of the transformation, the capillarity pressure exerts a substantial impact, resulting in slower transformation kinetics. However, as the ferrite precipitate matures, the influence of capillarity effects diminishes. The magnitude of capillarity-induced driving pressure ($|\sigma\kappa|$), is higher when the precipitate is smaller due to increased curvature, intensifying the associated driving pressure. As the particle grows, both curvature and the associated driving pressure decrease. So, for a larger or well established ferrite grains or particles, curvature effects are generally negligible during a phase transformation within the characteristic time scale of interest. However, in the case of small ferrite grains or when the ferrite phase is in its nucleus form, curvature effects play a significant role in governing the growth or dissolution of the nuclei.

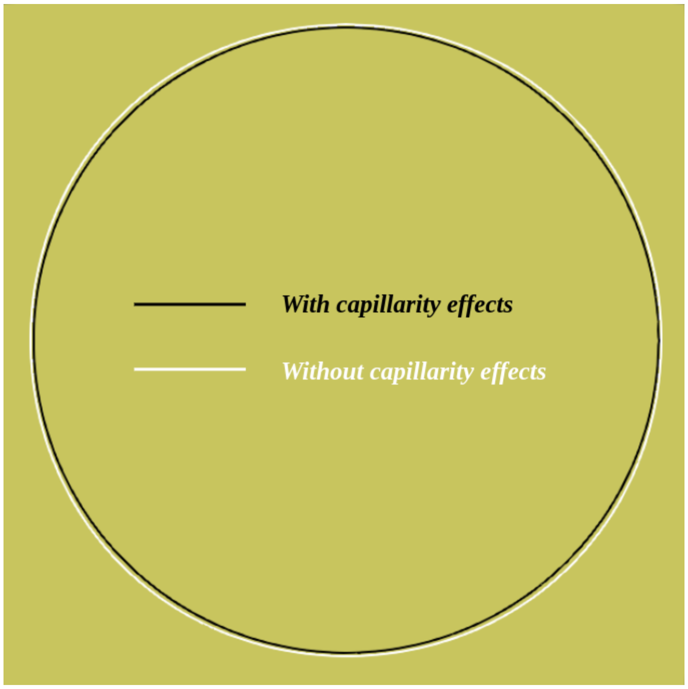

Figure 3.10: Comparison of the steady state positions of the phase interface contours

Incorporating capillarity effects not only influences kinetics but also shifts the equilibrium position of the thermodynamic system. For instance, the numerical predictions for equilibrium carbon concentrations in the two phases are as follows: (i) With capillarity effects - $x^{\alpha}_{eq,r} = 0.002717$ wt%C and $x^{\gamma}_{eq,r} = 0.05069$ wt%C; (ii) Without capillarity effects - $x^{\alpha}_{eq,\infty} = 0.00295$ wt%C and $x^{\gamma}_{eq,\infty} =$

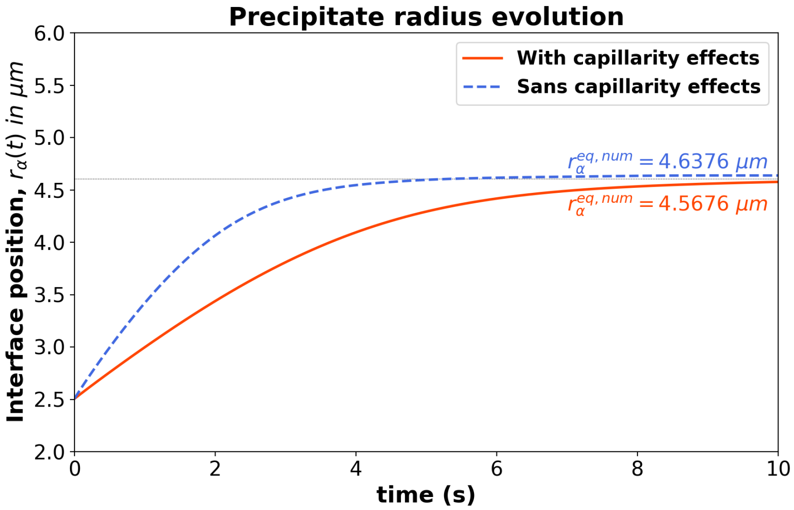

Figure 3.11: Comparison of the ferrite precipitate evolution during the transformation. The dotted black line references the ThermoCalc prediction at equilibrium

0.0551 wt%C. It's evident that the equilibrium concentrations are slightly skewed towards the lower end of the scale due to the influence of capillarity pressure. To elucidate this, Fig.3.12 showcases the variation of representative Gibbs free energy curves concerning carbon composition at a specific temperature, expected during austenite decomposition. The solid red curve represents the Gibbs free energy of the ferrite phase with zero curvature or infinite radius, while the dashed red curve portrays the same in the presence of a curved interface. The additional contribution arising from capillarity effects elevates the α-phase Gibbs free energy curve. Consequently, the common tangent line used for determining equilibrium positions undergoes a shift, resulting in lower equilibrium concentrations in this scenario. Depending on the stability of the phases involved, equilibrium concentrations might also shift to the right in other contexts. The extent of this shift depends on the strength of the capillarity effects, namely the interface curvature and the interfacial energy.

3.3 Comparison with state-of-the-art semi-analytical sharp interface model: Benchmarking

To benchmark this numerical framework, we consider the semi-analytical mixed-mode sharp interface model formulated by Bos et al. [8].

Sharp interface model: For a $\gamma \rightarrow \alpha$ phase transformation, the semi-analytical sharp interface model in [8] is based on the following assumptions:

- The solute concentration profile in front of the α/γ interface in the γ phase (x^γ) in a semi-

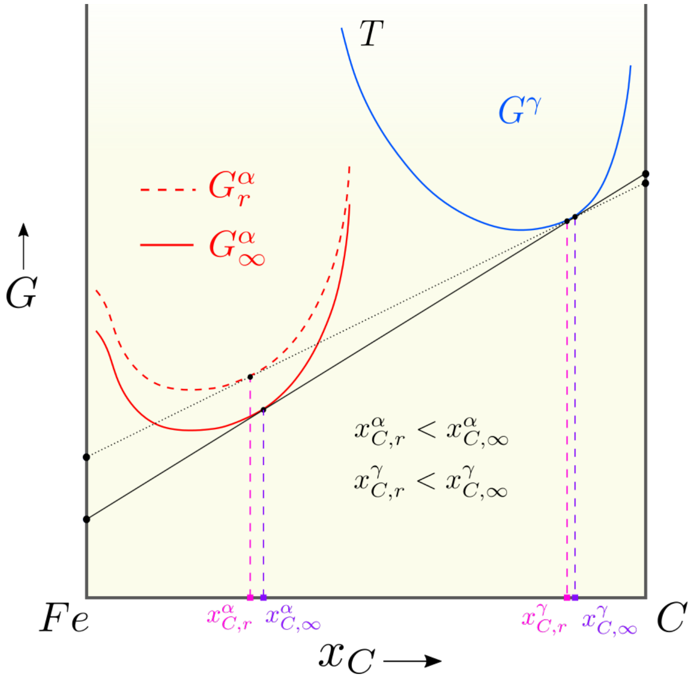

Figure 3.12: Influence of the capillarity induced pressure on the equilibrium position

infinite domain is assumed to be a function of position z as follows:

$$x^\gamma(z) = x_0 + \left(x^\gamma_\Gamma - x_0\right) \exp\left(-\frac{z}{z_0}\right), \tag{3.3}$$

where x_0 is the nominal alloy composition, $x^\gamma_\Gamma = x^\gamma|_\Gamma$ is the composition in the γ phase at the interface $\Gamma(t)$, z is the position in front of the interface (with $z = 0$ at the interface), and z_0 is coined as the width of the profile as depicted in Fig.3.13.

- Diffusion in the α phase is assumed to be instantaneous and so the concentration in this phase is imposed to be homogeneous at its equilibrium concentration, x^α_{eq}.
- The driving pressure for phase transformation is assumed to be proportional to the deviation of x^γ_Γ from its equilibrium concentration as in Eq.(2.81):

$$\Delta G_{\gamma\to\alpha} = \Upsilon\left(x^\gamma_{eq} - x^\gamma_\Gamma\right), \tag{3.4}$$

where Υ is a temperature dependent proportionality factor derived from thermodynamic databases. The interface migration velocity is based as,

$$v = M_{\gamma\alpha}\Delta G_{\gamma\to\alpha}, \tag{3.5}$$

with $M_{\gamma\alpha}$ being the phase interface mobility.

- A single α-grain of volume V^α and surface area A^α at any instant, t, is considered in an infinite γ phase matrix.

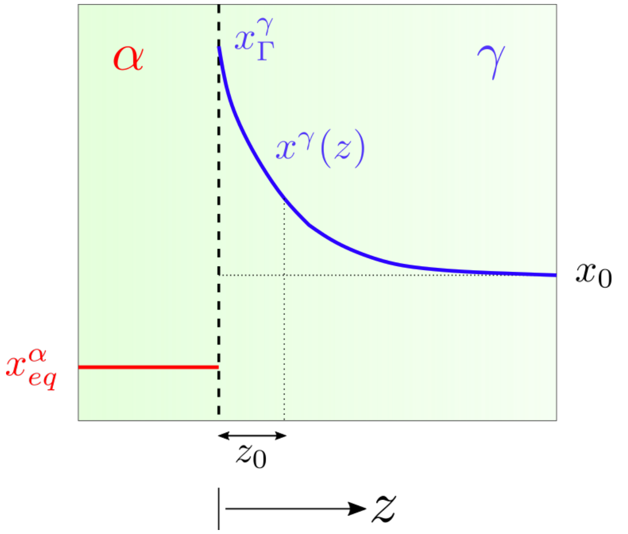

Figure 3.13: Concentration profile described in the semi-analytical model by Bos et al. [8]

Considering mass balance at any instant, t, we obtain:

$$V^\alpha \left(x_0 - x_{eq}^\alpha\right) = \int_0^\infty A(z)\,[x^\gamma - x_0]\,dz, \tag{3.6}$$

where $A(z)$ is the surface area of the grain at the position z. The width of the profile, z_0, is derived using the above mass balance relation as:

$$z_0 = \frac{V^\alpha}{\Omega A^\alpha}\left(\frac{x_0 - x_{eq}^\alpha}{x_\Gamma^\gamma - x_0}\right). \tag{3.7}$$

As summarized in Bos et al. [8], Ω can be analytically computed to be:

- $\Omega = 1$ for systems with a constant surface area such as 1D cases,
- $\Omega = 1 + \frac{z_0}{r_\alpha}$ for growing α disks in 2D, and
- $\Omega = 1 + 2\frac{z_0}{r_\alpha} + 2\left(\frac{z_0}{r_\alpha}\right)^2$ for growing spheres in 3D,

with r_α being the characteristic size of the α-grain at time, t.

Flux balance at the phase interface under the considered assumptions yields:

$$v\left(x_\Gamma^\gamma - x_{eq}^\alpha\right) = -D_\gamma^i \frac{\partial x^\gamma}{\partial z}, \tag{3.8}$$

with i being the solute element.

Combining equations (3.3) to (3.5), (3.7), and (3.8), we can deduce the solute concentration in the

γ phase at the interface as:

$$x_{\Gamma}^{\gamma} = \frac{\mathcal{Z}x_0 + \Delta x_0 x_{eq}^{\alpha+\gamma} + \sqrt{\left(\mathcal{Z}x_0 + \Delta x_0 x_{eq}^{\alpha+\gamma}\right)^2 - \left(\mathcal{Z} + 2\Delta x_0\right)\left(\mathcal{Z}x_0^2 + 2\Delta x_0 x_{eq}^{\alpha} x_{eq}^{\gamma}\right)}}{\mathcal{Z} + 2\Delta x_0}, \tag{3.9}$$

where $\Delta x_0 = x_0 - x_{eq}^{\alpha}$, and $x_{eq}^{\alpha+\gamma} = x_{eq}^{\alpha} + x_{eq}^{\gamma}$. The $\mathcal{Z}$ parameter is defined as:

$$\mathcal{Z} = 2\Omega \frac{D_{\gamma}^{i}}{M_{\gamma\alpha}\Upsilon} \frac{A^{\alpha}}{V^{\alpha}}. \tag{3.10}$$

The dependence of $\mathcal{Z}$ on Ω which eventually depends on x_{Γ}^{γ}, renders the Eq.(3.9) non-linear. Thus, an iterative procedure is needed to compute the interface concentration.

The α-grain size, $r_{\alpha}(t)$, is then evolved according to the following relation:

$$\frac{dr_{\alpha}}{dt} = v \tag{3.11}$$

The resolution procedure at each time step could be summarized as follows:

- The non-linear equation in Eq.(3.9) is resolved using an iterative procedure. At the initial time step, when $r_{\alpha} = 0$, Ω is assumed as 1, but thereafter, Ω is computed according to the dimensionality of the grain as discussed previously.
- Having computed the interface concentration, the interface migration velocity, v, is computed using the Eq.(3.5).
- The interface is then migrated through an explicit Euler time scheme applied to Eq.(3.11) as: $r_{\alpha}^{k+1} = r_{\alpha}^{k} + v\Delta t$, where Δt is the time step and k is the index for time stepping.

Simulation conditions: To benchmark the level-set based numerical model with this sharp interface semi-analytical model (SAM), an isothermal austenite decomposition ($\gamma \to \alpha$) in a steel alloy (Fe - 0.1 wt%C - 0.5 wt%Mn) at 1000 K is considered. This is the same case studied by Mecozzi et al. [9] in their comparison of a phase-field numerical model with the above semi-analytical method. The phase transformation is assumed to take place under para-equilibrium (PE) hypothesis. The solute drag aspects potentially induced by the Mn element are not taken into account for this study, and the capillarity effects of the phase interface have been neglected.

For the description of the driving pressure, as discussed in 2.3.4 in Eq.(2.88), the driving pressure is assumed to be proportional to the local undercooling: $\Delta G_{\gamma\to\alpha} = \Delta S^{\gamma\alpha}\Delta T$, through a local linearization of the phase diagram at a certain reference temperature. As demonstrated in the previous chapter in 2.3.4, based on this linearization, the local undercoolings of each solvus line ($\Delta T_{\alpha}, \Delta T_{\gamma}$) of the phase diagram can be expressed as:

$$\begin{aligned} \Delta T_{\alpha} &= T_{\alpha}^{eq} - T = T^{R} - T + m_{A-i}^{\alpha/(\alpha+\gamma)}\left(x_i^{\alpha} - x_i^{\alpha}\big|_{R}\right) = m_{A-i}^{\alpha/(\alpha+\gamma)}\left(x_i^{\alpha} - x_i^{\alpha}\big|_{eq}\right) \\ \Delta T_{\gamma} &= T_{\gamma}^{eq} - T = T^{R} - T + m_{A-i}^{\gamma/(\alpha+\gamma)}\left(x_i^{\gamma} - x_i^{\gamma}\big|_{R}\right) = m_{A-i}^{\gamma/(\alpha+\gamma)}\left(x_i^{\gamma} - x_i^{\gamma}\big|_{eq}\right) \end{aligned}. \tag{3.12}$$

As a reminder, $x_i^{\alpha}\big|_{eq}$ and $x_i^{\gamma}\big|_{eq}$, in the above equations are the equilibrium concentrations at the current temperature, T, derived according to the linearized solvus lines.

For this particular case study, following [9], we impose an additional hypothesis of equal undercoolings in both the phases (as illustrated in fig.3.14):

$$\Delta T = \Delta T_{\alpha} = \Delta T_{\gamma} = m_{A-i}^{\gamma/(\alpha+\gamma)} \left(x_i^{\gamma} - x_i^{\gamma}\big|_{eq} \right). \tag{3.13}$$

This additional hypothesis makes it possible to use a consistent thermodynamic description between the sharp interface model and the numerical model.

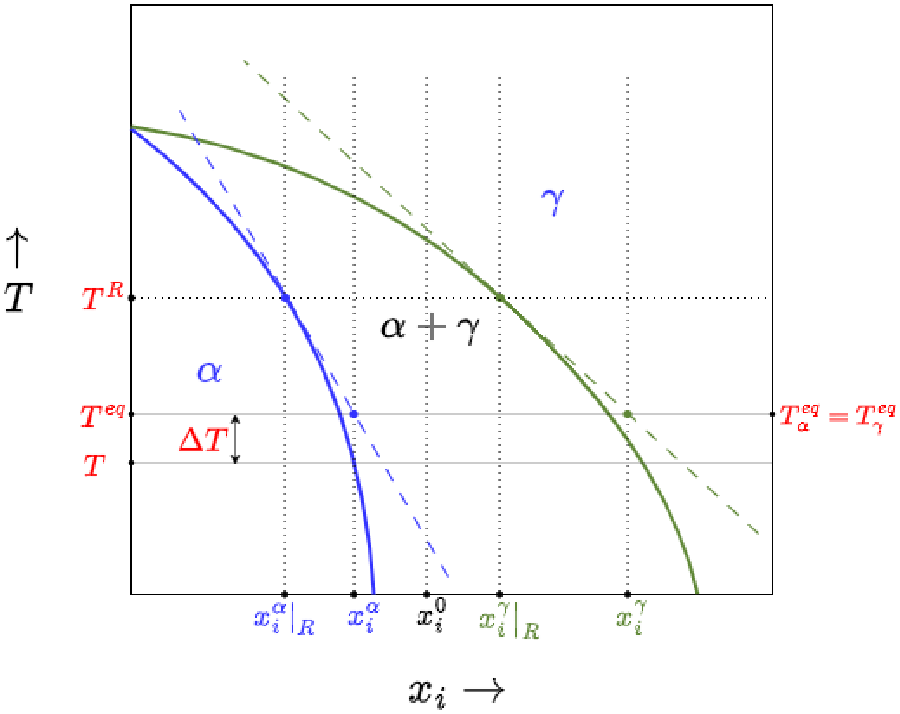

Figure 3.14: Local linearization of the phase diagram under equal undercooling in both the phases ($\Delta T_{\alpha} = \Delta T_{\gamma}$)

So, the driving pressure for the numerical model is described as:

$$\Delta G_{\gamma \rightarrow \alpha} = \Delta S^{\gamma\alpha} m_{A-i}^{\gamma/(\alpha+\gamma)} \left(x_i^{\gamma} - x_i^{\gamma}\big|_{eq} \right). \tag{3.14}$$

Comparing the above equation with the driving pressure description of the semi analytical sharp interface model in eq.(3.4), it can be deduced that, $\Upsilon = -m_{A-i}^{\gamma/(\alpha+\gamma)} \Delta S^{\gamma\alpha}$.

The necessary mobility, carbon diffusivity, and the thermodynamic data have been taken from [9] to be consistent with the comparison. The temperature dependence of phase interface mobility, and the carbon diffusivity in the austenite phase is thus defined as:

$$\begin{aligned} M_{\gamma\alpha} &= 3.5 \times 10^{17} \exp\left(\frac{-Q_m}{RT}\right) \quad in \quad \mu\text{m}^4\cdot\text{J}^{-1}\cdot\text{s}^{-1} \\ D_\gamma^C &= 1.5 \times 10^{7} \exp\left(\frac{-Q_\gamma^C}{RT}\right) \quad in \quad \mu\text{m}^2\cdot\text{s}^{-1} \end{aligned}, \tag{3.15}$$

where $Q_m = 140\,\text{kJ}\cdot\text{mol}^{-1}$, and $Q_\gamma^C = 142.1\,\text{kJ}\cdot\text{mol}^{-1}$.

The thermodynamic data extracted following [9], at a reference temperature of $T^R = 1073\,\text{K}$, has been tabulated in the table 3.3. These data have been deduced by linearizing the pseudo-binary Fe-C phase diagrams under the para-equilibrium hypothesis.

T^R (K)	$x_C^\alpha\big\rvert_R$ (wt%)	$x_C^\gamma\big\rvert_R$ (wt%)	$\Delta S^{\gamma\alpha}$ (J·K^{-1}·µm^{-3})	$m_{Fe-C}^{\alpha/(\alpha+\gamma)}$ (K·wt%$^{-1}$)	$m_{Fe-C}^{\gamma/(\alpha+\gamma)}$ (K·wt%$^{-1}$)
1073	0.009	0.279	3.46×10^{-13}	−10250	−186.2

Table 3.3: ThermoCalc data extracted at $T^R = 1073\,\text{K}$ from [9] for
Fe - 0.1 wt%C - 0.5 wt%Mn

Two cases are considered in this comparison: (i) A pseudo-1D domain of length 100 µm (with a relatively minute and insignificant breadth of 0.15 µm), and (ii) A square 2D domain of size 100×100 µm^2. The domain is supposed to be initially fully austenitic. As the temperature is instantaneously cooled below the T^{A3} temperature to 1000 K, a ferrite nucleus is allowed to grow at the center of the domain for a time period of 200 s. In the level-set based numerical model (LS-NM), the initial ferrite nucleus radius (r_α^i) has been set to 0.25 µm due to numerical limitations linked to the FE mesh size (while it grows from 0 µm in the semi-analytical model). In the LS-NM, the initial ferrite nucleus composition is set to 0.001832 wt%C, which is the critical nucleus composition at $T = 1000\,\text{K}$ under the para-equilibrium (PE) constraints, extracted from ThermoCalc. However, in the SAM, the nucleus composition is straight away set to the equilibrium composition for the ferrite phase (0.016013 wt%C) under PE since it is assumed to diffuse instantaneously in this phase. During the numerical simulation, a uniform time step of $\Delta t = 0.01\,\text{s}$ is considered. An adaptive meshing/ remeshing strategy is employed with the thickness for the diffuse interface being $\eta = 0.3$ µm for the 1D case, and $\eta = 1$ µm for the 2D case. The mesh resolution within the diffuse interface (h_{min}) is set to 5 nm, and 70 nm for the 1D, and the 2D cases, respectively.

At each time step, the evolution of the ferrite phase radius (r_α) in the case of the numerical model is tracked from the ferrite fraction as follows:

- 1D domain: $r_\alpha(t) = d\frac{f^\alpha(t)}{2}$,
- 2D domain: $r_\alpha(t) = d\sqrt{\frac{f^\alpha(t)}{\pi}}$,

where d is the size of the domain (100 µm), and f^α is the ferrite fraction.

Results and discussion: Figs.3.15 illustrate the phase distribution at the initial state and at the end of $t = 200\,\mathrm{s}$, obtained by the LS-NM for the 1D domain case. Figs.3.16 demonstrate the corresponding solute concentration profiles along the length of the 1D domain. Likewise, Figs.3.17 depict these characteristics for the 2D case.

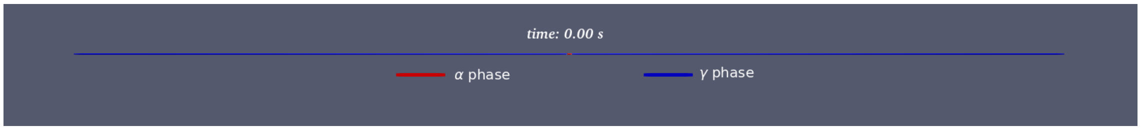

(a) $t = 0\,\mathrm{s}$

(b) $t = 200\,\mathrm{s}$

Figure 3.15: Phase distribution obtained by the level-set based numerical model (LS-NM) - 1D case

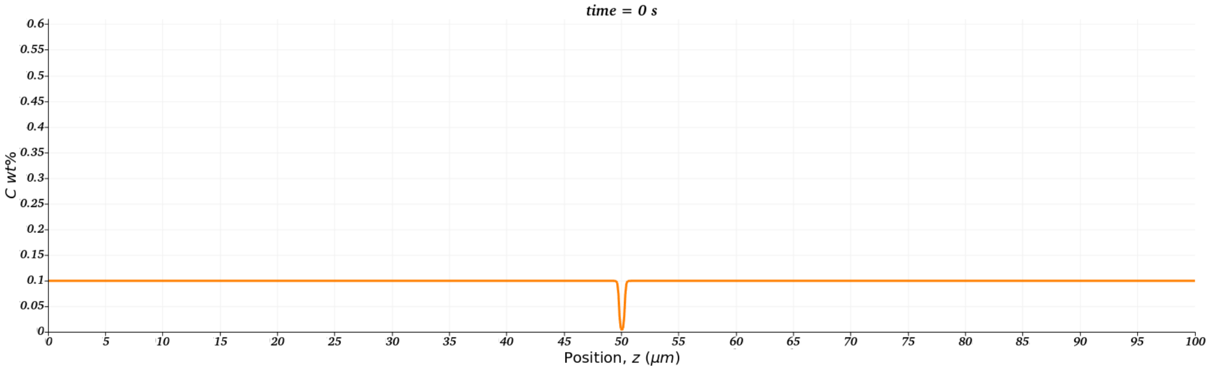

(a) $t = 0\,\mathrm{s}$

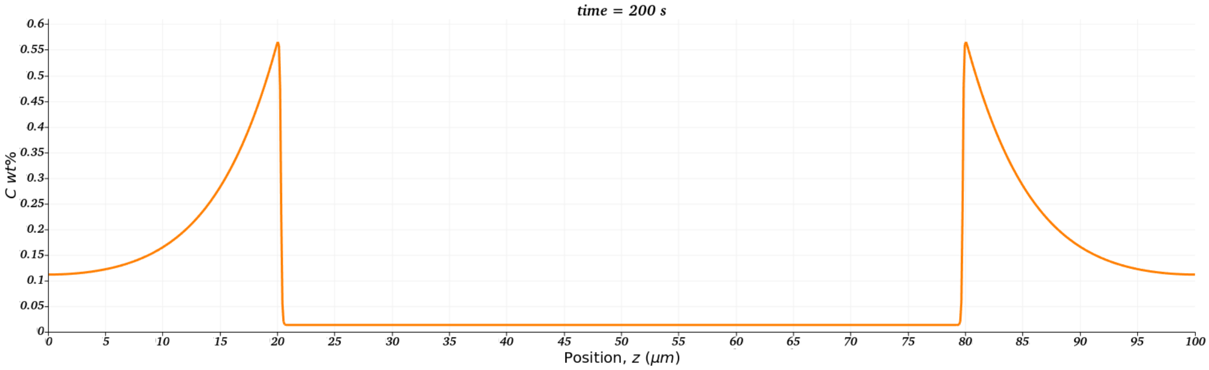

(b) $t = 200\,\mathrm{s}$

Figure 3.16: Total carbon concentration profiles predicted by the level-set based numerical model (LS-NM) - 1D case

The ferrite phase is depicted by red color, while the parent austenite phase is in blue. As the ferrite phase grows into the austenite phase, as discussed previously, the carbon solubility difference between the two phases results in a solute build up near the phase interface in the austenite side. Consequently, this creates a concentration gradient relative to the far field concentration. In the numerical model, the Fick's laws of diffusion govern the phenomenon of bulk diffusion in the austenite phase due to the resultant flux of carbon atoms. However, in the case of the sharp interface semi-analytical model, these concentration gradients are modeled with the help of an analytical function (exponential in this case), constrained by flux and mass balance relations.

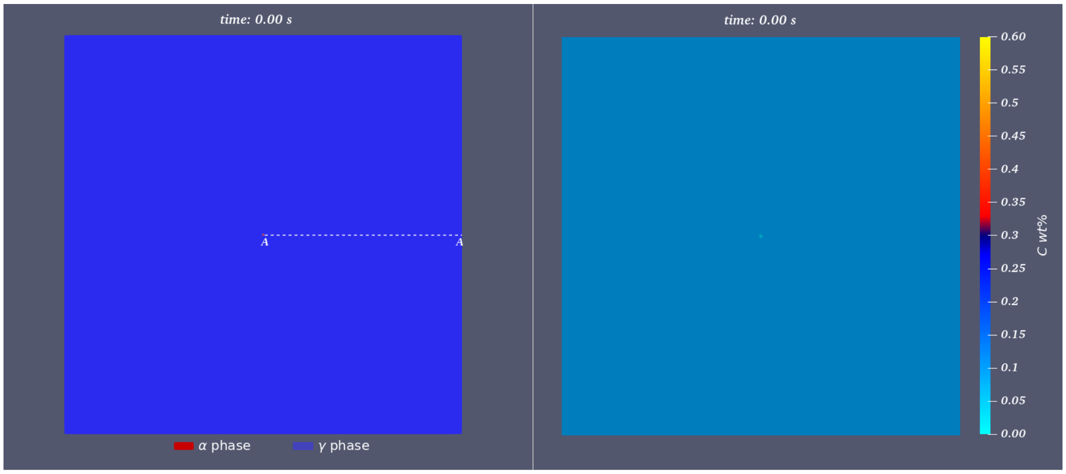

(a) $t = 0$ s

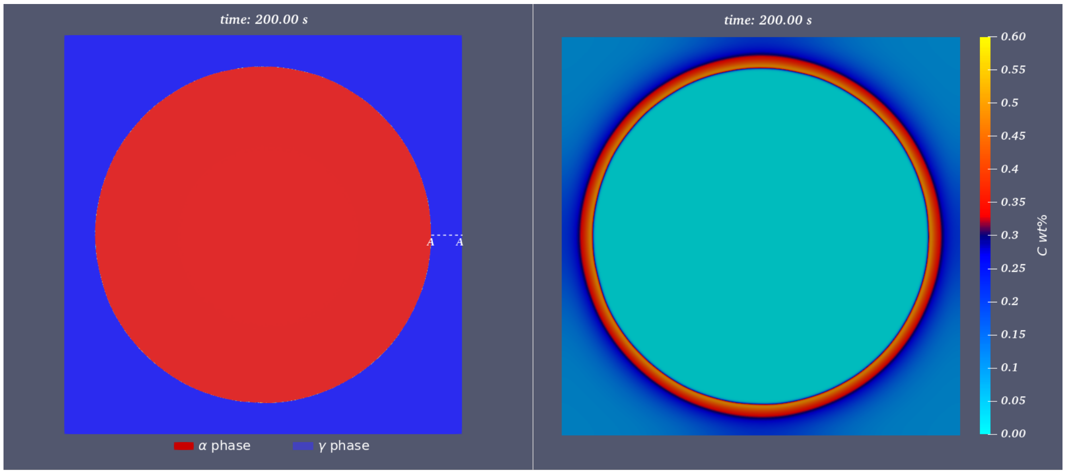

(b) $t = 200$ s

Figure 3.17: Phase (left) and carbon (right) fields predicted by the level-set based numerical model (LS-NM) - 2D case

Fig.3.18 compares the level-set based numerical (LS-NM) and the semi-analytical model (SAM) solutions for the evolution of the carbon concentration profiles in front of the α/γ phase interface in the austenite side at various instants for the 1D case. The solid lines highlight the numerical solution, while the open circular markers represent the semi-analytical solution. Fig.3.19 illustrates the same for the 2D case. The numerical solution of the austenite phase concentration has been extracted at any instant through an explicit computation using the Eq.(2.15):

$$x_C^{\gamma} = \frac{x_C}{1 + \phi(k_p^C - 1)}. \tag{3.16}$$

This computation is performed over a discrete set of nodes in front of the phase interface such that $\varphi_\alpha \leq 0$ or $0 \leq \phi \leq 0.5$ (corresponding to the austenite phase). For the 2D case, this profile is extracted along the length of the x-axis (passing through the center of the domain) from the phase interface to the domain boundary, represented by A-A in the Figs.3.17. In this context, k_p^C is the equilibrium partitioning ratio of carbon between the phases α and γ at $T = 1000\,\mathrm{K}$ and is computed as the ratio of equilibrium carbon concentration in ferrite to that of austenite at this temperature. The curves in Fig.3.18 and Fig.3.19 demonstrate good agreement at different instants between the LS-NM and the SAM in their ability to predict the solute concentration profiles in the parent phase for both the 1D and the 2D case. For the 2D case, one could observe small discrepancy between the predictions of the two models at $t = 200\,\mathrm{s}$. This could be attributed to the effects of boundary conditions of the 2D domain in the numerical model as the phase interface approaches the boundaries. In contrast, in the 1D case, as the numerically predicted position of the phase interface at $t = 200\,\mathrm{s}$ is farther from the boundaries, it is devoid of any relevant effects from the boundary conditions. It should be reminded that the semi-analytical model operates within a semi-infinite domain, while the numerical model is used on a bounded domain with imposed boundary conditions. Examining these concentration profiles highlights the mixed-mode nature of the transformation kinetics. It's evident that the interfacial concentration doesn't immediately reach the local equilibrium concentration, resulting in finite interface migration. Simultaneously, diffusion in the bulk of the austenite phase isn't instantaneous, leading to a disparity between the interfacial concentration and the bulk concentration.

In Figs.3.20, the evolution of the phase interface position in terms of the radius of the ferrite phase nucleus is compared between the SAM, LS-NM, and a phase-field based numerical model (PF-NM). On the other hand, in Figs.3.21, the comparison focuses on the evolution of the interfacial carbon concentration in the austenite side across these different models. The PF-NM results used in these plots were sourced from [9], where a similar analysis was performed. The LS-NM predictions of the interfacial concentrations have been computed by averaging x_C^{γ} over the interface (corresponding to $\varphi_\alpha = 0$ or the center of the diffuse interface with $\phi = 0.5$) at each instant. It is apparent from these curves that the LS-NM based predictions closely resemble those of the sharp interface SAM compared to the PF-NM, which predicts slower transformation kinetics. However, from Figs.3.21, the PF-NM seems to predict relatively lower interfacial carbon concentrations which in turn should provide more driving pressure during the transformation. This is supported by the curves in Figs.3.22, demonstrating the available driving pressure (multiplied by the physical interface mobility, $M_{\gamma\alpha}$) during the evolution. Yet, the higher driving pressure in PF-NM does not ultimately translate to faster interface kinetics. It's important to note that the migration of interface kinetics in a PF-NM is formulated in the form of an effective or numerical interface mobility, directly dependent on the numerical diffuse interface thickness parameter and the physical interface mobility. As detailed in [9], during the phase-field simulation, the effective interface thickness is not constant and is lower than the initially imposed value. This variation could cause the actual phase-field profile to deviate from the ideal steady-state interface contour, resulting in the effective interface mobility being lower than the imposed physical mobility, and hence yielding slower

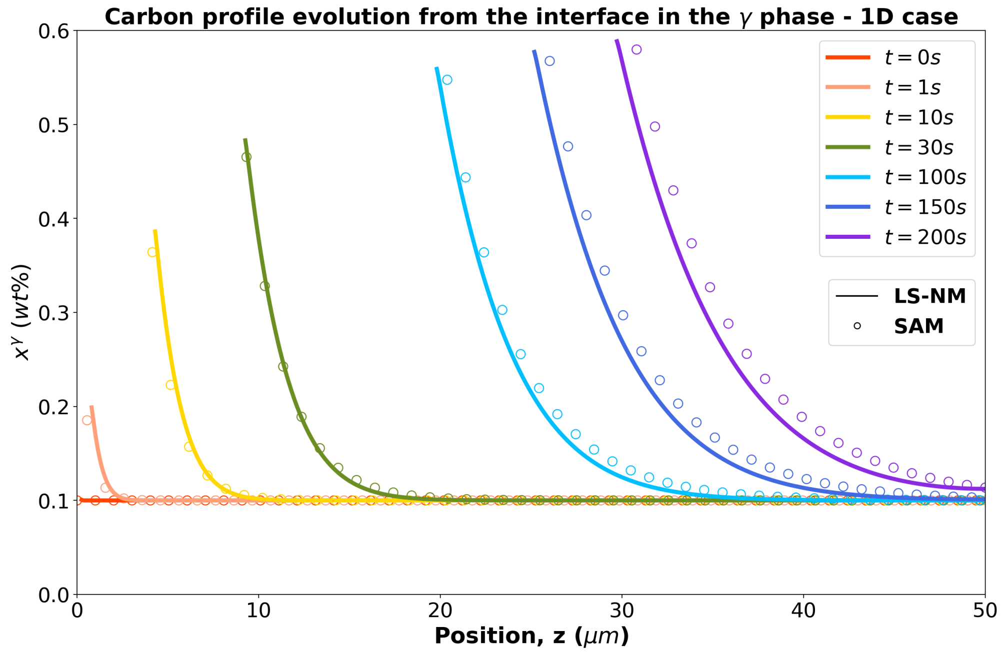

Figure 3.18: Evolution of the carbon concentration profiles in the austenite phase - 1D case

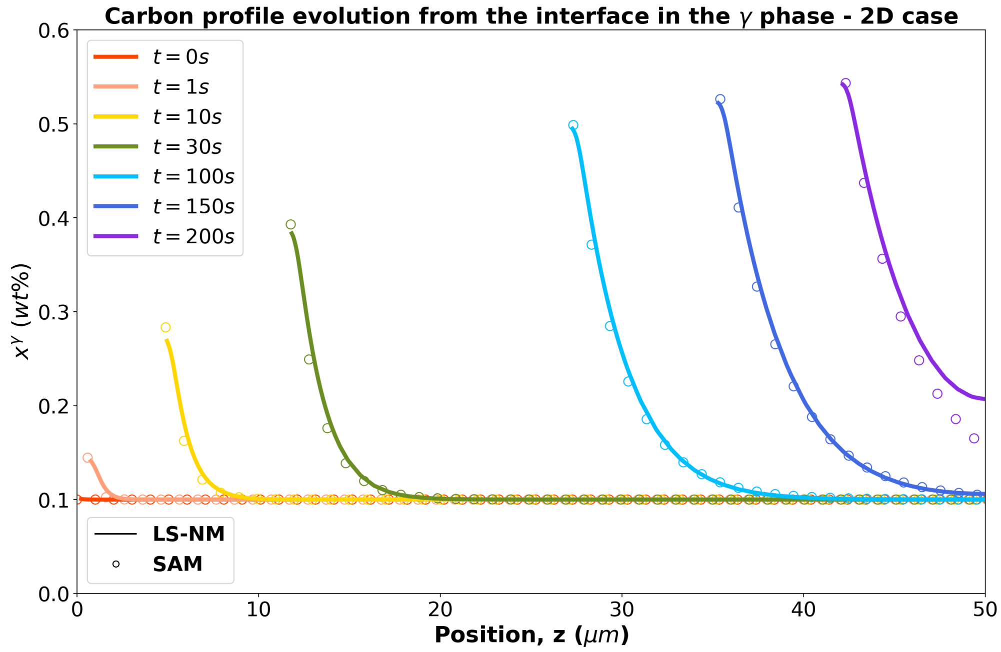

Figure 3.19: Evolution of the carbon concentration profiles in the austenite phase - 2D case, along A-A

transformation kinetics. Unlike the phase-field method, the LS-NM exclusively prescribes the interface migration kinetics using the physical interface mobility. Since the migration of level-sets is theoretically synonymous to that of the sharp interface method, only the velocity field over the iso-zero contour of the level-set ($\varphi_\alpha = 0$) is of prime importance. This stands in contrast to PF-NM where the kinetics have sense over the entire diffuse interface. So, the sharp interface nature of LS-NM in interface migration could perhaps reflect the closer resemblance observed in the predictions compared to the fully diffuse approach of PF-NM.

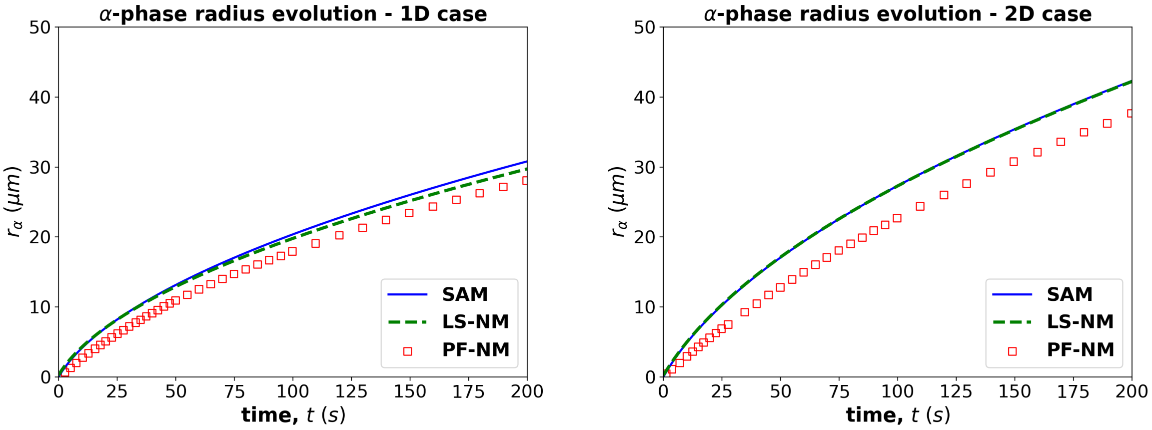

(a) 1D case (b) 2D case

Figure 3.20: Comparison of the evolution of phase interface predicted by different models

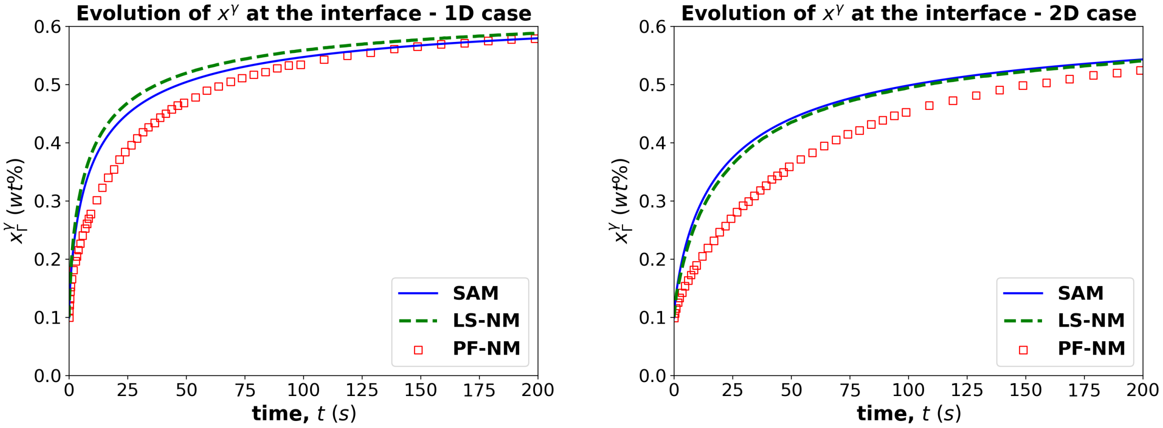

(a) 1D case (b) 2D case

Figure 3.21: Comparison of the evolution of interfacial carbon concentration in the austenite side as predicted by different models

However, it's pivotal to emphasize that the LS-NM described in this work also incorporates a diffuse interface hypothesis, albeit solely during the resolution of the diffusion equation. This could

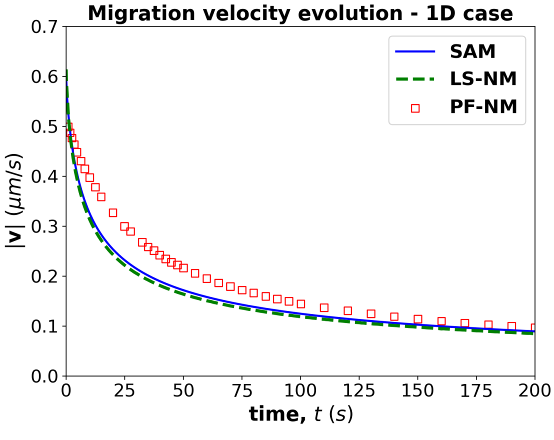

(a) 1D case

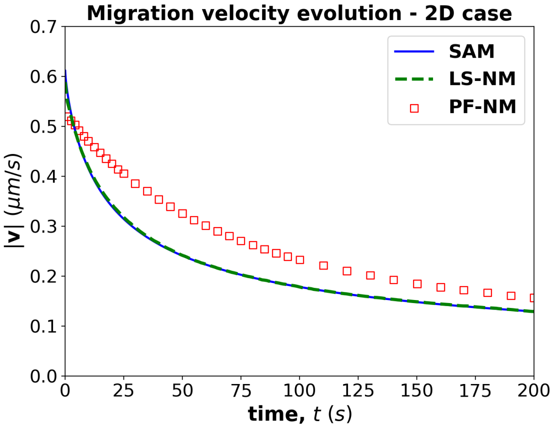

(b) 2D case

Figure 3.22: Evolution of the measure of the driving pressure available for phase transformation (multiplied by the physical interface mobility, $M_{\gamma\alpha}$) $\Rightarrow M_{\gamma\alpha}\Delta G_{\gamma\rightarrow\alpha}$

potentially exhibit a partial similarity to the behavior of the phase-field method, though within a restricted scope. The makeshift diffuse interface description, established through a phase-field like profile, computed using the hyperbolic tangent relation in Eq.(2.11): $\phi = 0.5\tanh\left(\frac{3\varphi_\alpha}{\eta}\right) + 0.5$, represents one of the steady-state solutions of a phase-field variable subject to a certain constraints and boundary conditions outlined in [4]. This solution portrays a diffuse interface of constant thickness, moving at a constant velocity along a specific normal (parameterized by a signed distance function such as φ_α). So, the level-set based numerical framework detailed in this work enforces a stationary phase-field profile at each instance during the resolution of the diffusion equation. While the diffuse interface thickness parameter in LS-NM doesn't explicitly influence interface kinetics as in PF-NM, it could impact the resolution of the solute concentration, solute mass conservation in the domain, and thus the driving pressure available. Hence, this might implicitly influence the kinetics of the transformation process. It is thus crucial to have an account of the effects of its choice in conjunction with the mesh resolution. Mecozzi et al. [9] indeed demonstrate in the context of PF-NM that enhancing mesh resolution and ensuring sufficient discretization points within the diffuse interface exhibits better convergence in their model's predictions.

3.4 Sensitivity analysis - mesh resolution, time step, diffuse interface thickness

To investigate the sensitivity of mesh size (Δx), time step (Δt), and the diffuse interface thickness (η) in the DSSPT LS-NM, we revisit the same test case previously examined, using the semi-analytical model results as our reference point.

3.4.1 Convergence with mesh resolution

The initial investigation focuses on convergence behavior concerning mesh resolution. To explore coarser mesh sizes, the initial ferrite nucleus radius is rather set to $r_\alpha^i = 2.5\,\mu\text{m}$ in this study. The diffuse interface thickness remains constant at $\eta = 1\,\mu\text{m}$, and the time step is fixed at $\Delta t = 0.01$ s. In order to mitigate intensive computational demands, unstructured FE isotropic meshes of appropriate size are selectively utilized, focusing primarily within a thick zone surrounding the interface, thus avoiding the necessity for fine resolution across the entire domain. The thick zone with fine mesh also helps in avoiding frequent remeshing. Thus, periodic remeshing is executed intermittently solely to sustain this zone around the interface throughout the evolution. Figs.3.23 provide an overview of the above idea for a particular case, depicting the meshes at both the initial and final configurations. Additionally, the analysis is constrained to $t = 100$ s, ensuring the final phase interface position remains distant from the boundaries. This approach helps in effectively isolating and mitigating potential interference from boundary conditions, subject to the selected parameters, throughout the analysis. As a comparative baseline, the identical test case is simulated using the previously described semi-analytical method, maintaining the initial ferrite radius at 2.5 µm. A local view of the meshes around the diffuse phase interface considered for this analysis is portrayed in Figs.3.24.

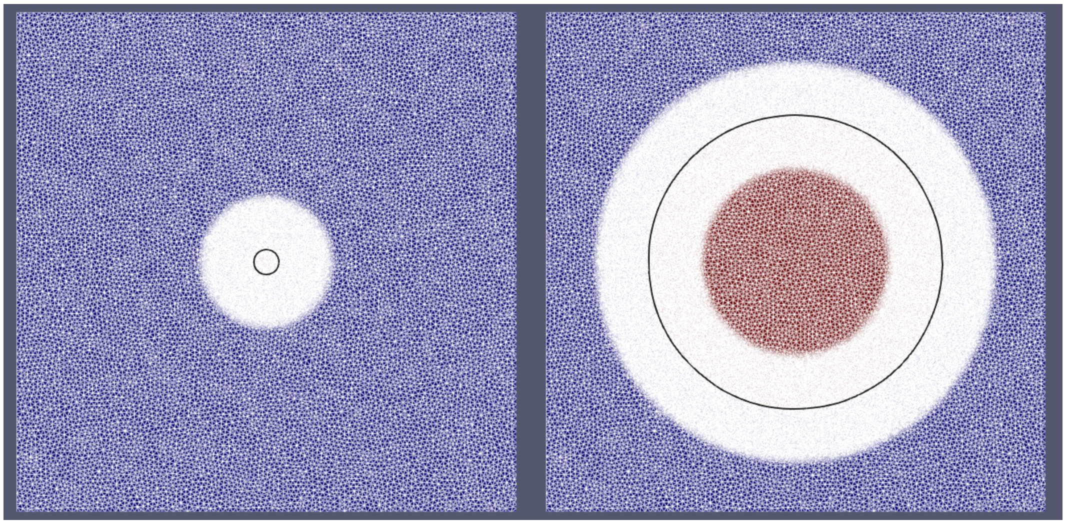

(a) Initial configuration

(b) Final configuration

Figure 3.23: Illustration of the meshing strategy considered for the analysis: the interface position is highlighted through its iso-zero contour in black

The post-analysis results are depicted in Fig.3.25, Fig.3.26, and Fig.3.27 highlighting the evolution of the phase interface, interfacial concentration and the error in mass conservation, respectively. The convergence in interface kinetics and γ-phase concentrations obtained at the interface with varying mesh resolution is notably apparent. In the case where $\Delta x = 0.5\,\mu\text{m}$ results in only about 2 mesh elements within the diffuse interface, the solute mass is visibly not conserved, as observed in Fig.3.27, attributed to poor resolution across the phase interface. Consequently, the phase interface

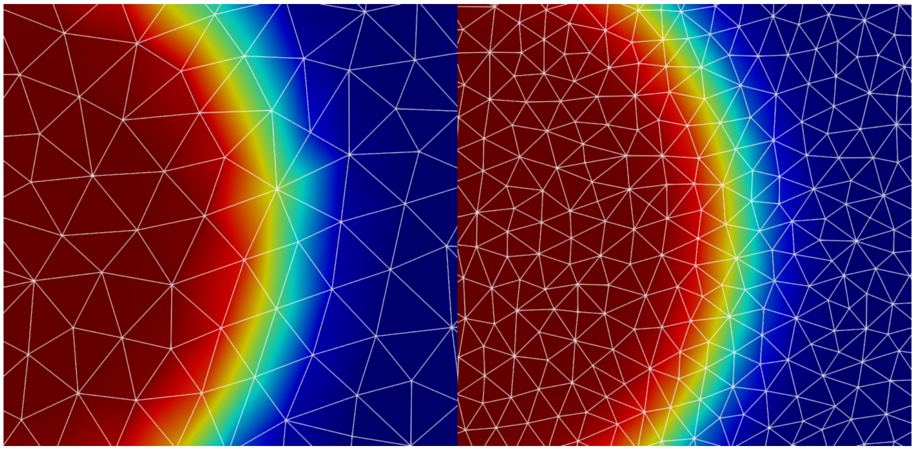

(a)
$\Delta x \approx 0.5\,\mu\text{m}$

(b)
$\Delta x \approx 0.25\,\mu\text{m}$

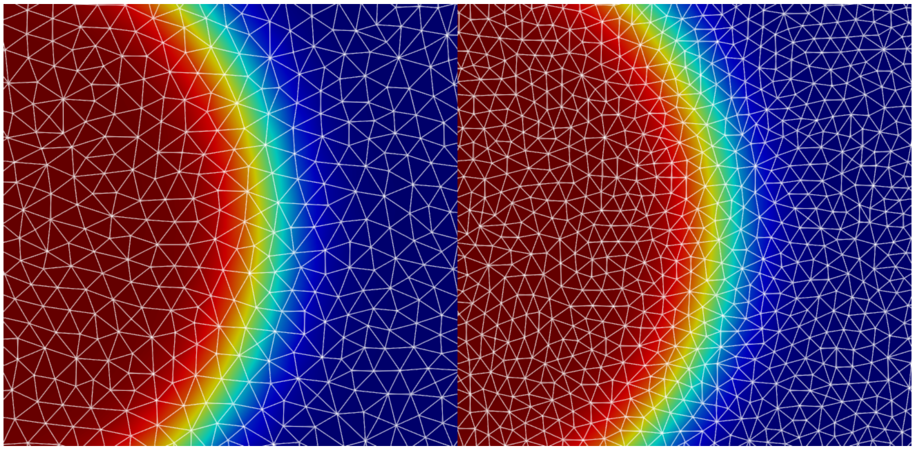

(c)
$\Delta x \approx 0.2\,\mu\text{m}$

(d)
$\Delta x \approx 0.14\,\mu\text{m}$

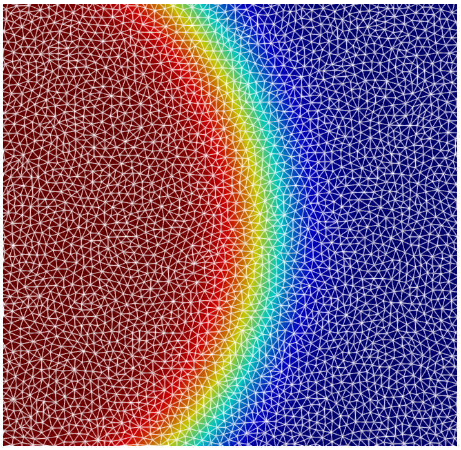

(e)
$\Delta x \approx 0.07\,\mu\text{m}$

Figure 3.24: Local view of the different meshes considered across the diffuse phase interface

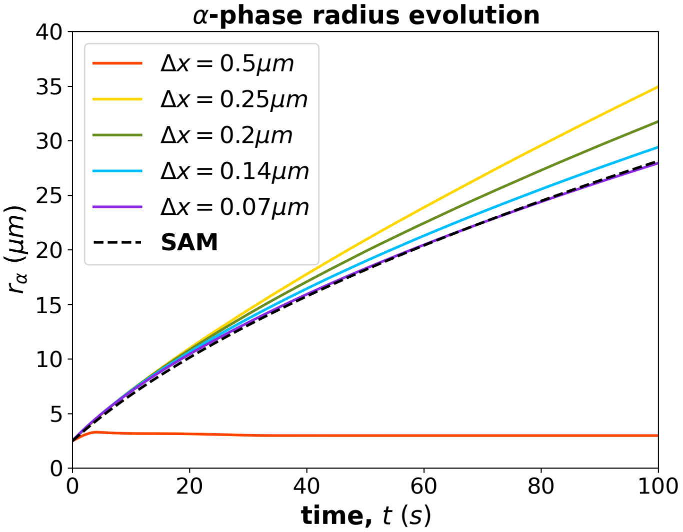

Figure 3.25: Convergence in interface kinetics as influenced by mesh resolution

remains stationary, indicated by the red curve in Fig.3.25. Decreasing the mesh size increases the number of discretization elements ($\eta/\Delta x$) within the diffuse interface. This enhances the accurate depiction of the notoriously sharp gradients present across the phase interface during the resolution of the diffusion equation. A finer mesh around the phase interface also enhances the description of the prescribed velocity field for interface migration, providing more precise positions of the iso-zero level-set contours. The mass conservation also improves with better mesh resolution as emphasized in Fig.3.27. In Fig.3.26, it's notable that the SAM marginally overestimates the interface concentration at the initial time step. The formulation of this sharp interface model theoretically assumes a zero initial ferrite nucleus, where the interface concentration then gradually deviates from the nominal composition of 0.1 wt%C as the nucleus grows. Enforcing a non-zero ferrite nucleus while maintaining the nominal composition at the interface creates this small jump in the sharp interface model's first prediction.

3.4.2 Influence of diffuse interface thickness

As emphasized in one of the earlier sections, though the diffuse interface thickness (η) in this LS-NM shares a semblance with that in a PF-NM, its implications and role in the interface migration scheme of the model may not align in the same manner. Unlike in PF-NM, η doesn't directly take part in the interface migration process, and its impact on interface kinetics is not as explicit as in the case of a PF-NM. Its selection rather influences the resolution of solute redistribution across the phase interface and the resultant quality of mass conservation. Ultimately, this can potentially influence the kinetics prescribed for migration. Theoretical considerations advocate for η to align with the physical thickness of a phase boundary, which typically spans a few inter-atomic distances. However, computational constraints hinder the use of extremely small values due to the impractical mesh resolution required at the mesoscopic scale. Hence, the numerical choice of η is primarily constrained by the practicality of the underlying mesh resolution.

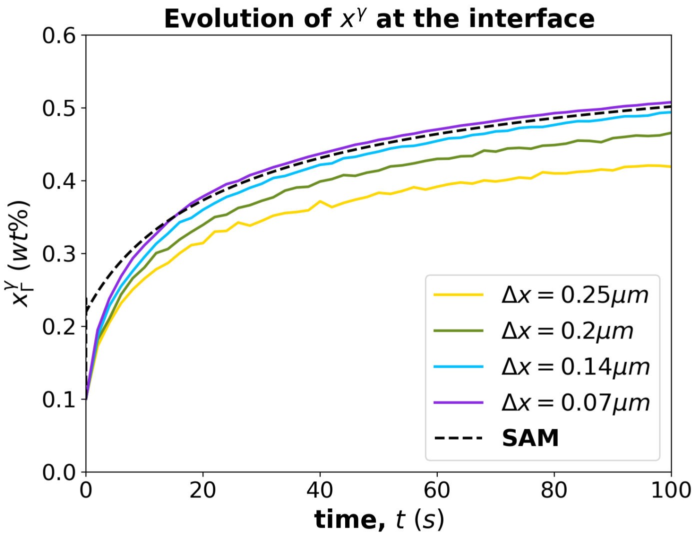

Figure 3.26: Convergence in γ phase concentration at the interface with mesh resolution

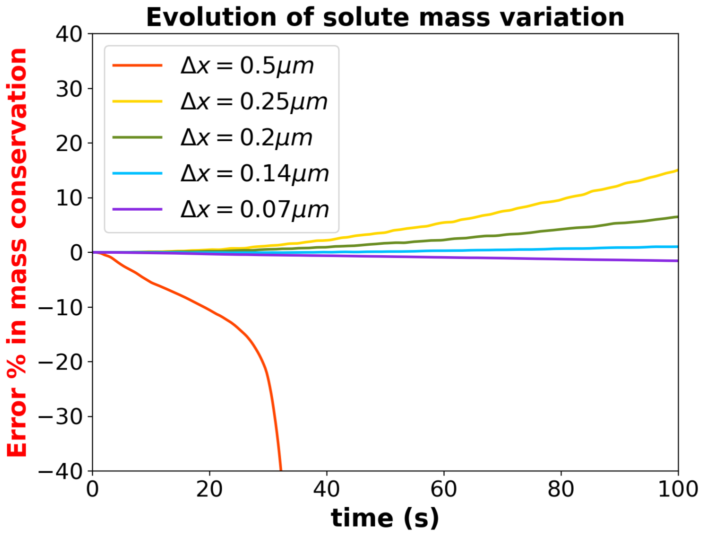

Figure 3.27: Evolution of mass conservation error with mesh size

To explore the impact of η, we consider the same setup as the previous analysis but with a fixed mesh size of $\Delta x = 0.07$ µm. The initial ferrite radius remains at $r_\alpha^i = 2.5$ µm to allow the analysis of larger η values. The interface thickness is varied as a function of the number of discretization elements approximately within the diffuse interface. Fig.3.28, Fig.3.29 and Fig.3.30 compare the results obtained for different η values with those obtained from the SAM. It could be inferred that, a certain minimum number of mesh elements is essential within the diffuse interface zone. For a specific mesh resolution, smaller η values result in steeper gradients across the diffuse interface, making them more susceptible to discretization and interpolation errors. Increasing η tends to smoothen gradients across the interface, aiding in a more accurate representation or capture of

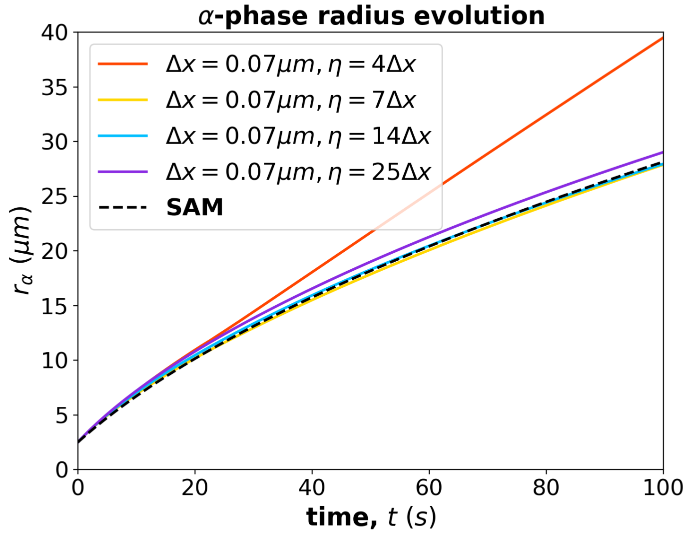

Figure 3.28: Influence of diffuse interface thickness on interface kinetics

the behavior within the diffuse region. In Fig.3.30, it's evident in the case with 4 mesh elements (η = 0.28 µm) that mass conservation is compromised, contributing to an underestimation of the interface concentration depicted in Fig.3.29. A lower interface concentration results in increased driving pressure and consequently faster kinetics, explaining the overestimated interface position in Fig.3.28. Conversely, for other cases with increased η values comprising of sufficient mesh elements, the predicted interface kinetics exhibit fairly consistent behavior, displaying minimal variation for this chosen mesh size.

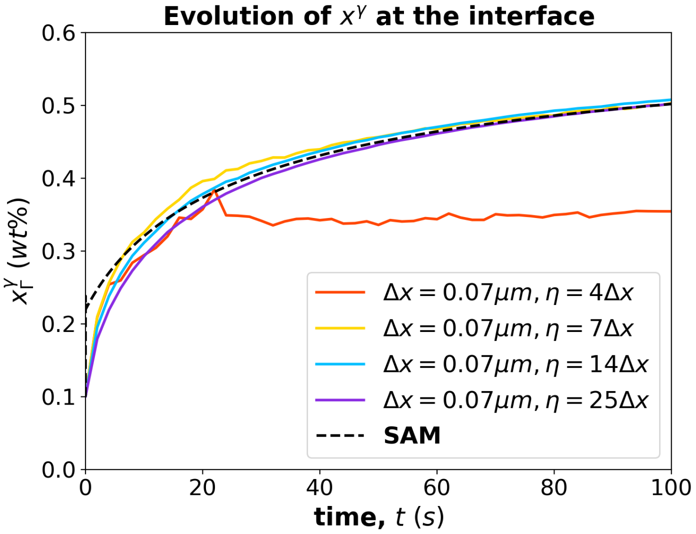

Figure 3.29: Variation in interfacial concentration observed across different selections of the parameter η

Larger η values may allow for the utilization of a coarser mesh resolution. Hence, there might

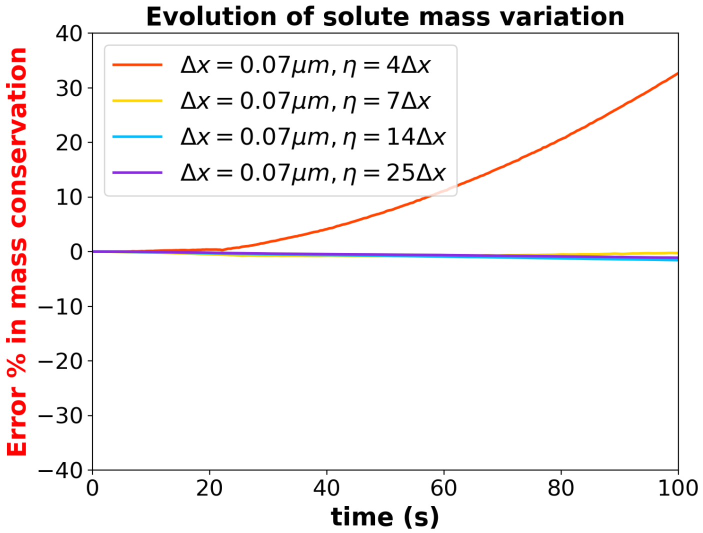

Figure 3.30: Impact of diffuse interface thickness on solute mass conservation

be a temptation to decrease computational costs by opting for a larger mesh resolution. However, increasing η may lead to a less meaningful representation of physical fields like concentration, introducing more nonphysical aspects into the model. Moreover, a coarser mesh might compromise the precision of level-set representation and interface migration. Figs.3.31, and Fig.3.32 showcase a similar analysis conducted using a coarser mesh (and hence larger η values). Despite maintaining good mass conservation, the variability in interface kinetics becomes more pronounced with η, and these predictions seem to slightly deviate from the expected reference curves obtained from the SAM.

Although mesh resolution stands as a primary criterion for choosing the diffuse interface thickness, other contributing factors could also influence this selection. Considering the characteristic size of a grain representing a phase is also important to avoid setting unrealistically large η values relative to the grain size. Mecozzi et al. in [4] also propose an upper limit for η in their PF-NM, set to the characteristic diffusion length in austenite phase ($L_\gamma = \frac{D_\gamma^C}{\|v\|_{max}}$), to prevent potential numerical instability problems. However, based on the author's knowledge, the utilization of η values larger than the diffusion length in the current LS-NM did not seem to cause any stability issues.

On the other hand, the choice of η also impacts the behavior of grains or particles nearer to domain boundaries, affecting their interaction with the boundary conditions. As discussed in the previous chapter, the local nature of boundary conditions shifts from pure Neumann type to Robin type when a portion of the phase interface nears or contacts the boundaries. This condition may revert to pure Neumann type as the interface moves away from that local region of the boundary. Fig.3.33 illustrates a magnified portion of a particular case showcasing the solute contours (thick lines) in a scenario where the phase interface evolves in proximity to a boundary region. On the left, the depiction shows the initial stage when the diffuse phase interface has yet to contact the boundaries. At this point, the solute contours run orthogonal to the boundaries, complying with pure Neumann

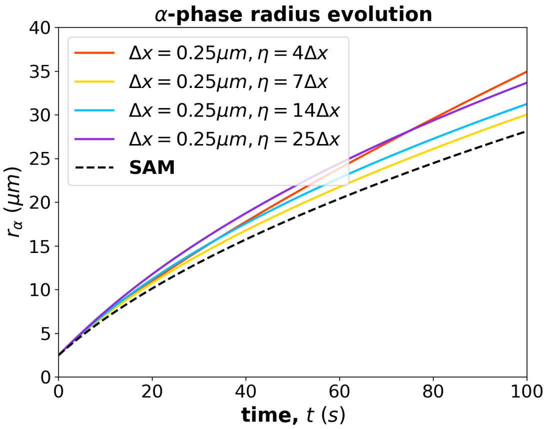

(a) 1D case (b) 2D case

Figure 3.31: Influence of larger η on interface kinetics and interface concentrations using a coarser mesh

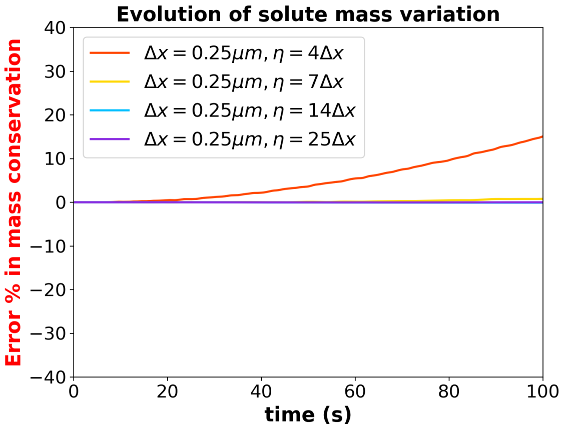

Figure 3.32: Impact of diffuse interface thickness on solute mass conservation for the coarser mesh scenario

type boundary conditions. On the right, in a subsequent moment, a segment of the diffuse phase interface is in contact with the boundaries. In this scenario, the solute contours surrounding the boundary-adjacent region no longer maintain orthogonality, trying to transition to the Robin type boundary conditions within that localized area. During this transition between boundary condition types, sharp solute gradients or their flux within the interfacial zone might introduce errors in solute mass conservation, depending on mesh resolution and time step. A thicker interface has an extended interaction with the boundaries. An uncharacteristically larger η could also alter the dynamics between nearby grains or particles of the same phase. Hence, selecting the diffuse interface thickness demands caution, striking a balance between employing a reasonably coarse mesh with enough elements within the diffuse interface and avoiding unrealistically large η values. As a general guideline, about $7-20$ mesh elements within the diffuse interface often represents a reasonable compromise. However, specific simulation cases or situations might necessitate finer discretization within the interface to achieve greater accuracy in solute mass conservation.

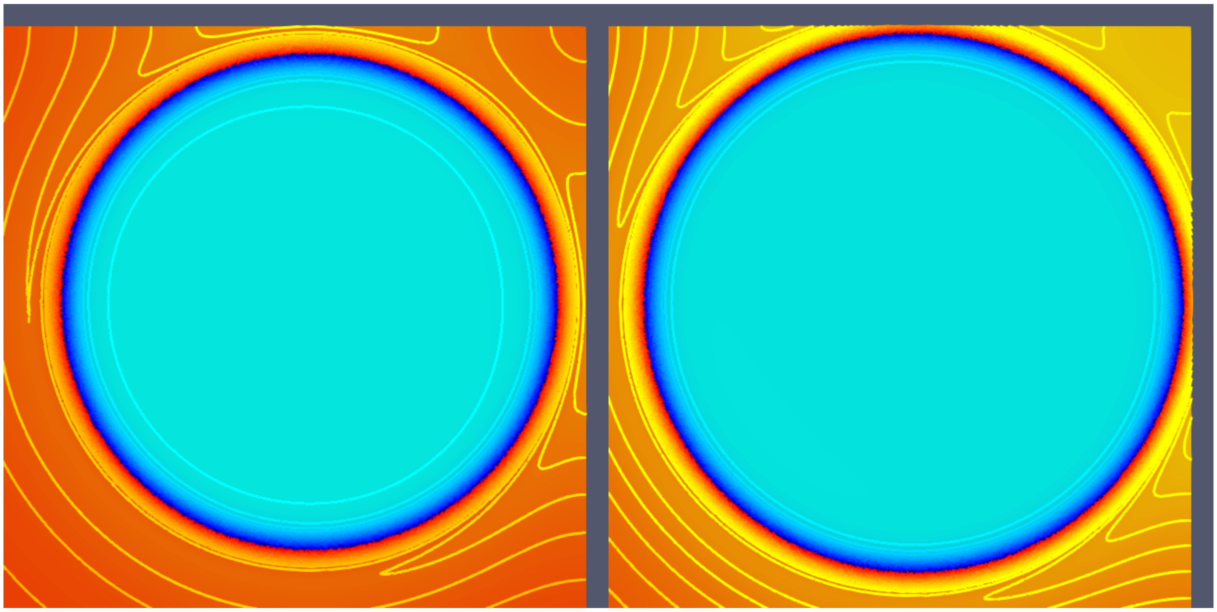
(a) Pure Neumann boundary conditions

(b) Local switch to Robin type

Figure 3.33: Illustration of solute contours as the phase interface interacts with the boundary region: solute contours respecting null Neumann boundary conditions (left), solute contours respecting Robin type boundary conditions locally (right)

3.4.3 Time step analysis

We now examine the convergence behavior of the LS-NM with time steps using the same test case. We maintain a fixed mesh resolution of $\Delta x = 0.07$ µm and a constant diffuse interface thickness of $\eta = 1$ µm. The ferrite nucleus is set to zero radius (theoretically, but numerically $r_{\alpha}^{i} = 0.25$ µm) in this analysis, since we are not restricted in terms of the choice of mesh size or the interface thickness.

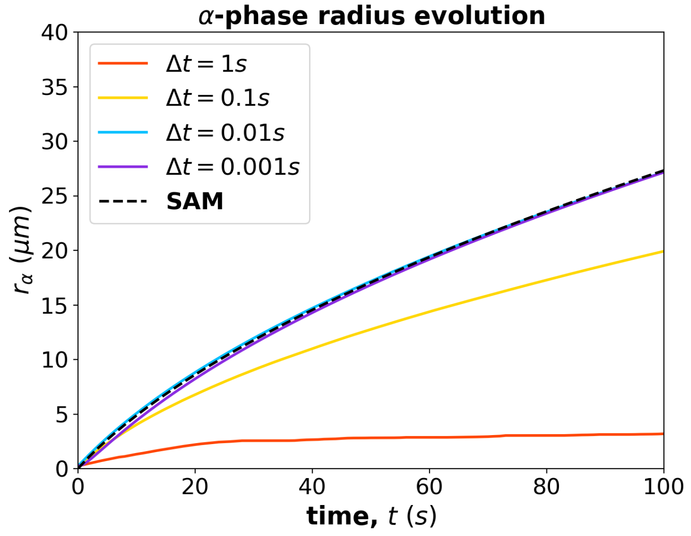

Figure 3.34: Convergence of interface kinetics with time step

The results post analysis are demonstrated in Fig.3.34, Fig.3.35 and Fig.3.36. Smaller time steps clearly establish convergence in interface kinetics and interfacial concentrations. Moreover, the quality of mass conservation demonstrates improvement with reduced time steps, as illustrated in Fig.3.36. The choice of resolution time step becomes crucial to accurately capture topological changes, especially in scenarios with rapid evolution kinetics.

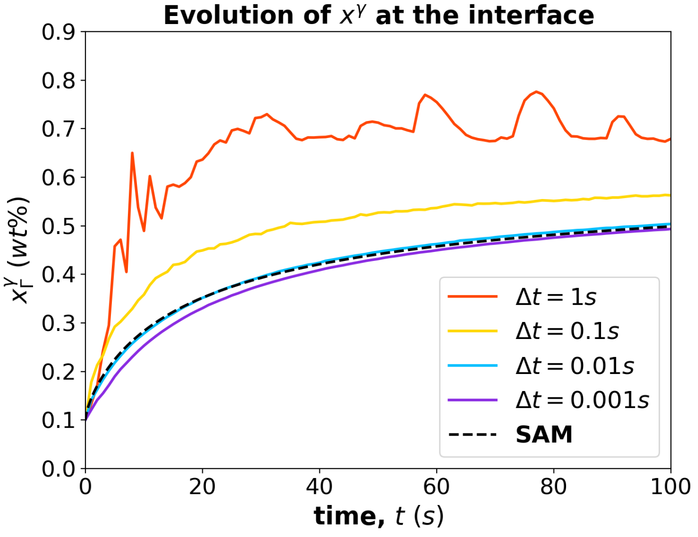

Figure 3.35: Convergence in evolution behavior of interfacial concentration with time step

Even if an implicit time scheme strategy is considered in this work, as a general rule of thumb and as our time scheme is of the first order, the time step can be roughly estimated by ensuring a CFL-like condition such that the maximum distance migrated by the interface within each time step

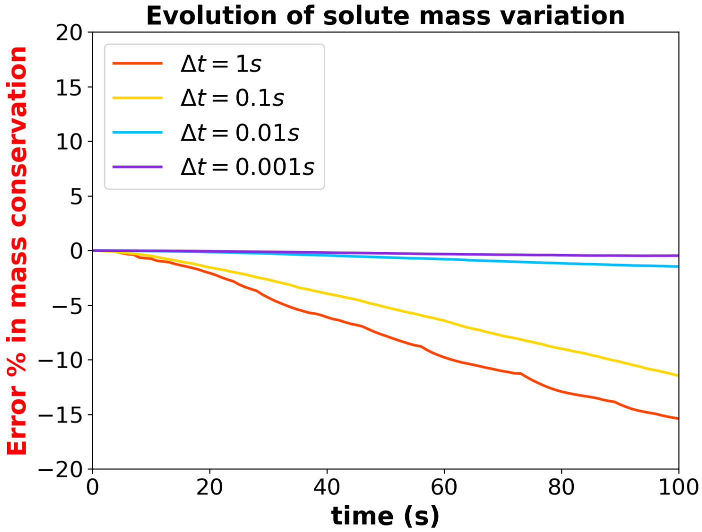

Figure 3.36: Impact of choice of time step on solute mass conservation

remains within the bounds of the characteristic mesh size (Δx) to avoid important error in time:

$$\Delta t = k_{\Delta t} \frac{\Delta x}{\max \|\boldsymbol{v}\|}, \tag{3.17}$$

where $k_{\Delta t}$ is a constant (< 1) and $\boldsymbol{v}$ is the migration velocity.

Documented in [10], the direct reinitialization method contributes as a minor source of numerical errors. Given that this reinitialization procedure is executed at each time step within the current numerical formulation, employing extremely small time steps might result in the accumulation of these errors. Hence, it's equally essential to avoid excessively reducing time steps when unnecessary. For computational efficiency, one could easily employ the strategy of adaptive time stepping following the ideology outlined in Eq.3.17. However, within the scope of this work, constant time stepping law is predominantly utilized across most simulations.

3.5 Proposition of a new 1D semi-analytical mixed-mode model

Most classical sharp interface semi-analytical models for phase transformation impose the hypothesis of instantaneous diffusion in the product phase to simplify and close the mathematical formulation. This enables to model and resolve only the concentration profiles in the parent phase. The driving pressure is then only influenced by the interfacial concentration of the parent phase. In this section, an attempt is made to allow for finite diffusion in the product phase as well, along with that of the parent phase. A semi-analytical sharp interface formulation for mixed-mode phase transformation is thus proposed for a bounded 1D domain. The bounded domains help provide necessary conditions in the quest to close the mathematical formulation. This semi-analytical formulation is based on an extension of the existing model proposed in the works of Chen et al. [11] for a semi-infinite domain assuming instantaneous diffusion in the product phase.

The proposed model has been published in the context of this Ph.D. work [12], and certain figures shall be reproduced here to explain the formulation. As proposed in the works of Chen et al. [11], the idea is to assume the solute concentration profile in the γ phase ($x^{\gamma}(z)$) at time t to be a quadratic function of position (z):

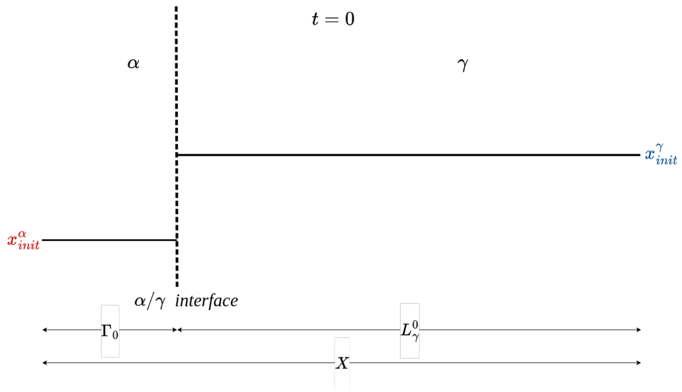

(a) Initial concentration profile at $t = 0\,\mathrm{s}$

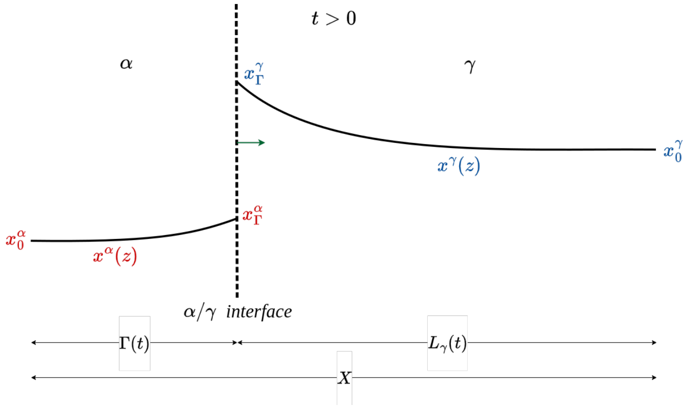

(b) Expected concentration profile at $t > 0\,\mathrm{s}$

Figure 3.37: Illustration of concentration profiles expected at different instants

$$x^{\gamma}(z) = A_1 + A_2(z - \Gamma) + A_3(z - \Gamma)^2 \qquad \forall \{z : \Gamma(t) < z \leq X\}\,, \tag{3.18}$$

where A_1, A_2 *and* A_3 are pre-factors, $\Gamma(t)$ is the phase interface position at time t. However, Chen et al. assumed diffusion to be instantaneous in the α phase, thus immediately attaining the equilibrium concentration, $x^{\alpha}|_{eq}$. This assumption is however not mandatory. Instead, one can assume that the solute concentration profile in the α phase follows a similar quadratic function of z:

$$x^{\alpha}(z) = B_1 + B_2(z - \Gamma) + B_3(z - \Gamma)^2 \qquad \forall \{z : 0 \leq z < \Gamma(t)\}\,. \tag{3.19}$$

Fig.3.37 illustrates an example of concentration profiles expected in a domain of length X. The length of γ side at any instant is given by $L_{\gamma}(t)$, such that $X = \Gamma(t) + L_{\gamma}(t)$. x^{α}_{Γ} and x^{γ}_{Γ} are the concentrations at the sharp interface of the α and γ phases, respectively. Likewise, x_0^α and x_0^γ are the far-field concentrations in the corresponding phases.

The pre-factors of Eqs.(3.19) and (3.18) can be determined by applying the following boundary conditions:

$$\begin{cases} x^\alpha(z=\Gamma^-) = x_\Gamma^\alpha & x^\gamma(z=\Gamma^+) = x_\Gamma^\gamma \\ x^\alpha(z=0) = x_0^\alpha & x^\gamma(z=X) = x_0^\gamma \\ \frac{\partial x^\alpha}{\partial z}\Big|_{z=0} = 0 & \frac{\partial x^\gamma}{\partial z}\Big|_{z=X} = 0 \end{cases} \quad \forall t > 0. \tag{3.20}$$

The concentration profiles are then found to be:

$$\begin{cases} x^\alpha(z) = x_0^\alpha + \left(x_\Gamma^\alpha - x_0^\alpha\right)\left(\frac{z}{\Gamma}\right)^2, & \forall\{z : 0 \le z < \Gamma(t)\} \\ x^\gamma(z) = x_0^\gamma + \left(x_\Gamma^\gamma - x_0^\gamma\right)\left(1 - \frac{(z-\Gamma)}{L_\gamma}\right)^2, & \forall\{z : \Gamma(t) < z \le X\} \end{cases} \quad \forall t > 0. \tag{3.21}$$

L_γ serves as the width of the concentration profile (x^γ) on the γ side. Likewise, the width of the profile (x^α) on the α side is controlled by Γ.

Considering the boundary conditions, the solute mass needs to be conserved at any time. So, applying macroscopic solute mass balance at the time, $t > 0$, we obtain:

$$\int_0^{\Gamma(t)} x^\alpha(z)dz + \int_{\Gamma(t)}^{X} x^\gamma(z)dz = \int_0^{\Gamma_{init}} x_{init}^\alpha dz + \int_{\Gamma_{init}}^{X} x_{init}^\gamma dz. \tag{3.22}$$

By imposing that the solute concentrations at the interface redistribute at a constant ratio equal to the partitioning ratio at equilibrium (Eq.(2.14)) and that the far-field concentrations also respect this ratio at any instant, we obtain:

$$x_\Gamma^\alpha = k_p x_\Gamma^\gamma \quad and \quad x_0^\alpha = k_p x_0^\gamma, \tag{3.23}$$

with k_p computed using Eq.(2.95). Expanding Eq.(3.22) with the above hypotheses, we obtain:

$$x_0^\gamma = \frac{x_\Gamma^\gamma\left[\left(\Gamma^3 - X^3\right)k_p - L_\gamma\Gamma^2\right] + 3\Gamma^2\Gamma_{init}\left[x_{init}^\alpha - x_{init}^\gamma\right] + 3x_{init}^\gamma X\Gamma^2}{2L_\gamma\Gamma^2 + k\left[4\Gamma^3 - X^3\right]}. \tag{3.24}$$

The kinetic equation for interface migration is given by:

$$\frac{\partial\Gamma}{\partial t} = \boldsymbol{v}\cdot\boldsymbol{n} = v_n, \tag{3.25}$$

with $v_n = M_{\gamma\alpha}\Delta G_{\gamma\to\alpha}$ without capillarity effects. The driving pressure, $\Delta G_{\gamma\to\alpha}$ is given by the linearization of the phase diagram as already detailed in the previous chapter (section 2.3.4):

$$\Delta G_{\gamma\to\alpha} = \Delta S^{\gamma\alpha}\left[\left(T^R - T\right) + 0.5m_{A-i}^{\alpha/(\alpha+\gamma)}\left(x_\Gamma^\alpha - x^\alpha|_R\right) + 0.5m_{A-i}^{\gamma/(\alpha+\gamma)}\left(x_\Gamma^\gamma - x^\gamma|_R\right)\right]. \tag{3.26}$$

Considering no accumulation of solutes at the interface, the inward and outward solute fluxes at the interface must respect the following balance equation:

$$v_n\left[x_\Gamma^\gamma - x_\Gamma^\alpha\right] = [\![\boldsymbol{J}]\!]\big|_\Gamma\cdot\boldsymbol{n} = D_\alpha^i\frac{\partial x^\alpha}{\partial z}\bigg|_\Gamma - D_\gamma^i\frac{\partial x^\gamma}{\partial z}\bigg|_\Gamma. \tag{3.27}$$

Further expanding and making necessary substitutions, one can rewrite this equation as:

$$f(x_\Gamma^\gamma) = M_{\gamma\alpha}\Delta G_{\gamma\to\alpha} x_\Gamma^\gamma \left(1 - k_p\right) - \frac{2D_\alpha^i k_p}{\Gamma}\left(x_\Gamma^\gamma - x_0^\gamma\right) - \frac{2D_\gamma^i}{L_\gamma}\left(x_\Gamma^\gamma - x_0^\gamma\right) = 0. \tag{3.28}$$

Since $\Delta G_{\gamma\to\alpha}$, and x_0^γ are both functions of x_Γ^γ, the above Eq.(3.28) is a non-linear equation.

Resolution procedure:

- Eq.(3.28) is resolved iteratively for $f(x_\Gamma^\gamma) = 0$ to compute x_Γ^γ.
- From x_Γ^γ; x_Γ^α, and v_n are computed.
- The interface is then migrated using Eq.(3.25) with an explicit Euler scheme:

  $$\Gamma^{n+1} = \Gamma^n + v_n \Delta t,$$

  where n is the index for time stepping and Δt is the chosen time step. $L_\gamma^{n+1} = X - \Gamma^{n+1}$ can then be computed.
- x_0^γ, x_0^α, and the concentration profiles $x^\alpha(z)$ and $x^\gamma(z)$ at time $t^{n+1} = (n+1)\Delta t$ are then computed

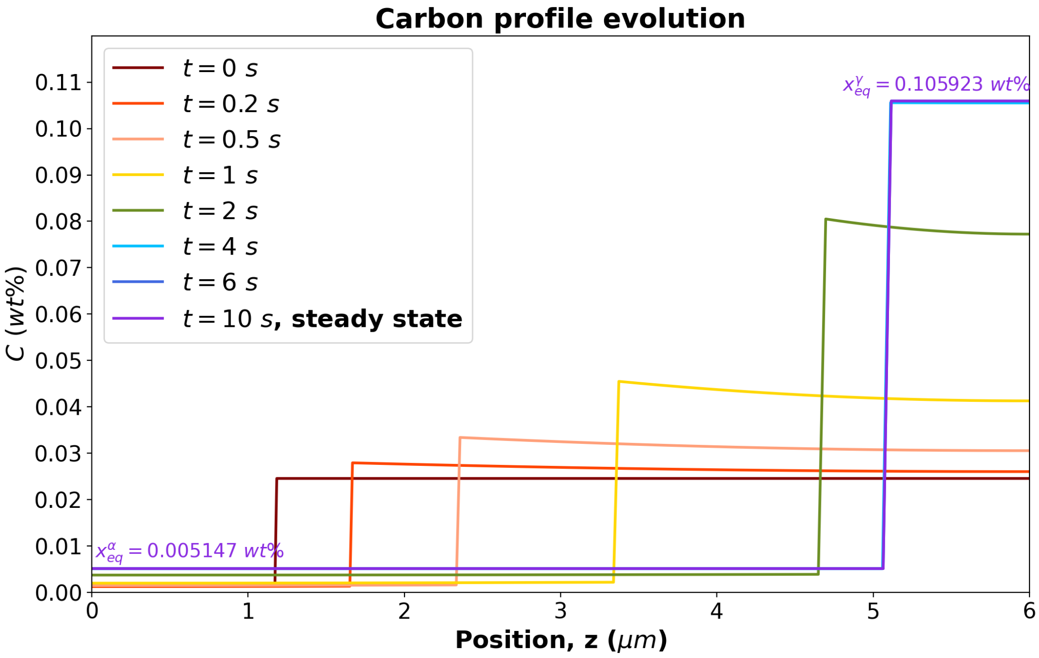

Figure 3.38: Carbon profiles predicted by the semi-analytical model for the case with instantaneous cooling

Illustration test case: In order to compare the predictive capabilities of the above semi-analytical model with that of the level-set based numerical model (LS-NM), the same pseudo-1D test case considered in section 3.2.1 under instantaneous cooling for Fe - 0.02 wt%C is utilized. Both the methods use the same form of description for the driving pressure. Fig.3.38 shows the evolution of carbon profiles along with the equilibrium concentrations predicted by the semi-analytical model for the instantaneous cooling case. The concentrations obtained correspond closely with that of the LS Simulation ($x_{eq}^{\alpha}\big|_{num} = 0.0051456$ wt%, and $x_{eq}^{\gamma}\big|_{num} = 0.10586$ wt%).

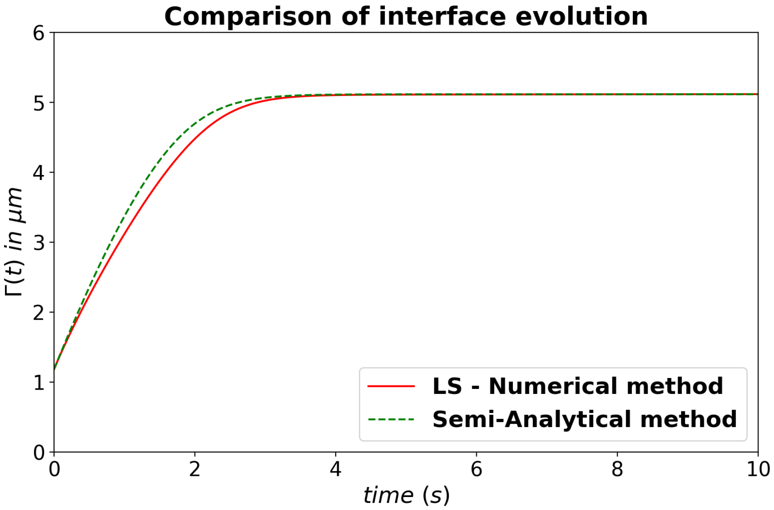

Figure 3.39: Comparison of interface evolution predicted by the semi-analytical and the LS based numerical model

Fig.3.39 compares the kinetics of interface evolution by the two methods. The kinetics and also the steady state interface position obtained are in general good agreement between the two methods. During the initial stages, the interfacial carbon concentrations predicted by the semi-analytical method seem to be slightly lower as demonstrated in Figs.3.40. Lower local concentrations imply higher driving pressure, and hence relatively faster kinetics as observed in the Fig.3.39 during the early stages. Nevertheless, as the transformation proceeds, they seem to converge well, especially as the equilibrium is approached. The strong hypothesis in Eq.(3.23) of forcing the far-field concentrations to also respect the equilibrium partitioning ratio becomes more reasonable and valid as the two phases tend towards their state of equilibrium. The general trends are similar and congruent which explains the good agreement with the steady state interface position as well the kinetics.

Figs.3.41 further demonstrate that the above semi-analytical model is reasonably capable of reproducing certain trends of the transformation kinetics for the non-isothermal scenarios as well.

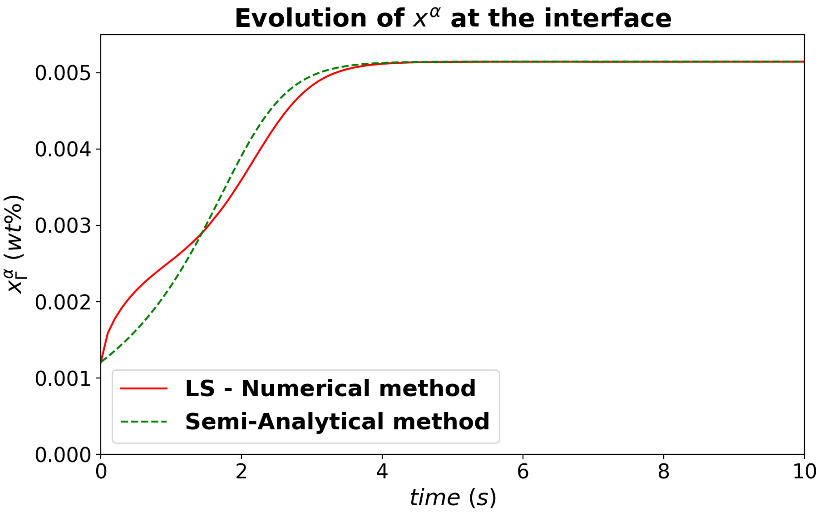

(a) x_Γ^α evolution

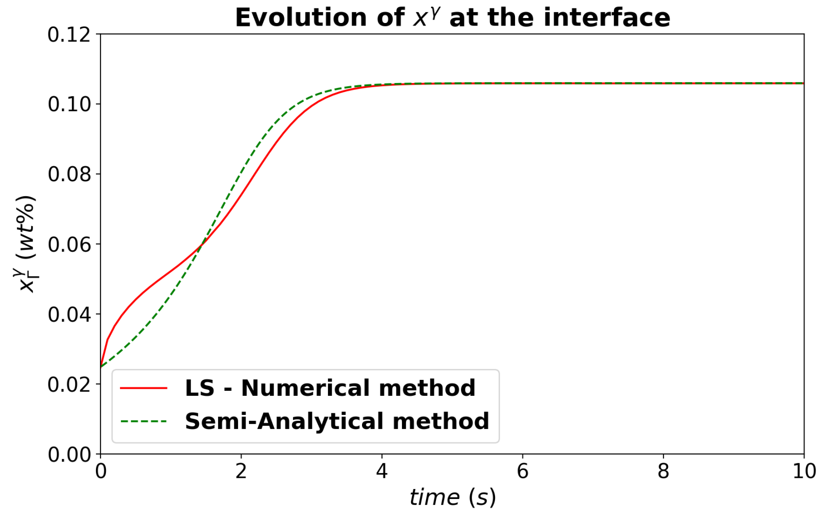

(b) x_Γ^γ evolution

Figure 3.40: Comparison of the evolution of carbon concentration at the interface predicted by the semi-analytical and the numerical model

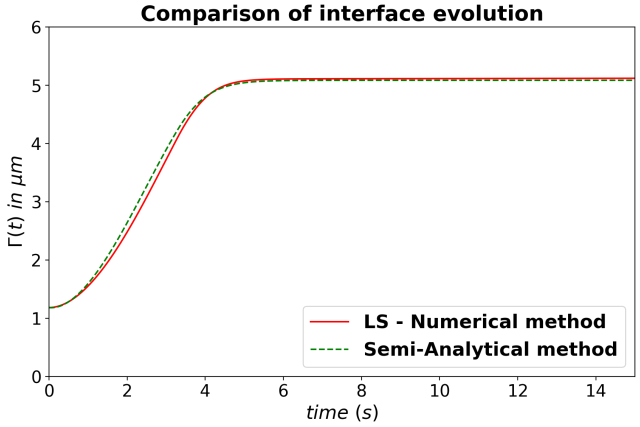

(a) Rapid cooling, $\dot{T} = -10\,\mathrm{K{\cdot}s^{-1}}$

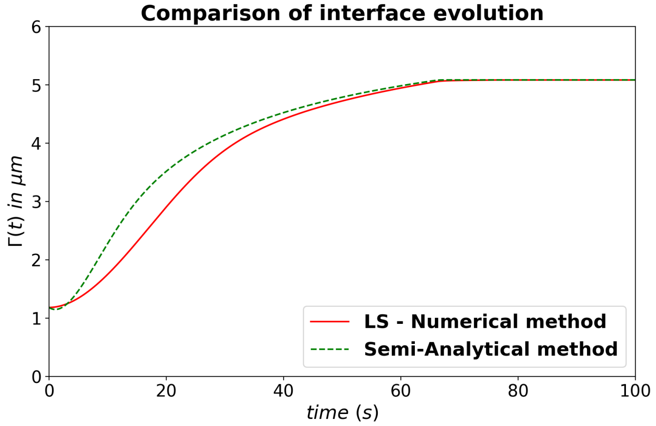

(b) Slow cooling, $\dot{T} = -0.5\,\mathrm{K{\cdot}s^{-1}}$

Figure 3.41: Comparison of interface evolution predicted by the semi-analytical and the LS based numerical model for non-isothermal scenarios

3.6 Summary

Austenite decomposition in steels is simulated in a pseudo-1D domain using the level-sets based numerical framework. The expected carbon enrichment in the austenite phase is observed during the migration of the interface as the ferrite phase rejects it. The minor yet critical influence of capillarity effects on phase transformation kinetics and the equilibrium position is demonstrated in a 2D matrix-precipitate case. The capillarity effects play an important role in controlling the kinetics during the early stages of the transformation when the growing phase is in its nucleus form. In the context of austenite decomposition, the capillarity effects slightly lower carbon equilibrium concentrations. Validation with ThermoCalc estimations confirms the quantitative predictions of the above simulations.

The level-set numerical model (LS-NM) is benchmarked against a state-of-the-art sharp interface semi-analytical model (SAM), alongside comparisons with predictions from a corresponding phase-field numerical model (PF-NM) for austenite decomposition in a steel alloy. The LS-NM is capable of effectively reproducing the concentration profiles and the interface kinetics predicted by the SAM and also the PF-NM. The LS-NM reflected a closer resemblance in predictions with the SAM compared to the PF-NM, possibly due to the inherent sharp interface character of migrating interfaces in a level-set method.

Convergence in predictions with better mesh resolution and time step is demonstrated through a sensitivity analysis of the LS-NM. Additionally, the examination of diffuse interface thickness parameter (η), along with local mesh size, highlights the necessity of sufficient number of mesh elements within the diffuse interface zone to accurately capture significant field variations across the phase interface. The computational practicality of the underlying mesh resolution primarily dictates the selection of interface thickness parameter. The predicted interface kinetics exhibit relatively consistent behavior with varying interface thickness, showing minimal variation when the underlying mesh resolution is fine enough and provides sufficient elements within the diffuse interface. While mesh resolution remains a primary criterion for selecting η, other influencing factors must be considered. Therefore, caution is necessary in choosing this parameter, aiming to strike a balance between employing a reasonably coarse mesh with enough elements within the diffuse interface and avoiding the use of unrealistically large η values. Generally, aiming for around 7 to 20 mesh elements within the diffuse interface represents a reasonable compromise.

A semi-analytical sharp interface model is proposed to simulate mixed-mode transformation kinetics within a bounded 1D domain. It extends an existing approach with additional hypotheses and demonstrates the capability to reproduce the quantitative predictions achieved by the LS-NM across various cooling scenarios in the pseudo-1D case.

The promising outcomes presented here set the stage for the next chapter, which will delve into illustrations in a complex polycrystalline context using the proposed numerical model.

References

[1] *Thermo-Calc Software*. `http://www.thermocalc.se/`.

[2] S.R. Logan. “The origin and status of the Arrhenius equation”. In: *Journal of Chemical Education* 59.4 (1982), p. 279.

[3] G.P. Krielaart and S. Van der Zwaag. “Kinetics of $\gamma \rightarrow \alpha$ phase transformation in Fe-Mn alloys containing low manganese”. In: *Materials science and technology* 14.1 (1998), pp. 10–18.

[4] M.G. Mecozzi. “Phase field modelling of the austenite to ferrite transformation in steels”. PhD thesis. Delf University of Technology, 2006.

[5] D.R. Lide. *CRC handbook of chemistry and physics*. Vol. 85. CRC press, 2004.

[6] I. Loginova et al. “The phase-field approach and solute drag modeling of the transition to massive $\gamma \rightarrow \alpha$ transformation in binary Fe-C alloys”. In: *Acta Materialia* 51.5 (2003), pp. 1327–1339.

[7] C.J. Huang, D.J. Browne, and S. McFadden. “A phase-field simulation of austenite to ferrite transformation kinetics in low carbon steels”. English. In: *Acta Materialia* 54.1 (2006), pp. 11–21. DOI: `10.1016/j.actamat.2005.08.033`.

[8] C. Bos and J. Sietsma. “A mixed-mode model for partitioning phase transformations”. In: *Scripta materialia* 57.12 (2007), pp. 1085–1088.

[9] M.G. Mecozzi et al. “Quantitative comparison of the phase-transformation kinetics in a sharp-interface and a phase-field model”. In: *Computational Materials Science* 50.6 (2011), pp. 1846–1853.

[10] S. Florez et al. “A new finite element strategy to simulate microstructural evolutions”. In: *Computational Materials Science* 172 (2020), p. 109335.

[11] H. Chen and S. van der Zwaag. “Modeling of soft impingement effect during solid-state partitioning phase transformations in binary alloys”. In: *Journal of materials science* 46.5 (2011), pp. 1328–1336.

[12] N. Chandrappa and M. Bernacki. “A level-set formulation to simulate diffusive solid/solid phase transformation in polycrystalline metallic materials-Application to austenite decomposition in steels”. In: *Computational Materials Science* 216 (2023), p. 111840.

Chapter 4

Illustration of diffusive solid-state phase transformation: Biphasic polycrystals

Abstract

This chapter explores the capabilities of the proposed numerical model in replicating phase transformation behavior in complex polycrystalline microstructures. Building upon promising outcomes from simpler test cases, the model's adaptability to mimic intricate interactions within realistic microstructures is investigated. The nexus between different input parameters governing the phase transformation dynamics is analyzed in the context of austenite decomposition in steels. Additionally, the model's versatility is showcased by simulating other diffusive solid-state phenomena. Through this exploration, the chapter aims to elucidate the model's range, identify potential challenges, and emphasize its applicability in scenarios pertinent to industrial applications.

Résumé

Ce chapitre examine les capacités du modèle numérique proposé à reproduire le comportement de transformation de phase dans des microstructures polycristallines complexes. La capacité du modèle à reproduire des interactions complexes dans des microstructures réalistes est étudiée sur la base des résultats positifs obtenus dans des cas d'essai plus simples. La corrélation entre les différents paramètres d'entrée gouvernant la dynamique de la transformation de phase est analysée dans un contexte de décomposition de l'austénite dans les aciers. La polyvalence du modèle est également mise en évidence par la simulation d'autres phénomènes diffusifs à l'état solide. Grâce à cette exploration, le chapitre vise à élucider la portée du modèle, à identifier les défis potentiels et à souligner son applicabilité dans des scénarios pertinents pour les applications industrielles.

4.1 Introduction

In the preceding chapter, our preliminary analyses on simpler test cases yielded promising results. Now, we aim to push the boundaries of our numerical model by investigating more complex scenarios that replicate realistic polycrystalline microstructures. This chapter serves as an exploration into the capabilities of the model to reproduce complex transformation behaviors observed in real-world contexts.

While our earlier demonstrations primarily focused on single nuclei or grains during transformation, the context of polycrystalline materials introduces a new layer of complexity. Multiple nuclei or grains contribute to the growing phase, significantly altering the dynamics of transformation. Here, our aim is to evaluate the model's ability to replicate these multifaceted interactions and their consequential impact on transformation kinetics and microstructural topology.

Various factors come into play in shaping the final microstructure post-transformation. These include the mode of nucleation, the selection of nucleation sites, the temperature range involved in nucleation, cooling rates, duration of transformation, the influence of physical aspects like capillarity, solute drag etc. The correlation among some of these parameters adds additional complexity. In this chapter, we aim to explore the interplay of some of these factors using our numerical model.

Our initial focus will be on DSSPT in binary alloys, in the context of austenite decomposition in steels, utilizing simpler polycrystalline microstructures to investigate the impact of nucleation parameters in tandem with cooling rates. Subsequently, we'll simulate a large-scale microstructure relevant to industrial settings. Additionally, we'll touch upon the role of solute drag effects in a ternary alloy scenario. Finally, we aim to showcase the model's versatility by simulating other diffusive solid-state phenomena without any alterations to the numerical framework.

The overarching goal of this chapter is to document the range of the numerical model's capabilities, identify potential challenges for future exploration, and demonstrate its applicability to scenarios relevant in industrial applications.

4.2 DSSPT simulation in binary alloys: 2D polycrystals

4.2.1 Comparison with nucleation modes

In this study, we investigate the impact of different temporal modes of nucleation. As previously discussed in Chapter 1 (Section 1.2.1.1.1) and Chapter 2 (Section 2.3.5), nucleation can occur in a site-saturated or continuous manner. In site-saturated nucleation, all nuclei form simultaneously below the nucleation start temperature (T_{N_s}), causing the nucleation temperature range to approach zero ($\delta T_N \rightarrow 0$) during non-isothermal transformations. In contrast, continuous nucleation involves nuclei forming gradually over a period. In the context of transformations involving continuous cooling, this translates to $\delta T_N \neq 0$. To explore their influence on final grain statistics and microstructure morphology, we examine austenite decomposition in a binary steel alloy, specifically Fe - 0.02 wt%C. At atmospheric pressure, the austenitization temperature for this alloy is approximately $T_{A3} = 1175\,\mathrm{K}$. We consider an initial microstructure in a square domain of size 1 mm, situated slightly above the T_{A3} temperature with $T^i = 1176\,\mathrm{K}$. At this stage, the microstructure is composed entirely of austenite grains. Fig.4.1 depicts the morphology of the initial microstructure, featuring 317 austenite grains, and the respective grain coloration used to represent them.

The initial grain size distribution of the austenite grains is illustrated in Fig.4.2, where the mean equivalent radius (calculated in number) of the grains is about 31 µm. In this context, the size of

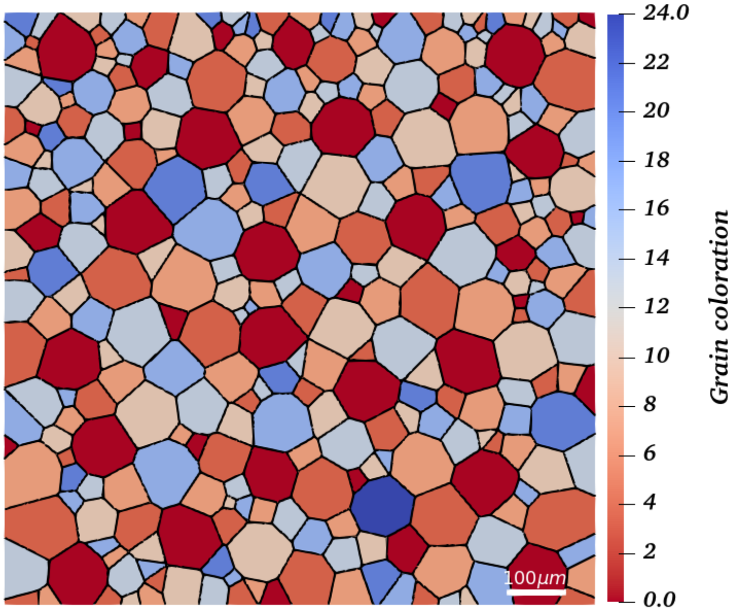

Figure 4.1: Grain coloration adopted for the initial austenitic grain morphology (the grain interfaces are highlighted in black)

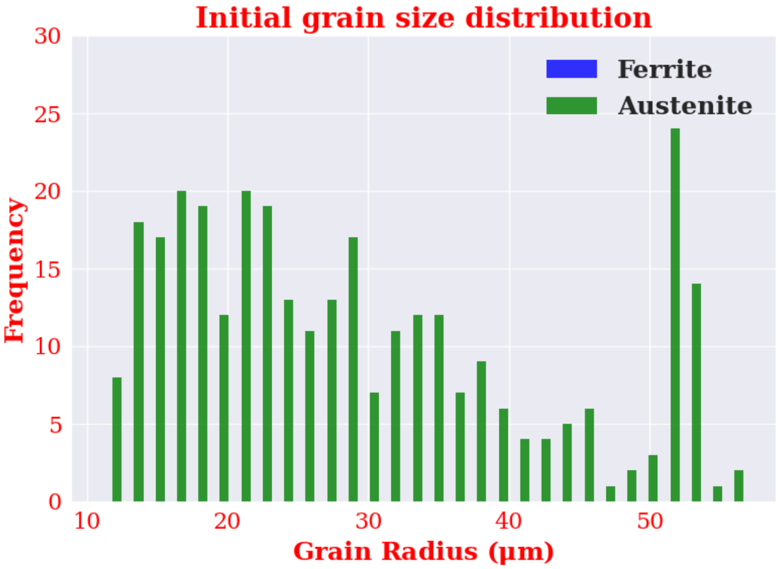

Figure 4.2: Grain size distribution of the initial microstructure

a particular grain is defined as the radius of an equivalent circle (sphere in 3D) having the same area (volume in 3D). Considering the available driving pressures for ferrite nucleation at different temperatures below the austenitization temperature, and factoring in the capillarity effects, the nucleation start temperature is established at $T_{N_s} = 1166\,\mathrm{K}$. This temperature is selected to provide ferrite nuclei a higher likelihood of entering the growth regime of the transformation. This delay in nucleation could also loosely represent the concept of an incubation time. The final temperature is set to, $T^f = 990\,\mathrm{K}$, where ThermoCalc [1] predicts a complete transformation to ferrite. The temperature profile during the transformation is illustrated in Fig.4.3, with a cooling rate set to $\dot{T} = -20\,\mathrm{K{\cdot}s^{-1}}$. Considering the high cooling rate, the nuclei density is consequently expected to be higher. It is computed using the 2D equivalent of Eq.2.103 for $f_f^{\alpha} = 1$, and for an expected mean ferrite grain size of approximately 15 µm. So, for the considered domain, and the computed nuclei density, about 1400 ferrite nuclei are set to be imposed. Two scenarios are simulated in this study: (i) Site-saturated nucleation, where all 1400 ferrite nuclei are imposed at $T = 1166\,\mathrm{K}$, and (ii) Continuous nucleation, with a nucleation temperature range of $\delta T_N = 40\,\mathrm{K}$, imposing 1400 nuclei steadily at a constant rate of $35\,\mathrm{K}^{-1}$. The radii of the nuclei are estimated using the scheme outlined in Eq.2.101. Due to the rapid cooling and subsequent high nucleation density, nuclei can form at both triple junctions and the austenite grain boundaries in this study.

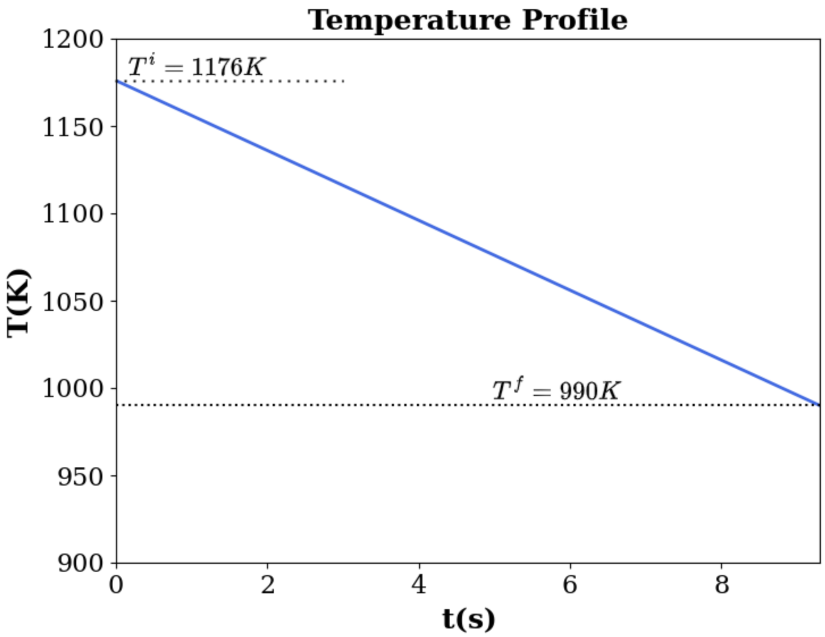

Figure 4.3: Temperature profile imposed during the transformation

The interface mobility and carbon diffusivity data used here are consistent with those listed in

Chapter 3 (3.2.1), i.e.,

$$\begin{aligned} M &= 6\times 10^{17}\exp\left(\frac{-140000}{RT}\right), \quad \text{in} \quad \mu\text{m}^4\cdot\text{J}^{-1}\cdot\text{s}^{-1} \\ D_\alpha^C &= 2.2\times 10^{8}\exp\left(\frac{-122500}{RT}\right), \quad \text{in} \quad \mu\text{m}^2\cdot\text{s}^{-1} \\ D_\gamma^C &= 1.5\times 10^{7}\exp\left(\frac{-142100}{RT}\right), \quad \text{in} \quad \mu\text{m}^2\cdot\text{s}^{-1} \end{aligned} \tag{4.1}$$

The interface energy is set at $1\times10^{-6}\,\text{J}\cdot\text{mm}^{-2}$, as previously employed in section 3.2.2. In this study, mobility and interfacial energy are assumed to be homogeneous and identical across phase and grain interfaces of both phases. The resolution time step is fixed at, $\Delta t = 0.01\,\text{s}$. An adaptive mesh with periodic remeshing is utilized following the strategy of mesh metric intersection detailed in Chapter 2 (2.3.3). The local mesh size within the diffuse phase interface is set as 0.5 µm, and the diffuse phase interface thickness is $\eta = 8\,\mu\text{m}$. The local mesh view at a particular instant of the simulation in Fig.4.4 highlights the finer adaptive mesh around the phase interfaces, contrasting with a relatively coarser mesh size (1 µm) adapting to the grain interfaces.

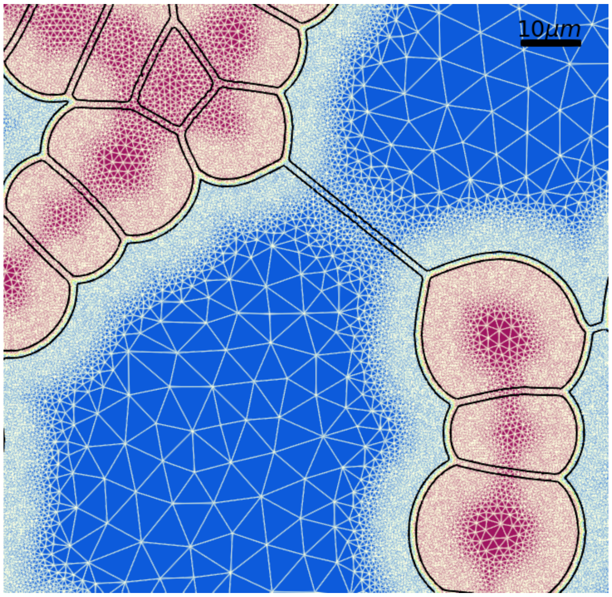

Figure 4.4: Illustration of the meshing strategy employed for simulation in biphasic polycrystals: the interfaces are highlighted in black through iso-contours of φ_{max} which is the max of all the φ_i functions involved

In Figs.4.5, the comparison of phase evolution in the two cases at various temperatures during the transformation is depicted. Correspondingly, the carbon distribution maps for these two cases are shown in Figs.4.6. In the site-saturated scenario, where all nuclei germinate simultaneously, resulting in identical initial radii, the growth pattern of most nuclei is nearly uniform, as observed in Fig.4.5b. The immediate onset of hard impingement between nuclei uniformly restricts the growth of adjacent ferrite grains along the austenite grain interfaces. This interaction generates straight interfaces between the neighboring ferrite grains and they tend to grow into the bulk of the austenite grains. Conversely, in the continuous nucleation case, the initial nuclei that form gain an early advantage in growth over subsequently appearing nuclei. Initially, these first few nuclei experience minimal hard impingement until new neighboring nuclei gradually emerge. This discrepancy leads to a noticeable variation in the sizes of the final ferrite grains. The hard impingement in continuous nucleation is only momentarily delayed due to rapid cooling, as the grains eventually make contact forming straight interfaces as in the case of site-saturated nucleation. In both nucleation modes, the elevated nucleation rate leads to the formation of ferrite nuclei arranged in a necklace-like structure along the austenite grain boundaries, a common occurrence in metallic alloys. In Figs.4.6, as the

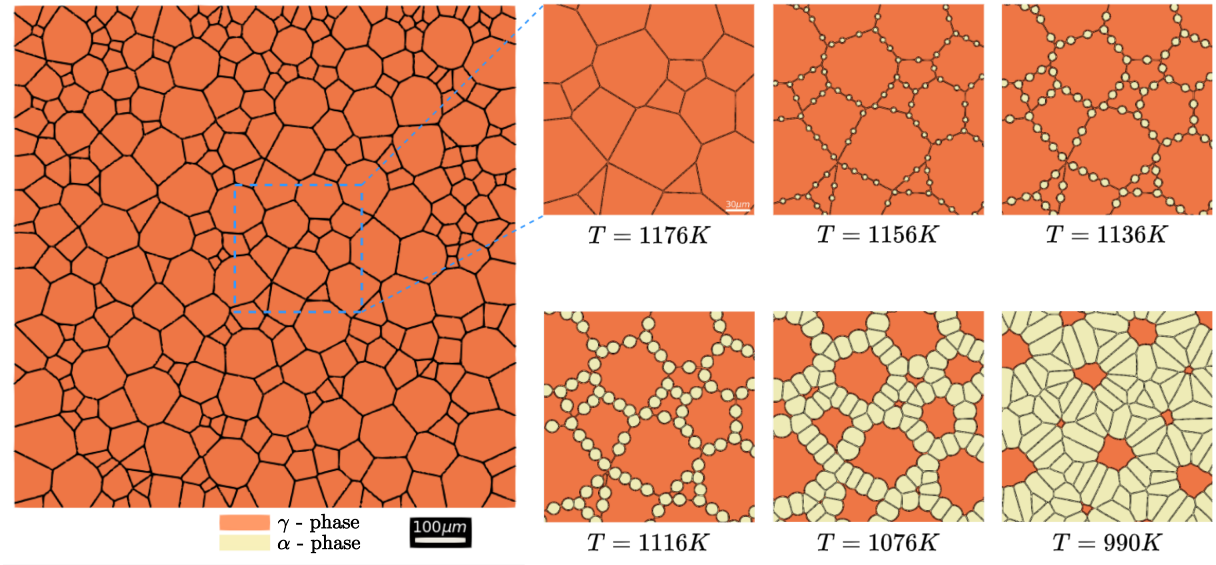

(a) Site-saturated nucleation

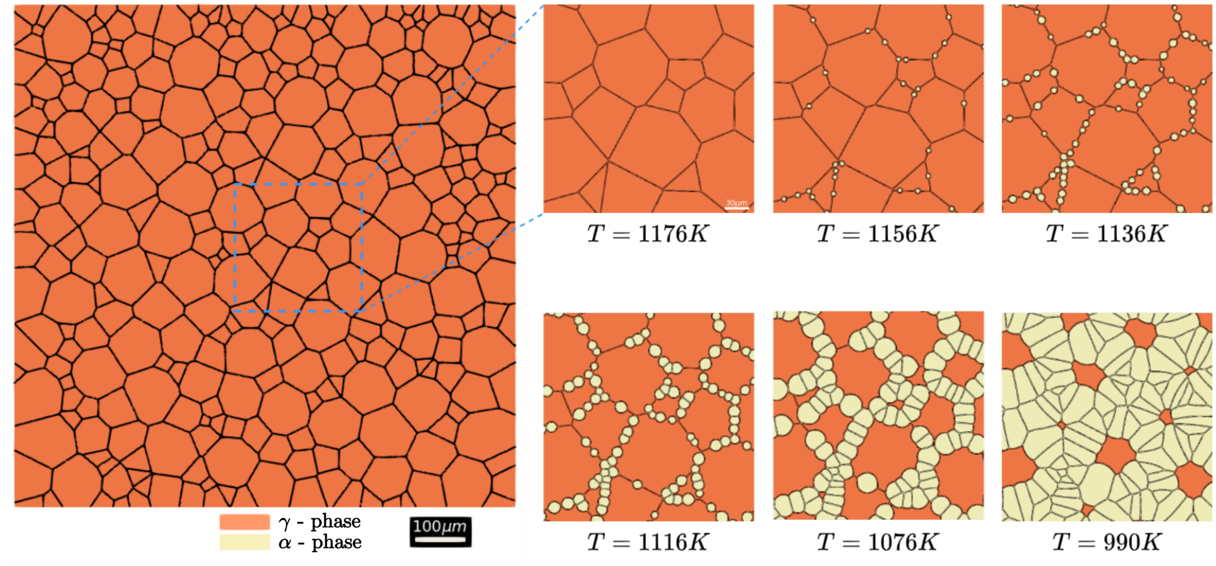

(b) Continuous nucleation case

Figure 4.5: Snapshots of phase evolution for different modes of nucleation

transformation proceeds, a noticeable enrichment of carbon in the austenite phase becomes evident. During the later stages, pockets of austenite grains trapped by the surrounding ferrite become apparent, especially prevalent at higher cooling rates. The rapid evolution leads to a significant influx of carbon atoms rejected by the neighboring ferrite grains into these austenite pockets. This substantial carbon enrichment notably reduces the driving pressure for phase transformation in these areas, as local equilibrium is rapidly achieved, resulting in trapped austenite grains characterized by visible solute gradients. When given enough time, these gradients may diffuse into the bulk of the grains, facilitating the additional growth of ferrite grains that extend into these confined austenite islands. In Figs.4.7, the microstructure morphologies and phase distribution at the conclusion of cooling are presented. Globally, both nucleation modes exhibit similar trends and features in the microstructure, particularly regarding the austenite phase. However, in the continuous nucleation

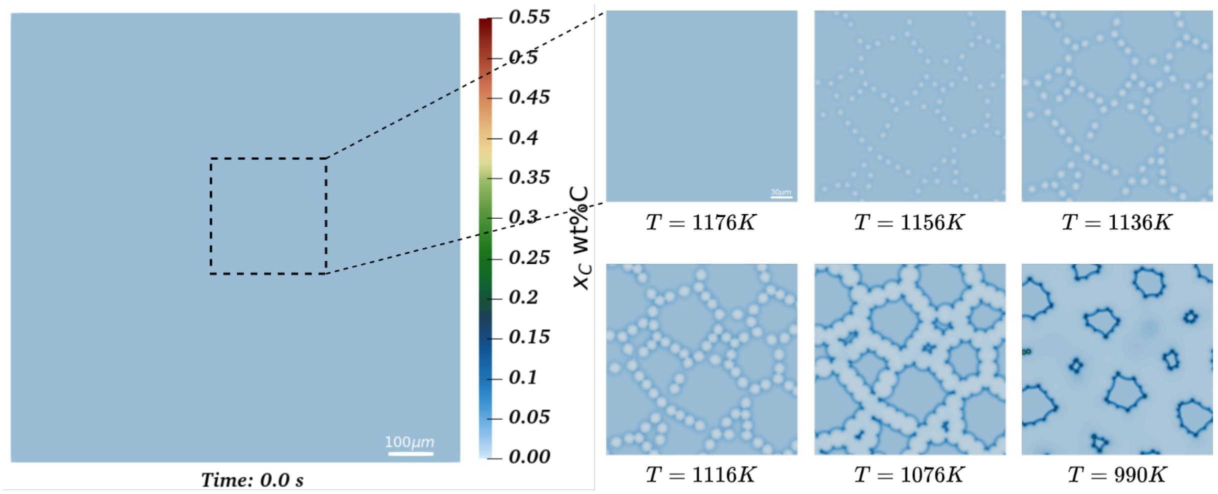

(a) Site-saturated nucleation

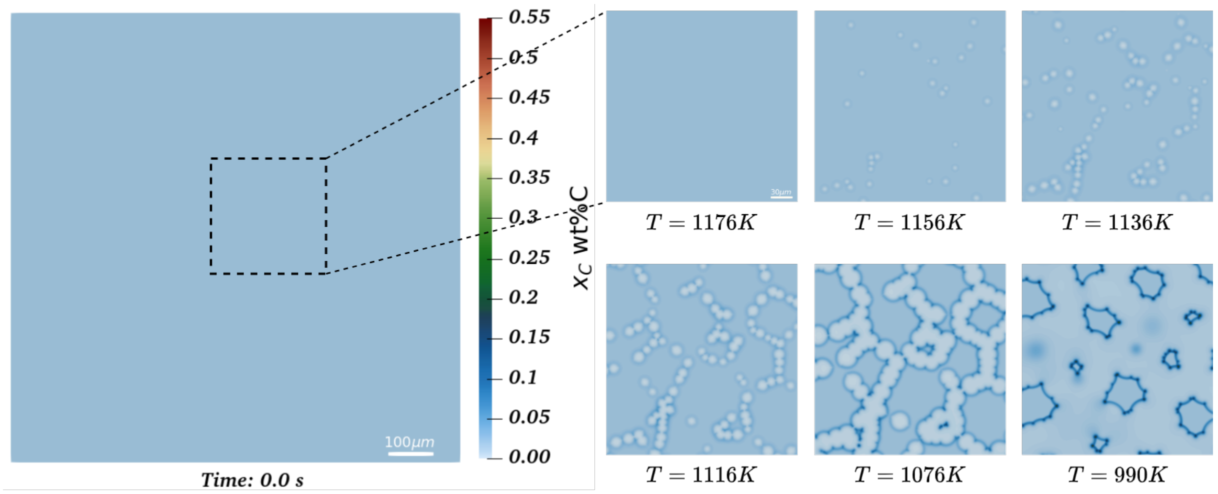

(b) Continuous nucleation case

Figure 4.6: Snapshots of carbon distribution for different modes of nucleation

case, the ferrite grain sizes appear more dispersed compared to the site-saturated case, where the distribution of ferrite grain sizes appears more compact and uniform. This distinction is further highlighted by the grain size distribution plots depicted in Figs.4.8. The relative difference in variance among the normal distributions for the ferrite phase in both cases is apparent. Moreover, the final mean grain sizes for both the phases are quite comparable as further suggested by the mean grain size evolution plots in Figs.4.9.

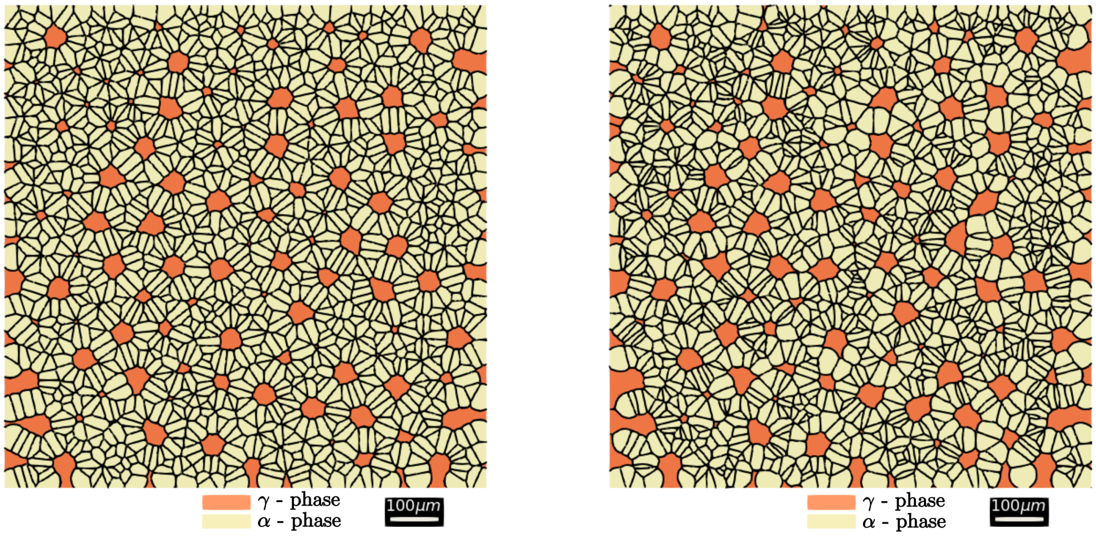

(a) Site-saturated nucleation

(b) Continuous nucleation case

Figure 4.7: Final phase distribution at the end of the cooling for the two nucleation modes

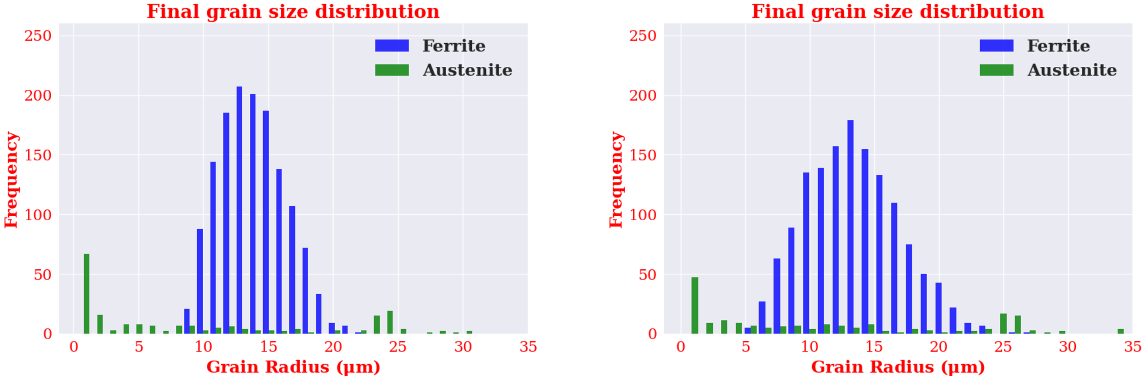

(a) Site-saturated nucleation

(b) Continuous nucleation case

Figure 4.8: Final grain size distributions obtained for the two nucleation modes

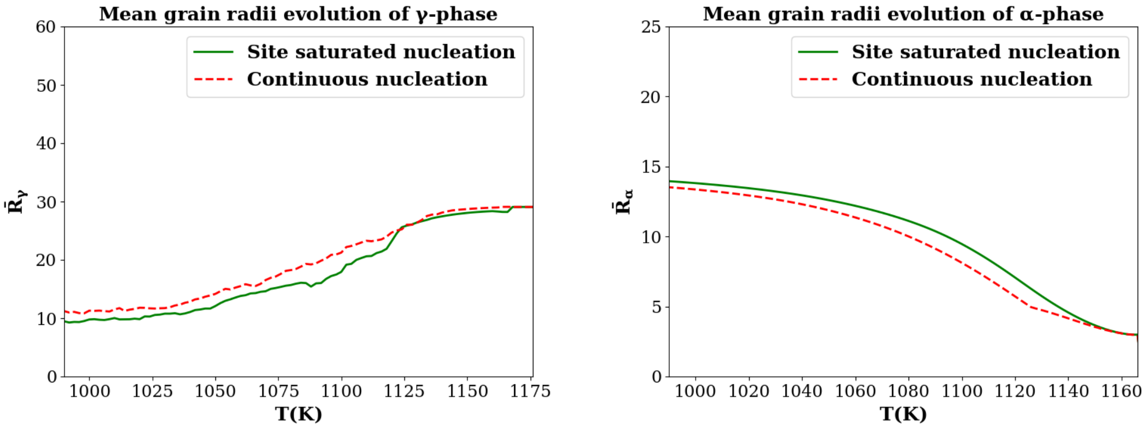

(a) Austenite phase (b) Ferrite phase

Figure 4.9: Comparison of mean grain size evolution of both the phases for different nucleation modes

Fig.4.10 illustrates the evolution of the ferrite fraction during the temperature cooling throughout the transformation. During the transformation, the site-saturated nucleation case consistently predicts a slightly higher fraction at any given temperature. This trend arises because the nucleation regime completes faster in the site-saturated scenario, swiftly transitioning to the growth stage just below the T_{N_s}. On the other hand, the continuous nucleation case completes its nucleation stage only at $T = 1127\,\mathrm{K}$. However, by $T^f = 990\,\mathrm{K}$, at the conclusion of cooling, the difference in predictions between the two cases is minimal. In both instances, due to rapid cooling, there isn't ample time to approach closer to their final equilibrium fraction ($f_f^\alpha = 1$, according to ThermoCalc).

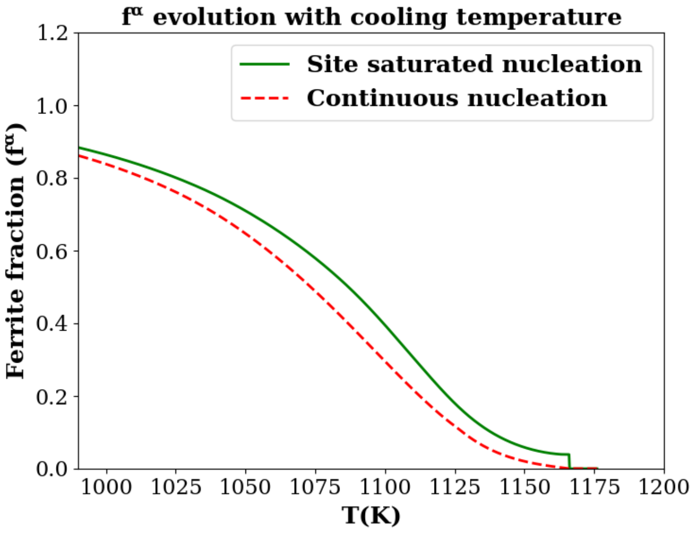

Figure 4.10: Evolution of ferrite fraction during transformation for the two nucleation modes

In the context of these simulations within a polycrystal, Fig.4.11 showcases the error variation in conserving solute mass. The site-saturated case demonstrates a maximum error of around 11%, while the continuous nucleation case displays an error of about 8%. These error margins appear reasonable considering the complex nature of a polycrystalline system with a high number of grains.

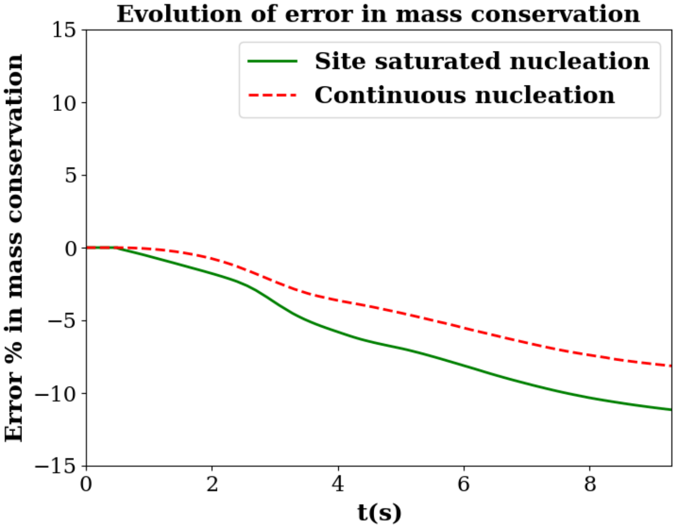

Figure 4.11: Variation of error in carbon mass conservation

4.2.2 Comparison with cooling rates

In this analysis, we are investigating the influence of cooling rates on transformation kinetics, exploring subsequent topological evolution, and analyzing grain statistics. We maintain the identical initial microstructure as in Fig.4.1 and the same simulation setup as the prior study. However, we focus on two distinct cooling rates, both operating under continuous nucleation mode. Fig.4.12 indicates the temperature profiles for the two cooling rate cases of $\dot{T} = -10\,\mathrm{K{\cdot}s^{-1}}$ and $\dot{T} = -20\,\mathrm{K{\cdot}s^{-1}}$. The resolution time step for the rapid cooling case is maintained at 0.01 s, while for slower cooling case, a bigger time step of $\Delta t = 0.02\,\mathrm{s}$ is employed.

In the relatively slower cooling scenario, the nucleation density is anticipated to be lower compared to the faster cooling case. For achieving an expected final mean ferrite grain size of about 25 µm, we estimate imposing approximately 500 ferrite nuclei, contrasting with 1400 nuclei for the faster cooling instance. As indicated in [2] and applied in works such as [3], the nucleation temperature range is also expected to be lower in the slower cooling case. To replicate this trend, δT_N is set to 20 K for the slower cooling scenario, compared to the 40 K range used for the faster cooling case. For comparison, ferrite nuclei in both scenarios are allowed to initiate at triple junctions and also along austenite grain boundaries.

Figs.4.13 and 4.14 illustrate the evolution of phases and carbon redistribution for the slower cooling rate case. Previously, faster cooling results were showcased in Figs.4.5b and 4.6b under continuous nucleation mode. For a comprehensive view of the final microstructures in both scenarios, refer

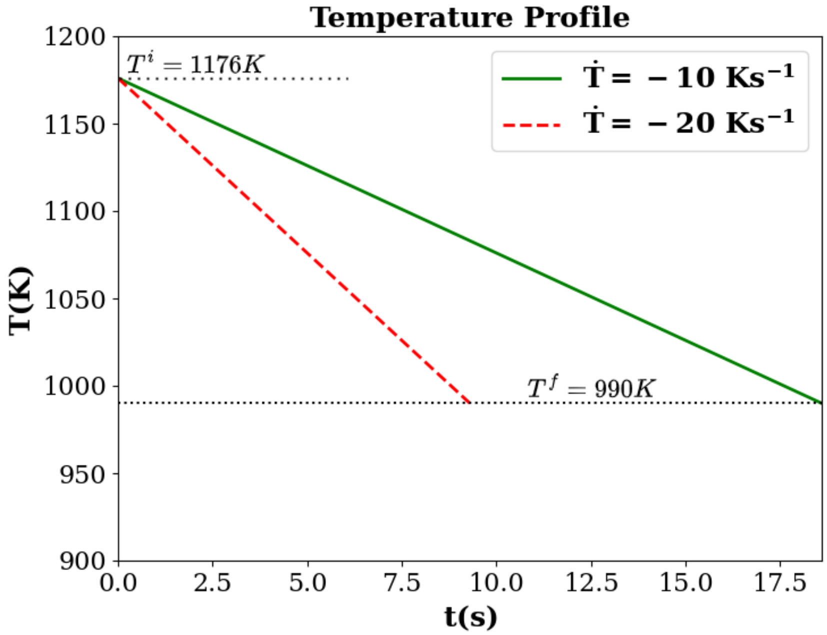

Figure 4.12: Temperature profiles imposed during the transformation for the two different cooling scenarios

to Figs.4.15. Notably, the slower cooling scenario, characterized by reduced nucleation density, exhibits less pronounced hard impingement effects than the faster cooling case. This scenario favors coarser equiaxed grain formation due to the less restricted growth of ferrite nuclei. However, even at $\dot{T} = -10\,\mathrm{K{\cdot}s}^{-1}$, which is considered a high cooling rate, there might be some local nuclei clusters that hinder the growth of certain ferrite nuclei. This could cause a few elongated ferrite grains to grow into the bulk of parent austenite grains, similar to what's seen in the rapid cooling scenario. Higher nucleation density in the rapid cooling case results in more local nuclei clusters and enhanced impediment to ferrite growth, primarily yielding elongated plate like ferrite grains. From the observations in Fig.4.15, it's evident that equiaxed ferrite growth occurs less frequently at cooling rates as high as $\dot{T} = -20\,\mathrm{K{\cdot}s}^{-1}$, particularly when the nuclei also germinate along the grain boundaries. Comparing Figs.4.14 and 4.6b, the major difference is the longer time available for carbon diffusion in the slower cooling case. The relatively prolonged diffusion period contributes to the reduction in the size of the trapped austenite grains, allowing the continued growth of ferrite grains into the parent austenite matrix, compared to the rapid cooling case.

The dispersion in ferrite grain size distribution associated with continuous nucleation is notably more pronounced at lower cooling rates as demonstrated by the plots in Figs.4.16. As anticipated, the slower cooling case shows a higher mean ferrite grain size. The mean grain size evolution in Figs.4.17 affirms this trend, converging towards the expected mean ferrite grain size that was utilized to determine the nucleation density for the respective cooling scenarios. Moreover, the mean austenite grain size is notably smaller for the slower cooling case by the end of the cooling process at 990 K, implying a higher ferrite fraction. This trend is corroborated by the ferrite fraction curves in Fig.4.18. It appears that given more time, the rapid cooling case could potentially

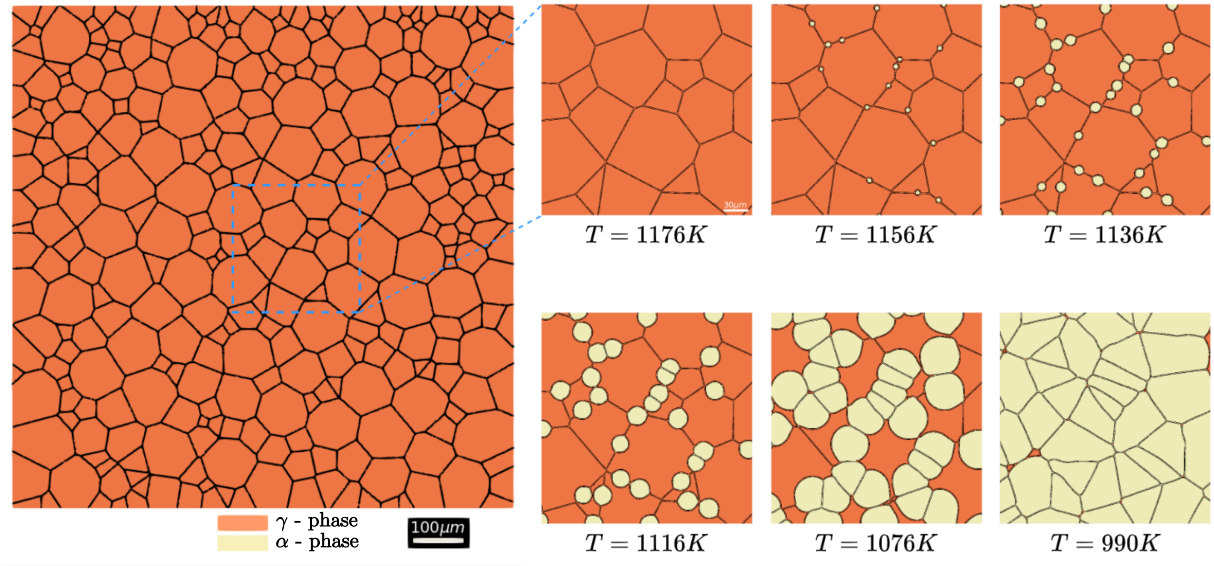

Figure 4.13: Phase evolution for the $\dot{T} = -10\,\mathrm{K{\cdot}s^{-1}}$ cooling case

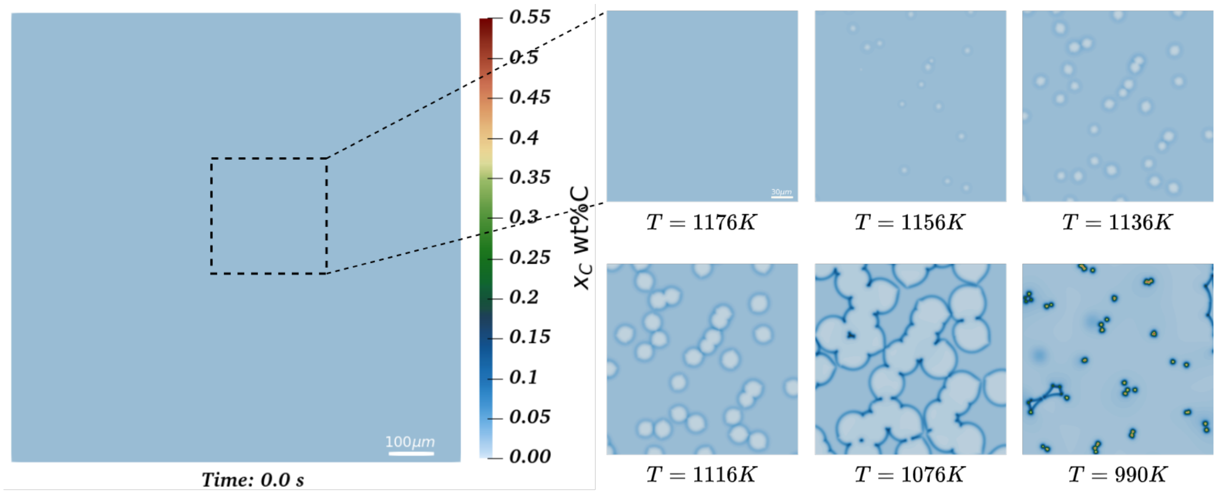

Figure 4.14: Carbon concentration maps during the transformation for the $\dot{T} = -10\,\mathrm{K{\cdot}s^{-1}}$ cooling case

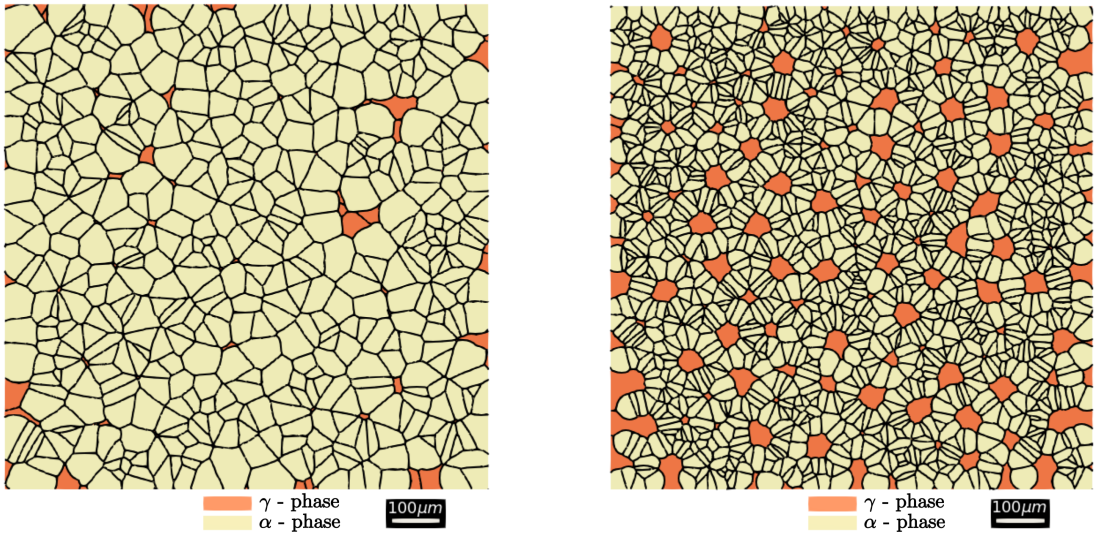

(a) $\dot{T} = -10\,\mathrm{K{\cdot}s}^{-1}$

(b) $\dot{T} = -20\,\mathrm{K{\cdot}s}^{-1}$

Figure 4.15: Final phase distribution at the end for the two different cooling rates

converge towards a similar ferrite fraction as observed in the slower cooling scenario.

It's important to emphasize that throughout these simulations, the effect of capillarity-induced grain growth on the ferrite grains at the conclusion of the cooling phase is minimal. The triple junctions established by these ferrite grains are far from the expected equilibrium configurations, which are typically observed during isotropic grain growth. This behavior is entirely in line with the selected range of final temperatures in these simulations. Consequently, the temperature-dependent mobility decreases substantially to observe any grain growth effects of significance within a reasonable time frame. Moreover, due to the high cooling rate employed, the magnitude of the phase transformation driving pressure significantly outweighs that of the capillarity-induced driving pressure when the nuclei start to establish as grains. Under conducive thermal conditions or with sufficient time, the numerical model should seamlessly transition to simulating the grain growth regime of the microstructure following the phase transformation.

In Fig.4.16a depicting the slower cooling case, there's a noticeable prevalence (high frequency) of extremely small austenite grains towards the end. The have been notably observed at the eventual triple junction locations of the ferrite grains. Curiously, these grains appear to persist rather than dissolve (as one might expect due to increased capillary effects in smaller grains). Two potential scenarios might explain this behavior:

(i) The small austenite pockets could possess a concave surface as depicted in Fig.4.19a, causing capillarity-induced driving pressure to orient to grow the grain. Simultaneously, carbon rejection from surrounding ferrite could elevate the interface concentration closer to the local equilibrium value, thus reducing the phase transformation's driving pressure. In this case, the two driving pressures would be oriented opposite to each other. This counterbalance might stall austenite grain

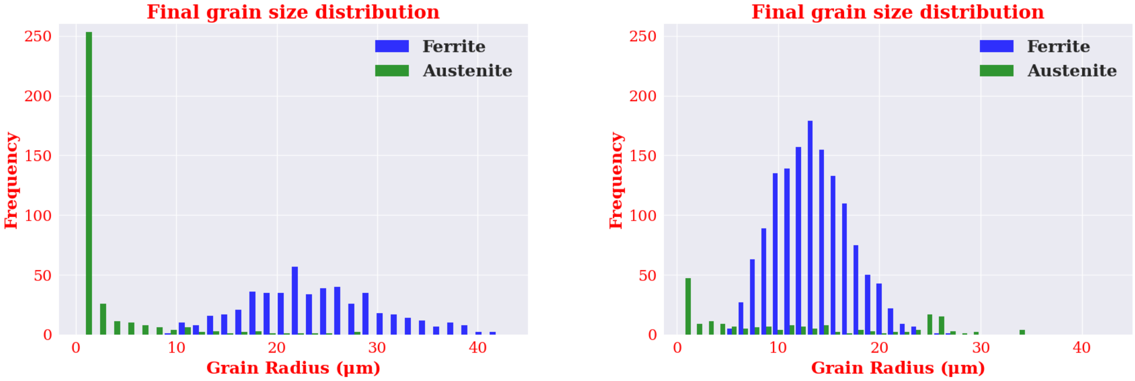

(a) $\dot{T} = -10\,\mathrm{K{\cdot}s^{-1}}$ (b) $\dot{T} = -20\,\mathrm{K{\cdot}s^{-1}}$

Figure 4.16: Final grain size distributions obtained for the two cooling scenarios

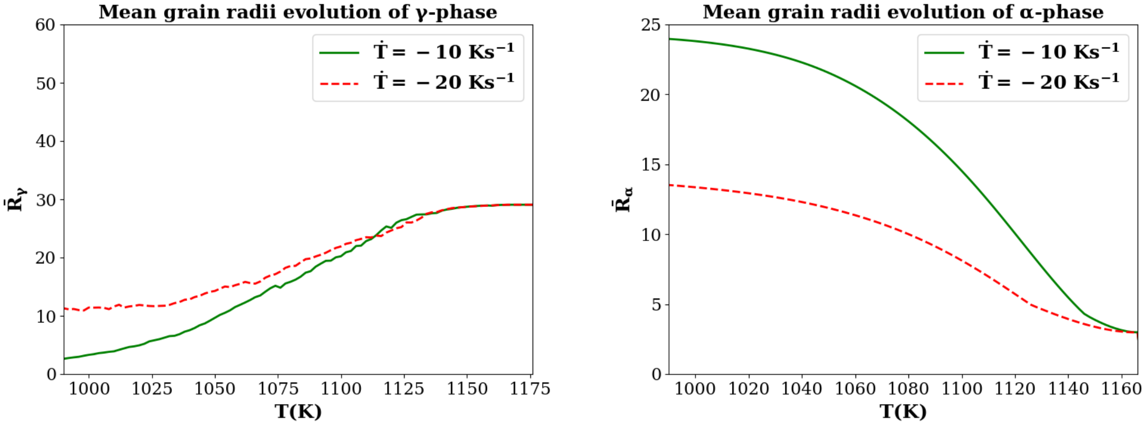

(a) Austenite phase (b) Ferrite phase

Figure 4.17: Comparison of mean grain size evolution of both the phases for different nucleation modes

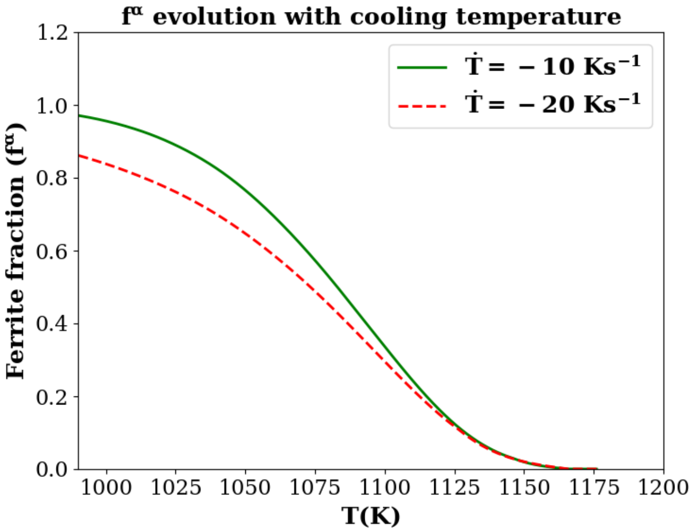

Figure 4.18: Evolution of ferrite fraction during transformation for the two cooling rates

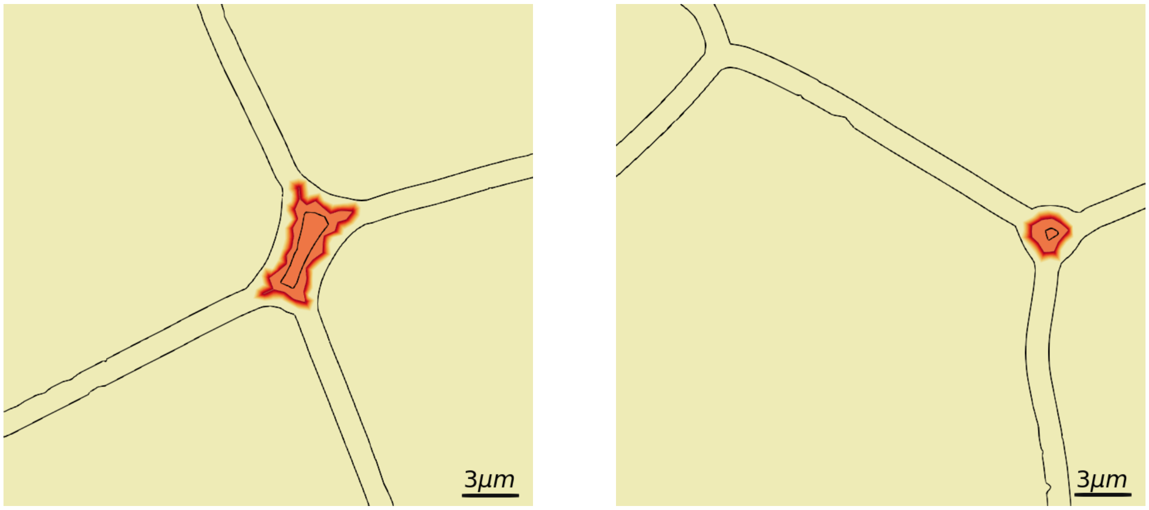

(a) A scenario with physical sense

(b) Uncharacteristic scenario

Figure 4.19: Tiny trapped austenite islands at the eventual triple junctions of ferrite grains

growth or decomposition if the magnitudes of these opposing pressures are similar. So some of these tiny grains could be due to this scenario.

(ii) Alternatively, a high and rapid influx of carbon into the trapped austenite pockets could elevate the interface concentration beyond the local equilibrium value. Such a situation might result in the driving pressure description ($\Delta G_{\gamma \rightarrow \alpha}$) in Eq.2.92 turning negative. If the cooling rate is slower, this negative value might persist for longer duration, as the anticipated equilibrium concentrations for the current temperature would not increase rapidly enough to counter the rise in interface concentration. This uncharacteristic negative driving pressure might either act opposite to the capillarity-induced driving pressure, stalling grain kinetics (in the convex interface case) or might encourage the austenite grain to grow into ferrite grains (in the concave interface case). This scenario is depicted in Fig.4.19b.

The first scenario is a purely physical phenomenon. However, the second scenario appears to be a numerical artifact potentially linked to factors like the mesh resolution, time step, or even the diffuse interface thickness etc., requiring investigation. If grain kinetics stall due to the negative driving pressure and simultaneously experience further carbon influx, it could compromise the mass conservation by increasing the total solute mass for the given phase distribution. This could explain the relatively higher error (at 16%) in mass conservation for the slow cooling case compared to the 8% error observed in the rapid cooling case. A potential solution might involve refining the mesh resolution or improving the time step to mitigate this issue. When we reran the simulation for the slower cooling scenario using a finer mesh resolution (0.3 µm) within the diffuse interface thickness, the mass conservation error reduced to only about 5%, and there was a noticeable decrease in the occurrence of trapped tiny austenite pockets. However, this improvement isn't practically viable due to the increased computational demands associated with a finer mesh. It's intriguing that achieving better mass conservation in the slower cooling case required a finer mesh resolution compared to the scenario with rapid cooling.

Further investigation revealed that employing the semi-analytical method (utilizing Eq.(2.29)) to compute the reactive term ($\mathcal{R}$) for the diffusion equation encounters inaccuracies at the triple junctions in a polycrystalline context. The issue might stem from the computation and utilization of the Laplacian of the signed distance function, $\Delta\varphi_\alpha$, in Eq.(2.29). $\Delta\varphi_\alpha$ is known to be particularly ill-defined at these triple junctions. In Chapter 3, it was observed that the method exhibited no issues in simple domains lacking triple junctions and, in fact, was more accurate than numerical computation. However, within a polycrystalline context, it appears that this method is generally less accurate than numerically computing ($\mathcal{R}$) using divergence operators and numerical transformation to a P1 FE field. Consequently, for polycrystalline settings, numerical computation seems to be a more suitable approach for determining the strongly varying reactive term, $\mathcal{R}$. Curiously, it remains unclear why these errors become more pronounced, particularly at slower cooling rates.

The same case was rerun without altering the time step or mesh resolution from the initial setup, focusing solely on modifying the computation of the reactive term. Remarkably, the error in mass conservation did not exceed 1.45%, indicating a significant improvement. Notably, the occurrence of unusually small trapped austenite pockets at the triple junctions was significantly reduced. Furthermore, when tested with much slower cooling rates, no issues were encountered. Fig.4.20 illustrates the final grain size distribution obtained for the rerun case after resolving the issue. It is evident that the frequency of these small grains are reduced. However, it's important to note that instances of negative driving pressure may persist if the resolution time step, or local mesh size remains inadequate.

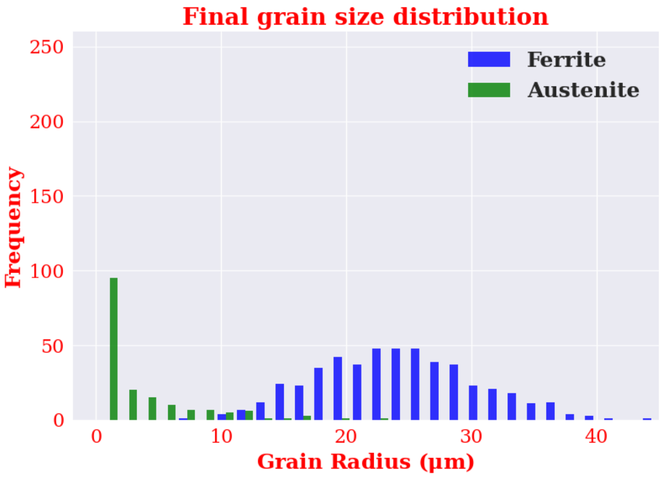

Figure 4.20: Final grain size distribution obtained for the slower case after changing the approach to compute $\mathcal{R}$

4.2.3 A step towards simulating large-scale microstructures

Now, we'll showcase the simulation in a large-scale microstructure, emulating the complexity often found in industrial settings, characterized by a multitude of grains. This scenario maintains the same thermodynamic conditions and alloy composition as our previous cases within a similar domain. The initial austenitic microstructure comprises 1592 grains, visually detailed in Fig.4.21. Notably, the austenite grain size displays a well-dispersed distribution, evident from the representation in Fig.4.22, with an average grain radius of approximately 14 µm. The mesh parameters are identical to those previously used.

For this simulation, the cooling rate is set to $\dot{T} = -10\,\mathrm{K{\cdot}s^{-1}}$, and a time step of 0.02 s is selected. The interface energy is assumed to be the same value as before ($1{\times}10^{-6}\,\mathrm{J{\cdot}mm^{-2}}$). The mobility and the diffusion parameters likewise remain the same as in Eq.(4.1). Following the cooling phase to the final temperature of $T^f = 976\,\mathrm{K}$, the microstructure is maintained at this temperature for an additional 80 seconds to ensure complete transformation. It is then rapidly reheated to 1100 K at a rate of $20\,\mathrm{K{\cdot}s^{-1}}$ to increase grain boundary mobility and thus enhance grain growth effects. Following the reheating stage, the microstructure is maintained at 1100 K for the remaining duration of the simulation until $t = 1000\,\mathrm{s}$. The thermal path corresponding to this scenario is depicted in Fig.4.23. In contrast to previous cases, the nucleation in this scenario is setup to exclusively generate ferrite nuclei at the triple junctions (grain corners), continuously, until these sites are saturated. A total of 2207 ferrite nuclei are imposed, commencing at $T_{N_s} = 1166\,\mathrm{K}$ and spanning a temperature range of 40 K.

In Fig.4.24, the evolution of the ferrite fraction over time is depicted. The ferrite fraction converges to unity with time, aligning with the ThermoCalc prediction of complete transformation to a ferritic microstructure below 990 K.

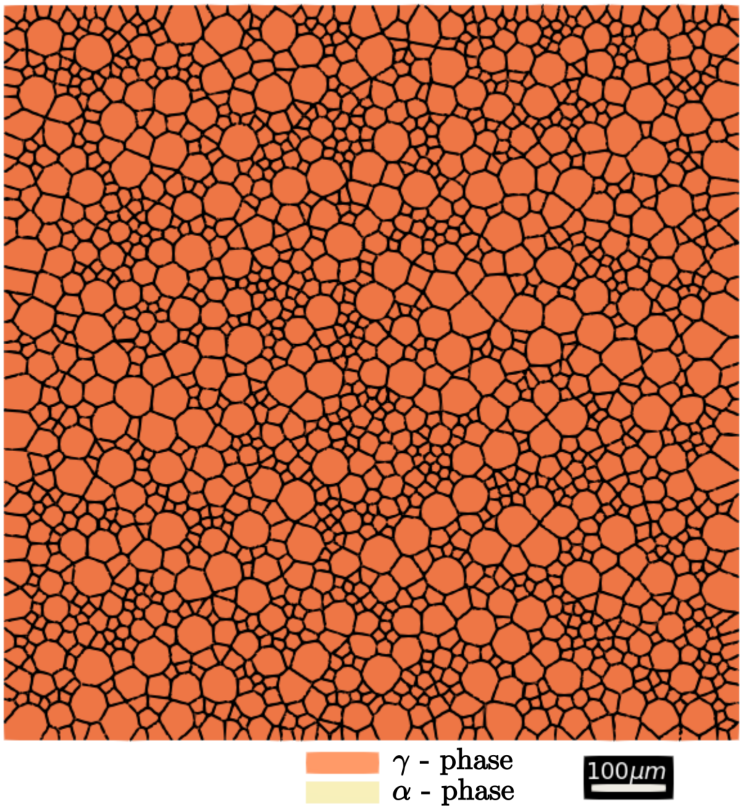

Figure 4.21: Illustration of the initial austenitic microstructure with 1592 grains

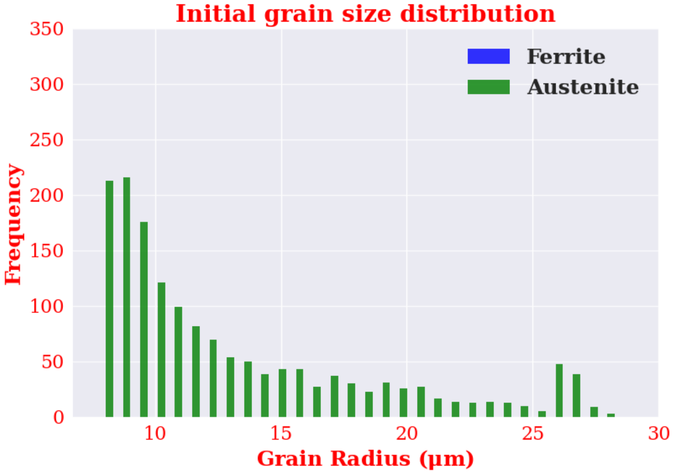

Figure 4.22: Grain size distribution of the initial large-scale microstructure

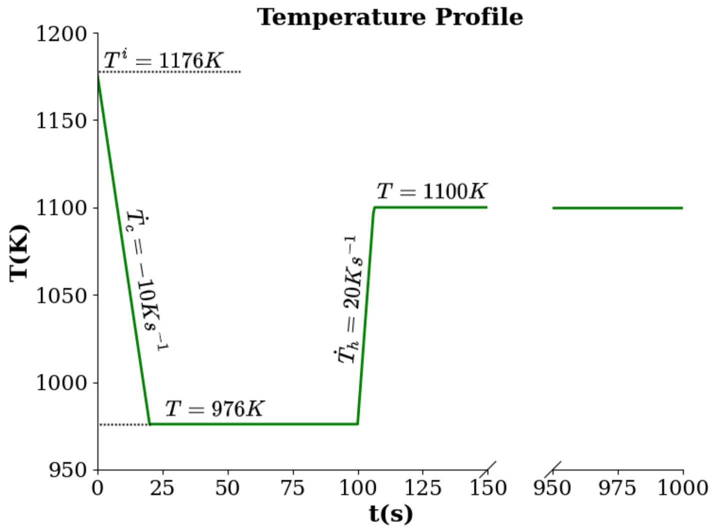

Figure 4.23: Thermal path imposed during the transformation: the broken axis representation indicates that the same temperature is maintained during that period

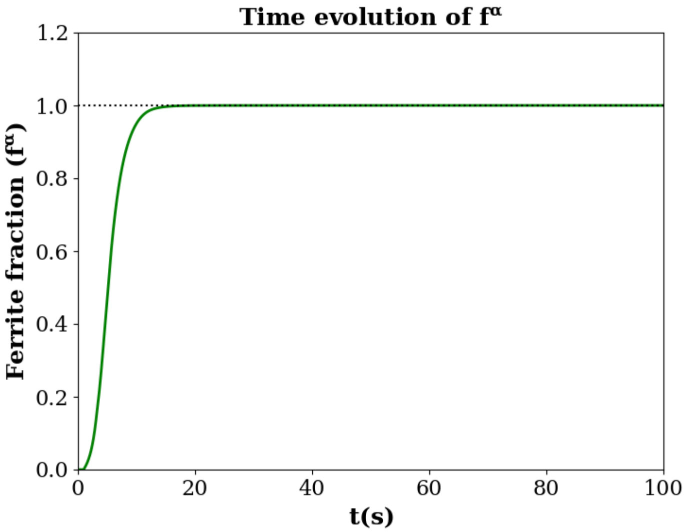

Figure 4.24: Time evolution of the ferrite fraction during the transformation

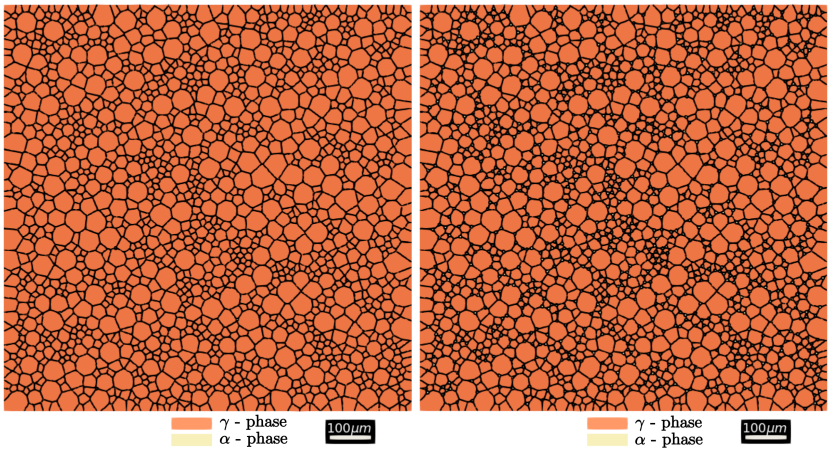

(a) $t = 1\,\mathrm{s}, T = 1166\,\mathrm{K}$ (b) $t = 2\,\mathrm{s}, T = 1156\,\mathrm{K}$

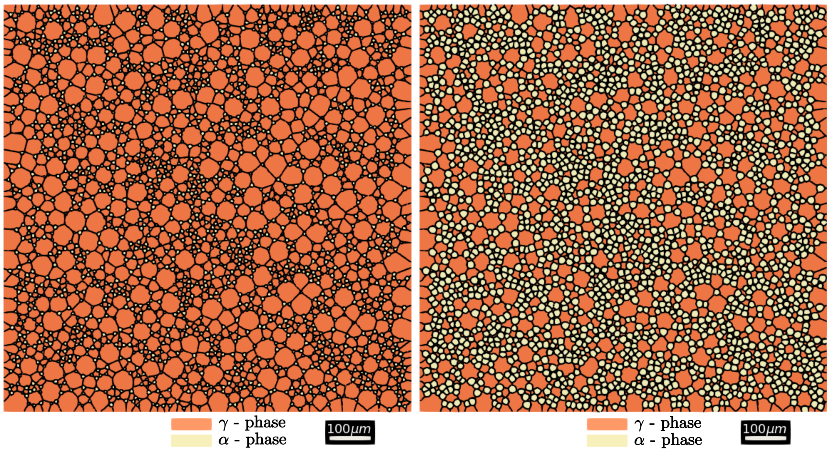

(c) $t = 3\,\mathrm{s}, T = 1146\,\mathrm{K}$ (d) $t = 5\,\mathrm{s}, T = 1126\,\mathrm{K}$

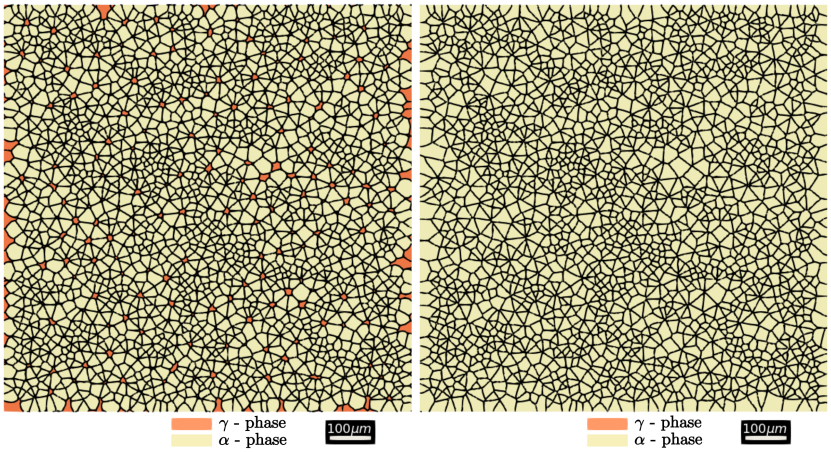

(e) $t = 10\,\mathrm{s}, T = 1076\,\mathrm{K}$ (f) $t = 20\,\mathrm{s}, T = 976\,\mathrm{K}$

Figure 4.25: Snapshots of austenite decomposition into ferrite in a large-scale microstructure, at different instants till the end of cooling

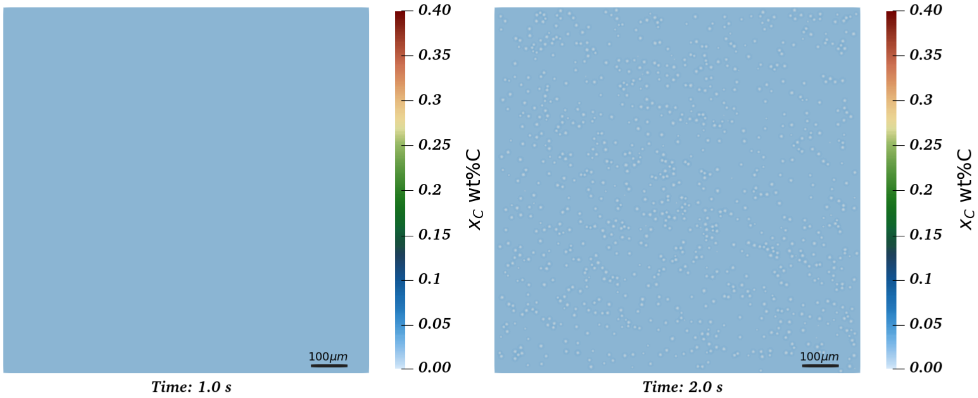

(a) $t = 1\,\mathrm{s}, T = 1166\,\mathrm{K}$ (b) $t = 2\,\mathrm{s}, T = 1156\,\mathrm{K}$

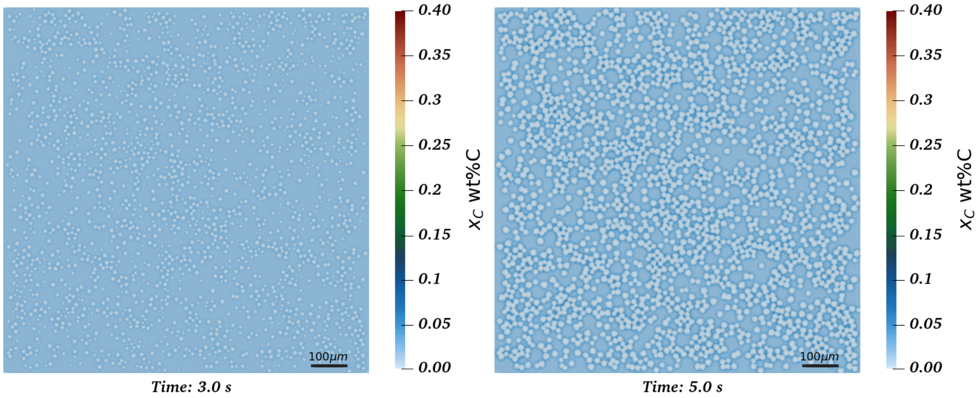

(c) $t = 3\,\mathrm{s}, T = 1146\,\mathrm{K}$ (d) $t = 5\,\mathrm{s}, T = 1126\,\mathrm{K}$

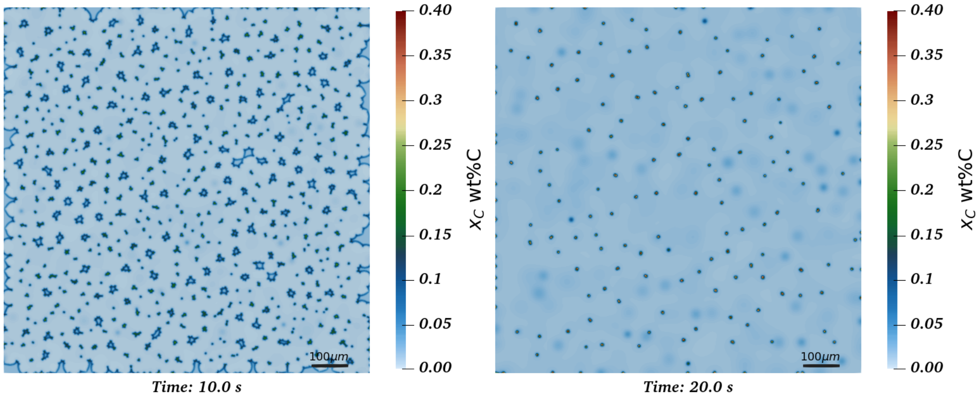

(e) $t = 10\,\mathrm{s}, T = 1076\,\mathrm{K}$ (f) $t = 20\,\mathrm{s}, T = 976\,\mathrm{K}$

Figure 4.26: Snapshots of carbon evolution between the phases at different instants in a large-scale microstructure till the conclusion of cooling

Snapshots of the transforming microstructure at various intervals until the conclusion of the cooling stage are presented in Figs.4.25 along with the associated carbon redistribution shown in Figs.4.26. In this cooling scenario, the ferrite nuclei formed solely at the triple junctions tend to develop into finer equiaxed grains overall. This contrasts with the previous rapid cooling case, where elongated ferrite grains were formed due to nucleation along grain boundaries, resulting in necklace-like structures. Figs.4.27 illustrate the microstructure's state, including the associated phase distribution and concentration map after the transformation stage (at $t = 100\,\mathrm{s}$). The minuscule dark regions apparent in the concentration map are a result of the persisting tiny trapped austenite islands previously discussed.

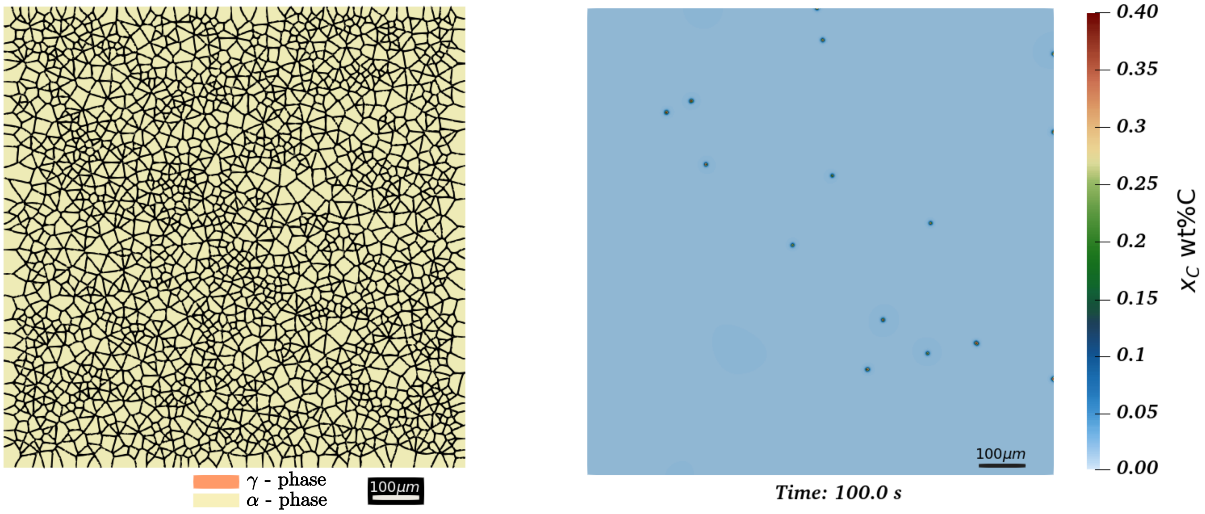

Figure 4.27: Configuration obtained post complete transformation to ferrite at the end of $t = 100\,\mathrm{s}$: Phase distribution (left), Carbon concentration field (right)

Figs.4.28 showcase the grain size distribution achieved post phase transformation, while Figs.4.29 outline the evolution of mean grain size throughout this transformation regime. The mean grain radius of the ferrite grains converges to approximately 12 µm. At this stage, the ferrite grain size distribution exhibits reduced dispersion.

From Fig.4.27, it's evident that the triple junctions formed by the ferrite grains are far from equilibrium. With the correct activation, the system has the potential to further reduce the excess free energy, primarily existing as surface energy, through grain growth phenomena. However, at temperatures as low as 976 K, the interface mobility remains low, and the grain growth effects are negligible within the timescales of interest. Therefore, to initiate the necessary activation, the microstructure is reheated to a higher temperature (1100 K) and sustained there to enhance the grain growth effects. It should be highlighted that the grain growth stage of the simulation is resolved at a higher time step of 0.5 s in this case.

After the reheating stage, the impact of grain growth phenomena on the transformed ferrite grain morphology is vividly depicted in Figs.4.30. The growth of larger grains at the expense of smaller ones, aimed at reducing the interfacial area, is distinctly observed. Notably, the triple junctions approach the equilibrium angles (120°) characteristic of isotropic grain growth. Furthermore,

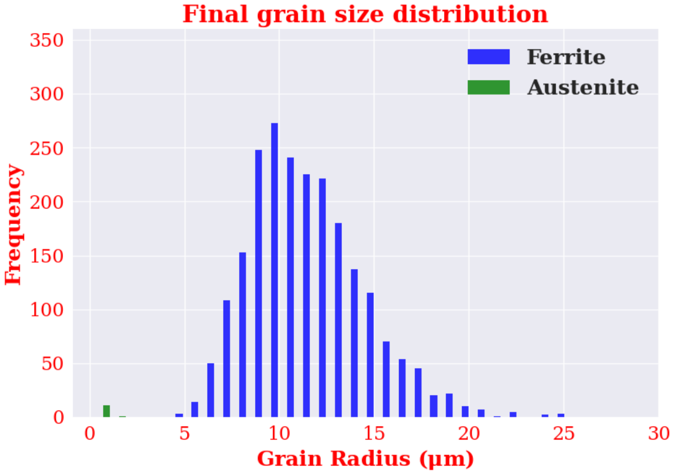

Figure 4.28: Grain size distribution obtained at the end of the transformation stage ($t = 100\,\mathrm{s}$)

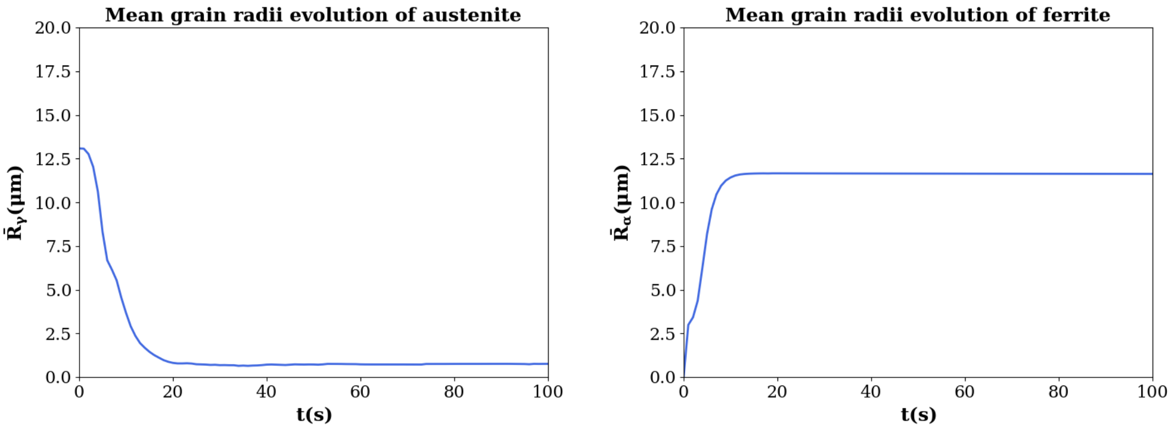

(a) Austenite grains

(b) Ferrite grains

Figure 4.29: Mean grain size evolution during transformation stage

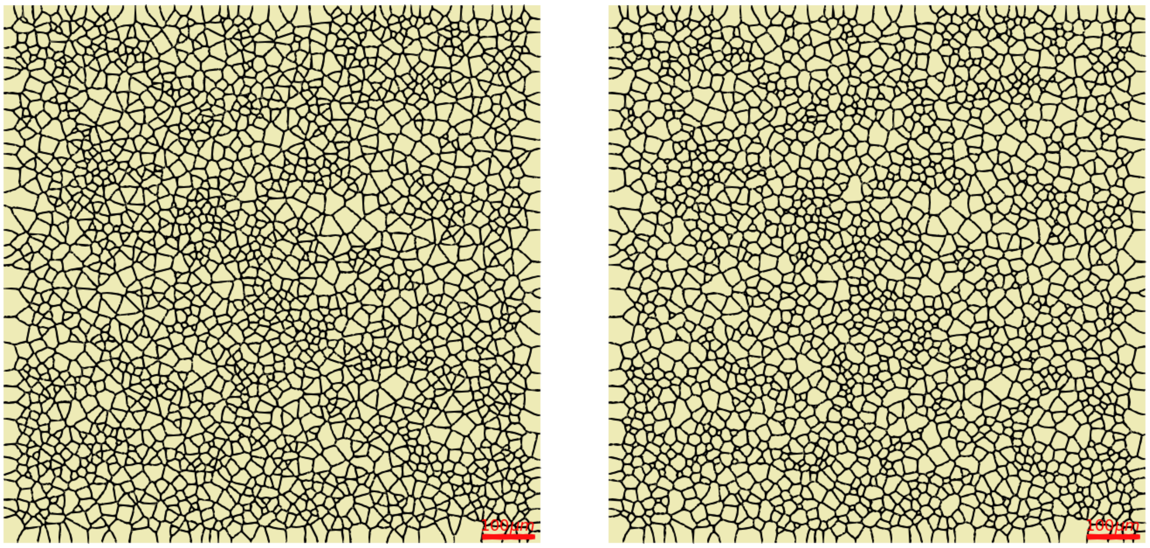

(a) $t = 200\,\mathrm{s}, T = 1100\,\mathrm{K}$ (b) $t = 400\,\mathrm{s}, T = 1100\,\mathrm{K}$

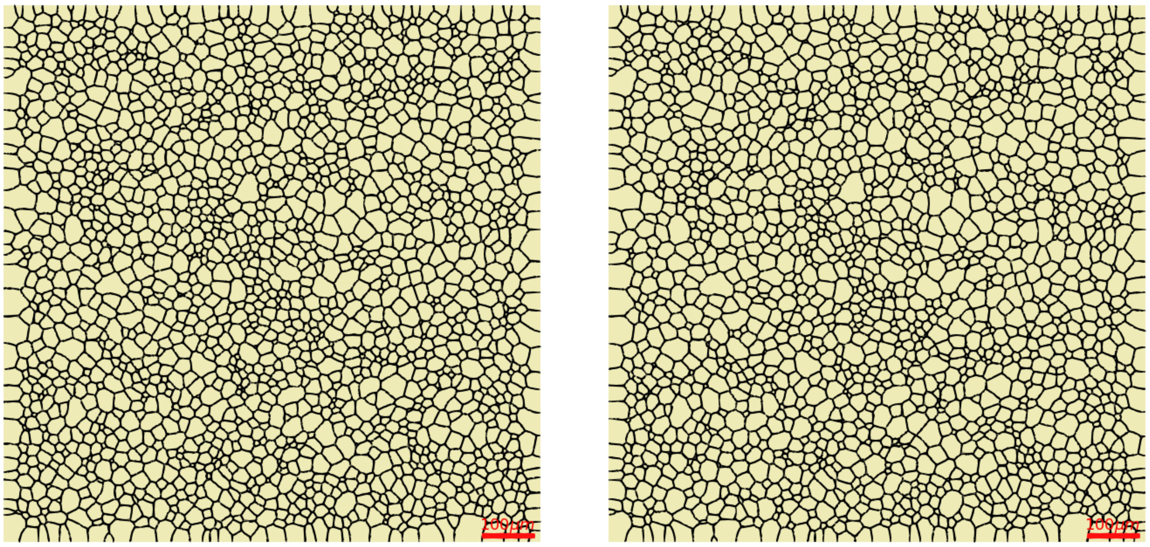

(c) $t = 700\,\mathrm{s}, T = 1100\,\mathrm{K}$ (d) $t = 1000\,\mathrm{s}, T = 1100\,\mathrm{K}$

Figure 4.30: Snapshots of grain growth effects observed in ferrite grains at different instants, post the transformation stage (after reheating)

Figs.4.31 showcases the differences in ferrite grain size distributions before the onset of the grain growth regime and at $t = 1000\,\text{s}$. As the grain growth progresses, the grain size distribution becomes more dispersed, with the mean grain size gradually shifting to the right. Additionally, Figs.4.32 further emphasize this phenomenon, illustrating the consistent decrease in the number of ferrite grains and the gradual increase in the mean grain size over time.

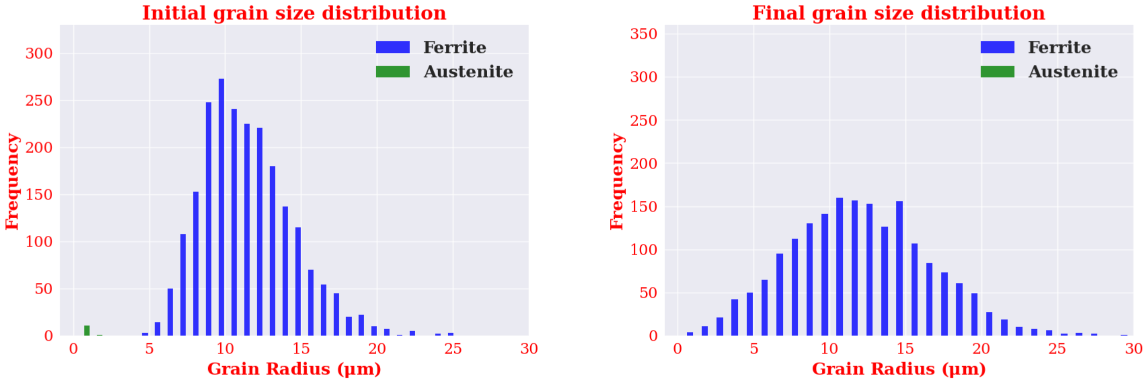

(a) At the beginning of GG stage ($t = 100\,\text{s}$)

(b) At $t = 1000\,\text{s}$

Figure 4.31: Ferrite grain size distribution during the grain growth (GG) stage

Figs.4.34 use grain coloration to showcase both the initial and final microstructures resulting from this thermal treatment. This scenario yields a relatively finer microstructure post the transformation and the grain growth. The variation in solute mass conservation error during the entire simulation of this large-scale microstructure is depicted in Fig.4.33. The maximum error incurred is only about 2%, which is a positive outcome given the magnitude of the simulation case. Due to the anticipated complete transformation, the final carbon concentration in the ferritic microstructure should ideally align with the nominal alloy composition of 0.02 wt%. However, a marginally lower average concentration of about 0.01961 wt% is obtained, correlating with the 2% loss in solute mass. These results show promise for the application of the numerical model in industrial-specific microstructures. It's important to note that the current model does not consider the reverse phase transformation during the reheating stage. However, since the driving pressure description remains consistent, adapting the existing framework to control the direction of the phase transformation should be relatively straightforward. This could be considered as a prospect for future work, involving additional complexities such as nucleation for the reverse transformation.

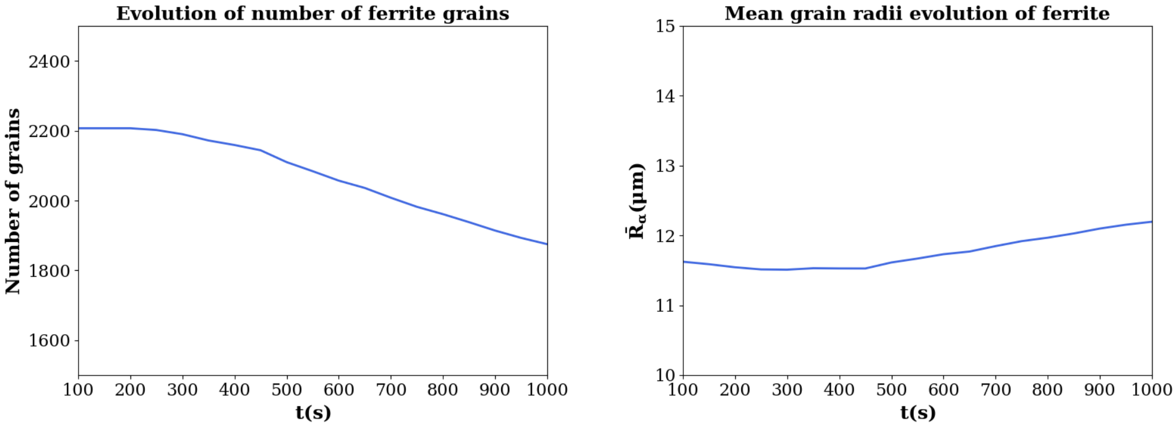

(a) Number of ferrite grains

(b) Mean grain radius of ferrite grains

Figure 4.32: Evolution of ferrite grain statistics during the grain growth stage

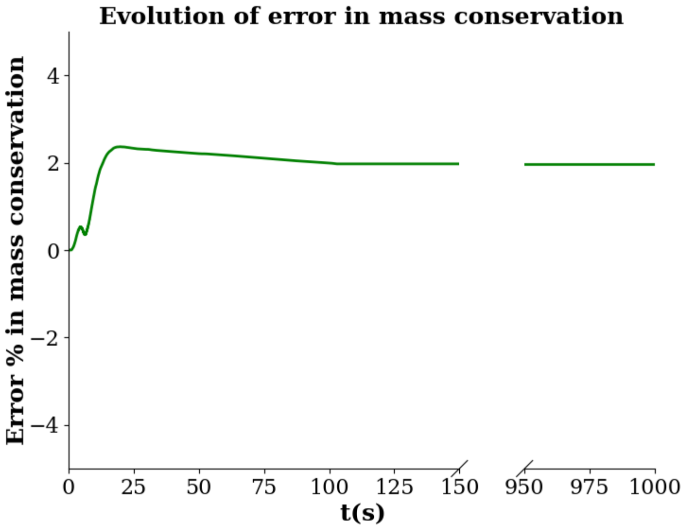

Figure 4.33: Variation of error in mass conservation during the entire simulation: the broken axis representation indicates that the same error % persists during that period

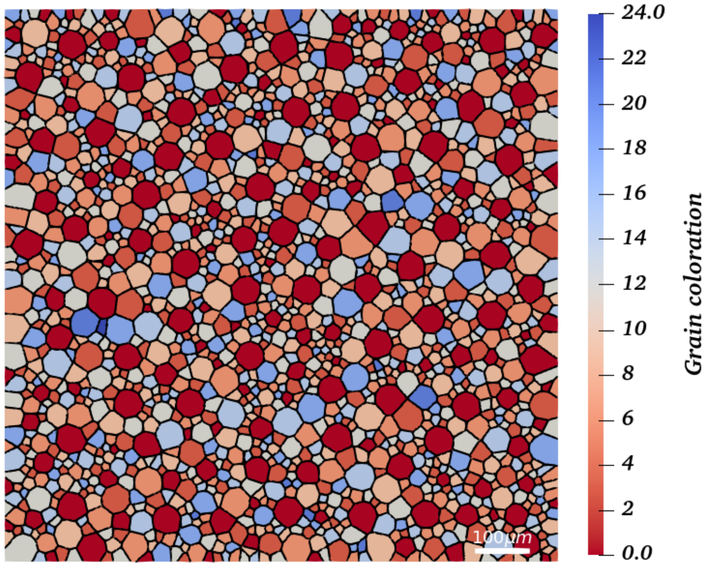

(a) Initial microstructure

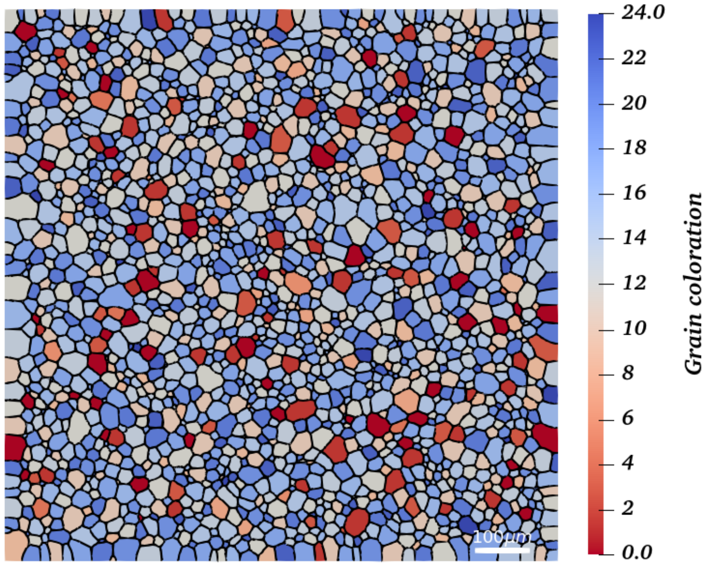

(b) Final microstructure

Figure 4.34: Comparison of the microstructure morphologies before and after the complete thermal treatment: represented by grain coloration

4.3 DSSPT simulation in a ternary alloy: 2D polycrystals

In this section, we will examine DSSPT in the presence of a substitutional element, whose effects on transformation kinetics are incorporated through solute drag aspects under para-equilibrium hypothesis. We're using the Fe-0.1 wt%C-0.5 wt%Mn steel alloy within the same basic microstructure as before (4.1) to illustrate this effect. The necessary thermodynamic data were obtained using the para-equilibrium (PE) assumptions, and we've utilized Eq.(2.100) to model the driving pressure ($\Delta G_{\gamma \rightarrow \alpha}$). For the Fe-0.1 wt%C-0.5 wt%Mn steel alloy, the calculated austenitization temperature under the PE hypothesis is approximately 1118 K. We've set the initial temperature to this T_{A3}^{PE} temperature. The microstructure is cooled to a final temperature of $T^f = 910\,\mathrm{K}$ at a cooling rate of $-10\,\mathrm{K \cdot s^{-1}}$. At end of cooling, the microstructure is maintained at the final temperature for an additional 30 s as illustrated in Fig.4.35 to provide ample time for phase transformation and the associated solute redistribution. The interfacial energy, mobility, diffusivity data, and most numerical parameters remain the same as in the earlier section (4.2.1). The time step is chosen as $\Delta t = 0.02\,\mathrm{s}$ for this case.

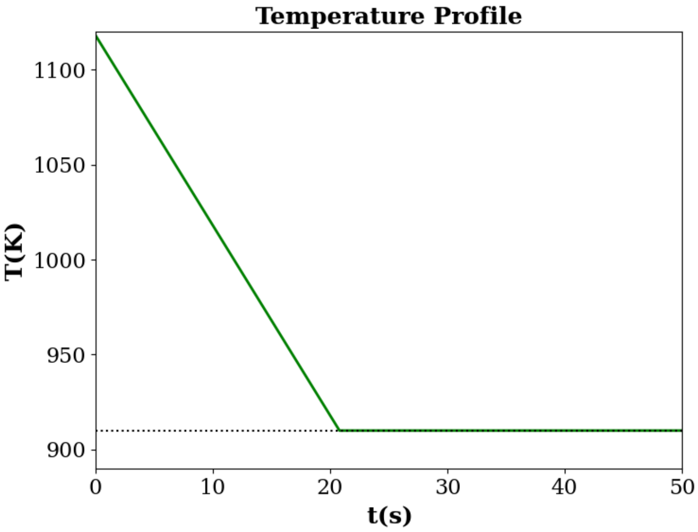

Figure 4.35: Thermal path imposed during the transformation

We've limited the appearance of ferrite nuclei exclusively to the triple junctions, introducing a total of 300 ferrite nuclei. While in practical scenarios, the count might be higher and could potentially extend to nucleation on grain boundaries owing to increased nucleation density, for the sake of clarity, we've kept a straightforward setup. The nucleation start temperature is set to $T_{N_s} = 1112\,\mathrm{K}$, and the range is assumed as $\delta T_N = 30\,\mathrm{K}$.

To model solute drag aspects, as detailed in Chapter 2 (2.3.2), we use the simplified description by Cahn's model [4]. In practical scenarios, the intention is to utilize the two parameters introduced by Cahn's solute drag pressure as fitting model parameters to align with the experimental results, rather than employing the analytical expressions provided by Cahn in Eqs.(1.58) and (1.59). However, for the purpose of demonstration in this context, we utilize the analytical expressions based on literature [5] to establish some parameters in Eqs.(1.58) and (1.59), aiming for a realistic representation as possible. Figs.4.36 provide a visualization of the Cahn's parameters computed in this simulation, depicting their variation with temperature. The graph depicting the variation of β_C^2 in Fig.4.36b suggests an increase in solute drag pressure at higher temperatures, gradually weakening as the temperature decreases. As a reminder, in the numerical formulation, the influence of solute drag is represented by the solute drag pressure coefficient ($\mathscr{M}_{SD}$) in Eq.(2.56). A higher value of $\mathscr{M}_{SD}$ corresponds to stronger solute drag effects. This value approaches unity when no solute drag effects are present.

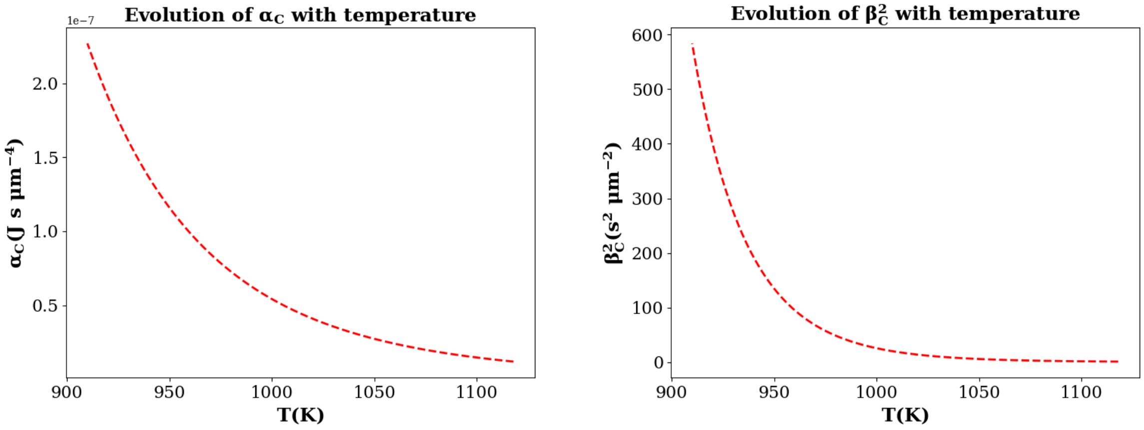

(a) $\alpha_C(T)$ (b) $\beta_C^2(T)$

Figure 4.36: Evolution of Cahn's solute drag parameters with temperature for the chosen case

Fig.4.37 illustrates the evolution of the ferrite phase fraction over time for two scenarios: without any solute drag effects, and with solute drag effects. In Fig.4.38, we observe the evolution of the ferrite phase fraction with temperature throughout the cooling process. Fig.4.38 shows that initially, enhanced drag effects at higher temperatures limit the phase fraction. However, with sufficient time given, both the scenarios eventually converge to a similar ferrite fraction value as depicted in Fig.4.37, since at lower temperatures the solute drag effects are significantly reduced.

The comparison between scenarios, one with solute drag effects and another without, is illustrated in Figs.4.39 for the phase evolution, complemented by the respective solute distribution presented in Figs.4.40. In both cases, where the nucleation density remains low and nucleation sites are restricted to triple junctions, the inhibition by neighboring nuclei is minimal. Consequently, both scenarios generally result in equiaxed grains. However, in the instance incorporating solute drag effects, the growth of ferrite nuclei at initial higher temperatures is initially sluggish due to strong drag effects. Generally, this could limit the potential dispersion in grain size distribution caused by continuous nucleation, resulting in a relatively uniform distribution of grains. However, as evident in Figs.4.42, in this case, the difference are minimal, possibly due to a smaller temperature range of nucleation for the considered cooling rate. The comparison between the final microstructure morphologies illustrated in Figs.4.41 demonstrates similar grain characteristics, including a comparable mean ferrite grain size. The noticeable distinctions primarily lie in the transformation kinetics between the two scenarios for the assumed solute drag parameters in this illustration.

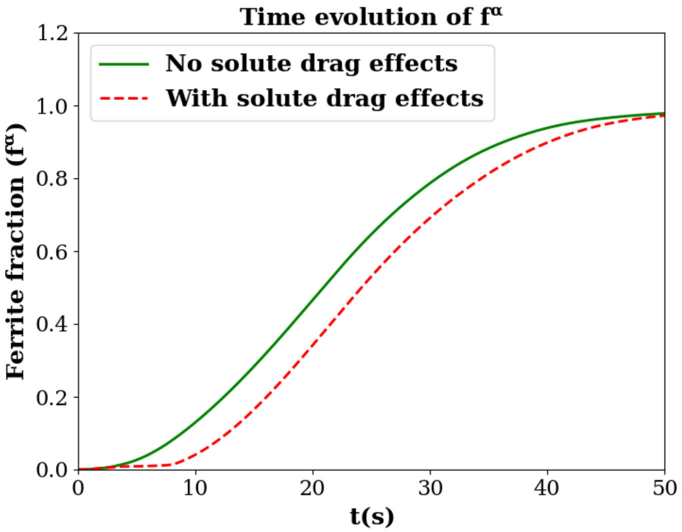

Figure 4.37: Evolution of ferrite fraction with time for the difference cases

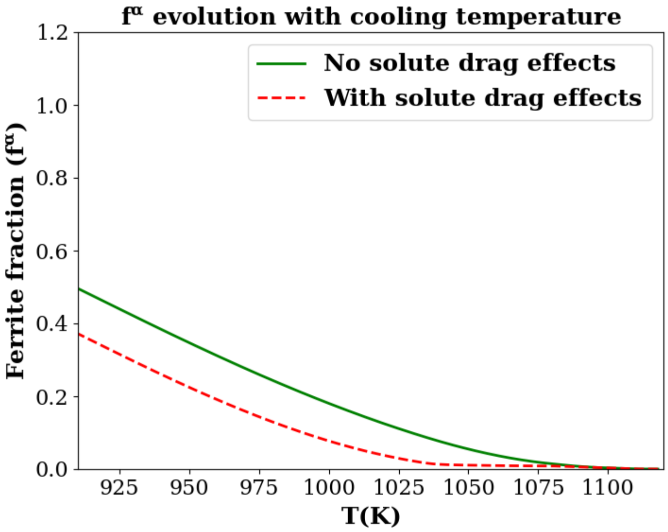

Figure 4.38: Evolution of ferrite fraction with temperature until the conclusion of cooling for different scenarios

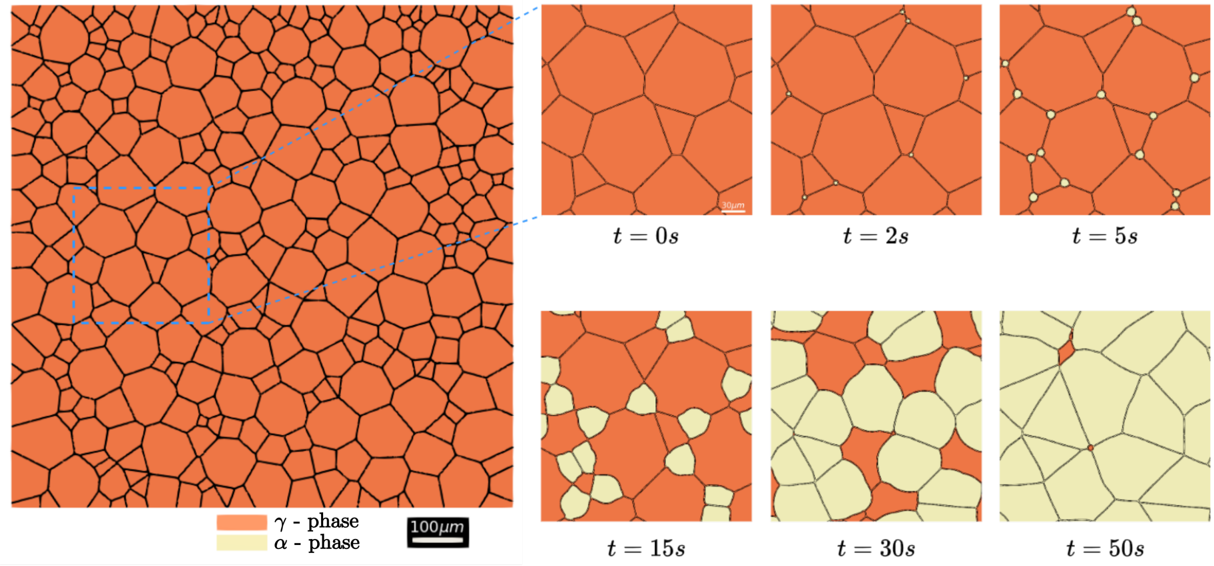

(a) Without solute drag effects

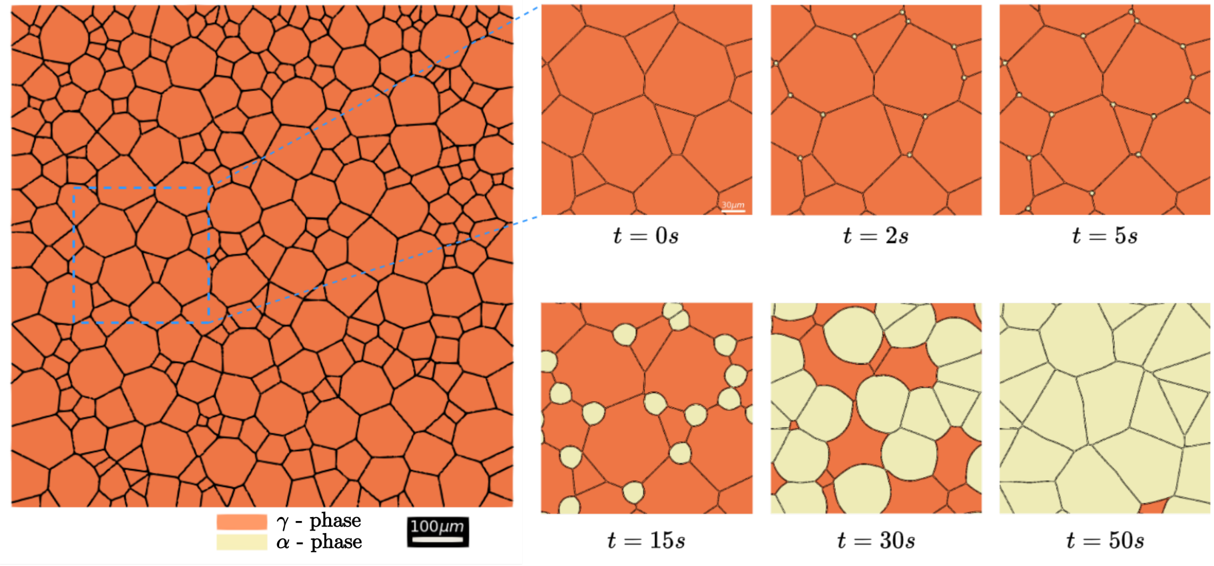

(b) With solute drag effects

Figure 4.39: Snapshots of phase evolution with and without the consideration of solute drag effects

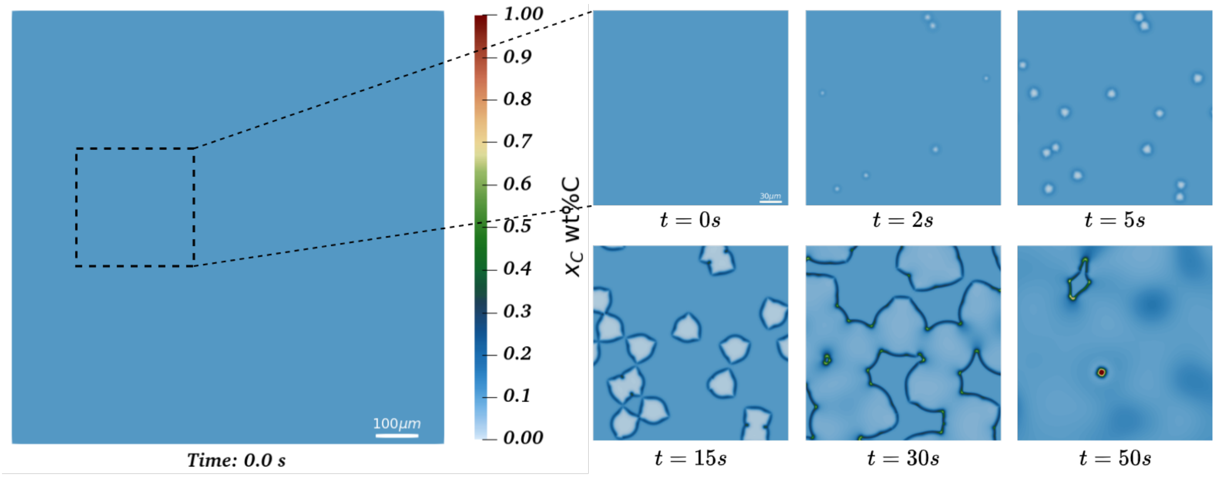

(a) Without solute drag effects

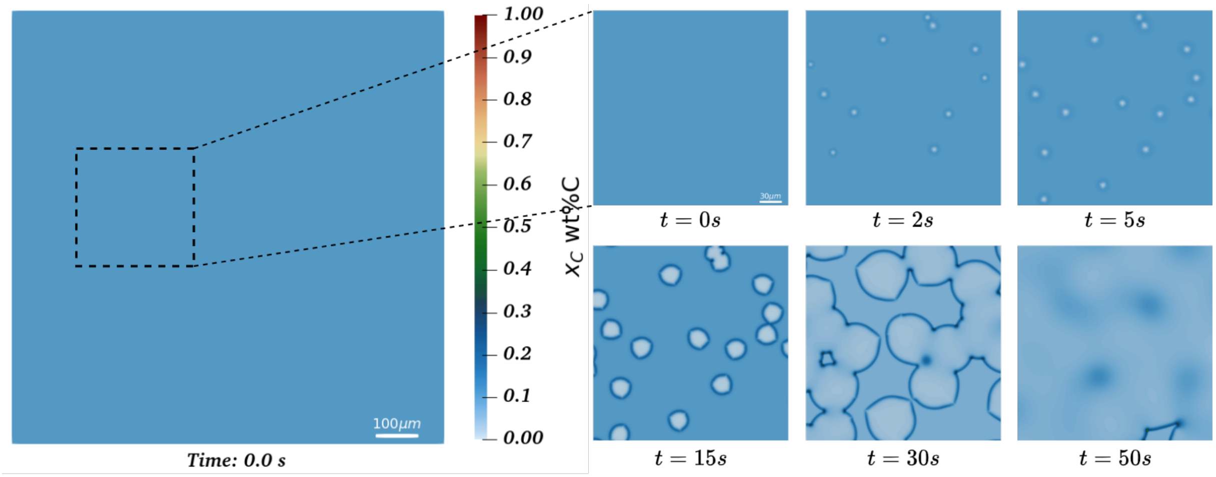

(b) With solute drag effects

Figure 4.40: Snapshots of carbon distribution with and without the consideration of solute drag effects

The mass conservation depicted in Fig.4.43 appears to be quite reasonable for this alloy in this specific illustrative case.

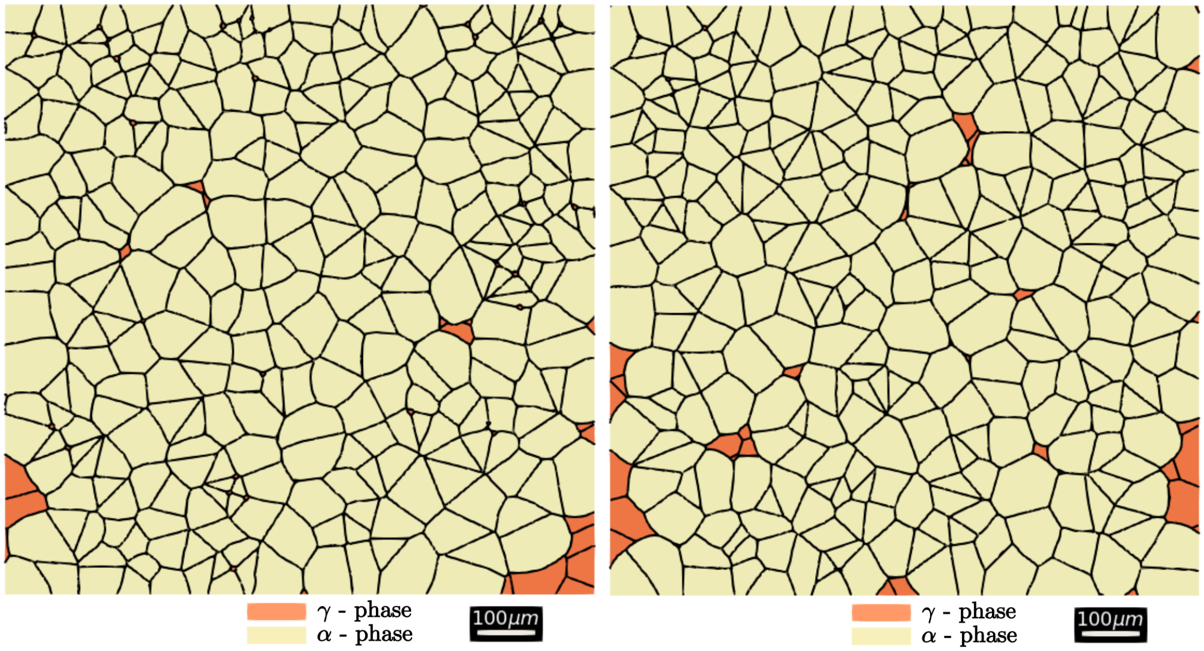

(a) No solute drag effects

(b) With solute drag effects

Figure 4.41: Final phase distribution obtained with and without solute drag effects

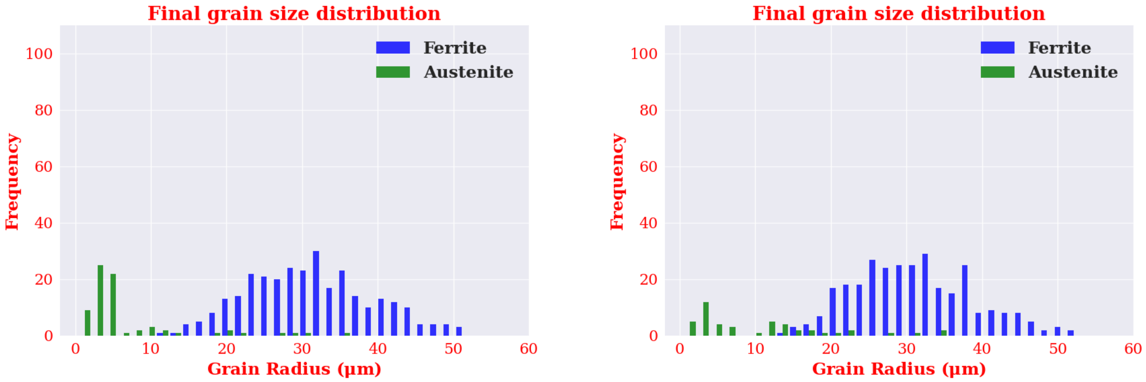

(a) Without solute drag effects

(b) With solute drag effects

Figure 4.42: Final grain size distributions obtained for the two cases

Thus, these two Cahn's solute drag parameters provide added flexibility in controlling the transformation kinetics, particularly when attempting to align with experimental transformation curves.

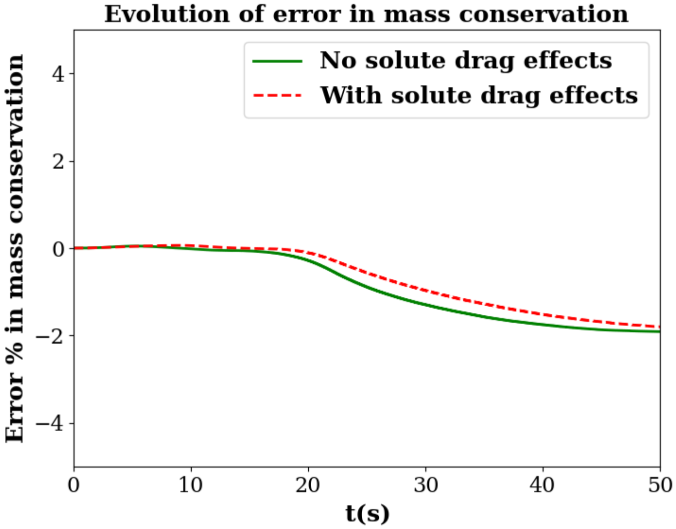

Figure 4.43: Variation of error in mass conservation for the considered simulations in the ternary alloy

4.4 Simulation of particle coarsening phenomenon but not quite the typical Ostwald ripening

In the context of a matrix phase, after a first-order diffusive phase transformation where second-phase particles (SPPs) separate, local equilibrium between the matrix and the SPPs might be attained. However, this state may not represent the system's minimum free energy configuration, particularly when the matrix phase consists of a dispersed or multi-modal distribution of second-phase particles. The interfacial energy of the SPPs contributes to the excess free energy in the system, which is thermodynamically unfavorable. As a result, the system attempts to alleviate this excess free energy by reducing the surface energy within the system. In the absence of any elastic misfits at the phase boundaries, the system achieves this by dissolving smaller particles in favor of larger ones. Consequently, the larger particles coarsen at the expense of the smaller SPPs, thereby decreasing the surface energy in the system. This process is brought about by diffusional mass transport from a region of higher concentration to an area of lower concentration. The variation in composition is created due to the multi-modal distribution of the particles. The local equilibrium concentrations (solubility limits) of the solute between the matrix and the SPPs are altered by Gibbs-Thomson effects (capillarity effects), determined by the curvature of the SPP as elucidated in Chapter 3 (3.2.2). Consequently, a gradient in concentration emerges, fueling the diffusive mass transport. This phenomenon is commonly referred to as particle coarsening or Ostwald ripening [6, 7]. In the typical Ostwald ripening phenomenon, diffusional mass transport occurs from smaller particles to larger particles, assuming that the capillary-induced pressure increases solubility with curvature for the underlying phase of the particles. However, as demonstrated in 3.2.2 with Fig.3.12, Gibbs-Thomson effects might not consistently increase the solubility limits of the product phase (particle phase).

Consider a hypothetical scenario with SPPs represented by the ferrite phase and the matrix as the austenite phase. Here, based on thermodynamic considerations, the capillary-induced pressure reduces solubility with curvature. Consequently, smaller particles with higher curvature could exhibit lower concentration at local equilibrium compared to larger particles. In such a scenario, the diffusive mass transport would occur from larger particles to smaller ones. To understand the underlying dynamics, the phenomenon of particle coarsening can be envisioned as a competition between the chemical driving pressure ($\Delta G_{\gamma\rightarrow\alpha}$) and the capillarity driving pressure ($\sigma_{\gamma\alpha}\kappa$). At local equilibrium, these two driving pressures balance each other out. However, the solute flux from larger particles would increase the interface concentration of smaller particles, reducing the $\Delta G_{\gamma\rightarrow\alpha}$ pressure to a level where $\Delta G_{\gamma\rightarrow\alpha} < \sigma_{\gamma\alpha}\kappa$. Consequently, this results in the dissolution of the smaller particles. Conversely, the solute flux transported from the larger particle would decrease its interface concentration. This decrease would raise the chemical driving pressure to a level surpassing that of capillarity, leading to the growth of the larger particle. In a realistic scenario where capillarity effects increase the solubility of the particle phase with curvature (typical Ostwald ripening), similar principles of competition between driving pressures can explain the dynamics of the phenomenon. The distinctive factor lies in the diffusional mass transport's direction, alongside the chemical driving pressure, where a higher interface concentration corresponds to a greater $\Delta G_{\gamma\rightarrow\alpha}$.

To simulate this phenomenon, given the unavailability of realistic test cases and required thermodynamic data for typical Ostwald ripening simulation due to time restrictions, we've chosen to use a hypothetical scenario: representing the SPPs as the ferrite phase and the matrix as the austenite phase. It's crucial to highlight that despite this hypothetical setup not mirroring the conventional appearance of Ostwald ripening, the inherent kinetics and dynamics remain identical. The primary objective is to showcase the numerical model's capability in simulating various diffusive solid-state phenomena, including particle coarsening, utilizing the same kinetic framework. Therefore, our simulation involves an austenite phase matrix within a 1 mm-sized domain, wherein the second phase consists of ferrite, forming a bimodal distribution of particles, as illustrated in Fig.4.44. The initial configuration is represented in Fig.4.45 through the grain coloration employed for this case.

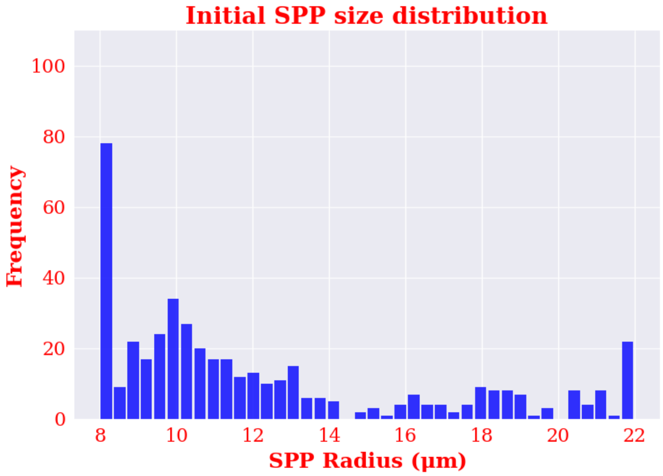

Figure 4.44: Initial size distribution of second-phase particles (SPPs)

The initial condition is set to a slight offset ($T^i = 1162\,\mathrm{K}$) from the isothermal simulation temper-

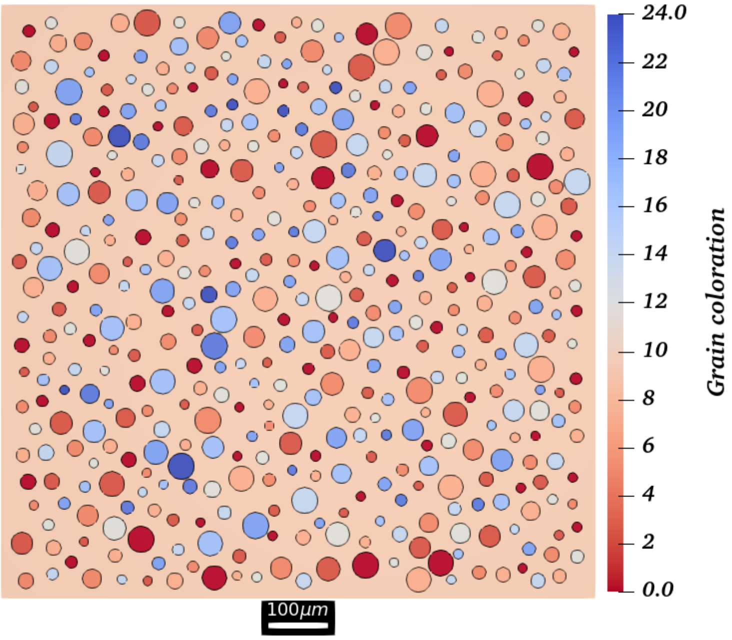

Figure 4.45: Initial grain coloration of the matrix-SPPs setup

ature of $T = 1160\,\text{K}$ for the Fe-0.02 wt%C alloy. This proximity ensures that the system is nearly at local equilibrium for phase transformation and can swiftly transition to the particle coarsening regime. The resolution time step is fixed at $\Delta t = 0.5\,\text{s}$. The diffuse interface thickness is set to 5 µm with a local mesh resolution of 0.5 µm (adaptive mesh). The mobility and carbon diffusivity data are consistent with previous cases. However, considering the long time scale of this phenomenon, for illustrative purposes, the interfacial energy is set to a higher value ($\sigma_{\gamma\alpha} = 2{\times}10^{-6}\,\text{J}{\cdot}\text{mm}^{-2}$) to accentuate the coarsening process. The simulation is run for a duration of 10000 s.

Figs.4.46 present a series of snapshots illustrating the particle evolution at different instants, while Figs.4.47 exhibit the corresponding concentration maps. The system is anticipated to reach local equilibrium after the initial phase transformation at approximately 50 s. Thus, the particle coarsening regime is assumed to commence from $t = 50\,\text{s}$. The expected coarsening of larger particles is visibly apparent, as the smaller particles dissolve over time. It's important to note that physical coalescence aspects are not accounted for in this simulation. However, numerical coalescence is prevented due to the grain coloration technique employed. Interestingly, none of the particles appear to make direct contact, likely due to the system's proximity to local equilibrium and thus exhibiting very slow kinetics. Nevertheless, soft impingement arising from the diffusion fields of adjacent particles is noticeable. Whenever two particles approach close proximity, the local diffusional flux and the interaction with capillarity pressure seem to flatten their interfaces.

Fig.4.48 depicts the ferrite fraction observed throughout the particle coarsening process. Theoretically, the ferrite fraction should remain constant. However, due to a non-negligible error in mass conservation (approximately 15%), slight variations in the ferrite fraction are evident. The red portion of the curve highlights the phase transformation regime, while the remainder illustrates the coarsening stage. Particle coarsening is characterized by monotonous decrease of SPPs with monotonous increase in the mean particle size. This is well reflected in Figs.4.49 showcasing the

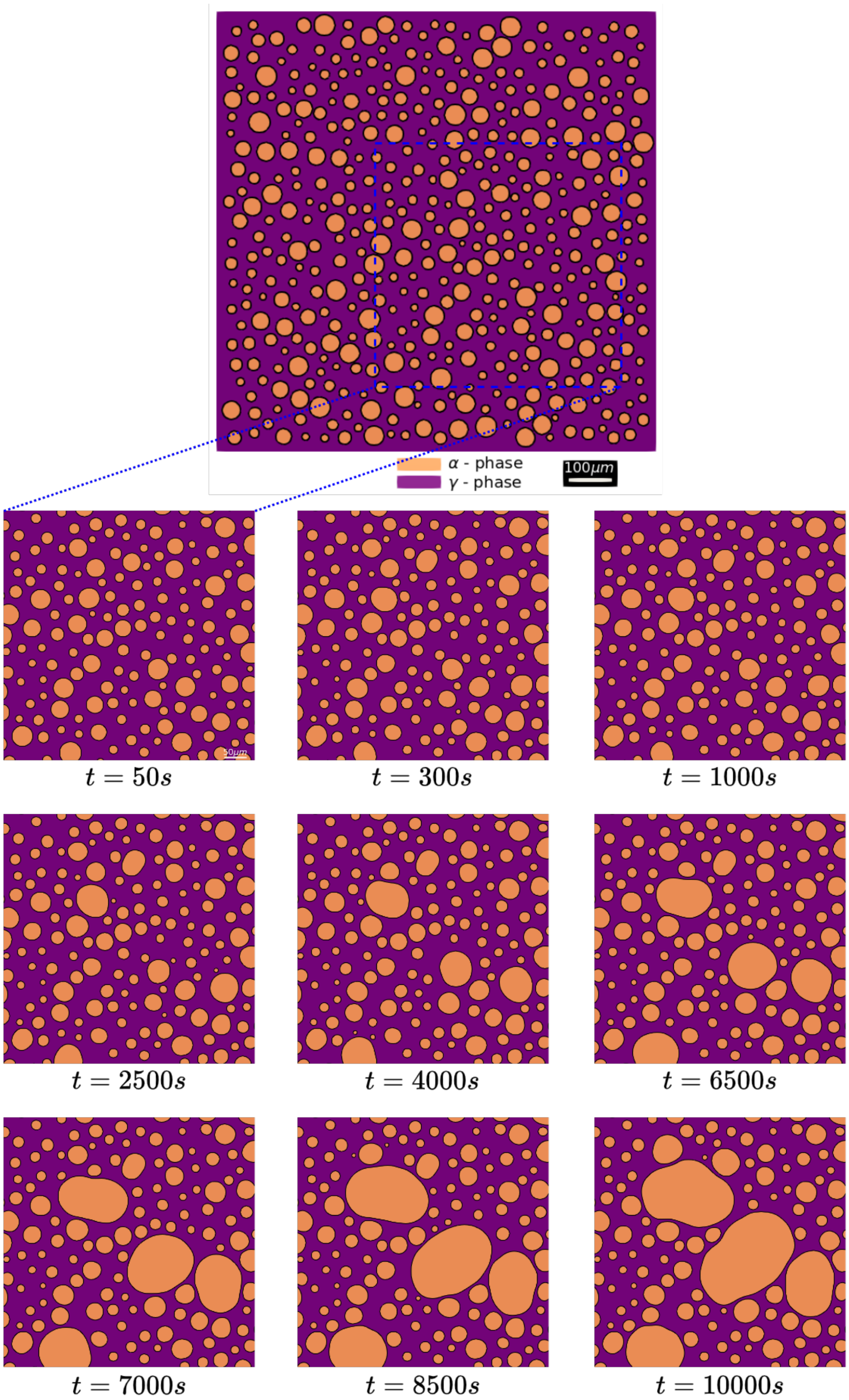

$t = 50s$ $t = 300s$ $t = 1000s$

$t = 2500s$ $t = 4000s$ $t = 6500s$

$t = 7000s$ $t = 8500s$ $t = 10000s$

Figure 4.46: Snapshots of coarsening and dissolution of second phase particles (SPPs)

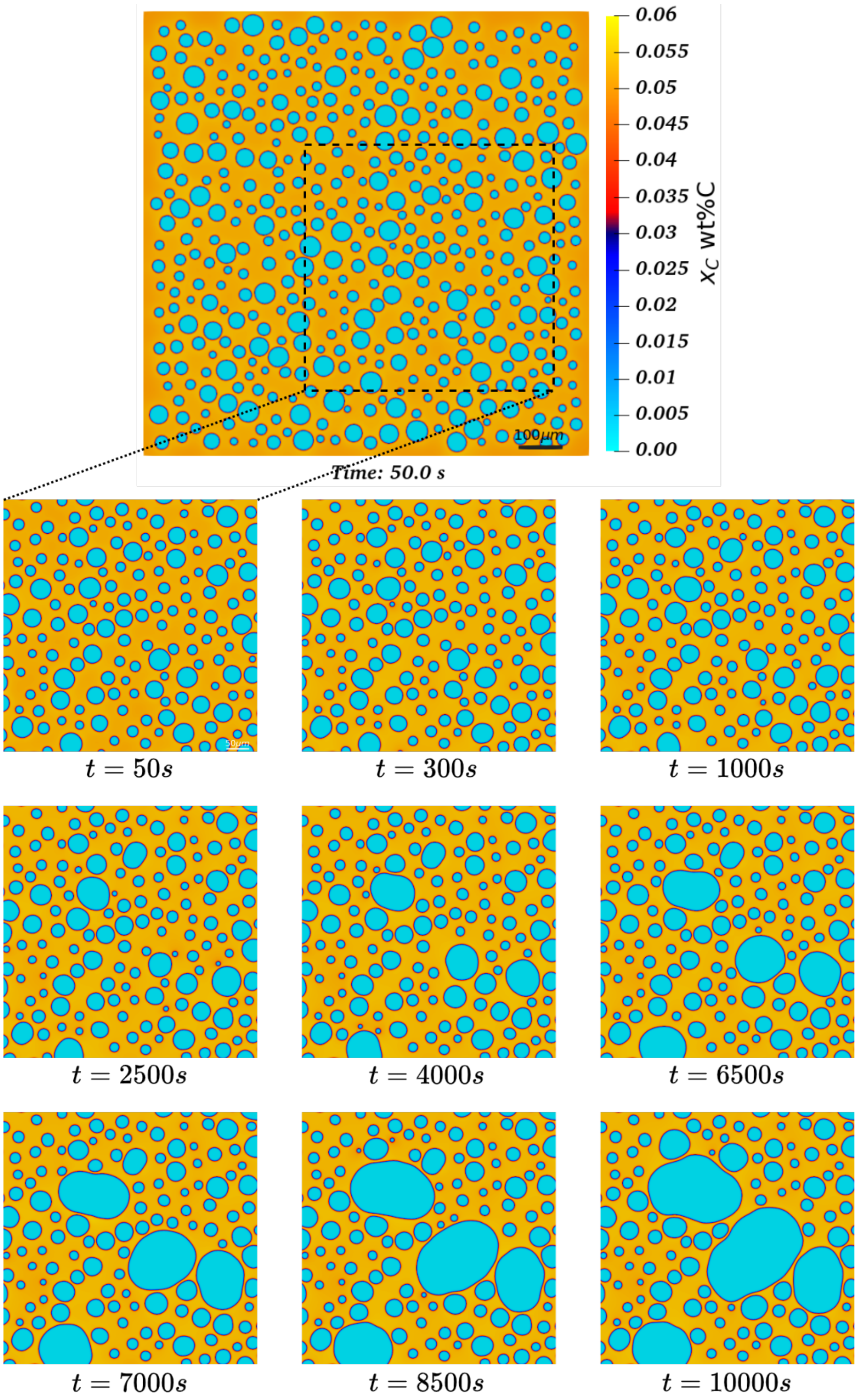

$t = 50s$ $t = 300s$ $t = 1000s$

$t = 2500s$ $t = 4000s$ $t = 6500s$

$t = 7000s$ $t = 8500s$ $t = 10000s$

Figure 4.47: Snapshots of solute distribution (SPPs) during the particle coarsening phenomenon

evolution of number of particles and the evolution of the mean particle size, respectively. Fig.4.50 demonstrates the particle size distribution obtained at the end of the simulation. It seems evident that, in comparison to Fig.4.44, there has been an increase in the frequency of larger particles over time as a result of coarsening.

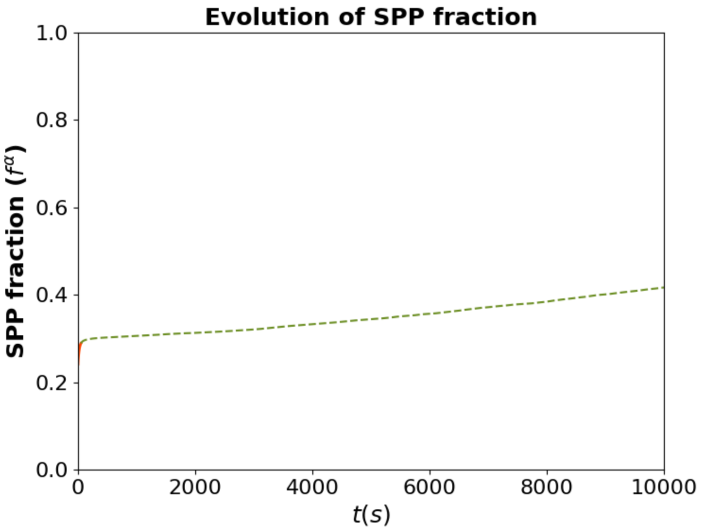

Figure 4.48: Evolution of the phase fraction of the SPPs

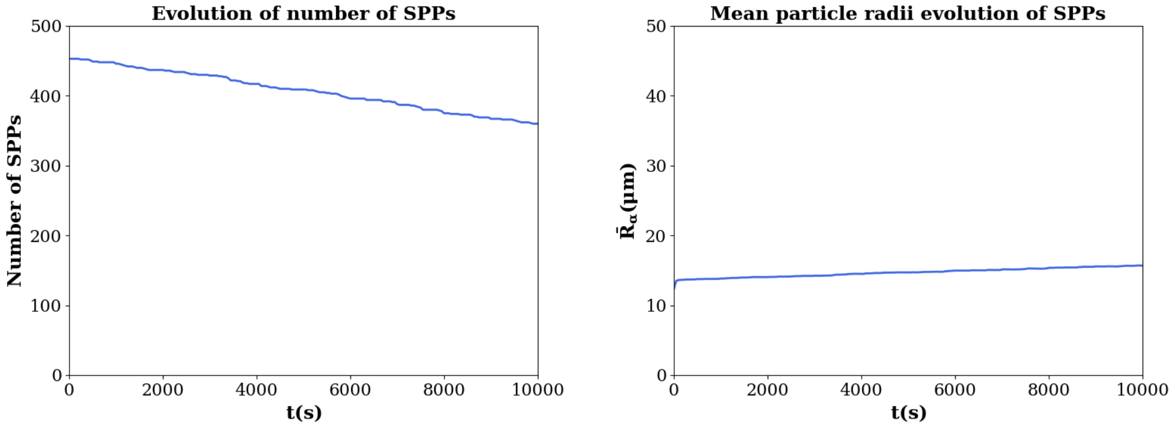

(a) Number of SPPs

(b) Mean particle size

Figure 4.49: Evolution of particle statistics

In the Fig.4.51, the kinetics of the particle size evolution are compared with the modern Ostwald ripening (OR) theories [8]. These theories are grounded on a generic expression:

$$\bar{R}_{\alpha}^{3} - \bar{R}_{\alpha}^{3}(0) = kt, \tag{4.2}$$

where $\bar{R}_{\alpha}$ is the mean particle size, $\bar{R}_{\alpha}^{3}(0)$ is the initial mean particle size, and k is a parameter characterized based on the concerned theory. It appears that the simulated mean particle size can be

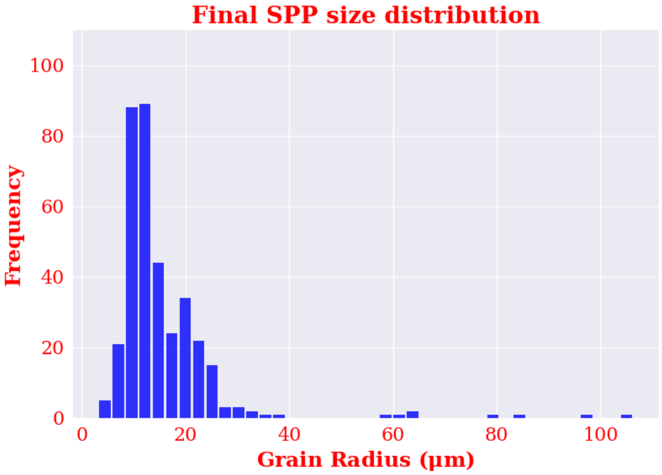

Figure 4.50: Final size distribution of second-phase particles (SPPs)

fit into the aforementioned expression, resembling the quantitative description provided by the OR theories. Therefore, the hypothetical scenario we've adopted demonstrates kinetic characteristics akin to those of a typical Ostwald ripening phenomenon. This serves as evidence of the numerical model's seamless potential to simulate a range of diffusive solid-state phenomena.

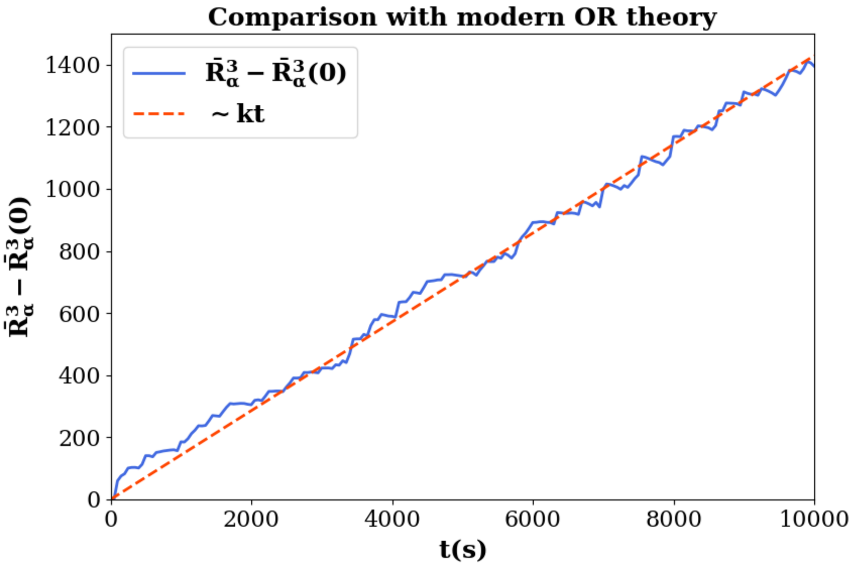

Figure 4.51: Comparison with modern Ostwald ripening theories

4.5 Summary

The numerical model showcases its capacity to simulate complex biphasic polycrystals undergoing diffusive solid-state phase transformation, demonstrated through austenite decomposition in steels. Investigating nucleation aspects in conjunction with cooling rates, the study reveals distinct transformation behaviors. At rapid cooling rates, nucleation on grain boundaries forms necklace-like nuclei structures along parent phase grain boundaries, resulting in elongated grains due to hard impingement effects. In contrast, nucleation limited to grain corners leads to the formation of equiaxed grains. Site-saturated nucleation fosters uniform growth of ferrite grains, yielding compact grain size distributions. Continuous nucleation introduces dispersion in grain sizes due to differing appearance times of nuclei.

Slower cooling rates with lower nucleation density produce coarser grains, while faster rates with higher nucleation density yield finer grains. Slower cooling allows ample diffusion time, leading to smaller trapped parent phase islands and a higher ferrite fraction at the conclusion of cooling. Addressing numerical artifacts, particularly the negative transformation driving pressure in some cases when a cluster of nuclei traps the parent phase, is crucial to prevent aberrant grain kinetics and maintain mass conservation. The semi-analytical computation of the reactive term in the diffusion equation tends to produce errors at the triple junctions within a polycrystal context. Therefore, it's preferable to numerically compute the reactive term for polycrystal scenarios to enhance solute mass conservation and reduce unphysical behavior at the triple junctions.

In ternary alloys, integrating solute drag aspects effectively replicates sluggish transformation kinetics, observed at certain stages of transformation. By incorporating Cahn's solute drag parameters as adjustable model parameters, it provides added flexibility to control transformation kinetics, to ensure alignment with experimental transformation curves.

The numerical model's adaptability to simulate various diffusive solid-state phenomena, like particle coarsening, using a unified numerical framework, is exemplified through an academic case. Overall, the model showcased promising outcomes, effectively capturing intricate transformation dynamics reflective of real-world scenarios. These results pave the way for exploring practical microstructures concerning industrial applications.

References

[1] *Thermo-Calc Software*. `http://www.thermocalc.se/`.

[2] S.E. Offerman et al. "Grain nucleation and growth during phase transformations". In: *Science* 298.5595 (2002), pp. 1003–1005.

[3] M.G. Mecozzi et al. "The role of nucleation behavior in phase-field simulations of the austenite to ferrite transformation". In: *Metallurgical and Materials Transactions A* 39 (2008), pp. 1237–1247.

[4] J.W. Cahn. "The impurity-drag effect in grain boundary motion". In: *Acta metallurgica* 10.9 (1962), pp. 789–798.

[5] F. Fazeli and M. Militzer. "Application of solute drag theory to model ferrite formation in multiphase steels". In: *Metallurgical and Materials Transactions A* 36 (2005), pp. 1395–1405.

[6] W.Z. Ostwald. “Blocking of Ostwald ripening allowing long-term stabilization”. In: *Phys. Chem* 37 (1901), p. 385.

[7] P.W. Voorhees. “The theory of Ostwald ripening”. English (US). In: *Journal of Statistical Physics* 38.1-2 (Jan. 1985). Copyright: Copyright 2007 Elsevier B.V., All rights reserved., pp. 231–252. ISSN: 0022-4715. DOI: `10.1007/BF01017860`.

[8] A. Baldan. “Review progress in Ostwald ripening theories and their applications to nickel-base superalloys Part I: Ostwald ripening theories”. In: *Journal of materials science* 37 (2002), pp. 2171–2202.

Chapter 5

Conclusion and Perspectives

Abstract

This chapter consolidates the accomplishments and key takeaways from this work, emphasizing the proposed level-set based numerical framework. It delves into highlighting the potential challenges encountered, and concludes with reflections on the framework's outcomes. Additionally, it outlines promising future directions facilitated by this work, offering a glimpse into prospective avenues for exploration

Résumé

Ce chapitre synthétise les réalisations et les principaux résultats de ce travail, en mettant l'accent sur le modèle numérique proposé, basé sur l'approche level-set. Il souligne les défis potentiels rencontrés et conclut par des réflexions sur les résultats du modèle. En outre, il expose les perspectives prometteuses facilitées par ce travail, en offrant des pistes d'exploration potentielles.

5.1 Conclusions

Chapter 1 provided a brief introduction to the concept of microstructural instability and the resulting array of transformation mechanisms, in the context of metallic alloys. Chapter 1 also elaborated on the fundamental aspects of diffusive solid-state phase transformation (DSSPT) theory, aligning with one of the primary objectives of this thesis: to model diffusive phase transformations at the solid state. DSSPT typically involves nucleation of the new stable phase, followed by their subsequent growth. Chapter 1 highlighted the lack of a consistent and comprehensive description of a nucleation event in phase transformation despite an abundance of literature in the field. The current state-of-the-art nucleation models rely on various assumptions and complex parameters, allowing for significant flexibility. Most of these parameters present enormous difficulties to precisely quantify them with any conviction. Consequently, at the mesoscopic scale, describing nucleation often involves relatively simple approaches based on strong assumptions. To capture transformation kinetics accurately during the growth stage, it's crucial to consider a mixed-mode transformation character. A portion of the driving pressure facilitating phase transformation is dissipated by interfacial processes involving lattice rearrangement between the phases, while the remaining part is attributed to long-range solute diffusion in the bulk of the phase. In contrast to certain diffusion-controlled models that assume instantaneous local equilibrium, achieving local equilibrium at the phase interface is a gradual process within a mixed-mode type phase transformation model. In metallic alloys containing slowly diffusing substitutional solute elements alongside fast diffusing interstitial elements, constrained phase equilibria assumptions are employed to describe transformation kinetics. This is due to the challenge of achieving complete local phase equilibrium for both types of solute elements simultaneously. A portion of the available driving pressure for transformation is consumed by the potential interaction of substitutional solutes with the migrating phase interface, resulting in solute drag effects. Therefore, it's crucial to account for the drag resistance caused by these solute drag effects to accurately replicate the sluggish transformation kinetics observed in these scenarios.

While Chapter 1 reflected the physical aspects of phase transformation, Chapter 2 offers the numerical modeling viewpoint of microstrucutral evolution. In the realm of DSSPT, the front capturing based method of level-set (LS) has not been explored to its full potential in the current state-of-the-art despite its successful application in simulating other microstructural changes like recrystallization (ReX) and grain growth (GG). Most of the existing approaches are insufficient to model the concomitant nature of microstructural transformations, especially in the context of industrial applications involving high plastic deformation and other complex thermomechanical treatments in multi-phase materials. This motivated the proposition of a global level-set formulation with a generalized kinetic framework, capable of effectively accounting for different contributions, enabling the modeling of diverse evolutions including DSSPT, ReX, and GG simultaneously. Chapter 2 provides an in-depth description of this proposed numerical framework in a finite element (FE) context, with a strong focus on modeling DSSPT in biphasic polycrystals at the mesoscopic scale. While this work primarily explores the level-set method's application for DSSPT using the proposed model, the generalized kinetic framework presented in Chapter 2 offers a promising avenue for future work, allowing seamless integration of additional physical aspects alongside phase transformation. The LS-based framework for modeling DSSPT involves two pivotal stages: a diffusion equation governing solute redistribution between the phases, and a level-set transport equation governing the resultant migration of microstructure topology. A unified diffusion equation across the computational domain is formulated by hypothesizing a diffuse interface description across the phase interfaces. This reformulation is reminiscent of the phase-field method's approach to modeling diffusion. In the context of a polycrystal, the presence of a multitude of grains is handled by utilizing the grain coloration scheme which effectively reduces the number of level-set functions needed. The interface migration is effected via a classical level-set description of the interface. While Cahn's solute drag model lacks physical applicability across interphase boundaries and is more suited for grain boundaries, its capacity to capture general trends in solute drag effects, whether at grain interfaces or phase interfaces, is noteworthy. Its straightforward description renders it attractive for numerical implementation. Hence, Cahn's simplified description of solute drag pressure is integrated into the existing kinetic framework to account for solute drag. This integration provides flexibility in conjunction with the choice to use Cahn's solute drag parameters as adjustable model parameters. The final kinetic formulation is finally equivalent to decreasing the interface mobility by a factor. This seems synonymous to some of the models in the current state-of-the-art that consider an effective interface mobility reduced by a constant factor to account for solute drag. However, in our proposed formulation, this factor (referred as solute drag pressure coefficient) is heterogeneous depending on the local interface kinetics, providing a richer description. A specific adaptive meshing/ remeshing strategy is employed to ensure the required detailed mesh resolution across the phase interfaces. Conversely, a less detailed resolution suffices across the grain interfaces, optimizing computational efficiency. The successful coupling with ThermoCalc interface helps with the piecewise linearization of the phase diagram, providing an enriched description for the phase transformation driving pressure. Recognizing the challenges in accurately describing nucleation events at the mesoscopic scale, Chapter 2 provided insight into the simplified nucleation model utilized within the current framework. This model enables the nucleation of spherical-shaped nuclei at grain corners, grain boundaries or other sites, as needed, subject to specific constraints.

An initial assessment of the proposed numerical framework is performed on benchmarking cases in Chapter 3. The proficiency of the numerical model in reproducing expected physical behaviors is demonstrated within simple domains, focusing on austenite decomposition in steels. Their quantitative predictions align well with the estimations obtained from ThermoCalc. The 2D matrix-precipitate case effectively demonstrates the subtle yet pivotal influence of capillarity effects on phase transformation kinetics and the equilibrium position. Capillarity plays a crucial role in governing the early-stage kinetics when the growing phase is in its nascent nucleus form, underlining the importance of taking them into account. The proposed level-set numerical model is benchmarked against a state-of-the-art sharp interface semi-analytical model and is compared with predictions from a corresponding phase-field numerical model for simulating austenite decomposition in a steel alloy. The results from this analysis demonstrated the level-set model's effectiveness in reproducing the solute concentration profiles and interface kinetics akin to both the semi-analytical and the phase-field model. A sensitivity analysis effectively demonstrated the convergence of numerical predictions with changes in mesh resolution and the time step. It emphasized the importance of having an adequate number of mesh elements within the presumed diffuse interface thickness to accurately capture field variations and ensure good solute mass conservation. The predicted interface kinetics exhibited consistent behavior with varying interface thickness, provided fine enough mesh resolution with sufficient mesh elements within the diffuse interface is utilized. Caution must be exercised when choosing the diffuse interface parameter, aiming to strike a balance between employing a reasonably coarse mesh with enough elements within the diffuse interface and avoiding the use of unrealistically large values. Aiming for 7 to 20 mesh elements within the diffuse interface usually establishes a reasonable compromise. Yet, under specific cases and conditions, achieving an acceptable level of mass conservation might necessitate a greater number of elements in the diffuse interface.

The potential of the proposed numerical framework to replicate the phase transformation behavior in complex polycrystalline microstructures is showcased in Chapter 4. Distinct transformation behavior, typically expected, emerge when different nucleation aspects are taken into account in conjunction with varying cooling rates. The numerical model also demonstrated its capability to simulate large-scale microstructures with thousands of grains, relevant to industrial settings. An illustrative case considering solute drag aspects in a ternary alloy showcased the model's ability to reproduce sluggish transformation kinetics. The adjustable Cahn's solute drag parameters offer additional flexibility to control the transformation kinetics, to be potentially in better agreement with the experimental transformation curves. In certain scenarios, especially at slower cooling rates, the transformation driving pressure has the tendency to become negative, stalling the grain kinetics and leaving behind tiny islands of the parent phase grains, especially at the eventual triple junctions of the product phase grains. This issue is attributed to the semi-analytical approach used to compute the reactive term in the diffusion equation, which tends to introduce errors at the triple junctions within a polycrystal context. Therefore, it is preferable to numerically compute the reactive term for polycrystal scenarios to enhance solute mass conservation and reduce unphysical behavior at the triple junctions. Chapter 4 also illustrated the numerical model's versatility to simulate other diffusive solid-state phenomena such as particle coarsening, without any modifications to the existing formulation.

Globally, the proposed level-set based numerical framework shows encouraging potential in simulating diffusive phase transformations at the solid-state. The generalized nature of the framework alongside the adaptive meshing capabilities offer diverse scope to seamlessly integrate other complex evolution aspects into the model, including simulations in 3D. The positive outcomes of this work are expected to guide future research, potentially expanding the range of modeling approaches available alongside the established phase-field method in the realm of diffusive solid-state phase transformation.

5.2 Prospective works

The proposed numerical framework in its budding stage offers an open field for exploring several perspectives and potential improvements. Some of these propositions will potentially be part of the future work within the current research team of our laboratory.

5.2.1 Experimental validation

In the context of this work, an intended validation using an experimental test case couldn't be realized as planned. We had arranged for the casting of a specific material composition for analysis with an industrial partner (ArcelorMittal, Maizières). Unfortunately, unexpected circumstances led to delays and altered our plans. We considered sourcing experimental curves from literature as potential references for fitting the numerical predictions. However, caution is essential in using such data by discussing the precision of the results, underlying choices in generating the experimental data, and uncertainties regarding nucleation data and parameters. Relying on this data might indeed provide too much flexibility for the numerical model to converge to these curves.

Nevertheless, this setback offers an opportunity for a comprehensive experimental analysis to validate the proposed numerical model. It also enables improvements to the current nucleation model, potentially refining it based on experimental observations. This would also provide a latitude to apply the numerical framework to super alloys, pertinent to critical applications. The existing model utilizes a steady nucleation rate, but there's potential to enhance it by incorporating principles from the Classical Nucleation Theory (CNT) [1–4]. The challenging aspect would then be to precisely quantify some of the complex parameters introduced by CNT.

Enriching the interface mobility and energy description to include heterogeneity and anisotropy aspects [5] is also an important prospective work to render realistic depiction of the microstructural evolution.

5.2.2 Extension to 3D simulations

While the illustrations in this work have primarily been in 2D, the numerical formulation presented in 2.3 is generic, allowing for seamless transition to 3D simulations. A 3D simulation would offer a more realistic and complete depiction of evolutionary aspects, offering insights that are typically overlooked in 2D. However, a significant challenge arises from the computational demands of adaptive meshing and remeshing operations in 3D, especially when ensuring the required precision across phase interfaces. As discussed in [6], remeshing in 3D could be less effective compared to utilizing a static fine mesh throughout, especially for large-scale microstructures. However, adopting static fine meshes in 3D poses its own set of challenges due to high memory demands. Thus, thoroughly considering the remeshing aspect in 3D becomes crucial for potential enhancements.

5.2.3 Short-circuit diffusion

The literature extensively details that solute diffusion occurs faster along the so-called short-circuit paths compared to the bulk of the grain [7–9]. In a polycrystalline context, various defects such as multiple junctions, triple lines (grain edges), grain boundaries, dislocations, etc., constitute as potential short-circuit paths. Notably, experimental findings have validated a hierarchy in diffusion rates: self-diffusion on a free surface demonstrates the highest diffusion rate (D_s), succeeded by diffusion along high-angle grain boundaries (D_{gb}), then low-angle grain boundaries or dislocation lines (D_d), and finally, bulk or volume diffusion (D_v), i.e.,:

$$D_s > D_{gb} > D_d > D_v. \tag{5.1}$$

In the proposed numerical framework, solute diffusion is assumed homogeneous within the bulk of a grain and across the grains of the same phase. Consequently, exploring the impact of short-circuit diffusion effects during phase transformation emerges as a potential avenue for future work. Various models in the literature precisely capture short-circuited diffusion at lower modeling scales by considering segregation aspects. At the mesoscopic scale within the current framework, the primary emphasis isn't on achieving high precision in modeling.

As an initial proposal, integrating short-circuited diffusion along grain and phase boundaries could involve assuming heterogeneous activation energy for solute diffusion. Particularly, a lower activation energy near the grain and phase boundaries could be considered. Thus, the activation energy for solute diffusion (say α phase) could be expressed as:

$$Q_\alpha^C(\boldsymbol{x}) = Q_\alpha^C\big|_0 \left(1 - \chi_i^{hgb}(\boldsymbol{x}) k_{scd}\right), \tag{5.2}$$

where $Q_\alpha^C\big|_0$ is the activation energy for solute C in the bulk of the grain, k_{scd} is a factor (< 1) by which the activation energy is reduced near the grain boundaries, and $\chi_i^{hgb}(\boldsymbol{x})$ is a characteristic function used to characterize a local region near the grain boundary of a particular grain depending on a certain chosen distance (δ_{scd}). This characteristic function could be defined as:

$$\text{For } i \mid \varphi_i^k(\boldsymbol{x}) \geq 0$$
$$\chi_i^{hgb}(\boldsymbol{x}) = \begin{cases} 1 & \text{if } 0 \leq \varphi_i(\boldsymbol{x}) \leq \delta_{scd} \, . \\ 0 & \text{otherwise} \end{cases} \tag{5.3}$$

The discontinuous characteristic function could be replaced by a smooth function to allow for a continuous transition from the bulk value to the grain boundary value. Fig.5.1 gives an illustration of this characteristic function within a grain. It would take 1 within the thin strip highlighted in green and 0 in the bulk of the grain. A potential variation of this activation energy along the line A-A is also demonstrated. With the computation of the heterogeneous activation energy, the temperature dependent Arrhenius type law in Eq.(3.1) could be applied to compute the heterogeneous diffusivity field with a higher diffusion rate near grain boundaries. A similar treatment could be extended to the other phase as well.

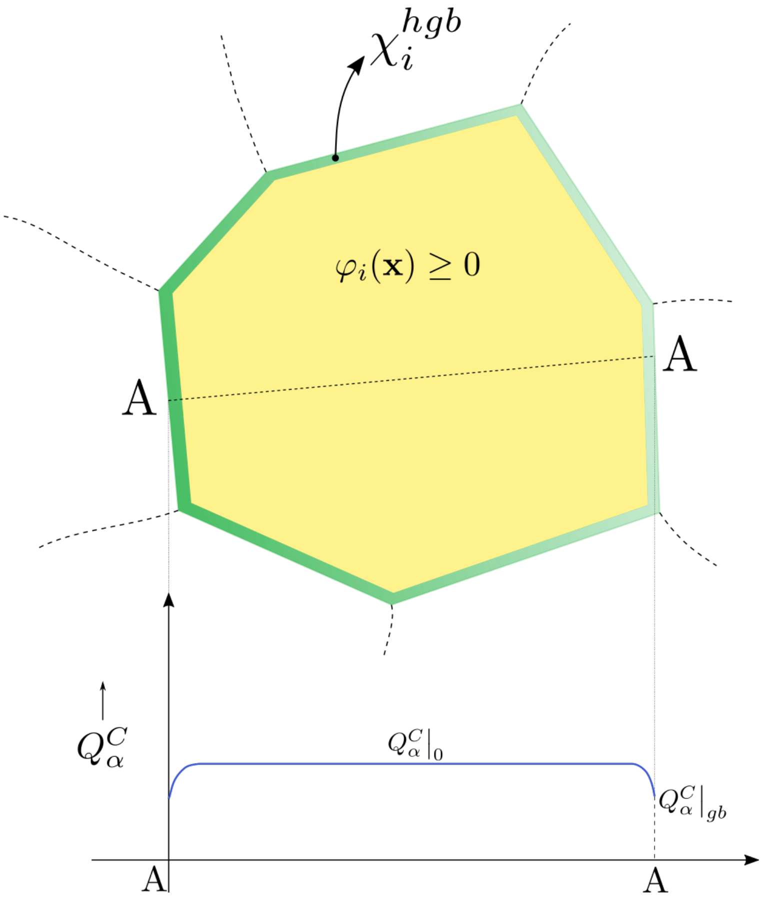

Figure 5.1: Illustration of the characteristic function within a particular grain to characterize the short-circuited region near the grain boundary

5.2.4 Switching to periodic boundary conditions

In the current numerical framework, the imposition of generic Robin-type boundary conditions for the solute concentration field [10] is complemented by the utilization of null Neumann conditions for the level-set functions. However, periodic boundary conditions (PBC) emerge as an appealing and widely used approach for modeling microstructural evolution in current state-of-the-art. PBCs offer a more versatile representation than Neumann or other boundary conditions, allowing emulation of a large system by simply considering a finite representative volume. They also potentially circumvent issues that can arise when phase interfaces interact with domain boundaries, commonly encountered with classical Neumann or Robin conditions. Most of the works in the literature based on phase-field method in the realm of DSSPT make use of regular meshes, and hence PBCs are generally easy to implement in this context. However, when employing adaptive meshes with remeshing, achieving mesh uniformity across opposing domain boundaries becomes challenging, posing numerical implementation difficulties. Notably, our current solvers lack the capability to incorporate PBCs within an adaptive meshing/ remeshing finite element context. Consequently, this stands as an area for potential future exploration and development.

5.2.5 Accounting for misfit elastic strains

During phase transformation, differences in lattice parameters between the crystal structures of involved phases can induce lattice distortion as the product phase tries to fit within the volume of the parent phase. This distortion leads to the incorporation of elastic misfit strains at interphase boundaries [11, 12].

Experimental findings suggest that these misfit strains could influence interface kinetics and hence the microstructural topology by contributing an additional driving pressure associated with elastic energy. For instance, during particle coarsening of dispersed second-phase particles in a matrix phase, the presence of misfit strains between the precipitate and matrix alters the equilibrium shape of the precipitate from a sphere. Instead, the equilibrium shape is now determined by minimizing both elastic and interfacial energies, often resulting in the formation of plate-shaped or rod-shaped precipitates under the influence of elastic misfits.

Integrating these effects into the current kinetic framework could thus enhance our understanding of interface kinetics, providing a more comprehensive description of the physics involved.

Elastic misfits play a critical role in diffusionless phase transformation, such as martensitic transformation, involving significant lattice distortions. Such transformation do not involve solute mass transport between the involved phases. Considering the influence of elastic misfits, it might be intriguing to extend the current numerical framework to simulate diffusionless phase transformations. This adaptation would require modifying the phase transformation driving pressure description accordingly. The time scales of topological evolution in such transformations are extremely short, demanding significantly smaller time step resolutions for precise capture of the topological evolution.

5.2.6 Improvements of computational efficiency

The primary focus of this work revolved around the numerical formulation and framework development, rather than emphasizing computational efficiency. However, considering the computational costs of the current framework, especially for large-scale cases, and anticipating even greater demands in a 3D context, a special emphasis could be put forward to enhance the computational efficiency of the numerical model.

Looking ahead, there's potential to adapt the current numerical formulation and concepts for integration with a new and efficient front tracking method called ToRealMotion [13–15]. This method is currently under development within our research team and exhibits promise in handling diverse microstructural evolution with significant gains in computational efficiency.

5.2.7 Simulation of recrystallization with phase transformation

The global objective of this work was to establish a kinetic framework capable of encompassing various evolution aspects simultaneously, notably in a high plastic deformation context. Several works have been successfully carried out in the realm of recrystallization in a monophase material using level-set method [16–20]. Consequently, the numerical tools and concepts devised for recrystallization could be integrated into the current framework and attempt to simulate recrystallization with phase transformation.

However, a significant challenge would be understanding the interplay between the nucleation models governing recrystallization and those relevant to phase transformation. Extending the nucleation criteria applied in recrystallization to phase transformation holds promise, as sites showcasing high dislocation density might also facilitate the germination of a new phase under right conditions. This aspect holds vast potential for extensive further research, including experimental analyses of these intricate microstructural evolution.

References

[1] A. Weber. “Keimbildung in übersättigten Gebilden”. In: *Zeitschrift für physikalische Chemie* 119.1 (1926), pp. 277–301.

[2] R. Becker and W. Döring. “Kinetische behandlung der keimbildung in übersättigten dämpfen”. In: *Annalen der physik* 416.8 (1935), pp. 719–752.

[3] J.W. Christian. *The theory of transformations in metals and alloys*. Newnes, 2002.

[4] V.I. Kalikmanov. “Classical nucleation theory”. In: *Nucleation theory*. Springer, 2012, pp. 17–41.

[5] B. Murgas et al. “Level-Set modeling of grain growth in 316L stainless steel under different assumptions regarding grain boundary properties”. In: *Materials* 15.7 (2022), p. 2434.

[6] B. Scholtes. “Development of an efficient level set framework for the full field modeling recrystallization in 3D”. PhD thesis. Université Paris sciences et lettres, 2016.

[7] J.C. Fisher. “Calculation of diffusion penetration curves for surface and grain boundary diffusion”. In: *Journal of Applied Physics* 22.1 (1951), pp. 74–77.

[8] B.S. Bokshtein, I.A. Magidson, and I.L. Svetlov. “On the diffusion in grains and grain boundaries”. In: *Fiz Met Metalloved* 6.6 (1958), pp. 1040–1052.

[9] I. Kaur and W. Gust. “Fundamentals of grain and interphase boundary diffusion”. In: *(No Title)* (1995).

[10] W. Wu et al. “Applying periodic boundary conditions in finite element analysis”. In: *SIMULIA community conference, Providence*. 2014, pp. 707–719.

[11] P. Fratzl, O. Penrose, and J. L. Lebowitz. “Modeling of phase separation in alloys with coherent elastic misfit”. In: *Journal of Statistical Physics* 95 (1999), pp. 1429–1503.

[12] P.W. Voorhees and W.C. Johnson. “The thermodynamics of elastically stressed crystals”. In: *Solid State Physics-Advances in Research and Applications*. Academic Press Inc, 2004, pp. 1–201.

[13] S. Florez et al. “A novel highly efficient Lagrangian model for massively multidomain simulation applied to microstructural evolutions”. In: *Computer Methods in Applied Mechanics and Engineering* 367 (2020), p. 113107.

[14] S. Florez et al. “A 2D front-tracking Lagrangian model for the modeling of anisotropic grain growth”. In: *Materials* 14.15 (2021), p. 4219.

[15] S. Florez et al. “Statistical behaviour of interfaces subjected to curvature flow and torque effects applied to microstructural evolutions”. In: *Acta Materialia* 222 (2022), p. 117459.

[16] M. Bernacki, R.E. Logé, and T. Coupez. “Level set framework for the finite-element modelling of recrystallization and grain growth in polycrystalline materials”. In: *Scripta Materialia* 64.6 (2011), pp. 525–528.

[17] B. Scholtes et al. “3D level set modeling of static recrystallization considering stored energy fields”. In: *Computational Materials Science* 122 (2016), pp. 57–71.

[18] L. Maire. “Full field and mean field modeling of dynamic and post-dynamic recrystallization in 3D – Application to 304L steel”. Theses. Université Paris sciences et lettres, Nov. 2018. URL: `https://pastel.archives-ouvertes.fr/tel-02418810`.

[19] M. Bernacki et al. *Numerical Modeling of Recrystallization in a Level Set Finite Element Framework for Application to Industrial Processes*. 2019.

[20] M. Bernacki. “Kinetic equations and level-set approach for simulating solid-state microstructure evolutions at the mesoscopic scale: state of the art, limitations, and prospects”. In: *Progress in Materials Science* (2023), p. 101224.

Appendices

A Integrated expressions for the solute drag pressure of Purdy-Brechet model

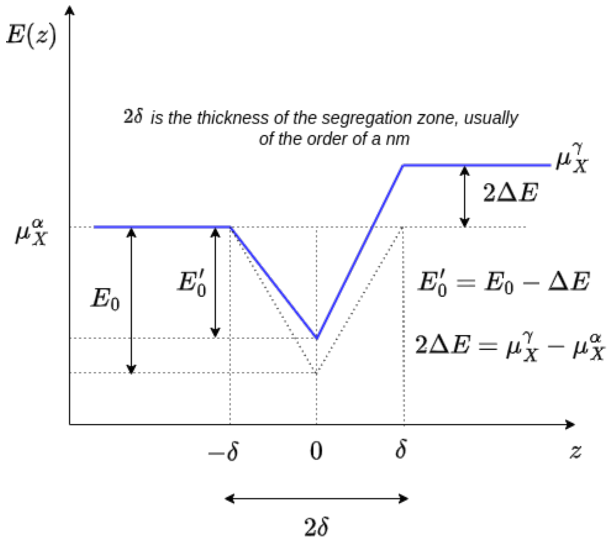

Figure A.1: Purdy and Brechet's assumption of the interaction energy profile, $E(z)$, assumed across an interface of width 2δ

For the considered interaction energy profile ($E(z)$) in Fig.A.1 and for constant interfacial solute diffusivity (D_Γ^X), the solute segregation profile ($x_X(z)$) obtained is given in Eq.(1.54). The solute drag pressure could be computed using the definition in Eq.(1.52) as:

$$\Delta G_{SD} = -x_X^0 N_V \int_{-\infty}^{\infty} \left(\frac{x_X}{x_X^0} - 1 \right) \frac{\partial E}{\partial z} dz. \tag{A.1}$$

From the $E(z)$ profile, $\partial E / \partial z$ could be easily computed and the integral could be rewritten as:

$$\begin{aligned} \Delta G_{SD} &= -x_X^0 N_V \left[\int_{-1}^{0} \left(\frac{x_X}{x_X^0} - 1 \right) (\Delta E - E_0)\, dz + \int_{0}^{1} \left(\frac{x_X}{x_X^0} - 1 \right) (\Delta E + E_0)\, dz \right], \\ &= I_1 + I_2 \end{aligned} \tag{A.2}$$

where,

$$\begin{aligned} I_1 &= -x_X^0 N_V \int_{-1}^{0} \left(\frac{x_X}{x_X^0} - 1 \right) (\Delta E - E_0)\, dz \\ I_2 &= -x_X^0 N_V \int_{0}^{1} \left(\frac{x_X}{x_X^0} - 1 \right) (\Delta E + E_0)\, dz \end{aligned} . \tag{A.3}$$

By prescribing the segregation profiles in Eq.(1.54) into the above Eq.(A.3), the integrals could be computed as:

$$
\begin{aligned}
I_1 = -\frac{x_X^0 N_V D_\Gamma^X \left(\Delta E - E_0\right)^2}{\left[k_B T v_n \delta + D_\Gamma^X \left(\Delta E - E_0\right)\right]^2} & \left[k_B T D_\Gamma^X \left(1 - e^{-\frac{k_B T v_n \delta + D_\Gamma^X \left(\Delta E - E_0\right)}{k_B T D_\Gamma^X}}\right)\right. \\
& \left. - k_B T v_n \delta - D_\Gamma^X \left(\Delta E - E_0\right)\right]
\end{aligned}
\tag{A.4}
$$

$$
\begin{aligned}
I_2 = -x_X^0 N_V \Bigg\{ & \frac{k_B T \left(\Delta E + E_0\right)}{k_B T v_n \delta + D_\Gamma^X \left(\Delta E + E_0\right)} \left[v_n \delta + \left(\frac{\left(D_\Gamma^X\right)^2 \left(\Delta E - E_0\right) e^{-\frac{k_B T v_n \delta + D_\Gamma^X \left(\Delta E - E_0\right)}{k_B T D_\Gamma^X}}}{k_B T v_n \delta + D_\Gamma^X \left(\Delta E - E_0\right)} \right.\right. \\
& \left.\left. + \frac{2 \left(D_\Gamma^X\right)^2 E_0 k_B T v_n \delta}{\left[k_B T v_n \delta + D_\Gamma^X \left(\Delta E - E_0\right)\right] \left[k_B T v_n \delta + D_\Gamma^X \left(\Delta E + E_0\right)\right]} \right) \left(1 - e^{-\frac{k_B T v_n \delta + D_\Gamma^X \left(\Delta E + E_0\right)}{k_B T D_\Gamma^X}}\right) \right] \\
& - \left(\Delta E + E_0\right) \Bigg\}
\end{aligned}
\tag{A.5}
$$

The sum of the above two expressions gives the Purdy-Brechet's solute drag driving pressure as a function of velocity norm (v_n).

B Thermodynamic data extraction using the TQ-interface

Regardless of the type of equilibrium conditions imposed, a full equilibrium calculation of the actual state is performed as a precursor before getting into the process of thermodynamic data extraction. This is highlighted by point E in a representative binary phase diagram illustrated in Fig.B.1. The process of data extraction is then dependent on the type of equilibrium conditions imposed.

For ortho-equilibrium (OE) conditions, the data extraction step is fairly straightforward as it is possible to seamlessly traverse anywhere on the true solvus surfaces (lines in 2D, indicated by solid lines in Fig.B.1) using the built-in function handles of ThermoCalc TQ-interface. The computation of equilibrium concentrations, the entropy difference between the two phases, or equilibrium phase fractions (f_R^α, f_R^γ, if requested) at temperature, T^R, is a matter of some explicit function calls to TQ-interface. If one wishes to compute the maximum driving pressure of nucleation of α phase ($\Delta g_V^\alpha\big|_{nuc}$), and also the corresponding nucleus compositions ($x_i^\alpha\big|_{nuc}$) at T^R, a new equilibrium calculation is performed by setting the status of the α phase as "dormant" (included in the calculation but not allowed to become stable). Now, with the help of relevant built-in function handles, the necessary data on nucleation could be extracted. In order to compute the slopes of the solvus lines, one needs to reach the point on the solvus line corresponding to the temperature of interest at the equilibrium compositions. These points are highlighted by M and N in Fig.B.1. To do so, the temperature constraint is dropped and set free, and instead, the phase fraction of one of the phases is constrained by fixing it to 0 (the status of the other phase is maintained as "entered"), i.e., $f_R^\alpha = 0$ to traverse over the $\gamma/(\alpha+\gamma)$ solvus line, and likewise $f_R^\gamma = 0$ for the other

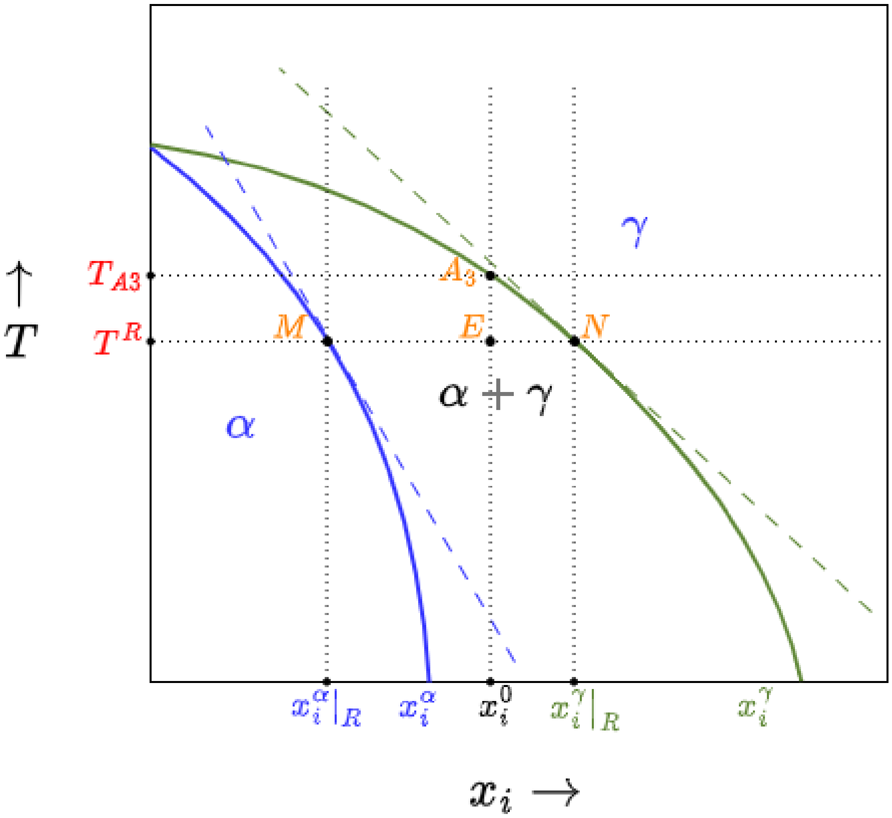

Figure B.1: A representative A-i binary phase diagram used to extract thermodynamic data at T^R under ortho-equilibrium conditions

solvus line. In addition, the concentration is set equal to that of the equilibrium concentration on the relevant solvus line. After performing the equilibrium calculation under these constraints, the M or N points could be exactly localized. Now the slopes could be computed using the built-in functions handles provided by TQ-interface. If one intends to compute the T_{A3} temperature, and the corresponding entropy difference at this temperature, the A_3 point (in Fig.B.1) needs to be localized on the solvus line. To do so, an equilibrium calculation is performed where the parent phase is set as "entered" to take part in the equilibrium calculation while the product phase fraction is fixed to 0, the temperature constraint is set free, and the compositions are set to be equal to the nominal compositions. Following this equilibrium calculation, we localize the point A_3, and the corresponding temperature could be extracted easily with functions calls. To obtain the entropy difference, the product phase is entered back into the calculation and the temperature is set to be equal to the extracted $A3$ temperature. $\Delta S_{A3}^{\gamma\alpha}$ could then be extracted after performing an equilibrium calculation.

For para-equilibrium (PE) conditions, the data extraction is quite involved, especially since the underlying quasi-binary phase diagram and hence its solvus lines are imaginary. So, an implicit approach is necessary involving manipulation of the status of a certain phase, carefully adjusting the concentration constraints and then performing the usual equilibrium calculation to reach the intended locations on these hypothetical solvus lines where the desired data has to be extracted.

The extraction of the PE concentrations, the molar driving force for nucleation (ΔG^n_{PE}), and the corresponding nucleus composition is relatively easy and involves only one call to a pertinent function handle of TQ-interface. However, to express the molar nucleation driving force in the form of driving pressure for nucleation, the molar volume of α phase (V^α_m) at the given conditions need to be separately computed. This is done by suspending the γ phase from the equilibrium calculation and by setting the composition equal to the α nucleus composition. The molar volume can then be computed by performing the usual equilibrium calculation and eventually invoking the relevant TQ-interface subroutine. The driving pressure for nucleation is then computed as $\Delta g^\alpha_V\big|_{nuc} = \Delta G^n_{PE}/V^\alpha_m$. Following this, to be able to perform any further calculations, the primary or the original equilibrium for the actual state needs to be recalculated. Under PE conditions, there are no default function handles to compute the phase fractions. They are instead computed by applying the Lever rule on the para-equilibrium concentrations (extracted previously). To compute the PE entropy difference between the two phases ($\Delta S^{\gamma\alpha}_{PE}$) at any temperature, the entropy of the individual phases is first computed and then their difference is calculated. A priori, in order to calculate the entropy of individual phases, one of the phases is suspended from taking part in the equilibrium calculation. Additionally, the concentration constraint is set equal to the PE concentration of the other phase. Subsequently, an equilibrium calculation is performed based on these constraints, and then the entropy can be determined by invoking the appropriate TQ-interface function handle. To compute the T^{PE}_{A3}, since there are no explicit approaches or function handles provided by TQ-interface, an iterative approach is adopted. The iterative method involves invoking the pertinent function handle to extract PE concentrations at any temperature T^* of an iteration and subsequently calculating the phase fractions and verifying if the phase fraction of the parent γ phase (f^γ) is close to 1.0 with a certain tolerance. An appropriate correction is applied to the temperature for the next iteration in case $f^\gamma(T^*)$ is not equal to 1.0 within the expected tolerances. The iteration is continued until $f^\gamma(T^*)$ converges to 1.0 or until the maximum number of iterations has been surpassed. The entropy difference at this T_{A3} temperature can then be computed as explained above by setting the temperature constraint equal to the T_{A3} temperature. In order to compute the slopes of the hypothetical solvus lines at T^R temperature, again there are no relevant function handles provided by TQ-interface for this scenario. The slopes ($1/\frac{\partial x^\alpha_C}{\partial T}, 1/\frac{\partial x^\gamma_C}{\partial T}$) are instead computed using a finite difference scheme. A set of closely spaced temperature points around the T^R temperature are chosen, and then the PE equilibrium concentrations are extracted for each of these temperature points to generate a discrete data-set, $\left(T_k, x^j_C\Big|^{PE}_{T_k}\right)$, $\forall j \in \{\alpha, \gamma\}$. In the current work, a fourth order centered difference scheme is used on this data-set to compute the slopes at T^R:

$$
\begin{aligned}
m^{\alpha/(\alpha+\gamma)}_{[A-C]_{PE}} &= \frac{1}{\frac{\partial x^\alpha_C}{\partial T}} \approx \frac{12h_T}{-\,x^\alpha_C\big|^{PE}_{T^R+2h_T} + 8\,x^\alpha_C\big|^{PE}_{T^R+h_T} - 8\,x^\alpha_C\big|^{PE}_{T^R-h_T} + x^\alpha_C\big|^{PE}_{T^R-2h_T}}, \\
m^{\gamma/(\alpha+\gamma)}_{[A-C]_{PE}} &= \frac{1}{\frac{\partial x^\gamma_C}{\partial T}} \approx \frac{12h_T}{-\,x^\gamma_C\big|^{PE}_{T^R+2h_T} + 8\,x^\gamma_C\big|^{PE}_{T^R+h_T} - 8\,x^\gamma_C\big|^{PE}_{T^R-h_T} + x^\gamma_C\big|^{PE}_{T^R-2h_T}}
\end{aligned}
\tag{B.1}
$$

where h_T is a small temperature step length.

RÉSUMÉ

La structure intrinsèque des matériaux s'adapte en réponse à des stimuli externes. La capacité d'adaptation se caractérise par des évolutions microstructurales qui peuvent impacter les performances du matériau, soulignant l'importance de comprendre et de prédire l'évolution des microstructures. L'intégration de la modélisation numérique est indispensable pour mieux comprendre ces phénomènes complexes. La numérisation des procédés d'ingénierie des matériaux est la force motrice qui permet de dessiner les matériaux de demain. Les avancées récentes des ressources computationnelles ont stimulé l'émergence de modèles numériques mésoscopiques, permettant des descriptions réalistes des aspects évolutifs. Au cours de la mise en forme à chaud des métaux comprenant une grande déformation plastique, l'évolution des alliages métalliques est caractérisée par une interaction complexe de multiples phénomènes simultanés qui déterminent la microstructure finale. Actuellement, les prédictions numériques mettent l'accent sur les évolutions microstructurales monophasiques ou isolent les transformations de phase, en négligeant souvent les contributions d'autres phénomènes concomitants. Cette approche restrictive pourrait empêcher une meilleure compréhension de l'évolution de la microstructure. Une formulation numérique en champ complet basée sur l'approche level-set avec un cadre cinétique généralisé adapté aux polycristaux métalliques biphasés est donc proposée dans ce travail. Ce schéma cinétique global est capable de prendre en compte de diverses transformations microstructurales, y compris la transformation de phase diffusive à l'état solide, la recristallisation et la croissance de grain. L'approche level-set permet de simuler efficacement la recristallisation et la croissance de grains dans le cadre d'une grande déformation plastique. Cependant, son potentiel pour traiter la transformation de phase diffusive à l'état solide restait peu approfondi. L'objectif principal de ce travail était donc de simuler la transformation de phase diffusive à l'état solide dans les polycristaux métalliques en utilisant le modèle numérique proposé afin d'explorer les possibilités de l'approche level-set dans ce contexte. Il est démontré que le modèle numérique reproduit efficacement les comportements physiques attendus, notamment pour la décomposition de l'austénite dans les aciers. Ce modèle numérique est évalué par rapport à un modèle semi-analytique performant. Le potentiel du cadre numérique proposé pour reproduire le caractère de la transformation de phase dans des microstructures polycristallines complexes est mis en évidence. La versatilité du modèle pour intégrer facilement d'autres évolutions complexes est également présentée.

MOTS CLÉS

Level-set, transformation de phase diffusive, décomposition de l'austénite, évolution de microstructure, ancrage par les solutés

ABSTRACT

The underlying fabric of materials adapts in response to external stimuli. This adaptability manifests through microstructural transformations that can significantly impact the material's performance, emphasizing the importance of understanding and predicting microstructural evolution. Integrating numerical modeling is pivotal for gaining deeper insights into these complex phenomena. Digitizing material engineering processes is the driving force behind shaping the materials of tomorrow. Recent progress in computational resources has spurred a demand for mesoscopic numerical models, offering realistic descriptions of evolutionary aspects. During hot metal forming involving high plastic deformation, the evolution of metallic alloys experiences a complex interplay of multiple simultaneous phenomena that shape their microstructure. Currently, cutting-edge numerical predictions emphasize single-phase microstructural changes or isolate phase transformations, often neglecting contributions from other coexisting phenomena. This narrow focus could impede a holistic understanding of microstructural evolution. A level-set-based full-field numerical formulation featuring a generalized kinetic framework tailored for two-phase metallic polycrystals is thus proposed in this work. This inclusive kinetic framework is capable of proficiently accommodating multiple microstructural transformations, including diffusive solid-state phase transformation, recrystallization, and grain growth. The level-set method proves effective in simulating recrystallization and grain growth under high plastic deformation. However, its potential in addressing diffusive phase transformation in the solid-state has not been extensively investigated. The primary focus of this work is thus to simulate diffusive solid-state phase transformation in metallic polycrystals using the proposed numerical framework to explore the potential of level-set method in this context. The numerical model is demonstrated to effectively reproduce expected physical characteristics, particularly emphasizing austenite decomposition in steels. The proposed level-set numerical model is benchmarked against a state-of-the-art sharp interface semi-analytical model. The potential of the proposed numerical framework to replicate the phase transformation behavior in complex polycrystalline microstructures is showcased. The versatility of the framework to seamlessly integrate other complex evolution is highlighted.

KEYWORDS

Level-set, Diffusive phase transformation, Austenite decomposition, Microstructure evolution, Solute drag